Shape formation via elastic instabilities

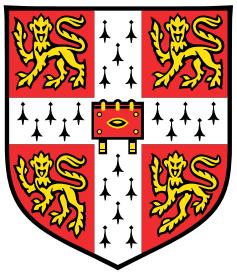

Nontawit Cheewaruangroj

Supervisor: Dr John S. Biggins

Department of Physics
University of Cambridge

This dissertation is submitted for the degree of
Doctor of Philosophy

Clare College March 2019

Declaration

I hereby declare that except where specific reference is made to the work of others, the contents of this dissertation are original and have not been submitted in whole or in part for consideration for any other degree or qualification in this, or any other university. This dissertation is my own work and contains nothing which is the outcome of work done in collaboration with others, except as specified in the text and Acknowledgements. This dissertation contains fewer than 60,000 words including summary/abstract, tables, footnotes and appendices.

Nontawit Cheewaruangroj
March 2019

Acknowledgements

Firstly, I would like to thank my supervisor, Dr John Simeon Biggins, who always provides a good advice and feedback throughout my PhD study, which would otherwise be impossible without his support. His guidance and motivation are valuable all the time of research and writing of this thesis. Thank you for always being patience and supportive.

My thanks also go to Prof. Neil Greenham, my undergraduate Director of Studies at Clare College, for giving me an opportunity to supervise Clare undergraduate students. Supervising makes me learn many things as well as drives my passion in physics. I am also grateful for his guidance during my undergraduate study, which was an important step in my life.

Thanks to the Royal Thai Government Scholarship for providing the funding for my PhD study as well as my undergraduate and master programmes.

I am also grateful to all support from my friends here in Cambridge, who make my student life more joyful and give many useful advices in both study and life. I will miss the time with everyone here.

Last but not least, I would like to thank my family: my parents, grandparents, and siblings, for their welfare and emotional support that help me carry on my study as well as taking a good care of me when I am home.

Abstract

When a solid object is placed under a load, it will deform to a new shape. Typically, these shape changes are modest and predictable, but sometimes, when a critical load is reached, the object will undergo an elastic instability and adopt a dramatically different and more complicated shape. Traditionally, elastic instabilities, such as buckling and wrinkling, have been studied as failure modes in stiff material systems. However, soft highly deformable solids, such as rubbers and biological tissues, can undergo instabilities without failure, offering the opportunity to utilize instabilities to change their shape. Furthermore, the large-strain mechanics of soft solids introduces many new instabilities not seen in traditional materials. Evolution is known to exploit soft elastic instabilities to sculpt brains, guts and other developing organs, and human engineers are interested in using them to create shape switching devices. There is a pressing need to understand what types of elastic instability exist, what shapes they form, and how these shapes can be controlled.

In this thesis, I address each of these challenges. I first present a new elastic instability, in which a cylindrical channel through a soft solid adopts a peristaltic shape upon loading with sufficient internal pressure. I then present a theory of pattern selection in surface elastic instabilities, including the compressive wrinkling of a stiff sheet on a soft substrate, and the gravitational fingering of a soft gel layer. Using higher order perturbation theory, I find, in both cases, that patterns of hexagonal dents are favoured, and I present a symmetry argument that hexagonal patterns are generic. Finally, I present a technique to manipulate the patterns formed in layer/substrate buckling by patterning the system with holes. This simple technique shows that instability patterns can be designed, opening new engineering opportunities.

Table of contents

List of figures

List of tables

Chapter 1

Introduction

1.1 What is a soft elastic solid?

When a solid object is subject to a mechanical load it will change shape. The defining feature of a purely elastic material is that, if the load is removed, the object recovers its original shape. Most conventional crystalline solids, such as metals, can only be strained elastically by a few percent before failure or plastic deformation. However, some soft solid materials, such as the rubber in an elastic band, can recover completely from strains of many hundreds of percent. This thesis centres on the mechanics of such highly deformable elastic materials, which we call soft elastic solids. The class of soft solids extends beyond rubbers and elastomers to include gels, sponges and many biological tissues including skins, muscles and brains.

The large elastic shape changes that are characteristic of soft solids cannot be described using the traditional linear theory of elasticity, but rather require a more sophisticated theory that captures the full non-linear nature of large deformation geometry [1]. In this introduction, I will discuss how to construct such a large strain theory, and how the resulting geometric non-linearities introduce a range of elastic instabilities into the mechanics of soft solids. Since these instabilities are geometric in origin, they are likely to be generic in all sufficiently deformable materials [2].

When a soft solid undergoes an elastic instability, it adopts a new and more complicated shape. These processes of shape formations can be used to understand morphogenesis — the origin of shapes in living organisms. Many examples of morphogenesis through soft-solid mechanical instabilities have been documented. For example, folding of mammalian brains is driven by growth of their outer layer relative to their inner layer [3–10]. Understanding these instabilities and their pattern formation would give us a deeper insight in developmental and evolutionary biology.

1.2 Theory of hyperelasticity

Soft elastic materials can undergo large deformations, which cannot be captured by linear elasticity. A better model—a hyperelastic model—is required to describe such large deformation mechanics [1]. Linear elastic energy can only describe behaviours in the small deformation regime. Thereby, we require an elastic energy that also works for a large deformation, which is called the hyperelastic energy. By finding and minimizing the hyperelastic energy, the configuration of such materials can then be determined.

1.2.1 Describing deformation

First of all, in order to describe the elastic behaviour, we need some quantities to describe the shape change (deformation) of an object. Let us consider an object under a deformation. The change in the position coordinate of the object from the deformation is defined as a displacement field,

$$\mathbf{u} = \mathbf{X} - \mathbf{x}, \tag{1.1}$$

where $\mathbf{X}$ is the coordinate of the final state (after deformation) and $\mathbf{x}$ is the coordinate of the initial state (before deformation). However, the displacement field, although having a very clear physical meaning, does not describe how the object is deformed. For example, a uniform displacement field simply translates material without shape change, and therefore without elastic energy. We need a quantity that can tell us the compression/stretch of the materials. To do this, we consider a small distance between two points in the object before and after the deformation. Consider $\mathbf{r} = \mathbf{x}_2 - \mathbf{x}_1$ and $\mathbf{R} = \mathbf{X}_2 - \mathbf{X}_1$ in Fig. 1.1. We can write $\mathbf{R}$ as

$$\begin{aligned}
\mathbf{R} &= \mathbf{X}_2 - \mathbf{X}_1 \\
&= \mathbf{X}(\mathbf{x}_2) - \mathbf{X}(\mathbf{x}_1) \\
&= \mathbf{X}(\mathbf{x}_1) + \frac{\mathrm{d}\mathbf{X}}{\mathrm{d}\mathbf{x}} \cdot (\mathbf{x}_2 - \mathbf{x}_1) - \mathbf{X}(\mathbf{x}_1) + \dots \\
&\approx \frac{\mathrm{d}\mathbf{X}}{\mathrm{d}\mathbf{x}} \cdot \mathbf{r},
\end{aligned} \tag{1.2}$$

where in the third line, $\mathbf{X}(\mathbf{x}_2)$ is Taylor expanded, using the fact that the distance between the two positions is small. Here, the dot " $\cdot$ " denotes matrix multiplication, in this case, between the tensor $\frac{\mathrm{d}\mathbf{X}}{\mathrm{d}\mathbf{x}}$ and the vector $\mathbf{r}$.

The transformation tensor $\frac{\mathrm{d}\mathbf{X}}{\mathrm{d}\mathbf{x}}$ captures the complete change of the vector $\mathbf{R}$ during the deformation including its rotation and its change in length. Thus, it captures all the

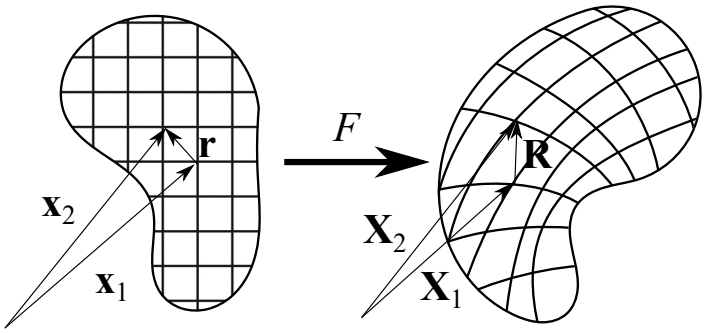

Fig. 1.1 Schematic diagram of transformation by the deformation gradient tensor F. The initial coordinate $\mathbf{x}$ is transformed to the deformed coordinate $\mathbf{X}$ through the deformation gradient.

information about the local shape change. This transformation tensor is called the deformation gradient, F, which, as the name suggests, can be written in terms of the gradient of the displacement field.

$$F = \frac{\mathrm{d}\mathbf{X}}{\mathrm{d}\mathbf{x}} = \frac{\mathrm{d}(\mathbf{x}+\mathbf{u})}{\mathrm{d}\mathbf{x}} = I + \nabla\mathbf{u}, \tag{1.3}$$

where I is the identity tensor, or in the indices notation $F_{ij} = \delta_{ij} + \partial_j u_i$, where $\partial_j u_i = \partial u_i / \partial x_j$ and δ_{ij} is the Kronecker delta. The deformation gradient maps the infinitesimal distance $\mathrm{d}\mathbf{x}$ into $\mathrm{d}\mathbf{X}$ such that $\mathrm{d}\mathbf{X} = F \cdot \mathrm{d}\mathbf{x}$ (Fig. 1.1).

However, the deformation gradient tensor includes more than just stretch and compression: it also includes a full description of material rotation, which is not associated with shape change, and hence should not change elastic energy. Using the polar decomposition theorem, the tensor F can be decomposed as a product of a rotation tensor and a symmetric deformation tensor [11, 12]. Fig. 1.2 describes the total transformation. We can write F as $U \cdot R_2$ or $R_1 \cdot V$, where R_1 and R_2 are rotation tensors, U and V are symmetric deformation tensors. These products must result in the same total transformations.

The symmetric deformation tensor can be diagonalized by using the principal directions as the basis:

$$U = \begin{pmatrix} \lambda_1 & 0 & 0 \\ 0 & \lambda_2 & 0 \\ 0 & 0 & \lambda_3 \end{pmatrix}, \tag{1.4}$$

where λ_1, λ_2 and λ_3 are the eigenvalues of U, which are equal to stretching ratio in each direction (Fig. 1.3). This means that the deformation is simpler, having only 3 independent components instead of 6, if we choose the right set of axes [11, 12].

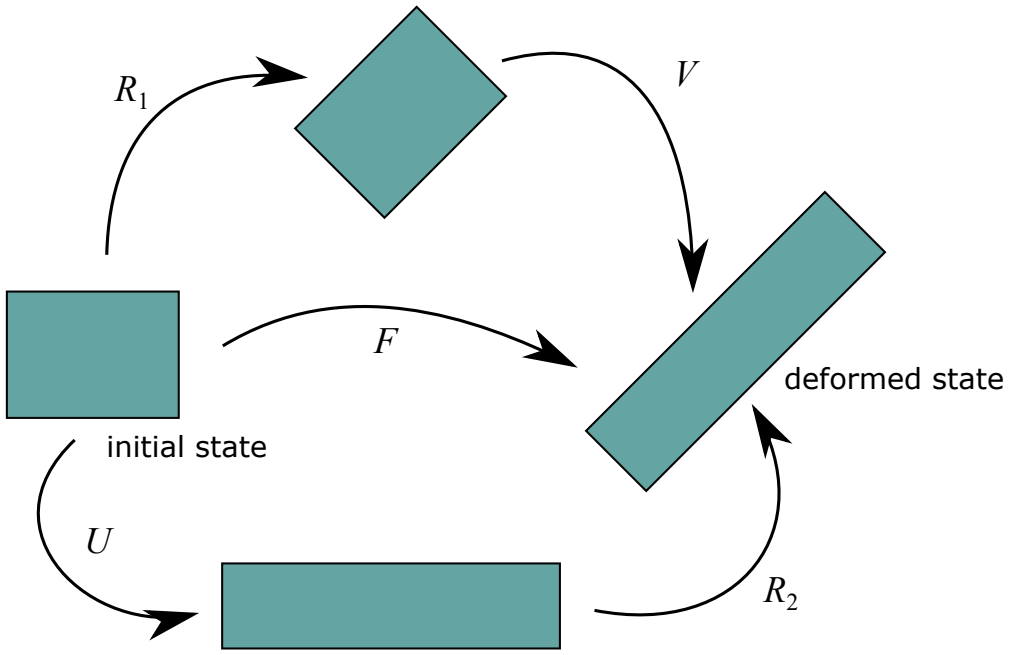

Fig. 1.2 Decomposing the deformation gradient tensor F into rotation R and symmetric deformation U and V.

1.2.2 Hyperelastic energy

We now turn to finding a suitable hyperelastic energy function to assign to the deformation gradient F. We expect this function to depend on the values of λ_1, λ_2 and λ_3. Hence, we must find some scalar quantities related to the deformation that are invariant under either the rotation of the initial state, R_1, or the final state, R_2. One possible way to obtain such a quantity is by contracting F with itself, i.e. $F_{ij}F_{ij}$, using Einstein summation convention, or equivalently $\mathrm{Tr}(F \cdot F^T)$ as

$$\begin{aligned}\mathrm{Tr}(F \cdot F^T) &= \mathrm{Tr}(U \cdot R_2 \cdot R_2^T \cdot U^T) = \mathrm{Tr}(U \cdot U^T) \\ &= \mathrm{Tr}(F^T \cdot F) \\ &= \mathrm{Tr}(V^T \cdot R_1^T \cdot R_1 \cdot V) = \mathrm{Tr}(V \cdot V^T) \\ &= \lambda_1^2 + \lambda_2^2 + \lambda_3^2, \end{aligned} \tag{1.5}$$

which does not depend on the rotation of either the initial or final states. Gratifyingly, we can evaluate this quantity using either V or U, to see that it only depends on the stretch ratios λ_1,

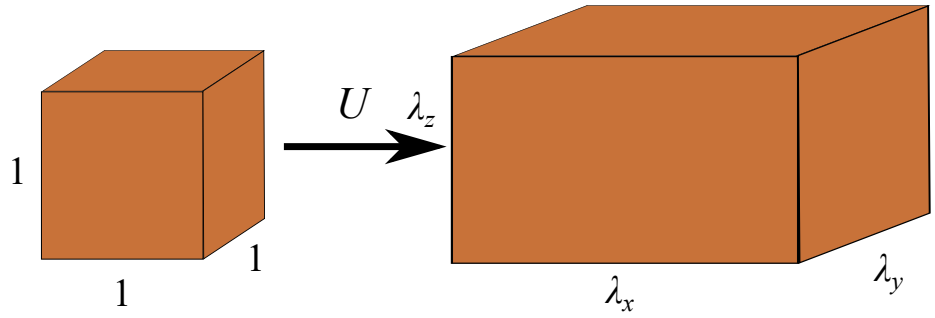

Fig. 1.3 Symmetric deformation tensor acting on a unit cube.

λ_2, and λ_3. The conventional invariant quantities derived from $F \cdot F^T$ are [11, 12]

$$I_1 = \mathrm{Tr}(F \cdot F^T) = \lambda_1^2 + \lambda_2^2 + \lambda_3^2 \tag{1.6}$$

$$I_2 = \frac{1}{2}\left[(\mathrm{Tr}(F \cdot F^T))^2 - \mathrm{Tr}((F \cdot F^T)^2)\right] = \lambda_1^2\lambda_2^2 + \lambda_2^2\lambda_3^2 + \lambda_3^2\lambda_1^2 \tag{1.7}$$

$$I_3 = J^2 = \mathrm{Det}(F \cdot F^T) = \lambda_1^2\lambda_2^2\lambda_3^2. \tag{1.8}$$

The scalar J has a simple physical interpretation: it is equal to the ratio of the volume of the final state to that of the initial state. As we only need three scalar quantities to determine the energy, we can use I_1, I_2 and I_3 to fully describe the energy. Therefore, the general from of the elastic energy density function can be written as

$$W = W(I_1, I_2, I_3). \tag{1.9}$$

With the form of hyperelastic energy density, one can find how an object deforms by minimizing the energy to find the optimal configuration in terms of $\mathbf{u}$ or F.

1.2.3 Incompressibility

For many soft materials, incompressibility is a good approximation. We can model soft materials as cross-linked polymers, where the polymers act as fluids with a finite large bulk modulus, κ. As fluids, they have no resistance to shear. However, cross-linking adds the shear modulus, μ, to the polymers. The bulk modulus of soft solids is around $10^9 - 10^{10}$ Pa, like fluids, whereas the shear modulus is around $10^4 - 10^6$ Pa. To see how much volume would change for a given stress σ, we write the strain ε as

$$\varepsilon \approx \frac{\sigma}{E}, \tag{1.10}$$

where E is the appropriate elastic modulus. This means that the ratio of the volumetric strain to the shear strain is proportional to the ratio μ/κ. We see that for soft materials $\mu/\kappa \approx 10^{-4}$, which means the change in volume is very small, and hence negligible in most cases.

A way to impose the incompressibility condition in the deformation is by constraining the principal stretches such that

$$\lambda_1\lambda_2\lambda_3 = 1, \tag{1.11}$$

or equivalently, and more generally, by setting

$$\mathrm{Det}(F) = 1. \tag{1.12}$$

I will model the solid as incompressible for most of the work in this thesis, using (1.12), except for the finite element analysis and some special cases where the solid will be modelled as compressible.

1.2.4 Minimizing hyperelastic energy

Once we have a hyperelastic energy, the shape changing behaviour of the solid will be determined by minimizing this energy subject to suitable external constraints such as an applied compression. This is generally done by considering the variation in the total energy E. For a hyperelastic energy density $W(F) = W(\mathbf{u}'(\mathbf{x}))$, the total energy is given by

$$E = \int_V W(\mathbf{u}'(\mathbf{x}))dV, \tag{1.13}$$

where V is the volume of the object in the reference coordinate, subjected to boundary conditions. The energy can be minimized with respect to variation in $\mathbf{u}$, $\delta E/\delta\mathbf{u} = 0$, by using the Euler-Lagrange equation

$$\frac{\partial W}{\partial u_i} - \sum_{j=1}^{3} \frac{\mathrm{d}}{\mathrm{d}x_j}\left(\frac{\partial W}{\partial(\partial_j u_i)}\right) = 0 \qquad \text{for} \quad i = 1,2,3. \tag{1.14}$$

These bulk equations are augmented by natural or essential boundary conditions

$$\sum_{j=1}^{3} \frac{\partial W}{\partial(\partial_j u_i)}(\mathbf{x})\hat{s}_j = 0 \quad \text{or} \quad u_i(\mathbf{x}) = 0 \quad \forall \mathbf{x} \in \partial V \quad \text{for} \quad i = 1,2,3, \tag{1.15}$$

where $\hat{\mathbf{s}}$ is the normal vector area to the boundary ∂V. Since W is independent of $\mathbf{u}$, the first term in (1.14) vanishes. Equation (1.14) can then be rewritten as

$$\nabla \cdot \boldsymbol{\sigma} = 0, \tag{1.16}$$

which are simply the mechanical equilibrium conditions of the first Piola-Kirchhoff (PK1) stress tensor, $\boldsymbol{\sigma}$, or the engineering stress, defined as

$$\boldsymbol{\sigma} = \frac{\mathrm{d}W}{\mathrm{d}F}. \tag{1.17}$$

The Cauchy stress tensor, T, or true stress tensor, is related to the PK1 stress tensor by

$$T = \frac{1}{J}\boldsymbol{\sigma}^T \cdot F^T. \tag{1.18}$$

This is the reason why, as we will see in the next chapters, the PK1 stress tensor appears regularly, as opposed to the Cauchy stress tensor, in my analysis as it emerges naturally from the energy minimization. Note that the PK1 stress tensor is an asymmetric two-point tensor like the deformation gradient, meaning that one index is attached to the initial state and the other to the final state and $\sigma_{ij} \neq \sigma_{ji}$. The boundary conditions (1.15) corresponds to the free ($\boldsymbol{\sigma} \cdot \hat{\mathbf{s}} = \mathbf{0}$) and fixed ($\mathbf{u} = 0$) boundary conditions or a mixture of them. For example, if a solid if clamped on one face and free on the remaining faces, the displacement on the clamped face is fixed whereas the stress must be zero on the other faces.

Alternatively, instead of fully minimizing the energy with respect to the displacement field, it is often helpful to use a function with some parameters as a trial solution for the displacement field and then minimize the energy with respect to the parameters. For instance, a sinusoidal solution, $A\sin(kx)$, would be a good trial solution for an instability with a periodic boundary condition. The parameters A and k can be determined by minimizing the total energy. This method, also known as the Ritz method, gives, at least, an energy upper bound [13], and is often helpful in building an intuitive understanding of instabilities. The finite element method, discussed in Chapter 2, follows this same approach, but with a very much larger class of parameters, and the minimization done on a computer.

If the system is coupled to external forces, we can include the external forces by adding their virtual work or potential energy into the total energy before minimization. For instance, a one-dimensional solid of length L with one end clamped at $x = 0$ is pulled by a constant force F_{ext} at $x = L$. The total energy can be modified as

$$E \longrightarrow E - F_{ext}u(L) = \int_0^L (W - F_{ext}u'(x))dx, \tag{1.19}$$

or equivalently the energy density becomes

$$W \longrightarrow W - F_{ext}u'(x). \tag{1.20}$$

The stress now becomes

$$\sigma \longrightarrow \sigma - F_{ext}. \tag{1.21}$$

This does not affect the Euler-Lagrange equation as the extra term is divergence-free. However, the boundary condition at $x = L$ will need to take the extra stress term into account.

For an incompressible solid, we can include the incompressibility condition, $\mathrm{Det}(F) = 1$, by adding a Lagrange multiplier term to the total energy:

$$W \longrightarrow W - P(\mathbf{x})(\mathrm{Det}(F) - 1), \tag{1.22}$$

where $P(\mathbf{x})$ is the pressure Lagrange multiplier (it is called pressure as the extra term is associated with volume change). Minimizing E with respect to variation in $P, \delta E/\delta P = 0$, gives the incompressible condition

$$\mathrm{Det}(F) = 1 \tag{1.23}$$

as intended.

We see that by minimizing the energy of the system, subjected to boundary conditions, the equilibrium of the system can be found. This can include any types of boundary conditions, effect of external forces as well as applying volume conservation. In the next subsection, we look at what the hyperelastic energy density looks like.

1.2.5 Neo-Hookean model

The simplest form of the energy density that can be written is

$$W = C(I_1 - 3) = C(\mathrm{Tr}(F \cdot F^T) - 3) = \frac{\mu}{2}(\mathrm{Tr}(F \cdot F^T) - 3) = \frac{\mu}{2}(\lambda_1^2 + \lambda_2^2 + \lambda_3^2 - 3), \tag{1.24}$$

where C is a constant. We subtract three from $\mathrm{Tr}(F \cdot F^T)$ to make W at the relaxed state equal to zero. The form of equation matches with that of linear elasticity provided that $C = \mu/2$, where μ is the shear modulus. This energy form is known as the neo-Hookean energy density [14]. To impose the incompressibility, one usually adds a Lagrange multiplier term to the energy density function:

$$W = \frac{\mu}{2}(\mathrm{Tr}(F \cdot F^T) - 3) - P(\mathrm{Det}(F) - 1). \tag{1.25}$$

We will be using the neo-Hookean energy density (1.24) in our calculation as it is simple yet powerful to describe large deformations, exhibiting non-linear relationship between applied stress and strain, which gives rise to elastic instabilities [15–21]. The PK1 stress and the Cauchy stress can be calculated from (1.17, 1.18) as

$$\sigma = \mu F - PF^{-T}, \tag{1.26}$$

$$T = \mu F \cdot F^T - PI, \tag{1.27}$$

where P can be solved from the incompressibility condition.

A compressible version of the neo-Hookean energy also exists

$$\begin{aligned} W &= C(\bar{I}_1 - 3) + D(J-1)^2 \\ &\approx \frac{\mu}{2}\left[\frac{\mathrm{Tr}(F\cdot F^T)}{(\mathrm{Det}(F))^{2/3}} - 3\right] + \frac{\kappa}{2}(\mathrm{Det}(F)-1)^2, \qquad \text{for } \kappa \gg \mu \end{aligned} \tag{1.28}$$

where $\bar{I}_1 = I_1/J^{2/3}$, $J = \mathrm{Det}(F)$ and D is another elastic constant, which is related to the Lamé parameter, λ, in linear elasticity [22]. For material with small compressibility, $\kappa \gg \mu$, where κ is the bulk modulus, we can approximate $\lambda \approx \kappa$. The PK1 and Cauchy stress for compressible neo-Hookean solids can be written as

$$\sigma = \left[\left(B - \frac{\mathrm{Tr}B}{3}I\right)\frac{\mu}{J^{2/3}} + \kappa J(J-1)I\right]F^{-T}, \tag{1.29}$$

$$T = \left(B - \frac{\mathrm{Tr}B}{3}\right)\frac{\mu}{J^{5/3}} + \kappa(J-1)I, \tag{1.30}$$

where $B = F\cdot F^T$. I will use the energy density (1.28) in the numerical simulation, where perfect incompressibility is difficult to implemented.

Another reason why the neo-Hookean elasticity is a good model is that the energy density can also be derived from a microscopic picture of the materials [23, 24]. The material is modelled as cross-linked long chain molecules (i.e. elastomers), see Fig. 1.4, which are accurate for rubbers and polymer gels. Consider a long chain polymer composed of N rods of length a freely jointed together. The whole chain can be modelled by a random walk. The mean square end-to-end length of the chain is

$$\left\langle \mathbf{R}^2 \right\rangle = a^2 N = aL, \tag{1.31}$$

where $\mathbf{R}$ is the end-to-end vector of the polymer chain and $L = Na$ is the contour length of

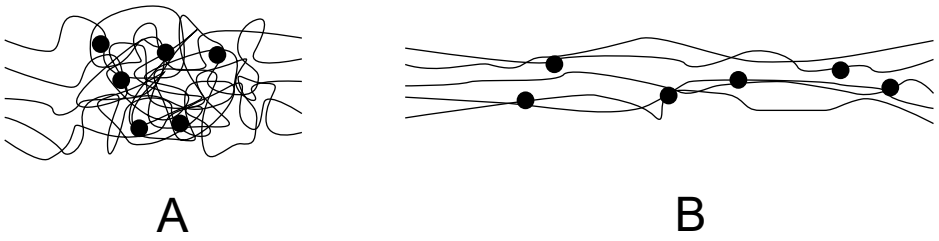

Fig. 1.4 A cross-linked polymer system (A) before and (B) after applying deformation. Dots denote cross-linking of the polymer chains.

the chain. The partition function can be written as

$$Z(\mathbf{R}) = p(\mathbf{R})Z, \tag{1.32}$$

where Z is the partition function of the chain and $p(\mathbf{R})$ is the probability to have the end-to-end vector $\mathbf{R}$, which is given by a Gaussian distribution

$$p(\mathbf{R}) = \left(\frac{3}{2\pi aL}\right)^{3/2} e^{-\frac{3\mathbf{R}^2}{2aL}}, \tag{1.33}$$

where aL is the variance of the distribution from (1.31). The free energy $\mathscr{F}$ of the polymer chain can be calculated by using $\mathscr{F} = -k_{\mathrm{B}}T \ln Z(\mathbf{R})$:

$$\mathscr{F}(\mathbf{R}) = \mathscr{F}_0 + k_{\mathrm{B}}T \left(\frac{3\mathbf{R}^2}{2aL}\right), \tag{1.34}$$

where $\mathscr{F}_0$ is a constant. The deformation gradient F can be incorporated into the free energy by using the relation

$$\mathbf{R} = F \cdot \mathbf{R}_{\mathrm{i}}, \tag{1.35}$$

where $\mathbf{R}_{\mathrm{i}}$ is the initial value of $\mathbf{R}$. The free energy becomes

$$\mathscr{F}(\mathbf{R}) = \frac{3}{2} k_{\mathrm{B}}T \, \frac{\mathbf{R}_{\mathrm{i}}^T \cdot F^T \cdot F \cdot \mathbf{R}_{\mathrm{i}}}{aL}. \tag{1.36}$$

Taking the average of $\mathscr{F}(\mathbf{R})$ over the span of $\mathbf{R}_{\mathrm{i}}$:

$$\mathscr{F} = \frac{3k_{\mathrm{B}}T}{2aL} \left\langle \mathbf{R}_{\mathrm{i}}^T \cdot F^T \cdot F \cdot \mathbf{R}_{\mathrm{i}} \right\rangle \tag{1.37}$$

$$= \frac{1}{2} k_{\mathrm{B}}T \, \mathrm{Tr}(F^T \cdot F), \tag{1.38}$$

where we have used $\left\langle R_i^{\mathrm{i}} R_j^{\mathrm{i}} \right\rangle = \frac{1}{3} aL\delta_{ij}$. For elastomers, the polymer chains are cross-linked in to a solid. The total energy can be evaluated by simply adding the contribution from each chain. Multiplying (1.38) by the number of chains per unit volume, n_{c}, we obtain the total energy density

$$W = \frac{1}{2} n_{\mathrm{c}} k_{\mathrm{B}} T \operatorname{Tr}(F^T \cdot F). \tag{1.39}$$

This is the same as (1.24) with $\mu = n_{\mathrm{c}} k_{\mathrm{B}} T$.

1.2.6 Other hyperelastic models

The neo-Hookean model can often describe a large deformation very well up to many times the original length, particularly in lightly cross-linked, highly extendable networks [24]. However, some real materials especially biological tissues cannot be stretched to such lengths: they have finite extensibilities. A simple model that is used to accounts these finite extensibilities is known as the Gent model [25]. The finite extensibility is based on the finite size of polymer chains that are constituents of rubbers [26, 27]. This is phenomenologically done by introducing a singularity to the energy density when the invariant tensor I_1 reaches a limiting value I_m. Then energy density function is given by [25]

$$W_{\mathrm{Gent}} = -\frac{\mu J_m}{2} \ln\left(1 - \frac{I_1 - 3}{J_m}\right), \tag{1.40}$$

where μ is the shear modulus and $J_m = I_m - 3$. The Gent model behaves similar to the neo-Hookean model except when I_1 is close to I_m, where the energy diverges. In the limit where $I_m \to \infty$, the Gent model reduces to the neo-Hookean model:

$$W \approx -\frac{\mu J_m}{2}\left(-\frac{I_1 - 3}{J_m}\right) = \frac{\mu}{2}(I_1 - 3). \tag{1.41}$$

The PK1 and Cauchy stress for incompressible Gent material are

$$\sigma_{\mathrm{Gent}} = -PF^{-T} + \frac{\mu J_m}{J_m - I_1 + 3} F \tag{1.42}$$

$$T_{\mathrm{Gent}} = -PI + \frac{\mu J_m}{J_m - I_1 + 3} B. \tag{1.43}$$

The Gent model is simple yet useful to describe rubber as well as much stiffer materials such as biological tissues [28]. For rubber, the value of J_m ranges from 35 to 100. In contrast, biological tissues are much stiffer and therefore take smaller values of J_m. For example, J_m for human artery wall is on the order of 0.4–2.3 [21, 29, 30].

Another common hyperelastic model is known as the Mooney-Rivlin model. The neo-Hookean model only has one parameter, the shear modulus (or two parameters for the compressible version). To describe real materials more accurately, more parameters might be required. Mooney [31] and Rivlin [32] proposed a phenomenological model which offers a simple form of energy density with two parameters by using a linear combination of two invariants, I_1 and I_2. The energy density for an incompressible Mooney–Rivlin material is given by

$$W_{\mathrm{MR}} = C_1(I_1-3)+C_2(I_2-3) \tag{1.44}$$

$$= C_1(\mathrm{Tr}(F\cdot F^T)-3)+C_2\left[\frac{(\mathrm{Tr}(F\cdot F^T))^2-\mathrm{Tr}((F\cdot F^T)^2)}{2}-3\right], \tag{1.45}$$

where C_1 and C_2 are constants. For consistency with linear elasticity, these two constants are related to the shear modulus by

$$\mu = 2(C_1+C_2). \tag{1.46}$$

The constants C_1 and C_2 are determined by fitting the predicted stress to the experimental data. For compressible solid, the energy density function is

$$W_{\mathrm{MR}} = C_1(\bar{I}_1-3)+C_2(\bar{I}_2-3)+D_1(J-1)^2, \tag{1.47}$$

where $\bar{I}_1 = I_1/J^{2/3}$ and $\bar{I}_2 = I_2/J^{4/3}$. The constant D_1 is related to the bulk modulus in the limit of small strains by

$$\kappa = 2D_1. \tag{1.48}$$

The stress tensors can be calculated as

$$\sigma_{\mathrm{MR}} = \left[2D_1(J-1)I+2(C_1+\bar{I}_1C_2)\bar{B}-2C_2\bar{B}\cdot\bar{B}-\frac{2}{3}(C_1\bar{I}_1+2C_2\bar{I}_2)I\right]F^T, \tag{1.49}$$

$$T_{\mathrm{MR}} = \frac{1}{J}\left[2D_1(J-1)I+2(C_1+\bar{I}_1C_2)\bar{B}-2C_2\bar{B}\cdot\bar{B}-\frac{2}{3}(C_1\bar{I}_1+2C_2\bar{I}_2)I\right], \tag{1.50}$$

where $\bar{B} = J^{-2/3}B = J^{-2/3}F\cdot F^T$. For incompressible solid, this becomes

$$\sigma_{\mathrm{MR}} = 2(C_1+I_1C_2)F-2C_2B\cdot F-\frac{2}{3}(C_1I_1+2C_2I_2)F^{-T}, \tag{1.51}$$

$$T_{\mathrm{MR}} = 2(C_1+I_1C_2)B-2C_2B\cdot B-\frac{2}{3}(C_1I_1+2C_2I_2)I. \tag{1.52}$$

Fig. 1.5 compares the engineering stress for a uniaxial extension such that the principal stretches are given by $\lambda_1=\lambda$ and $\lambda_2=\lambda_3=1/\sqrt{\lambda}$ for incompressible neo-Hookean solid,

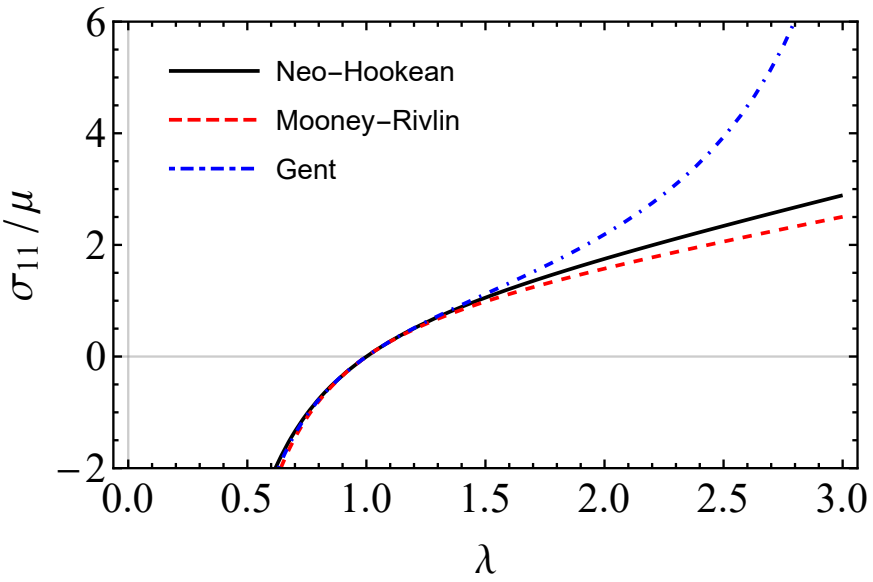

Fig. 1.5 Comparison of different hyperelastic models: the engineering stress as a function of uniaxial stretch, λ for incompressible neo-Hookean, Mooney-Rivlin ($C_1 = 1.6\mu, C_2 = 0.4\mu$) and Gent materials ($J_m = 20$).

Mooney-Rivlin solid with $C_1 = 1.6\mu$ and $C_2 = 0.4\mu$ and Gent sold with $J_m = 20$. The plot clearly shows the divergence of the stress as the stretching becomes large in the Gent model as opposed to the other two models. Generally, the neo-Hookean model is ideal for the case where the finite extensibility is irrelevant such as for very stretchy hydrogels or when the deformation is not too large. However, the Mooney-Rivlin offers another parameter, which can be useful to fit with experimental results when a one-parameter model such as the neo-Hookean does not suffice. Otherwise, the Gent model would be more suitable when finite extensibility becomes important.

1.3 Elastic instabilities

When a soft solid is placed under a critical load it may completely change its shape. This mechanism is known as an elastic instability [2]. When the load is removed, it recovers the original shape. Examples of elastic instabilities are wrinkling of skins and buckling of beams under compression. This shape changing essentially arises from energy minimization. At some critical 'threshold', the new non-trivial shape has lower energy than the original simple shape. For instance, the energy cost of bending from wrinkles on skin is lower than the compressive strain energy if the skin simply shrinks.

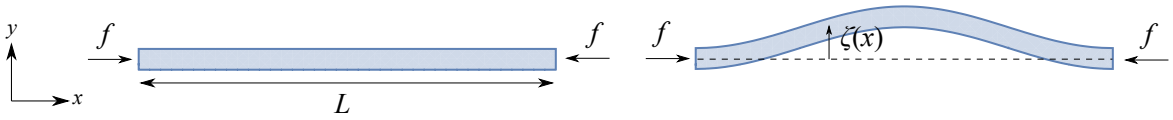

Fig. 1.6 Schematic diagram for Euler buckling. (left) $f < f_c$. (right) $f > f_c$.

Elastic instabilities are common in developmental biology. Evolution uses elastic instabilities as a way to form shapes out of the biological tissues. As mentioned, brain folds are caused by an elastic instability driven by growth [3–10]. Other examples are the formation of villi and looping of avian guts [33–36], folding in tubular organs [37–43], fingerprint pattern formation [44, 45], and creasing on cancerous tumours surface [46]. In addition to mechanical compression and biological growth, elastic instabilities can also be induced by various interesting means such as applied electric [47–50] and magnetic fields [51], swelling [52–55], surface tension [56–61] and gravity [62–64]. These instabilities also play a role in engineering. Classical buckling in engineering often leads to failure, and need to be prevented, but mechanical instabilities can also be utilized: for example, thermostats in kettles work via the snap-through instabilities of a bi-metal dome, and car crumple zones are designed to buckle in a way that absorbs maximum energy.

In this section, I will give a physically motivated overview of some well-studied elastic instabilities, and show how energy minimization can be used in each case to understand the instability. I will focus, in each case, on demonstrating the geometric origin of the instability via the neo-Hookean elastic energy. During the discussion, I will also demonstrate several different energy minimization techniques for understanding instabilities, including solving the full non-linear energy minimization equations, linear stability analysis around a base state, arguments from one-dimensional convexity, and arguments using trial solutions.

1.3.1 Euler buckling

The most well-known and simplest instability cannot be other than the Euler buckling. When a column of elastic solid is subject to compressive stress, it suddenly becomes deflected or buckled [65]. A characteristic of Euler buckling is that it occurs only when the compressive stress exceeds a certain threshold (Fig. 1.6). This is a feature of mechanical instabilities. The occurrence of the instability at a threshold is a bifurcation of the solution to mechanical equilibrium.

To understand this instability, we need to look at how buckling changes the energy of the system. Let us consider a two-dimensional thin incompressible neo-Hookean beam of length L with a shear modulus μ described with small vertical displacement field, $\zeta(x)$. The beam is under a compressive forces f as in Fig. 1.6. A beam segment is bent such that it

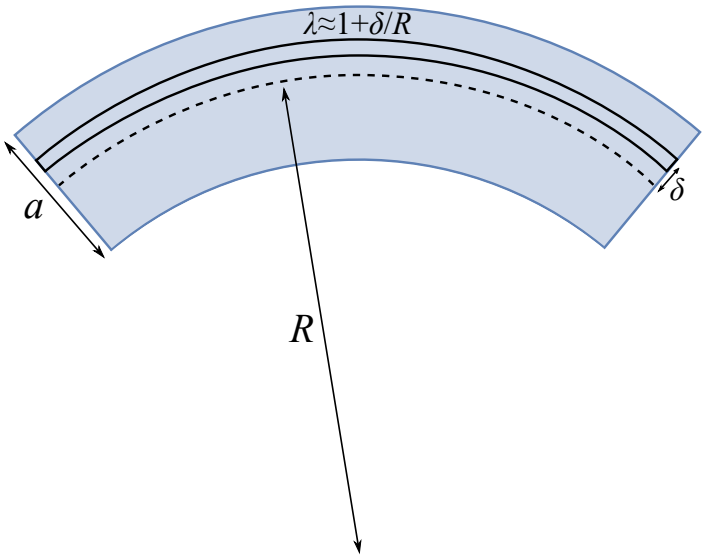

Fig. 1.7 Schematic diagram for bending of a beam.

becomes an arc with a radius of curvature $R \gg a$. The middle plane of the beam, signified by a dashed line in Fig. 1.7, is assumed to remain the same length while the upper and lower parts are stretched and compressed respectively. At distance δ from the middle plane, the beam is stretched by $\lambda = 1 + \delta/R$ and thinner by a factor of λ to conserve the volume. The deformation gradient can be written as

$$F = \begin{pmatrix} \lambda & 0 \\ 0 & 1/\lambda \end{pmatrix}. \tag{1.53}$$

The total energy E consists of the bending energy, E_B, and the compressive strain energy, E_C. The bending energy can be calculated from the neo-Hookean energy density (1.24),

$$E_B = \int_0^L \int_{-a/2}^{a/2} \frac{1}{2}\mu \left[\mathrm{Tr}(F \cdot F^T) - 2\right] d\delta dx, \tag{1.54}$$

where $\mathrm{Tr}(F \cdot F^T)$ is subtracted by 2 instead of 3 as it is a two-dimensional system. Substituting the form of F gives

$$E_B = \int_0^L \int_{-a/2}^{a/2} \frac{1}{2}\mu \left[\left(1+\frac{\delta}{R}\right)^2 + \frac{1}{\left(1+\frac{\delta}{R}\right)^2} - 2 \right] d\delta dx \tag{1.55}$$

$$\approx \int_0^L \int_{-a/2}^{a/2} \frac{1}{2}\mu \left(2\frac{\delta^2}{R^2}\right) d\delta dx \tag{1.56}$$

$$= \int_0^L \frac{1}{2}\mu \left(\frac{a^3}{4R^2}\right) dx, \tag{1.57}$$

where in the second line, the terms are Taylor expanded. The radius of curvature is related to the vertical displacement field by $1/R \approx \zeta''(x)$ for small deflections. The bending energy of the beam can therefore be written as

$$E_B = \int_0^L \frac{1}{2} B\zeta''(x)^2 dx, \tag{1.58}$$

where $B = \mu a^3/4$ is called the bending modulus of the beam. The compressive strain energy can be calculated by the work done against f

$$E_C = -f\Delta L \tag{1.59}$$

$$= -f \int_0^L \left(\sqrt{1+\zeta'(x)^2} - 1 \right) dx \tag{1.60}$$

$$= -\int_0^L \frac{1}{2} f\zeta'(x)^2 dx, \tag{1.61}$$

where ΔL is the change in the horizontal length assuming that the beam is inextensible. The total energy is therefore

$$E = E_B + E_C = \int_0^L \frac{1}{2} \left(B\zeta''(x)^2 - f\zeta'(x)^2 \right) dx. \tag{1.62}$$

To minimize this energy, I will use a trial function of the form

$$\zeta(x) = A\sin(kx), \tag{1.63}$$

where $k = n\pi/L$, with $n = 1, 2, 3, ...$, to satisfy the boundary conditions $\zeta(0) = \zeta(L) = 0$. With this ansatz, the total energy becomes

$$E = \frac{L}{4}\left(Bk^4A^2 - fk^2A^2\right). \tag{1.64}$$

The energy decreases as the amplitude grows if $f > k^2B$. The smallest $k = \pi/L$ would give the smallest force required to initiate buckling $f_c = B\pi^2/L^2$, i.e. the threshold for Euler buckling.

The amplitude A can be determined by using the condition that the length of the film remains the same when buckled (inextensibility):

$$\varepsilon = \int_0^L \frac{\left(\sqrt{1+\zeta'(x)^2} - 1\right)}{L} dx \approx \frac{\pi^2 A^2}{2L^2}, \tag{1.65}$$

where ε is the post-buckling compressive strain. The amplitude is therefore

$$A \approx \frac{\sqrt{2}L}{\pi}\sqrt{\varepsilon}. \tag{1.66}$$

The principle behind Euler buckling is the competition between the compressive and the bending energy. At $f \geq f_c$, bending the beam gives the system lower total energy than getting shortens hence allow the beam to buckle. The critical load is known the be the maximum load before the beam fails due to this buckling and therefore informs the loading limit to the beam when used in structure.

1.3.2 Wrinkling

There has been much attention paid to understand the physics of wrinkling of constrained thin films. Wrinkling of a stiff film on a compliant substrate was well studied by Allen [66]. Consider a thin inextensible film of shear modulus μ_f and thickness a on an infinitely deep incompressible substrate with shear modulus μ_s. The system is under a compressive stress s causing the film to buckle with a wavelength of l as in Fig. 1.8.

This problem is similar to the Euler buckling problem but now the substrate strain energy also needs to be considered. The energy of the film, consisting of the bending energy and the work done by compression, can be written as

$$E_f = \int_{-\infty}^{\infty} \frac{1}{2}\left(\frac{\mu_f a^3}{4}\zeta''(x)^2 - sa\zeta'(x)^2\right) dx, \tag{1.67}$$

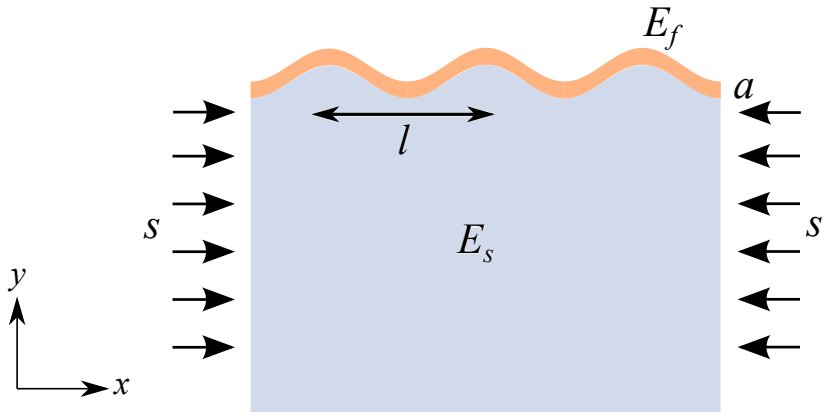

Fig. 1.8 Schematic diagram for wrinkling of a stiff layer on a deep soft substrate under a compressive stress

where I have used the compressive force on the stiff layer $f = sa$. The substrate energy will be complicated as the deformation varies as a function of the depth, y. Firstly, to understand what happens in the substrate, let us consider the energy of the substrate using incompressible neo-Hookean energy density,

$$E_s = \int_{-\infty}^{0}\int_{-\infty}^{\infty}\left(\frac{\mu_s}{2}\mathrm{Tr}\left(F\cdot F^T\right) - P(x,y)(\mathrm{Det}(F)-1)\right)dxdy, \tag{1.68}$$

where F is the deformation gradient and P is the Lagrange-multiplier pressure field for the incompressibility. The substrate deformation is not simple, but it can be approximated. To see this, let us consider the general form of the displacement fields in the substrate. This is done by minimizing E_s, which gives the mechanical equilibrium and incompressibility condition,

$$\nabla\cdot\sigma = \mathbf{0}, \qquad \mathrm{Det}(F) = 0, \tag{1.69}$$

where $\sigma = \mu_s F - PF^{-T}$. We then applying a small sinusoidal perturbation in the displacement field and pressure to the system

$$\delta\mathbf{u}(x,z) = \begin{pmatrix} u_x(x,y) \\ u_y(x,y) \end{pmatrix} = \varepsilon \begin{pmatrix} f_x(y)\sin(kx) \\ f_y(y)\cos(kx) \end{pmatrix}, \tag{1.70}$$

$$\delta P(x,y) = \varepsilon f_p(y)\cos(kx), \tag{1.71}$$

where $k = 2\pi/l$ is the wavenumber of the sinusoidal perturbation and ε is a small quantity. Substituting the perturbed fields into (1.69), we end up with

$$f_x(y) = \frac{f_y'(y)}{k} \tag{1.72}$$

$$f_p(y) = \mu_s \left(\frac{f_y^{(3)}(y)}{k^2} - f_y''(y) \right) \tag{1.73}$$

$$k^4 f_y(y) - 2k^2 f_y''(y) + f_y^{(4)}(y) = 0. \tag{1.74}$$

at linear order in ε. The solution to (1.74) is

$$f_y(y) = (A_1 + A_2 y)e^{ky} + (B_1 + B_2 y)e^{-ky}, \tag{1.75}$$

where A_1, A_2, B_1 and B_2 are arbitrary constants. The solution must vanish as $y \to -\infty$ and hence $B_1 = B_2 = 0$. Equation (1.75) suggests that the deformation in the substrate is oscillating in the x-direction while decaying in the y-direction. This is actually what one would expect even in linear elasticity as the displacement field usually obeys a biharmonic equation [67]. We could fully calculate the substrate energy using this solution for the displacement fields. However, to keep the model simple, as only scaling of the energy will be considered, the substrate energy can be approximated with linear elasticity

$$E_s \approx \int_{-\infty}^{0} \int_{-\infty}^{\infty} \frac{1}{2} \mu_s \varepsilon_{yy}(x,y)^2 \mathrm{d}x\mathrm{d}y, \tag{1.76}$$

where $\varepsilon_{yy}(x,y) = \partial u_y / \partial y$ is the vertical strain. Here, the horizontal deformation in the substrate is neglected for simplicity. As, the displacement field decays in the y direction, the vertical strain scales as

$$\varepsilon_{yy}(x,y) \sim \zeta(x) e^{ky}. \tag{1.77}$$

Using this form, the substrate energy can be integrated in the y direction giving

$$E_s \sim \int_{-\infty}^{\infty} \frac{1}{2} \mu_s \left(\frac{\zeta(x)}{l} \right)^2 l \mathrm{d}x. \tag{1.78}$$

This form of energy is equivalent to modelling the substrate as if the vertical deformation is uniform but only penetrates to a depth of the wavelength l. Ignoring any constants of proportionality, the total energy can be written as

$$E = E_f + E_s \sim \int \left(\mu_f a^3 \zeta''(x)^2 - s a \zeta'(x)^2 + \mu_s \frac{\zeta(x)^2}{l} \right) \mathrm{d}x. \tag{1.79}$$

Again, we can substitute the trial solution of the form

$$\zeta(x) = A\sin\left(\frac{2\pi x}{l}\right) \tag{1.80}$$

into the total energy,

$$E \sim \mu_f a^3 \frac{A^2}{l^4} - sa\frac{A^2}{l^2} + \mu_s \frac{A^2}{l}. \tag{1.81}$$

As in the Euler buckling problem, the coefficient of A^2 has to be negative if the instability lowers the total energy:

$$\frac{\mu_f}{l^4} - \frac{sa}{l^3} + \frac{\mu_s}{l} \geq 0. \tag{1.82}$$

The form of the optimum wavelength can be determined by minimizing energy with respect to l,

$$\frac{\mathrm{d}E}{\mathrm{d}l} \sim \mu_f a^3 \frac{A^2}{l^5} - sa\frac{A^2}{l^3} + \mu_s \frac{A^2}{l^2} = 0, \tag{1.83}$$

which satisfies (1.82) only if the applied stress s is greater than a critical value s_c

$$s \geq s_c \sim \mu_f \left(\frac{\mu_s}{\mu_f}\right)^{2/3}. \tag{1.84}$$

This is the threshold stress required to create wrinkle. At the threshold, $s = s_c$, the wrinkle wavelength can be obtained from (1.83) as

$$l \sim a\left(\frac{\mu_f}{\mu_s}\right)^{1/3}. \tag{1.85}$$

The amplitude can be determined by using the inextensibility condition:

$$\varepsilon = \int_0^{\lambda} \frac{\left(\sqrt{1+\zeta'(x)^2} - 1\right)}{l} dx \approx \frac{A^2}{l^2}, \tag{1.86}$$

where ε is the compressive strain. The amplitude is therefore

$$A \sim l\sqrt{\varepsilon}. \tag{1.87}$$

Rigorous treatments [66, 68] show that the stiff film begins to wrinkle when the compressive stress on the film is greater than a critical value

$$s_c = 3\mu_f \left(3\frac{\mu_s}{\mu_f}\right)^{2/3} \tag{1.88}$$

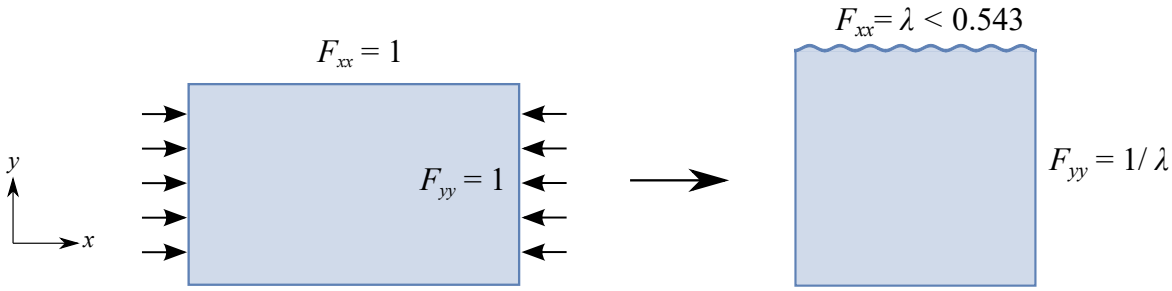

Fig. 1.9 Schematic diagram for Biot instability showing surface wrinkling when the compressive strain is beyond the critical value.

with a wavelength of

$$l = 2\pi \left(\frac{\mu_f}{3\mu_s} \right)^{1/3} a. \tag{1.89}$$

1.3.3 Biot instability

Buckling and layer/substrate wrinkling can occur at very modest strains, and hence are not restricted to soft solids. However, the highly deformable nature of soft solids introduces many additional elastic instabilities. A classic example of a large-deformation instability is Biot's surface instability. Consider a rubber (or neo-Hookean) material occupying a half space, under a plane strain by a factor of λ, as shown in Fig. 1.9. Biot [15, 16] discovered that the surface of such a compressed rubber half space becomes unstable towards a sinusoidal undulating instability when a critical degree compression of $\lambda = 0.543$ is reached. An example of this instability is wrinkling of skin when compressed, as in Fig. 1.10.

To understand this, let us consider a two-dimensional incompressible neo-Hookean half space with the shear modulus μ. The compressive pre-strain is applied to the solid such that $\lambda_x = \lambda$ and $\lambda_y = 1/\lambda$. Using the neo-Hookean energy density (1.25), we can write

$$W = \frac{\mu}{2} \mathrm{Tr}\left(F \cdot \Lambda \cdot \Lambda^T \cdot F^T\right) - P(x,y)(\mathrm{Det}(F) - 1), \tag{1.90}$$

where

$$\Lambda = \begin{pmatrix} \lambda & 0 \\ 0 & 1/\lambda \end{pmatrix}, \tag{1.91}$$

is the pre-strain deformation gradient and F is the deformation gradient after the pre-strain. The energy density, W, will be minimized with respect to F subject to the stress-free boundary condition at $y = 0$,

$$\sigma \cdot \hat{\mathbf{y}} = (\mu F \cdot \Lambda - P\Lambda^{-T} \cdot F^{-T}) \cdot \hat{\mathbf{y}} = \mathbf{0} \quad \text{at } z = 0. \tag{1.92}$$

Fig. 1.10 Wrinkle forms as the skin is being compressed.

First consider the homogeneous deformed state, $F = 1$. The pressure field can be solved from (1.92) giving

$$P(x,y) = \frac{\mu}{\lambda^2}. \tag{1.93}$$

Here, I will perform a linear stability analysis to characterize the instability. To see when the homogeneous state becomes unstable, consider a small sinusoidal perturbation in the displacement field and pressure

$$\delta\mathbf{u}(x,y) = \varepsilon \begin{pmatrix} f_x(y)\sin(kx) \\ f_y(y)\cos(kx) \end{pmatrix}, \tag{1.94}$$

$$\delta P(x,y) = \varepsilon f_p(y)\cos(kx), \tag{1.95}$$

where k is the wavenumber of the sinusoidal perturbation and ε is a small quantity. The deformation gradient reads $F = I + \nabla\delta\mathbf{u}$. Minimizing E with respect to the perturbations gives the mechanical equilibrium and incompressibility condition,

$$\nabla\cdot\sigma = \mathbf{0}, \qquad \mathrm{Det}(F) = 0. \tag{1.96}$$

Substituting the perturbed fields into (1.96), we end up with

$$f_x(y) = \frac{f_y'(y)}{k} \tag{1.97}$$

$$f_p(y) = \mu \left(\frac{f_y^{(3)}(y)}{k^2\lambda^2} - \lambda^2 f_y''(y) \right) \tag{1.98}$$

$$k^4\lambda^4 f_y(y) - k^2(1+\lambda^4) f_y''(y) + f_y^{(4)}(y) = 0. \tag{1.99}$$

at linear order in ε. The solution to (1.99) is

$$f_y(y) = A_1 e^{k\lambda^2 y} + B_1 e^{-k\lambda^2 y} + A_2 e^{ky} + B_2 e^{-ky}, \tag{1.100}$$

for $\lambda \neq 1$. The solution must vanish as $y \to -\infty$ and hence $B_1 = B_2 = 0$. The stress-free boundary conditions at linear order in ε, after some simplifications, can then be written as

$$\begin{pmatrix} 1+\lambda^4 & 2 \\ 2\lambda^2 & 1+\lambda^4 \end{pmatrix} \begin{pmatrix} A_1 \\ A_2 \end{pmatrix} = 0. \tag{1.101}$$

Equation (1.101) can admit non-zero solutions if and only if the determinant of the matrix on the left-hand side is singular. This gives

$$(1+\lambda^4)^2 - 4\lambda^2 = 0, \tag{1.102}$$

which has one positive real solution

$$\lambda = \frac{1}{3}\left((17+3\sqrt{33})^{1/3} - \frac{2}{(17+3\sqrt{33})^{1/3}} - 1 \right) = 0.5437\ldots, \tag{1.103}$$

regardless of the wavelength. This is where the homogeneous "base-state" solution becomes unstable towards the perturbation, i.e. the threshold compression for the Biot instability. Peculiarly, the critical threshold does not depend on the wavelength of the perturbation, meaning all the wavelengths become unstable at the same degree of loading: this is quite different to buckling and wrinkling where the first unstable mode has a specific wavelength. The wavelength-independent nature of the instability arises from the fact that there are no length scales in the system. All wavelengths are totally equivalent. In practice, any real system will have a finite depth, and we might expect the instability to appear as surface wrinkles whose wavelength are proportional to this depth. However, this expectation is not quite right: linear stability analysis in finite depth systems actually reveals that the

zero-wavelength mode is the first to become unstable [69]. Defects or imperfections that exist in the solid may also control the wavelength as well [16].

1.3.4 Sulcification

In experiment, the Biot instability is never really observed. Instead of a wave-like wrinkle, a sharp localized crease appears instead, and at a significantly smaller degree of compression than that predicted above. This is because Biot instability is always preceded by the formation of sulci. Sulci are cusped furrows that appear on the surface of a soft material, as opposed to global undulation for surface wrinkling. As Biot only considered a linearized analysis, he could not capture the non-linear nature of the stress and strain singularities at the cusped heart of a sulcus. Studies on instability that leads to sulci formation were recent [70–73]. In particular, Hohlfeld and Mahadevan [74, 75] investigated the formation of a sulcus in a bent slab of soft elastomer (Fig. 1.11A) numerically and experimentally. They found that sulcification is a non-linear instability without a length scale. Furthermore, sulcification is discontinuous (subcritical) for loading but continuous (supercritical) while unloading (see Section 1.4 for definitions of supercritical and subcritical instabilities). This is illustrated in Fig. 1.11B. As the slab is compressed, a sharp fold emerges abruptly at $\lambda = 0.543$, the Biot instability threshold. This is called B point or Biot point. When the strain is released, the sulcus unfolds smoothly to the smooth unfolded state at $\lambda = 0.655$, called the T point. This very unusual instability behaviour puts sulcus formation beyond the reach of current analytic theory, so this understanding is entirely based on finite element numerical analysis.

Similar to wrinkling, sulcification is involved in the shape development of biological organs such as the brain [76, 77]. Figs 1.11B and C show the sulci pattern form under uniform growth numerically and experimentally, which resembles the pattern of brain folding. Sulcus can also form as a second bifurcation after wrinkling in bilayer systems, which are responsible in many pattern formations in biological organs [46, 54, 55, 78–88].

1.3.5 Gravity driven instability

A well-known instability in fluids is the Rayleigh-Taylor instability, where the fingers of heavier fluids invade underlying lighter fluids under influence of gravity or acceleration [89, 90]. Examples are water suspended above the oil and mushroom clouds from volcanic eruption. An easy way to understand the Rayleigh-Taylor instability is to consider the dispersion relation of gravity wave in fluids, $\omega = \sqrt{gk}$, where g is the gravity, ω and k are the angular frequency and wavenumber [91]. If the gravity is instead upward, the angular frequency becomes $\omega = \pm i\sqrt{-gk}$, which suggests that the amplitude of fluctuation increases

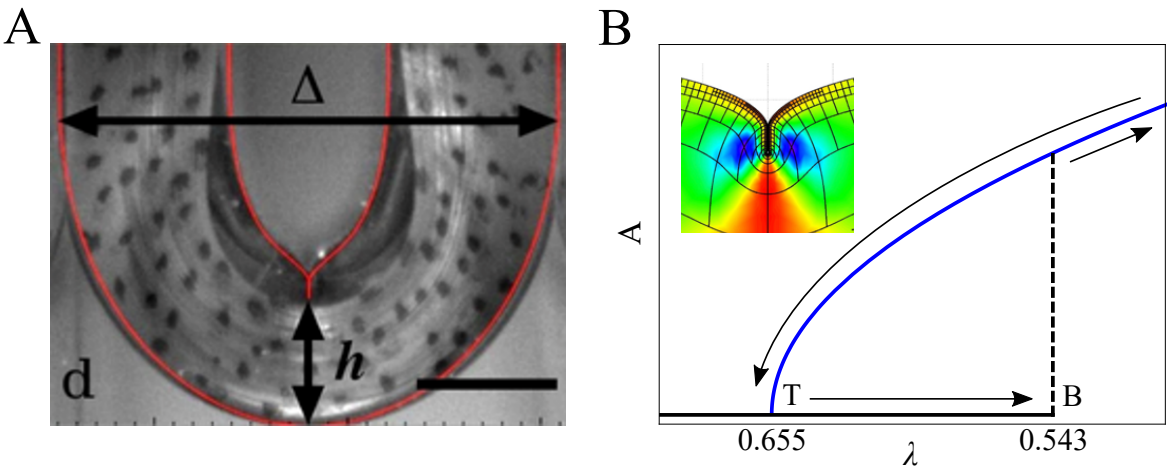

Fig. 1.11 (A) Bent slab of polydimethylsiloxane (PDMS) showing formation of sulcus, taken from [74] (B) Bifurcation diagrams for the sulcus formation. Sulcus forms abruptly at B point when solid is compressed but disappears smoothly at T point. Blue branch denotes the folded state (inset from [74]) while the black branch is the unfolded state.

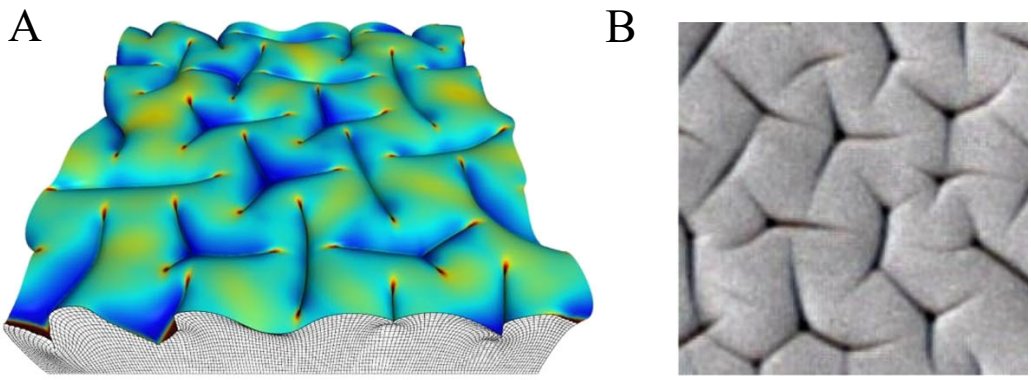

Fig. 1.12 (A) Simulated unfolding of a compressed and sulcified solid layer. (B) Experimental sulcal patterns are shown in a swelling gel. Taken from [76].

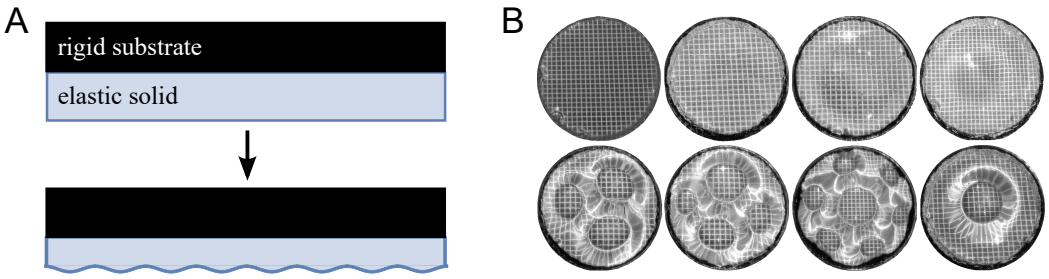

Fig. 1.13 (A) Schematic diagram for the gravity driven instability. (B) Surface of gel under the gravity driven instability as the shear modulus decreases, taken from Mora et al. [62].

with time and hence the surface is unstable. One could imagine whether gravity could introduce a similar instability in a case of soft solid. Recently, Mora et al. [62] observed gravity driven instability in elastic solid, in a slab of gel with its upper surface fixed to a rigid body and the lower surface free (Fig. 1.13).

To understand how the instability reduces the overall energy, consider a gel slab of thickness a, density ρ and shear modulus μ. A sinusoidal perturbation $z = \varepsilon \sin(kx)$ is applied to the surface. The associated gravitational potential energy per unit area, averaging over a wavelength, $l = 2\pi/k$, is decreased by

$$E_g \sim \frac{1}{2l}\int_0^l \rho g z^2 dx = \frac{1}{4}\rho g \varepsilon^2. \tag{1.104}$$

For the corresponding elastic energy, the strain scale as ε/a and hence the average elastic energy per unit area is

$$E_{el} \sim a\mu \left(\frac{\varepsilon}{a}\right)^2. \tag{1.105}$$

Therefore, the condition for the instability depends on the parameter $\alpha \equiv \rho g a/\mu$, which decides whether the perturbation reduces overall energy or not. Using linear stability analysis (see Section 5), Mora et al. showed that the surface is first unstable when $\alpha \approx 6.223$ at a finite wavenumber of $k \approx 2.12a$. For the Earth gravity and a slab of 10 cm thick, this requires the shear modulus to be smaller than $\sim 10^2$ Pa, softer than most materials but gels.

The instability is also observed when a heavier layer is placed on top of a lighter layer similar to the Rayleigh-Taylor instability in water suspended on oil [64]. A gravity induced wrinkle to crease transition like one generated by growth is also observed [63].

1.3.6 Elastic fingering

Fingering instabilities are commonly observed in viscous fluid. The Saffman-Taylor instability involves two fluids move in the narrow space between two plates, known as Hele-Shaw

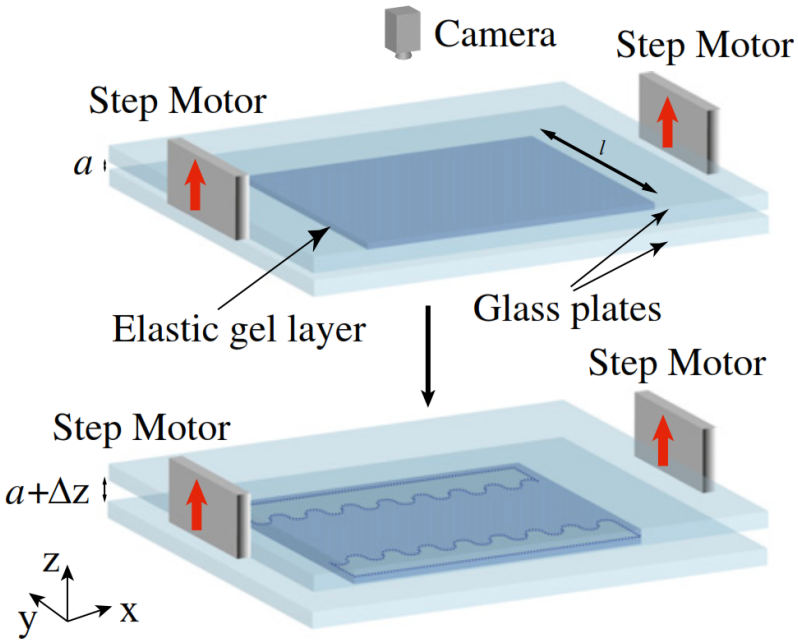

Fig. 1.14 Experimental setup for studying fingering of an elastic gel layer. The fingering is formed as the glass plates are being pulled apart, from [95].

cell, in which less viscous fluid is pushed into a more viscous fluid, producing finger interface [92, 93]. The size of the finger is determined by the balance between the pressure gradient due to different viscosities, and the surface tension [92].

A similar instability is observed in an elastic layer where fingers of air invade into the elastic layer when the layer is under strain [94, 95] or the air is pumped into a confined elastic cavity (Fig. 1.14) [96, 97].

Biggins et al. [95] shows that when an elastic solid of width w and thickness a is confined between two rigid plates that are being pulled apart, without loss of adhesion to the plates, as in Fig. 1.14A, the fingers of air invaded the elastic layer when the separation exceeds a threshold. They suggest that this happens because some of the elastic material reduce the shear stress by expanding outwards while the rest recedes into the material, forming fingers, in order to conserve the volume. An easy way to think about this is to imagine that when the gel is pulled apart, there is a uniform force pulling the solid inwards to conserve the volume. This force is like gravity in the gravity driven instability, except now the energy being reduced by fingering is elastic energy rather than gravitational energy. Experimental and numerical results show a discontinuous transformation between the normal and the fingering states, which is different from the continuous fluid Saffman-Taylor instability. Their linear stability

analysis gives the threshold separation

$$\Delta z \approx 1.69a^2/w, \tag{1.106}$$

and the wavelength of the fingers is given by

$$l \approx 2.74a, \tag{1.107}$$

independent of material parameters but only scales with the geometry of the system. This demonstrates that the origin of the instability is purely geometric and should be applicable to many systems.

Elastic layers are often used as joints between solid bodies as adhesives for example. Fingering could occur in these joints when they are under stress. This could lead to failure of the structure and so the instability has to be considered when designing such a structure.

1.3.7 Cavitation

It is common to have small voids in rubber. These voids are known to grow rapidly from a tiny size into large cavities when the hydrostatic pressure approaches the critical value, a phenomenon known as cavitation. Using the neo-Hookean model, Gent and Lindley [98] demonstrate that cavitation is another elastic instability. A small spherical cavity dilates as the applied cavity pressure increases until the radius diverges infinitely at

$$P_c = \frac{5}{2}\mu, \tag{1.108}$$

where μ is the shear modulus of the rubber. This means cavitation can occur at any point in the rubber at which the hydrostatic component of the stress reaches the critical value. The threshold of cavitation sets the limit of the pressure that a rubber can handle before forming cavities, which can lead to internal rupture.

To understand this, consider a spherical cavity of radius a in a neo-Hookean full space (Fig. 1.15). The cavity is pressurised with a pressure P_{in}, causing the cavity to expand. The solid is under a radial displacement field $\mathbf{u}(r,\theta,\phi) = u_r(r)\hat{\mathbf{r}}$. The deformation gradient, in spherical polar coordinates (r,θ,ϕ), can be calculated as

$$F = \begin{pmatrix} 1+u_r' & 0 & 0 \\ 0 & 1+\frac{u_r}{r} & 0 \\ 0 & 0 & 1+\frac{u_r}{r} \end{pmatrix} \tag{1.109}$$

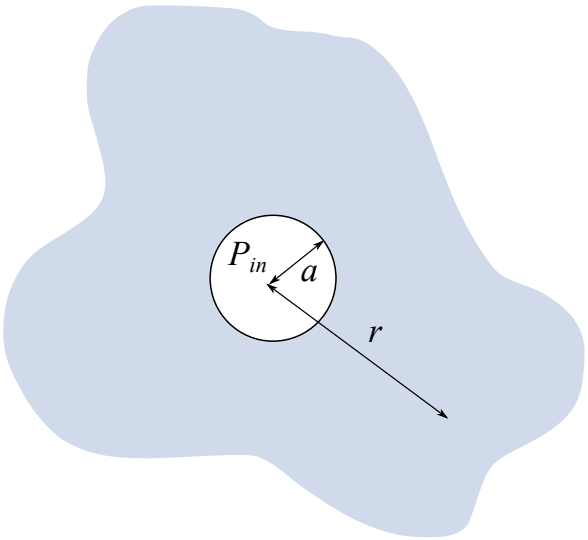

Fig. 1.15 Spherical cavity of radius a under an internal pressure P_{in}

(see Appendix A for vector and matrix identities such as $\nabla \mathbf{u}$ in spherical polar coordinate). The energy comes from the elastic energy density (1.24) and the work done by cavity pressure

$$E = E_{el} + E_P \tag{1.110}$$

$$= \int_a^\infty \left[\frac{\mu}{2}(\mathrm{Tr}(F \cdot F^T) - 3) - P(r)(\mathrm{Det}(F) - 1)\right] 4\pi r^2 dr - P_{in}V. \tag{1.111}$$

The cavity dilates until the energy is minimized, i.e. $\mathrm{d}E/\mathrm{d}V = 0$. Therefore, the cavity pressure can be related to the elastic energy via

$$P_{in} = \frac{dE_{el}}{dV}. \tag{1.112}$$

The incompressibility condition requires

$$\mathrm{Det}(F) = 1, \tag{1.113}$$

which gives a differential equation for $u_r(r)$:

$$(r + u_r(r))^2(1 + u_r'(r)) - r^2 = 0. \tag{1.114}$$

Solving (1.114) gives solution to u_r of the form

$$u_r(r) = (c^3 + r^3)^{1/3} - r, \tag{1.115}$$

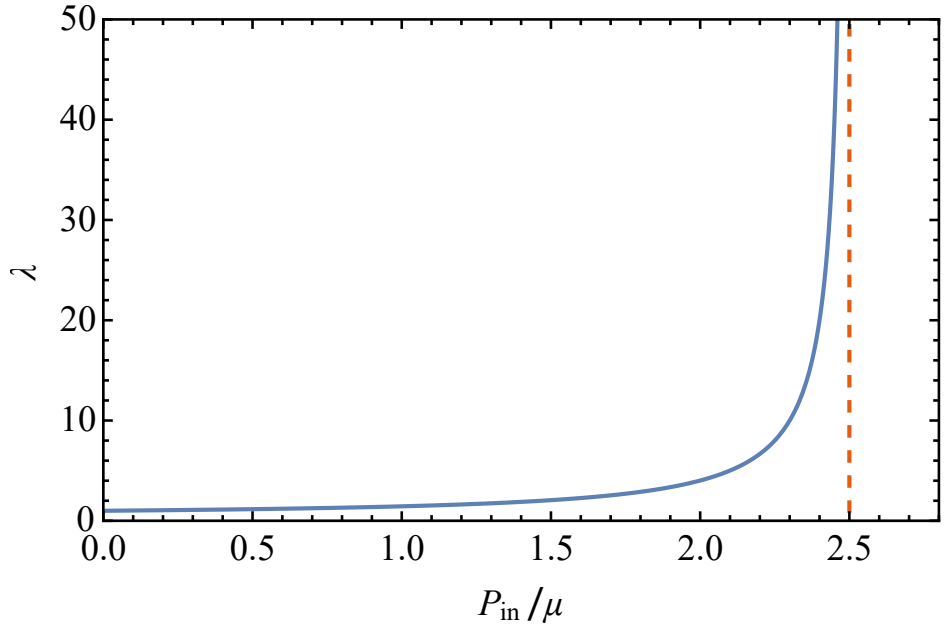

Fig. 1.16 Cavity dilation, λ, as a function of cavity pressure, P_{in}, for a pressurised spherical cavity in a bulk neo-Hookean solid. Dashed line shows a divergence at the critical pressure.

where c is a constant. Substituting the solution of u_r into (1.112) yields

$$P_{in} = \frac{dE_{el}}{dc}\frac{dc}{dV} \tag{1.116}$$

$$= \int_a^\infty 2\pi\mu \frac{d}{dc}\left[2\left(c^3+r^3\right)^{2/3} + \frac{r^4}{(c^3+r^3)^{4/3}} - 3\right] dr \left(\frac{1}{4\pi c^2}\right) \tag{1.117}$$

$$= \mu\left(\frac{5}{2} - \frac{5a}{2(c^3+a^3)^{1/3}} + \frac{c^3 a}{2(c^3+a^3)^{4/3}}\right) \tag{1.118}$$

where I have used $V = \frac{4}{3}\pi(r+u_r(a))^3$ for the cavity volume. In terms of the cavity dilation, $\lambda \equiv (a+u_r(a))/a = (c^3+a^3)^{1/3}/a$, the cavity pressure can be written as

$$P_{in} = \frac{\mu}{2}\left(5 - \frac{4}{\lambda} - \frac{1}{\lambda^4}\right), \tag{1.119}$$

which diverges at $\frac{5}{2}\mu$. Fig. 1.16 shows the cavity dilation as a function of cavity pressure. This shows that the cavity would expand infinitely as soon as the cavity reaches the critical value, allowing tiny defects to grow into noticeable cavities.

In reality, the cavity would never expand infinitely. This is because the neo-Hookean model is not suitable for such a large strain. A more suitable model such as the Gent model,

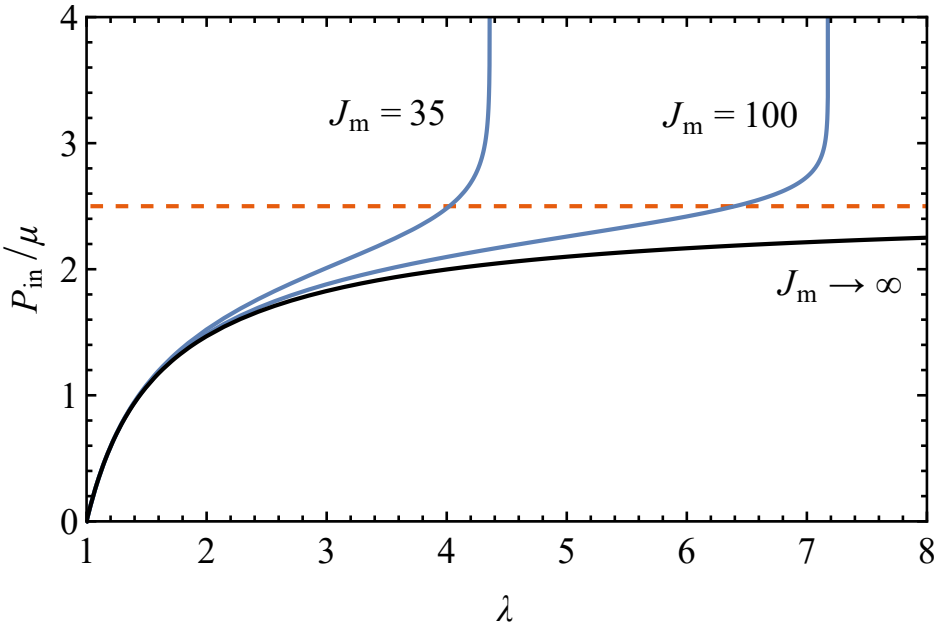

Fig. 1.17 Cavity pressure, P_{in}, as a function of cavity dilation λ for a pressurised spherical cavity in a Gent solid for $J_m = 35, 100$ and $J_m \to \infty$ (neo-Hookean). Dashed line is the cavitation threshold pressure for neo-Hookean solid.

which includes finite extensibility, would produce large but finite size cavities beyond the threshold [99, 100]. Fig. 1.17 shows how the finite extensibility limits the size of the cavities.

1.3.8 Ballooning

Cavitation also applies to systems like spherical balloons, but with a small finite outer radius, which would reduce the threshold pressure. We see that the balloon can get inflated easily without increasing internal pressure as it dilates close to the threshold [22, 99–103]. Consider a neo-Hookean balloon of radius a with a thickness $t \ll a$. The balloon is inflated with the cavity pressure P_{in}, with the radius increased by a factor of λ. The analysis is the same as that of the cavitation. In equation (1.117), the integral can be replaced with

$$P_{in} = 2\pi\mu \frac{d}{dc}\left[2\left(c^3+a^3\right)^{2/3} + \frac{r^4}{(c^3+a^3)^{4/3}} - 3\right] t\left(\frac{1}{4\pi c^2}\right) \tag{1.120}$$

$$= 2\mu t\left(\frac{1}{(c^3+a^3)^{1/3}} + \frac{a^6}{(c^3+a^3)^{7/3}}\right) \tag{1.121}$$

$$= \frac{2\mu t}{a}\left(\frac{1}{\lambda} - \frac{1}{\lambda^7}\right). \tag{1.122}$$

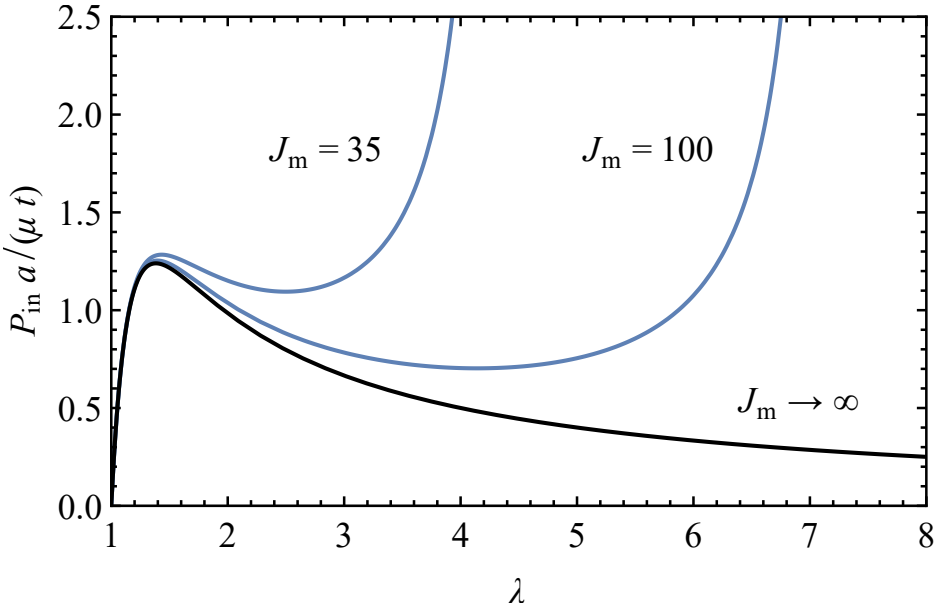

Fig. 1.18 Cavity pressure, P_{in}, as a function of cavity dilation λ for an inflated thin spherical balloon for $J_m = 35, 100$ and $J_m \to \infty$ (neo-Hookean).

The result from (1.122) is plotted in Fig. 1.18 (black). We can see that as the cavity pressure approaches the maximum (at $\lambda = 7^{1/6}$ and $P_{in} = 12/7^{7/6} \approx 1.239t\mu/a$), it will inflate greatly without requiring to input any further pressure. Again, we never see a balloon expand infinitely and this is because of the finite extensibility of the solid. Using the Gent model, Fig. 1.18 (blue), we see that the cavity pressure rises again close to a maximum dilation limited by the finite extensibility. The curve that we see here is similar to what we see in the isotherms of the Van der Waals gas below the critical temperature, where the phase separation occurs. What would happen here is that as the balloon is inflated further it will separate into a lightly stretched and a highly stretched region while the balloon remains roughly spherical [100]. This phase separation also applies to a long cylindrical balloon [100, 102]. Here the phase separation is more obvious. The balloon separates into smaller and larger regions (Fig. 1.19), similar to an aneurysm, as we often see in long party balloons.

The ballooning can be thought in terms of energy. Cavity pressure is the rate of change of energy with respect to the cavity volume, $\mathrm{d}E/\mathrm{d}V$. At the threshold of the instability, the predicted cavity pressure in Fig. 1.18 begins to decrease. This correspond to loss of the convexity of the energy curve, a signature of phase separation. For a λ within the non-convex region, it is more energetically favourable to split in to to regions (see Subsection 1.3.9 for another example), which is what happens to the balloons as the ballooning instability begins.

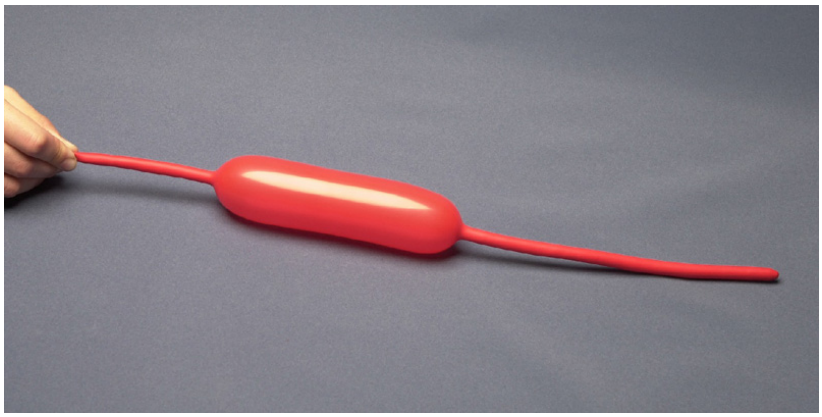

Fig. 1.19 Long balloon with a phase separation. Taken from www.doitpoms.ac.uk.

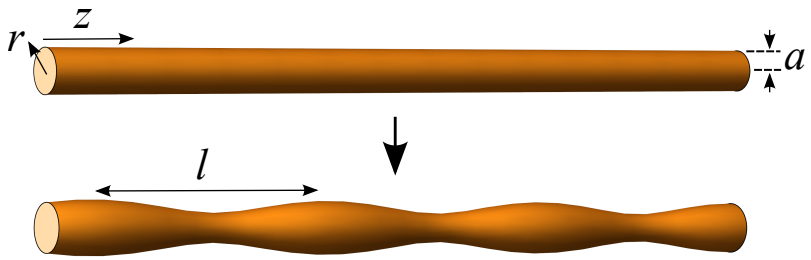

Fig. 1.20 Schematic diagram for the surface tension driven instability in a soft solid cylinder: (top) stable cylinder, (bottom) unstable cylinder with an instability wavelength $l = 2\pi/k$.

1.3.9 Surface tension driven instability

In fluids, surface tension plays many important roles such as forming droplets and puddles, capillary effect, surface wetting [104], and the Rayleigh-Plateau instability, where a stream of fluids breaks into droplets [105]. These phenomena reduce the surface area relative to the volume, decreasing the total energy of the fluids. The length scale at which the surface tension is important is when it dominates gravity energy, below the capillary length

$$l_c = \sqrt{\frac{\gamma}{\rho g}}. \tag{1.123}$$

In solids, the surface tension can deform solid when the surface energy is comparable to the shear elastic energy. The effect is called elastocapillarity. This occurs below the elastocapillary length

$$l_c = \frac{\gamma}{\mu}, \tag{1.124}$$

which is small, less than 10^{-9} m, for most solids. However, the elastocapillary length can be 10^{-6}–10^{-3} m for soft elastic solids. Many studies observed the elastocapillarity effect

in experiments and nature [106–108]. In particular, an analogue to the Rayleigh-Plateau instability has been observed in soft solid cylinders [57–60]. Consider an infinitely long neo-Hookean cylinder of radius a, shear modulus μ and surface tension γ (Fig. 1.20). Linear stability analysis shows that the cylinder becomes first unstable with infinite wavelength ($k = 0$) at [57, 60]

$$\Gamma \equiv \frac{\gamma}{\mu a} = 6. \tag{1.125}$$

This suggests that the wavelength of the instability will depend on the geometric constraint such as the length of the cylinder. However, the threshold Γ goes to infinity as $k \to 1/a$, which sets the limit on the length of the cylinder required. The long-wavelength nature of the instability suggests that long wavelength reduces the surface area more. It is also found that the cylinder can be unstable towards a short-wavelength instability under negative surface tension, which can be possible for solids [109].

The solid Rayleigh-Plateau instability can also be understood as a simple phase separation [61] by considering convexity of the energy curve. The total energy of the cylinder can be written as

$$E = \gamma A + \int \frac{1}{2}\mathrm{Tr}\left(F \cdot F^T\right) dV, \tag{1.126}$$

where A is the surface area of the cylinder. Let the cylinder be stretched homogeneously from the length L to λL. The radius would contract from a to $a/\sqrt{\lambda}$ to conserve the volume. The energy (1.126) becomes

$$E(\lambda) = \pi \mu L a^2 \left(2\Gamma\sqrt{\lambda} + \frac{1}{2}\left(\lambda^2 + \frac{2}{\lambda}\right)\right). \tag{1.127}$$

The square root term is concave whereas the rest are convex. This could mean that the energy $E(\lambda)$ loses its convexity, i.e., the concave region begins to emerge, as the square root term gets bigger, by increasing Γ. This occurs when Γ approaches $\sqrt{32}$ as illustrated Fig. 1.21. For a λ value within the non-convex region, it is more energetically favourable to split into regions with smaller and larger λ, at each end of the dashed line in Fig. 1.21. However, only at $\Gamma \geq 6$ that the phase separation can occur from an initially non-stretched cylinder, agreeing with the linear stability analysis.

The long-wavelength instability can also be observed in an incompressible cylindrical cavity through an elastic solid. The threshold is reduced to $\Gamma = 3$. However, for a compressible cylindrical cavity, the surface tension would reduce the radius of the cavity even when it is not enough to cause the instability. The cavity becomes first unstable with a finite wavelength at $\Gamma \approx 2.543$ and $k \approx 3.145/a$ instead [60]. Further from thresholds, the

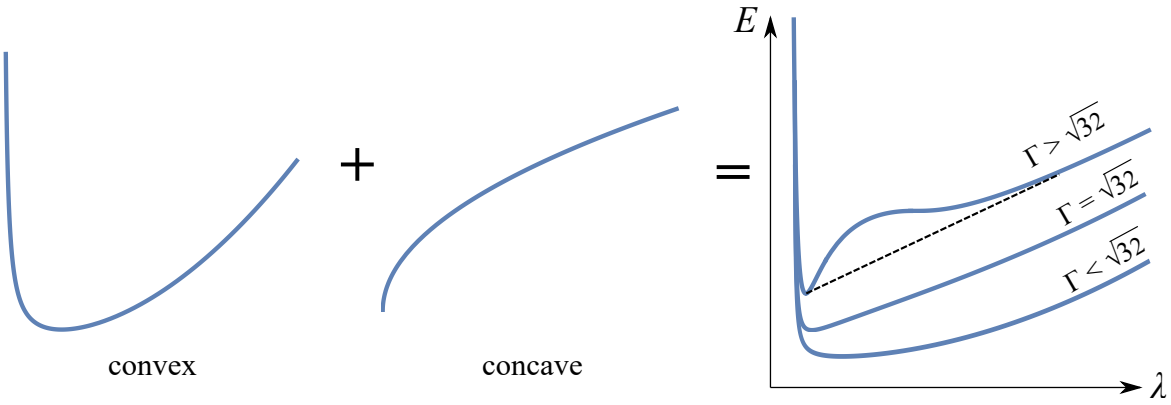

Fig. 1.21 Schematic diagram showing addition of the convex and concave terms in the energy leading to the loss of convexity and phase separation. Dashed lines show possible phase separations for $\Gamma > \sqrt{32}$.

undulation can cause channel closure. This is observed in pulmonary airway closure or atelectasis, when the surfactant which reduces the surface tension is absent [110, 111].

1.4 Energy method for the instabilities

One way to understand the development of systems through elastic instabilities is to look at how their energy changes at the threshold. Close to the instability threshold, where the instability amplitude is small, we can expand the system total energy, E, as a series expansion in the amplitude of the instability, ε:

$$E = E_0 + \sum_{n=1}^{\infty} \varepsilon^n E_n, \tag{1.128}$$

where E_0 is the base state energy and E_n is the energy at order $O(\varepsilon^n)$. The first order term E_1 always vanishes as the initial base state is always an equilibrium and hence a stationary point in the energy landscape, so its first order energy variation vanishes for all perturbations. At the next order, we expect that increasing the amplitude will lower the energy of the system only if the instability parameter, such as compression or growth, which I will call g, exceeds a threshold value g^*. Hence, we expect the energy series to take the Landau-like form, $E = E_0 + C_2(g - g^*)\varepsilon^2$, where the constant $C_2 < 0$, inspired by Landau theory for phase transition [112].

To determine the instability amplitude, we would need to expand the energy series up to at least the fourth order, at which the energy can be bounded from below:

$$E = E_0 + C_2(g-g^*)\varepsilon^2 + C_3\varepsilon^3 + C_4\varepsilon^4 + O(\varepsilon^5), \tag{1.129}$$

where the constants $C_3 = E_3(g=g^*)$ and $C_4 = E_4(g=g^*)$ are called Landau energy coefficients or just energy coefficients. The third energy coefficient, C_3, may vanish. For example, if the system possesses an inversion symmetry in the buckling amplitude, the odd-order energy coefficients are zero since $+\varepsilon$ and $-\varepsilon$ are equivalent. In this case, the energy expansion becomes

$$E = E_0 + C_2(g-g^*)\varepsilon^2 + C_4\varepsilon^4 + O(\varepsilon^5). \tag{1.130}$$

If $C_4 > 0$, then, for small amplitude, one can truncate this energy at $O(\varepsilon^4)$ and minimize over ε to find the minimum energy amplitude

$$\varepsilon^* = \begin{cases} \sqrt{\frac{-C_2(g-g^*)}{2C_4}} & g > g^*, \\ 0 & g < g^*. \end{cases} \tag{1.131}$$

The amplitude increases continuously for $g > g^*$. Using this solution for amplitude, the energy of the buckled state is

$$E = \begin{cases} E_0 - \frac{C_2^2(g-g^*)^2}{4C_4} & g > g^*, \\ E_0 & g < g^*. \end{cases} \tag{1.132}$$

We call this a **supercritical** instability, where the amplitude and energy changes continuously at the threshold, similar to a second order phase transition. On the other hand, if C_3 does not vanish, we have instead

$$E = E_0 + C_2(g-g^*)\varepsilon^2 + C_3\varepsilon^3 + C_4\varepsilon^4. \tag{1.133}$$

The cubic term is always unbounded from below, so one still needs the fourth order term before truncating the energy series. In this energy, a second minimum appears (separate to the one at $\varepsilon^* = 0$) for $g > g^* + \frac{9C_3^2}{32C_4C_2}$ at

$$\varepsilon^* = -\frac{3C_3}{8C_4}\left(1 + \sqrt{1 - \frac{32C_4C_2(g-g^*)}{9C_3^2}}\right). \tag{1.134}$$

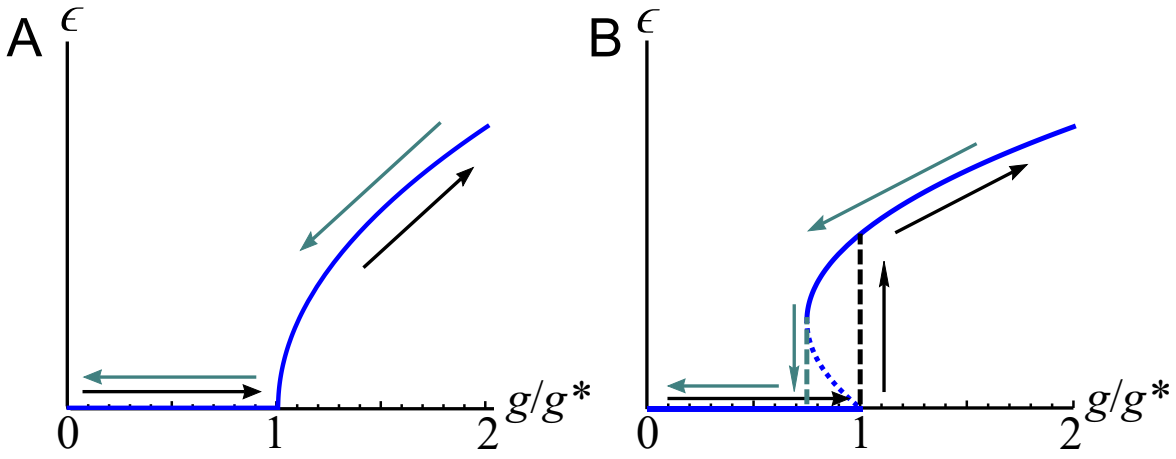

Fig. 1.22 The loading-unloading curve for (A) supercritical instability and (B) subcritical instability. The black arrow denotes loading, the grey arrow unloading. Dashed line shows the jump of the amplitude at the threshold. Dotted line denotes a branch of an unstable solution.

In loading (i.e. increasing g) when g exceeds g^* the $\varepsilon = 0$ minimum becomes a maximum and loses stability, and the solution will jump to the second minimum which, at threshold, has a finite amplitude of

$$\varepsilon = -\frac{3C_3}{4C_4}. \tag{1.135}$$

In unloading, this high-amplitude minimum remains stable until it vanishes when $g = g^* + \frac{9C_3^2}{32C_4C_2}$, at which point the system will jump back to the flat $\varepsilon = 0$ state. The kind of instability is called a **subcritical** instability. It has a non-trivial hysteresis loop in the amplitude plot, similar to a first order phase transition. The energy also jumps at the threshold to a value of:

$$E = E_0 - \frac{27C_3^4}{256C_4^3}. \tag{1.136}$$

These two different behaviours are illustrated in Fig. 1.22. However, if C_4 is negative for either cases, the energy series need to be evaluated to higher orders ($O(\varepsilon^6)$ or higher) to make the amplitude bounded from below. In this case, the instability will be subcritical as there will be a jump in amplitude at the threshold.

1.5 What is not known?

We have seen that there exist different elastic instabilities that can produce different and dramatic shape changes, and that some of these are known to be responsible for the shapes of biological organs, and can help us understand morphogenesis. However, there are still

many outstanding questions that have not been addressed in this topic. What types of elastic instability exist? What shapes or patterns can be formed out of elastic instabilities and how can we predict them? How can we control these shapes? Answering these questions would provide us methods to produce shape, beneficial for understanding morphogenesis and designing shape-changing devices.

Firstly, what is the set of all the elastic instabilities that exist? In this introduction, I have discussed elastic instabilities that arise under many different types of load, including compression, growth, surface tension and gravity. These are not a list of all existing instabilities and I will not be able to complete the list. Nonetheless, in Chapter 3, I add to the list a previously undiscovered instability that forms unexpected shapes, the peristaltic instability in an inflated cylindrical channel. The instability is studied experimentally, numerically and theoretically and can also be observed in a biological system.

Secondly, what shapes do these instabilities form? Although linear stability analysis has proved a powerful tool for predicting when instabilities occur (with the conspicuous exception of sulcification), our understanding of pattern selection and large-amplitude shape formation is still very limited. In Chapter 4 and 5, I build on Koiter's [113] classic work on buckling pattern selection in shells, to build a theory of pattern formation in surface elastic instabilities. This theory is able to explain why hexagonal dents pattern appears in both equibiaxial layer/substrate wrinkling and the gravitational instability of a soft solid slab. Furthermore, the approach is general to any surface elastic instabilities, which will be useful to predict or manipulate patterns formed on surfaces.

Thirdly, in Chapter 6, I look at how one can manipulate wrinkling formation. One simple way to do this is by explicitly patterning the system with a lattice of holes. This hole lattice introduces strain localization, allowing wrinkles to form in a chosen pattern. The generated wrinkling patterns can be varied by simply changing the lattice geometry.

Finally, I discuss possible further work that regard these questions in Chapter 7.

Chapter 2

Finite Element Method

In the introduction, I have discussed how energy minimization can be used to understand shape generation in elastic instabilities. Methods such as linear stability analysis are useful to characterize the onset of the instabilities. However, to understand the complete behaviours of the instabilities beyond the threshold, we need to fully minimize the elastic energy, i.e. go beyond the linear analysis. Minimizing the energy exactly using analytical methods is generally impossible as the associated equations are non-linear. A numerical method such as the finite element method (FEM) can be used to solve this problem.

The finite element method is a numerical method of solving problems such as partial differential equations or variational problems, usually for a system that cannot be solved analytically [114]. Its principle is to discretize the system into small areas or volumes, called finite elements, where they will be solved with linear equations. The elements can be in any shapes such as triangles or rectangles in two dimensions, cuboid or tetrahedra in three dimensions. In our elasticity problems, the elements are applied with some test strain fields. With these strain fields, the forces on the elements are calculated using the energy gradient, which will move the system towards the energy minimum. The deformation described using finite elements is thus a valid strain field, and the resulting energy is an upper bound on the true elastic energy.

2.1 Overview

In the finite element method, the continuous system is divided into a finite number of regions or "finite elements". A number of nodal points are established with the mesh that divides the region. They usually locate at the intersection of the mesh lines. A node can be associated with more than a single finite element as shown in Fig. 2.1. These nodal points are assigned with nodal parameters such as pressure, displacement components, velocity components

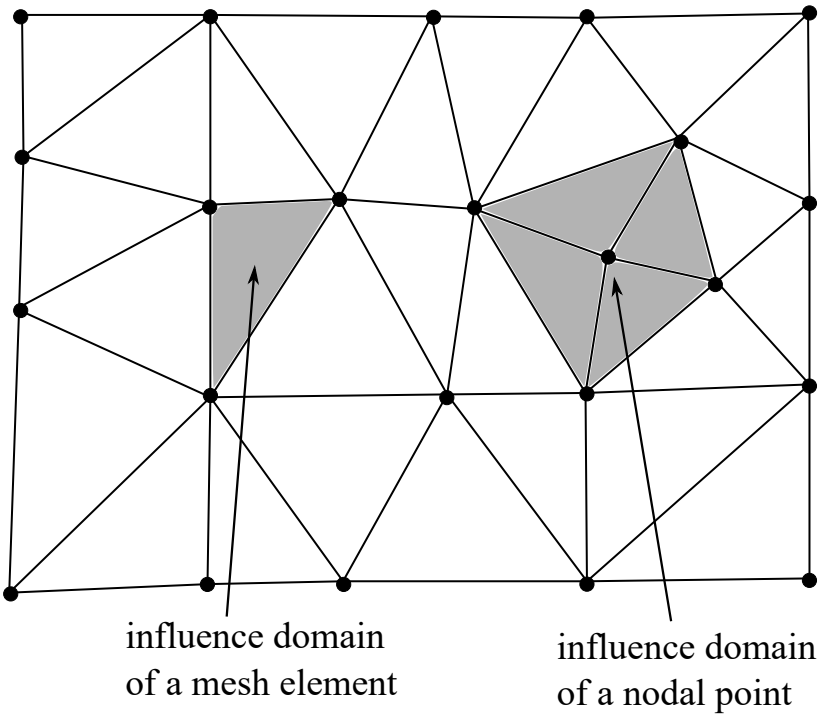

Fig. 2.1 Influence domains of a typical nodal point and a mesh element.

and force components. With this construction, we could establish variational models which involve finding the nodal parameters that result in the maximum or minimum value of the functional we want to extremize [114]. In solid mechanics, this functional would be the potential energy of the system. After the system is assembled, boundary conditions are required to be applied to the boundary nodes. These boundary conditions usually are constraints on the nodal parameters at the boundaries.

The solutions generated by the finite element method will contain some errors. These errors origin from the fact that within each mesh element, the equations governing the system are discretized. For instance, in our elasticity problems, the strain field in each mesh element is uniform. The resulting minimized energy would not be a true minimum but provide an upper bound. However, as there are more mesh elements in the system, the solution would become closer to the real energy minimum. Hence, one usually requires a large number of nodal points and mesh elements to generate an accurate solution at a cost of consuming a longer running time.

To understand how the method works, let us consider a simple one-dimensional problem of linear springs. A spring's behaviour is governed by its elastic potential energy,

$$U = \frac{1}{2}kd^2, \tag{2.1}$$

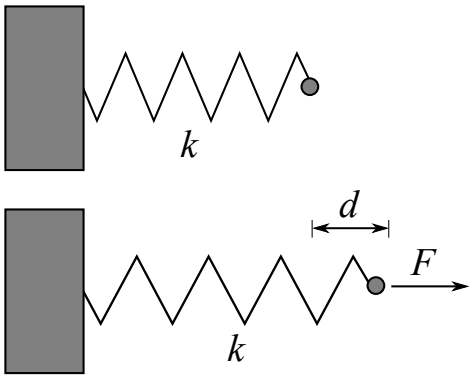

Fig. 2.2 A linear spring (top) with and (bottom) without the external force F.

where k is the spring's stiffness and d is the separation from its natural length. If the spring is loaded with a constant force F as in Fig. 2.2, the work done by the external force will be

$$W = Fd. \tag{2.2}$$

We minimize the total energy (elastic potential energy $-$ work done by the external force) to find the equilibrium separation

$$E = U - W = \frac{1}{2}kd^2 - Fd, \tag{2.3}$$

which simply gives $d = F/k$ as we expected.

Next, consider a slightly more complicated problem. Two springs are connected as in Fig. 2.3A with stiffness of k_a and k_b. We can assign the displacement x_1, x_2 and x_3 to the nodes 1,2 and 3. The force on each node will be called P_1, P_2 and P_3. These displacements and forces are the nodal parameters that we want to solve for the energy minimum. By breaking the two springs apart into two systems, i.e. two elements a and b (Fig. 2.3B), we can write down the equations governing the system for the element a:

$$F_{1,a} = k_a(x_1 - x_2) \tag{2.4}$$

$$F_{2,a} = k_a(x_2 - x_1), \tag{2.5}$$

and for the element b:

$$F_{2,b} = k_b(x_2 - x_3) \tag{2.6}$$

$$F_{3,b} = k_b(x_3 - x_2), \tag{2.7}$$

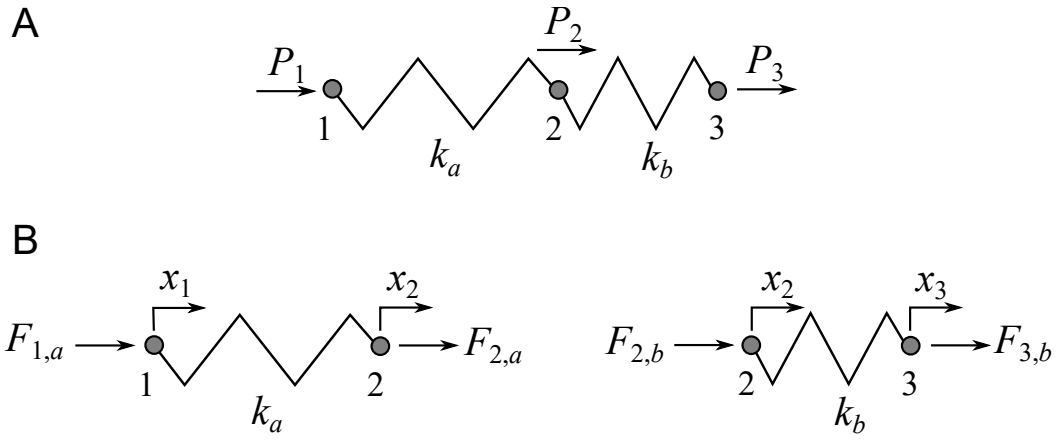

Fig. 2.3 (A) A system of two springs connected together under influences of external forces. (B) Breaking the system into two elements.

or equivalently in matrix notation

$$\begin{pmatrix} k_a & -k_a & 0 \\ -k_a & k_a & 0 \\ 0 & 0 & 0 \end{pmatrix} \begin{pmatrix} x_1 \\ x_2 \\ x_3 \end{pmatrix} = \begin{pmatrix} F_{1,a} \\ F_{1,b} \\ 0 \end{pmatrix} \tag{2.8}$$

$$\begin{pmatrix} 0 & 0 & 0 \\ 0 & k_b & -k_b \\ 0 & -k_b & k_b \end{pmatrix} \begin{pmatrix} x_1 \\ x_2 \\ x_3 \end{pmatrix} = \begin{pmatrix} 0 \\ F_{2,b} \\ F_{3,b} \end{pmatrix}. \tag{2.9}$$

The zero rows and columns imply that, for example, the element a is unaffected by the node 3. Adding (2.8) and (2.9) gives us

$$\begin{pmatrix} k_a & -k_a & 0 \\ -k_a & k_a+k_b & -k_b \\ 0 & -k_b & k_b \end{pmatrix} \begin{pmatrix} x_1 \\ x_2 \\ x_3 \end{pmatrix} = \begin{pmatrix} F_{1,a} \\ F_{1,b}+F_{2,b} \\ F_{3,b} \end{pmatrix} = \begin{pmatrix} P_1 \\ P_2 \\ P_3 \end{pmatrix}. \tag{2.10}$$

This matrix equation describes the whole system. The matrix on the left-hand side is called the stiffness tensor, K. Before we solve this equation, it is necessary to apply the boundary conditions. Suppose that the node 3 is fixed and the applied forces P_1 and P_2 are given by constants F_1 and F_2. Equation (2.10) is now

$$\begin{pmatrix} k_a & -k_a & 0 \\ -k_a & k_a+k_b & -k_b \\ 0 & -k_b & k_b \end{pmatrix} \begin{pmatrix} x_1 \\ x_2 \\ 0 \end{pmatrix} = \begin{pmatrix} F_1 \\ F_2 \\ P_3 \end{pmatrix}, \tag{2.11}$$

which can be solved by $(x_1, x_2, 0) = K^{-1} \cdot (F_1, F_2, P_3)$ for the unknown x_1, x_2 and P_3, giving the position of the first and second nodes and the load at the third node. This method can easily be generalized to find approximate solution to a problem with continuous solid within linear elasticity by breaking the solid into finite segments (elements) and treat each of them as a linear spring. In higher dimensional systems or other more complicated systems, a similar matrix equation as (2.10) can be constructed by finding how the nodal parameters depend on one another.

In general, solving the system exactly is not always possible. Firstly, if there are too many nodal points, it might take a very long time to solve the equations exactly. One way to overcome this is to use an iterative method, which moves the system towards the real solution at each iteration. Secondly, for non-linear problems such as ones in hyperelastic systems, constructing a matrix equation similar to (2.10) is more complicated as the stiffness matrix now depends on the nodal parameters. Again, using iterative methods allow us to evaluate and adjust the stiffness matrix at each iteration. One of the simplest iterative methods for variational problems is the Newtonian dynamics. Newtonian dynamics is the way that nature uses to find energy minimum of the system. This is done by calculating the forces at each node at each iteration, which I will call a time step, and then the change in the displacement can be calculated from the acceleration obtained from Newton's second law. This can be done via the forward Euler's method. First, the nodal velocity $\mathbf{v}$ is updated using the Newton's second law:

$$\mathbf{v}_{n+1} = \mathbf{v}_n + \frac{\mathbf{F}_n}{m} dt, \tag{2.12}$$

where $\mathbf{F}$ is the nodal force, m is the mass associated with the node and the subscripts n and $n+1$ denote the current and following time steps. The nodal displacement $\mathbf{x}$ can then be calculated from the velocity

$$\mathbf{x}_{n+1} = \mathbf{x}_n + \mathbf{v}_n dt. \tag{2.13}$$

As the time step increases, the nodes will move towards the mechanical equilibrium, which is the system energy minimum.

Throughout this thesis, finite element numerical simulations will be performed to verify theoretical predictions using a finite element method that I wrote, based on the code used in [7, 60, 61, 78] (see Appendix B for the full code). The code conducts the energy minimization by calculating the force on each node as the gradient of the total energy with respect to the node's displacement, and then moves the nodes using Newtonian dynamics. In the following sections, I will explain in detail how the code works, for two-dimensional, three-dimensional and axisymmetric calculations.

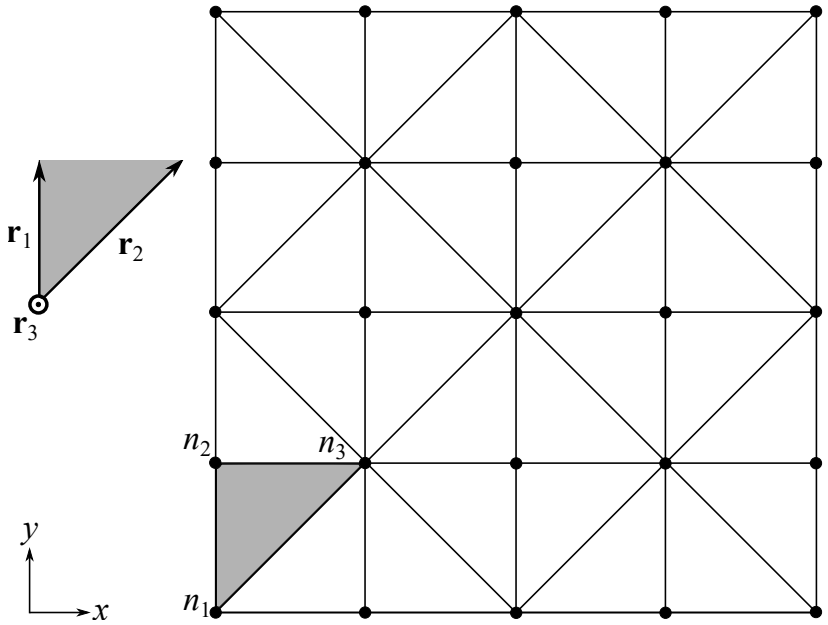

Fig. 2.4 Schematic diagram of triangular mesh elements used in the two-dimensional finite element method. The inset on the left shows construction of the prism elements with vectors $\mathbf{r}_1$,$\mathbf{r}_2$ and $\mathbf{r}_3$.

2.2 Two-dimensional system

The simplest code is a two-dimensional plane-strain code, that constructs a finite element triangular mesh in the x–y plane, in which the strain associated with each triangular element is uniform. First, we construct triangles for our nodes as shown in Fig. 2.4. Consider a triangular element (grey in Fig. 2.4), consisting of nodes n_1, n_2 and n_3 with $\mathbf{x}[n_1], \mathbf{x}[n_2]$ and $\mathbf{x}[n_3]$ as their initial coordinate, and $\mathbf{X}[n_1], \mathbf{X}[n_2]$ and $\mathbf{X}[n_3]$ as their current (deformed) coordinate respectively. From these three nodes, a triangular prism element will be constructed. Let the vector $\mathbf{r}_i$ and $\mathbf{R}_i$ be the initial and current element edge vectors of a triangular prism such that

$$\begin{aligned} \mathbf{r}_1 &= \mathbf{x}[n_2] - \mathbf{x}[n_1] & \mathbf{R}_1 &= \mathbf{X}[n_2] - \mathbf{X}[n_1] \\ \mathbf{r}_2 &= \mathbf{x}[n_3] - \mathbf{x}[n_1] & \mathbf{R}_2 &= \mathbf{X}[n_3] - \mathbf{X}[n_1] \\ \mathbf{r}_3 &= (0,0,1) & \mathbf{R}_3 &= (0,0,1). \end{aligned} \tag{2.14}$$

For each triangle, the code first calculates the matrices:

$$A_0 = (\mathbf{r_1}, \mathbf{r_2}, \mathbf{r_3}) \qquad A = (\mathbf{R_1}, \mathbf{R_2}, \mathbf{R_3}), \tag{2.15}$$

which are then used to calculate the deformation gradient for the triangle, using the fact that $A = F \cdot A_0$,

$$F = A \cdot A_0^{-1}. \tag{2.16}$$

Based on the energy density in (1.28), the energy density of the triangular prism element, W, consisting of the shear and volumetric energy is

$$W = \frac{\mu}{2}\left(\frac{\mathrm{Tr}\,B}{J^{2/3}} - 3\right) + \frac{\kappa}{2}(J-1)^2, \tag{2.17}$$

where μ and κ are shear and bulk modulus, the matrix $B = F \cdot F^T$ and a scalar $J = \mathrm{Det}(F)$. Here, we use a compressible neo-Hookean energy density because using perfect incompressibility in the finite element method leads to problems such as locking, where the elements appear to be stiffer than they are [115]. The energy, E, of the triangular prism is calculated by multiplying then energy density with the initial volume of the prism $V_0 = \mathrm{Det}(A_0)/2$. The total energy is then

$$E_{tot} = \sum E = \sum W V_0, \tag{2.18}$$

where the summation is over all the tetrahedron element. The Cauchy stress tensor is

$$T = \left(B - I\frac{\mathrm{Tr}\,B}{3}\right)\frac{\mu}{J^{5/3}} + I\kappa(J-1). \tag{2.19}$$

To calculate the force on each node, we need to evaluate normal area vectors on each face of the element:

$$\begin{aligned} \mathbf{N}_1 &= -\mathbf{R}_1 \times \hat{\mathbf{z}} \\ \mathbf{N}_2 &= \mathbf{R}_2 \times \hat{\mathbf{z}} \\ \mathbf{N}_3 &= (\mathbf{R}_1 - \mathbf{R}_2) \times \hat{\mathbf{z}}. \end{aligned} \tag{2.20}$$

We then increase the force on each node $\mathbf{F}[n_i]$, by the energy gradient on each node, which is calculated (exactly) as:

$$\begin{aligned} \mathbf{F}[n_1] &+= T\left(\frac{\mathbf{N}_1 + \mathbf{N}_2}{2}\right) \\ \mathbf{F}[n_2] &+= T\left(\frac{\mathbf{N}_1 + \mathbf{N}_3}{2}\right) \\ \mathbf{F}[n_3] &+= T\left(\frac{\mathbf{N}_2 + \mathbf{N}_3}{2}\right). \end{aligned} \tag{2.21}$$

Here, the notation $\pm=$ means adding/subtracting the original value by the value on the right-hand side. Having calculated the forces on all nodes, we then displace the nodes in accordance with Newtonian dynamics:

$$\begin{aligned}\mathbf{F}[n_i] &-= \gamma \mathbf{v}[n_i] \\ \mathbf{v}[n_i] &+= \mathbf{F}[n_i]/m[n_i]dt \\ \mathbf{X}[n_i] &+= \mathbf{v}[n_i]dt,\end{aligned} \tag{2.22}$$

where $\mathbf{v}[n_i]$ and $m[n_i]$ are the velocity and mass of the node n_i, γ is the damping coefficient and dt is the time step size. The damping is used to reduce oscillations in the system. The mass of the node is obtained by averaging the initial volume of the elements connected to the node, then multiplying with the density:

$$m[n_i] = \rho \frac{\sum V_0}{N}, \tag{2.23}$$

where the summation is over all N neighbouring tetrahedral elements. The process is then repeated until the system is close to equilibrium. One way to see whether the system is close to equilibrium is to apply a convergence test a measurable quantity such as buckling amplitude or energy. I will use the convergence test for the root-mean-square buckling amplitude:

$$\frac{|\varepsilon_n - \varepsilon_{n-1}|}{\varepsilon_{n-1}} < \tau, \tag{2.24}$$

where ε is the root-mean-square amplitude and the subscripts n and $n-1$ refer to the current and previous time steps and τ is the relative tolerance, for which I use $\tau = 10^{-6}$. When the criterion is met, the system is accepted to be the equilibrium solution.

2.3 Axisymmetric cylindrical system

Most of the steps will be similar to the two-dimensional case. The x–y plane represents the z–r plane. Instead of using a triangular prism element, we construct an annulus element by revolving the triangle through the nodes n_1, n_2 and n_3. We can treat the annulus element as if it is a regular prism element but the force on the nodes need to be calculated appropriately. This is done by "unwinding" the annulus element into a triangular prism with its length equal to the average circumference of the annulus (see Fig. 2.5). The average circumference in the initial coordinate is calculated from the average radius, $\rho_{av} = (y_1 + y_2 + y_3)/3$, as $2\pi\rho_{av}$, where y_i is the initial node's y coordinate, which corresponds to the radial coordinate in the

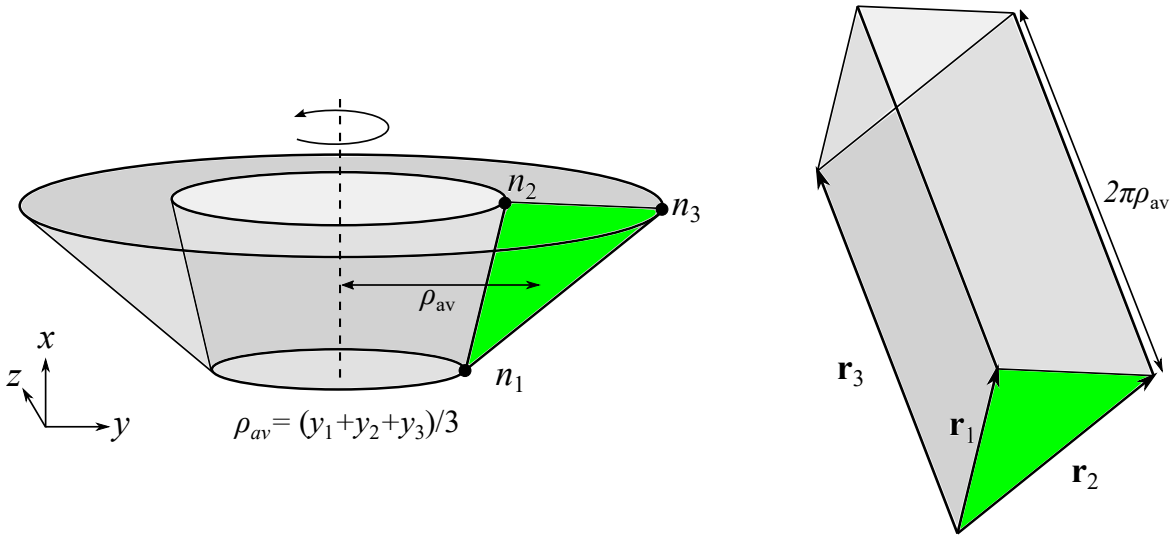

Fig. 2.5 Schematic diagram of annulus mesh element used in the axisymmetric cylindrical system. (left) The annulus element with three nodes n_1, n_2 and n_3 forming a triangle which its revolution forms an annulus. (right) A prism element forms by "unwinding" the annulus element.

cylindrical system. Similar calculation can be done for the current coordinate with Y_i for the current y coordinate. In (2.14), we therefore have

$$\begin{aligned}
\mathbf{r}_1 &= \mathbf{x}[n_2] - \mathbf{x}[n_1] & \mathbf{R}_1 &= \mathbf{X}[n_2] - \mathbf{X}[n_1] \\
\mathbf{r}_2 &= \mathbf{x}[n_3] - \mathbf{x}[n_1] & \mathbf{R}_2 &= \mathbf{X}[n_3] - \mathbf{X}[n_1] \\
\mathbf{r}_3 &= \left(0, 0, \frac{2\pi}{3}(y_1 + y_2 + y_3)\right) & \mathbf{R}_3 &= \left(0, 0, \frac{2\pi}{3}(Y_1 + Y_2 + Y_3)\right).
\end{aligned} \tag{2.25}$$

The energy can then be evaluated from (2.16–2.18). The forces on the node, however, will be calculated differently using exact derivative of the energy. Since the PK1 stress $\sigma = \frac{\partial W}{\partial F}$, the force $\mathbf{F}$ can be evaluated from the energy derivative via,

$$\mathbf{F}_i/V_0 = -\frac{\partial W}{\partial \mathbf{X}_i} = -\frac{\partial W}{\partial F_{jk}}\frac{\partial F_{jk}}{\partial \mathbf{X_i}} = -\text{Tr}\left(\sigma \frac{\partial F^T}{\partial \mathbf{X}_i}\right). \tag{2.26}$$

First, we calculate the PK1 stress tensor from:

$$\sigma = \left[\left(B - \frac{\text{Tr}B}{3}I\right)\frac{\mu}{J^{2/3}} + \kappa J(J-1)I\right]F^{-T}. \tag{2.27}$$

Then, we evaluate the exact derivative of F^T:

$$\left.\frac{\partial F^T}{\partial X}\right|_{n_1} = \frac{1}{S}\begin{pmatrix} y_2-y_3 & 0 & 0 \\ x_3-x_2 & 0 & 0 \\ 0 & 0 & 0 \end{pmatrix}$$
$$\left.\frac{\partial F^T}{\partial X}\right|_{n_2} = \frac{1}{S}\begin{pmatrix} y_3-y_1 & 0 & 0 \\ x_1-x_3 & 0 & 0 \\ 0 & 0 & 0 \end{pmatrix}$$
$$\left.\frac{\partial F^T}{\partial X}\right|_{n_3} = \frac{1}{S}\begin{pmatrix} y_1-y_2 & 0 & 0 \\ x_2-x_1 & 0 & 0 \\ 0 & 0 & 0 \end{pmatrix} \tag{2.28}$$
$$\left.\frac{\partial F^T}{\partial Y}\right|_{n_1} = \frac{1}{S}\begin{pmatrix} 0 & y_2-y_3 & 0 \\ 0 & x_3-x_2 & 0 \\ 0 & 0 & \frac{S}{r_s} \end{pmatrix}$$
$$\left.\frac{\partial F^T}{\partial Y}\right|_{n_2} = \frac{1}{S}\begin{pmatrix} 0 & y_3-y_1 & 0 \\ 0 & x_1-x_3 & 0 \\ 0 & 0 & \frac{S}{r_s} \end{pmatrix}$$
$$\left.\frac{\partial F^T}{\partial Y}\right|_{n_3} = \frac{1}{S}\begin{pmatrix} 0 & y_1-y_2 & 0 \\ 0 & x_2-x_1 & 0 \\ 0 & 0 & \frac{S}{r_s} \end{pmatrix}, \tag{2.29}$$

where $S = |\mathbf{r}_1 \times \mathbf{r}_2|$ and $r_s = y_1 + y_2 + y_3$. The force that needs to be added to each node can then be calculated from (2.26),

$$\mathbf{F}[n_i] \mathrel{-}= V_0 \left(\mathrm{tr}\left(\sigma \left.\frac{\partial F^T}{\partial X}\right|_{n_i} \right), \mathrm{tr}\left(\sigma \left.\frac{\partial F^T}{\partial Y}\right|_{n_i} \right), 0 \right). \tag{2.30}$$

The nodes are then displaced after assigning the forces to all nodes, using Newtonian dynamics (2.22).

2.4 Three-dimensional system

For a three-dimensional system, eight neighbouring nodes form a cuboid. Each cuboid can be broken into six tetrahedra as shown in Fig. 2.6. Note that this is not the only way to do so (see Fig. 2.7). To avoid breaking the symmetry in the mesh, we alternate the tetrahedra positions for each consecutive cuboid. Fig. 2.8A shows the arrangement of the nodal elements and

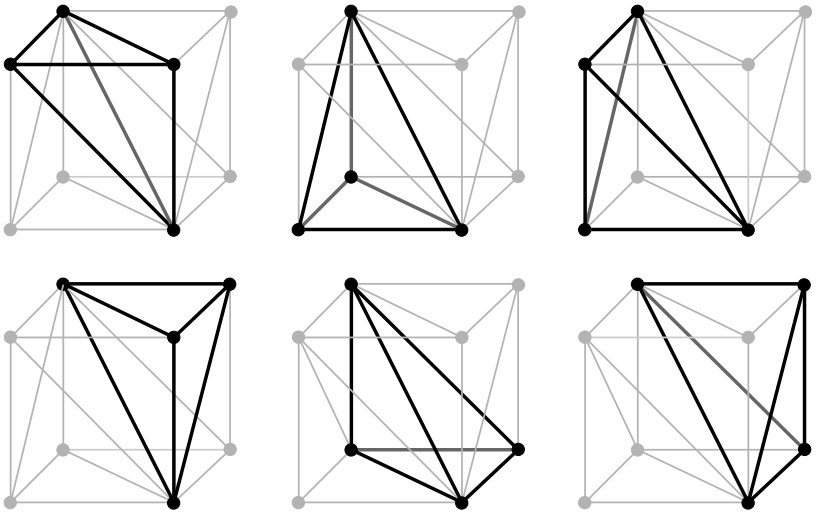

Fig. 2.6 Six tetrahedron elements from a cubic element.

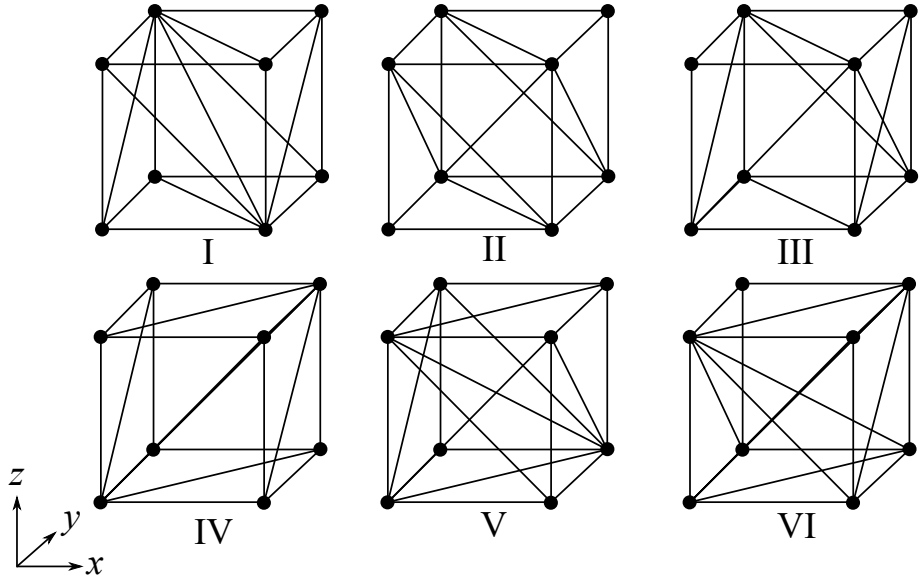

Fig. 2.7 Different ways of breaking a cuboid into six tetrahedra.

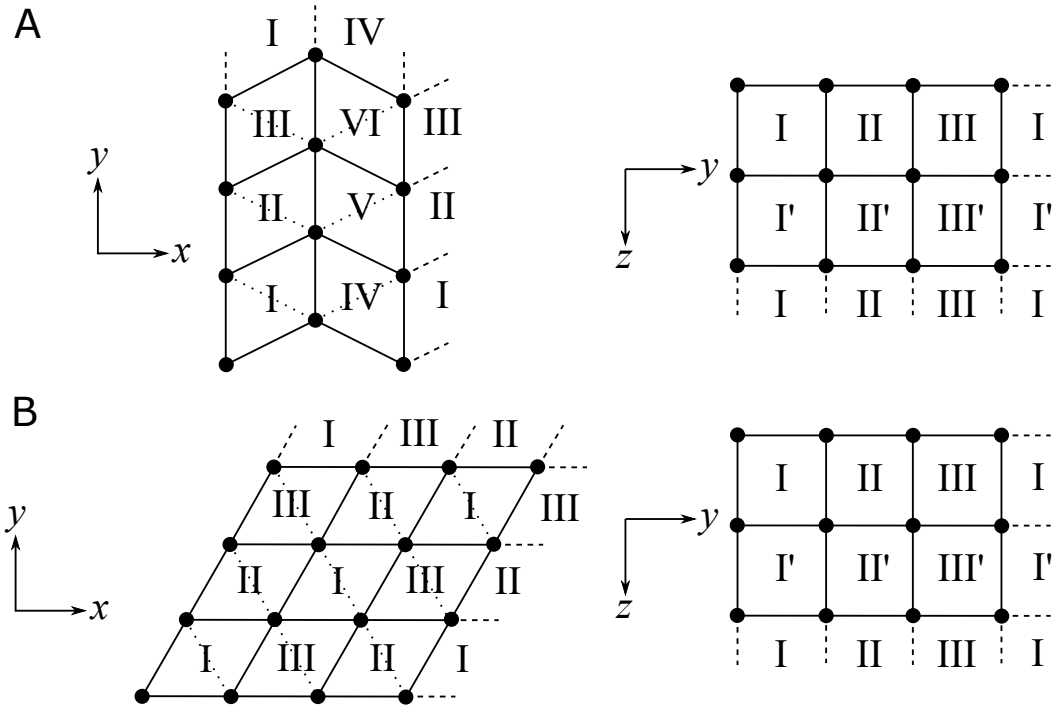

Fig. 2.8 Arrangement of tetrahedron elements used in the simulation (A) non-hexagonal, (B) hexagonal. Roman numbers correspond to the tetrahedra pattern in Fig. 2.7. Prime denotes z-reflection of the original arrangement. Dotted lines show the division of the cuboids before breaking into tetrahedron mesh elements.

tetrahedron element throughout the simulation domain used in most of the three-dimensional simulations in this thesis. However, a modified version of this mesh is used for a hexagonal symmetric simulation, shown in Fig. 2.8B, which is more suitable to simulate the hexagonal pattern that appears many times in this thesis.

From each tetrahedron with nodes, n_1, n_2, n_3 and n_4, the edges vector for the initial and current coordinates can be created as:

$$\begin{aligned} \mathbf{r}_1 &= \mathbf{x}[n_2] - \mathbf{x}[n_1] & \mathbf{R}_1 &= \mathbf{X}[n_2] - \mathbf{X}[n_1] \\ \mathbf{r}_2 &= \mathbf{x}[n_3] - \mathbf{x}[n_1] & \mathbf{R}_2 &= \mathbf{X}[n_3] - \mathbf{X}[n_1] \\ \mathbf{r}_3 &= \mathbf{x}[n_4] - \mathbf{x}[n_1] & \mathbf{R}_3 &= \mathbf{X}[n_4] - \mathbf{X}[n_1]. \end{aligned}$$

We then calculate the deformation gradient, elastic energy and Cauchy stress tensor using (2.16–2.19), noting that the volume of the element is now $V_0 = \mathrm{Det}(A_0)/6$. The normal area

vectors on each face of the element are:

$$\begin{aligned}\mathbf{N}_1 &= \mathbf{R}_3 \times \mathbf{R}_1 \\ \mathbf{N}_2 &= \mathbf{R}_2 \times \mathbf{R}_3 \\ \mathbf{N}_3 &= \mathbf{R}_1 \times \mathbf{R}_2 \\ \mathbf{N}_4 &= (\mathbf{R}_2 - \mathbf{R}_3) \times (\mathbf{R}_1 - \mathbf{R}_3).\end{aligned} \tag{2.31}$$

We then increase the force on each node $\mathbf{F}[n_i]$,

$$\begin{aligned}\mathbf{F}[n_1] &+= T\left(\frac{\mathbf{N}_1 + \mathbf{N}_2 + \mathbf{N}_3}{6}\right) \\ \mathbf{F}[n_2] &+= T\left(\frac{\mathbf{N}_1 + \mathbf{N}_3 + \mathbf{N}_4}{6}\right) \\ \mathbf{F}[n_3] &+= T\left(\frac{\mathbf{N}_2 + \mathbf{N}_3 + \mathbf{N}_4}{2}\right) \\ \mathbf{F}[n_4] &+= T\left(\frac{\mathbf{N}_1 + \mathbf{N}_2 + \mathbf{N}_4}{6}\right).\end{aligned} \tag{2.32}$$

The nodes are then displaced after assigning the forces to all nodes, using Newtonian dynamics (2.22).

2.5 Boundary condition

Several types of boundary conditions are needed to be applied to the system.

2.5.1 Periodic boundary condition

Since the pattern that occurs in instabilities is usually periodic and we cannot simulate an infinitely large domain, it is convenient to simulate a small repeatable unit cell with periodic boundary conditions. Firstly, the periodicity is applied to the mass of each element on the boundary. Let n_L and n_R represent the nodes on the left and right boundaries of the unit cell; we apply

$$m[n_L] \mathrel{+}= m[n_R] \tag{2.33}$$

$$m[n_R] = m[n_L]. \tag{2.34}$$

Then, the same thing is done to the force:

$$\mathbf{F}[n_L] \mathrel{+}= \mathbf{F}[n_R] \tag{2.35}$$

$$\mathbf{F}[n_R] = \mathbf{F}[n_L]. \tag{2.36}$$

For three dimensional systems, this is applied to both x and y directions.

2.5.2 Fixed boundary condition

The material displacement is fixed in this boundary condition such as when the solid is attached to a rigid substrate. This is done by setting the force to always be zero:

$$\mathbf{F}[n_{b.c.}] = \mathbf{0}. \tag{2.37}$$

2.5.3 Stress-free boundary condition

The free surface must have zero stress. This occurs naturally when the system is in Newtonian equilibrium.

2.6 External forces

To induce elastic instabilities, external forces or perturbations will be applied to our system. These include hydrostatic pressure, gravity and growth.

2.6.1 Hydrostatic pressure

In Chapter 3, I study pressurized cavities which can be simulated using an axisymmetric cylindrical geometry. Let us consider a hydrostatic pressure inside a cylindrical cavity, P_{in}. The associated force can be calculated via

$$\mathbf{F} = P_{in}\nabla V, \tag{2.38}$$

where V is the cavity volume. To calculate the force on each surface node, firstly, the cavity volume associated with each node is determined. Fig. 2.9 shows the volume enclosed, V_i by the node, n_i with can be treated as two jointed truncated cones. It can be shown that

$$V_i = \pi \frac{(Y_{i-1}^2 + Y_{i-1}Y_i + Y_i^2)(X_i - X_{i-1}) + (Y_i^2 + Y_iY_{i+1} + Y_{i+1}^2)(X_{i+1} - X_i)}{6}, \tag{2.39}$$

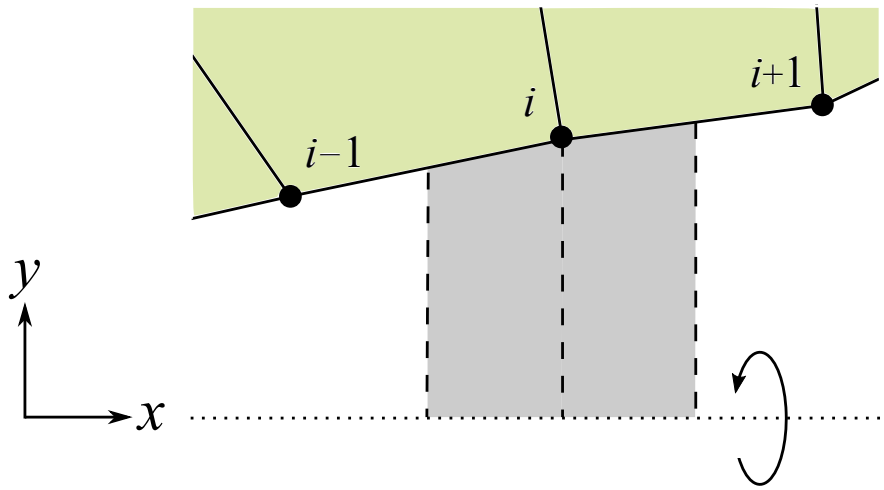

Fig. 2.9 Cavity volume associated with each surface node, given grey area revolving around the x-axis.

with $X_i = X[n_i]$ and $Y_i = Y[n_i]$ are the current coordinate of the node n_i. The incremental force can then be calculated from (2.38):

$$\mathbf{F}[n_i] \mathrel{+}= \left(P_{in} \frac{\partial V_i}{\partial X_i}, P_{in} \frac{\partial V_i}{\partial Y_i}, 0 \right) \tag{2.40}$$

The potential energy associated with the cavity pressure is evaluated from

$$E_P = - \sum_{i,\text{surface}} P_{in} V_i. \tag{2.41}$$

2.6.2 Gravity

A gravitational force is applied straightforwardly via

$$\mathbf{F}[n_i] \mathrel{-}= (0, 0, m[n_i] g), \tag{2.42}$$

where g is the gravitational field strength and z is the vertical direction. Similarly, the gravitational potential energy can be evaluated from

$$E_g = \sum_i m[n_i] g Z[n_i]. \tag{2.43}$$

2.6.3 Growth

Growth or swelling can be applied by modifying the tensor A_0 with

$$A_0 \rightarrow G \cdot A_0, \tag{2.44}$$

where G is the growth tensor, which can be expressed in terms of growth in each direction

$$G = \begin{pmatrix} g_x & 0 & 0 \\ 0 & g_y & 0 \\ 0 & 0 & g_z \end{pmatrix}. \tag{2.45}$$

This modifies the forces as well as the associated elastic energy.

Chapter 3

Peristaltic elastic instability in an inflated cylindrical channel

A fluid bearing channel through a soft solid is the prototypical element of biological plumbing [117], guiding fluid through the vascular, lymphatic, digestive, reproductive, renal and respiratory systems. Soft channels also underpin the blossoming field of soft microfluidics [118], which exploits the convenience of soft lithography for rapid prototyping [119, 120], the deformability of soft channels to actuate valves and pumps [118, 121, 122], and the mechanical compatibility between soft solids and soft tissues to build organs-on-chips and implantable clinical devices [123, 124]. In this chapter, I discuss a brand-new elastic instability that occurs in a cylindrical channel. I start by addressing a basic question about such channels: how do they change shape as their internal pressure increases? Thin-walled elastic tubes famously undergo long-wavelength bulging, bending and ballooning instabilities [22, 99–102, 125–130] under inflation, but a channel through a bulk solid arises in the opposite limit. This problem is perhaps more reminiscent of solid cavitation, but in two dimensions rather than three. We thus might expect the channel to expand greatly ("cavitate") at some threshold pressure, but what actually happens is much more interesting.

As summarized in Figs 3.1–3.3, while modest fluid pressures simply dilate soft solid channels, when the pressure becomes comparable to the solid's shear modulus, the channel undergoes a reversible elastic instability and adopts a peristaltically undulating morphology. Here, the term peristalsis refers to the alternation of contraction and expansion of the channel. Experimental, numerical and theoretical analysis were performed to investigate the instability. This is a collaborative work with K. Leonavicius and S. Srinivas [116] from Department of Physiology Anatomy and Genetics, University of Oxford, where I contribute theoretical and numerical analysis (Sections 3.2–3.3), while they contribute the experimental work (Section 3.1).

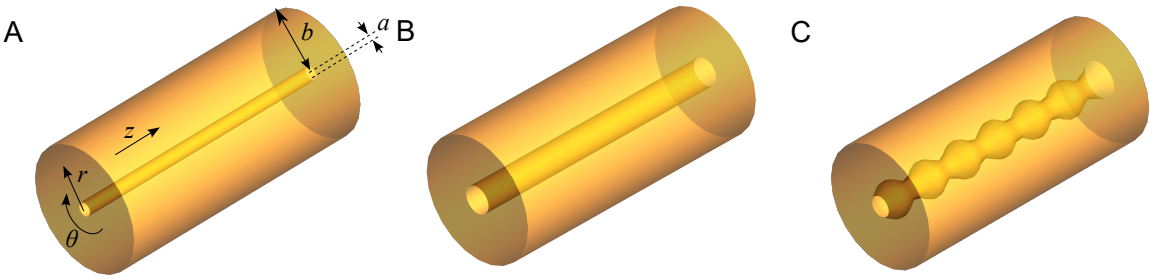

Fig. 3.1 Schematic images showing the shape evolution of (A) a cylindrical channel through a soft solid under increasing internal pressure. (B) At modest pressures the channel dilates simply, (C) but at high pressures it undergoes an elastic instability and adopts a peristaltic shape.

Fig. 3.2 The evolution of the experimental hydrogel channel as the pressure is increased. (A) initial cavity, (B) low pressure and (C) high pressure. Taken from [116].

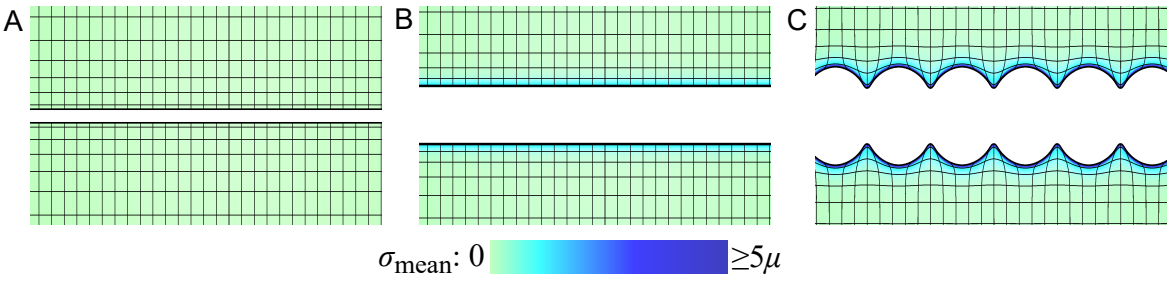

Fig. 3.3 The evolution of the numerically simulated cavity as the pressure is increased, at (A) $P = 0$, (B) $P = 1.9\mu$ and (C) $P = 2.2\mu$. The colour scheme denotes the mean hydrostatic stress, $\sigma_{\text{mean}} = (\sigma_{xx} + \sigma_{yy} + \sigma_{zz})/3$.

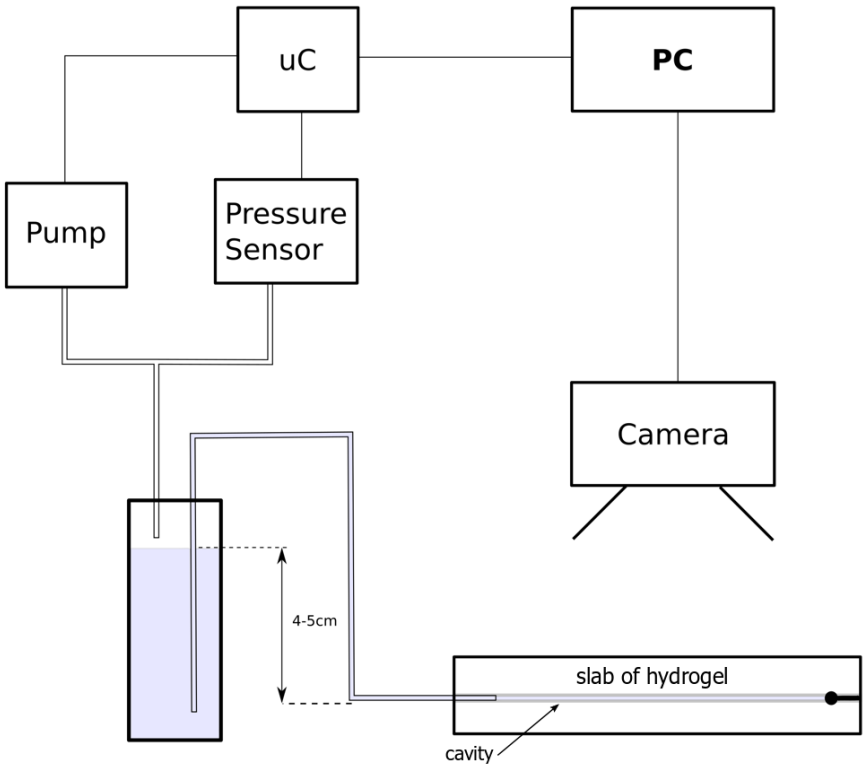

Fig. 3.4 Schematic experimental set up of the peristaltic instability. Taken from [116].

3.1 Experiment

The experiments were performed using hydrogel channels. Firstly, hydrogel channels of different moduli were made by moulding different concentrations of polyacrylamide/bisacrylamide mixture (39:1) in 1-mm thick slabs around 30μm wires. The wires were 35 mm in length and cast inside a hydrogel slab whose length was 12 mm. The mixture was then polymerized into a solid gel using a mixture of ammonium persulfate (0.1%) and tetra ethyl methyl diamine (TEMED, 1%) and the wire was pulled out to leave a cylindrical channel. Finally, phosphate buffered saline (PBS) was used to equilibrate the gels for 30 minutes after polymerization, prior to the experiments. Such cavities were made in batches of 5.

The channel inflation was then achieved using the experimental setup shown in Fig. 3.4. To pressurize the channels, a computer-controlled diaphragm air pump was connected to a glass capillary containing PBS solution. One of the capillary ends was pulled under flame to a 100–300 μm diameter in order to fit into the channel inside the hydrogel. A glass bead was used to plug the other side of the hydrogel channel. The pressure in the channel was then increased in stages of approximately 200 Pa, each lasting at least 2 seconds until the elastic deformation occurred. The resulting channel deformations were then imaged

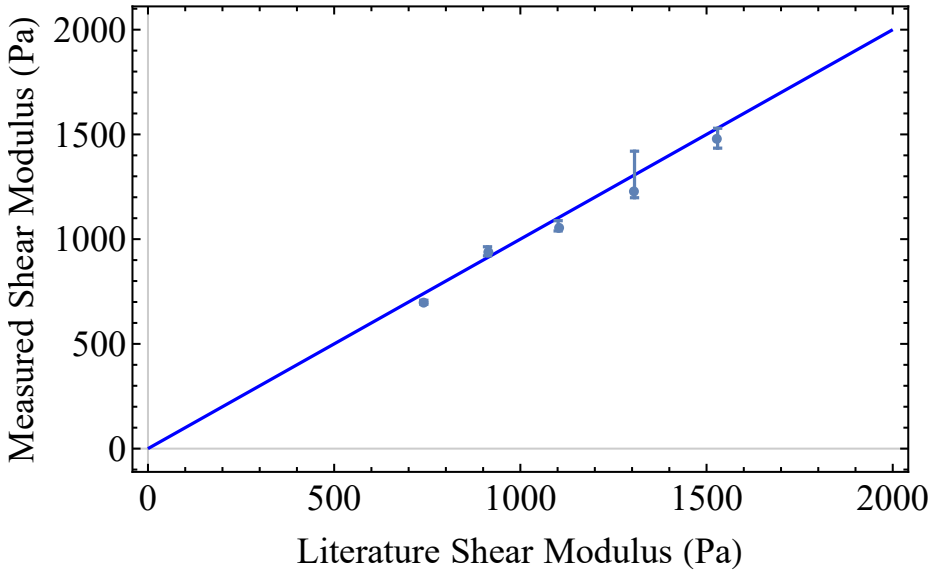

Fig. 3.5 Measured hydrogel modulus against value expected from composition. Each point combines multiple pressure-dilation measurements from five independent hydrogel channels. Taken from [116].

using a complementary metal–oxide–semiconductor (CMOS) camera sensor fitted to a Leica stereomicroscope eyepiece. The images were processed manually using ImageJ software [131] to measure the diameter of the channel at each recorded pressure value as well as the peristaltic wavelength in channels beyond the threshold of instability.

Five different hydrogel compositions were used, ranging between 4–5% bisacrylamide, to provide a range of shear moduli. The shear modulus, μ, was measured by comparing the relationship between the channel dilation λ and the cavity pressure while the channel is stable (see Section 3.3),

$$P_{in} = \frac{\mu}{2}\left[1 + \log(\lambda^2) - \lambda^{-2}\right].$$

As seen in Fig. 3.5, the measured moduli agree well with the literature values [132] for a given composition, validating the accuracy and equilibrium of the mechanical measurements.

As the fluid was pumped in to inflate, the cavity simply dilated at low pressure, but then deformed peristaltically beyond a threshold pressure, as shown in Fig. 3.2. The threshold pressure was measured as the lowest pressure required for the peaks to appear in the channel profile. For each gel composition, this critical pressure was measured in five different cavities. These five results were averaged to find the threshold pressure. In each cavity, the wavelength was also measured for each pressure beyond threshold to give the experimental wavelength points. After unloading a channel, and waiting for at most ~ 10 minutes for the gel to fully

Figure	P_{in}/μ	L/a	b/a	Mesh
3.6	0, 2.2	12	10	8×6
3.3	0, 1.9, 2.2	12.278	60	40×100
3.9	2.0–3.1	1–15	100	50×100
3.10, 3.12	0–2.75	12.278	60	40×100
3.14	1.4–3.1	2–16	5–100	100×50
3.16, 3.17	2.0–3.0	$2\pi/k_c$	50	100×55

Table 3.1 The parameters used in the numerical analysis for the peristaltic instability.

relax, it was found that the instability measurement experiments could be repeated in exactly the same manner.

3.2 Numerical analysis

In order to verify that the instability observed in the experiment can be captured by hyperelastic models such as the neo-Hookean model, we next performed explicit finite element calculations in three dimensions but with axisymmetry (see Section 2.3). The code constructs an elastic hollowed cylinder from constant-strain triangular elements in the r–z plane, each representing a triangular cross-sectioned torus of the body. The triangles form a rectangular mesh, spanning from the inner radius $r = a$ to the outer radius $r = b$, and from $z = 0$ to $z = L$, with the periodic boundary conditions at the two ends $z = 0, L$, which makes the simulation domain contain an integer number of a wavelength of the instability, as shown in Fig. 3.6 with a single wavelength. The grid here contains twice as many triangular elements as in Section 2.1 to improve the stability. The mesh is not uniform but is finer close to the inner surface and coarsens by 2% per element in the r-direction.

The simulation used finite compressibility with bulk modulus $\kappa = 10^2 - 10^3\mu$ to mimic incompressibility. In each calculation the changes were imposed slowly enough as to be quasi-static, so although the simulation uses Newtonian dynamics, the states reported in this chapter are all converged energy minima. It was made sure the bulk modulus was high enough, the mesh was fine enough, and the simulations were slow enough to mimic an incompressible, equilibrated continuum hollowed cylinder. The numerical parameters for each figure are summarized in the Table 3.1.

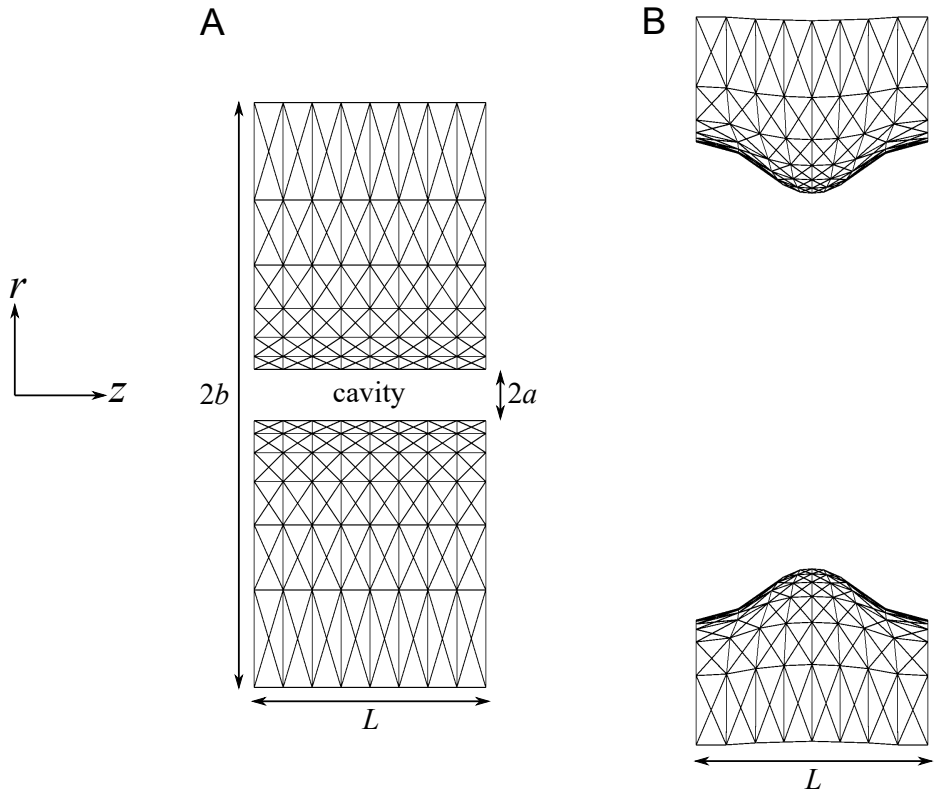

Fig. 3.6 Illustration of the finite element mesh used in the numerical simulation in (A) stable and (B) unstable states towards the instability under a cavity pressure. The mesh represents the $r-z$ cross-section of a hollowed cylinder. Both ends are subject to periodic boundary conditions. For clarity of visualization, we here show a sparse 8×6 mesh with dramatic mesh coarsening. The actual mesh used to produce results in this chapter is finer (see Table 3.1).

3.3 Theoretical analysis

Having observed the peristaltic instability experimentally and numerically, we now seek to understand it theoretically. We therefore perform a linear stability analysis to see whether adopting the undulating shape rather than remaining uniform lowers the total energy of the system. We start by considering a cylindrical cavity, with an initial radius a, running through soft elastic material initially occupying $a < r < b$, as shown in Fig. 3.1A. If the channel is subject to an internal pressure P_{in}, it will dilate, deforming the solid and causing it to store elastic energy E_{el}. The observed dilation and deformation will be determined by the minimum of the effective energy

$$E_{tot} = E_{el} - P_{in}V, \tag{3.1}$$

where V is the dilated channel's volume. If the deformed solid has undergone a displacement field $\mathbf{u}$, its local shape change is described by the deformation gradient tensor $F = I + \nabla\mathbf{u}$, and its elastic energy density is of the form $W(F)$. We model the solid as an incompressible ($\mathrm{Det}\,(F) = 1$) neo-Hookean material with shear modulus μ. The elastic energy is calculated from (1.24),

$$E_{el} = \int W(F)\mathrm{d}V = \int\int\int_{r=a}^{b} \left[\frac{1}{2}\mu\left(\mathrm{Tr}\left(F\cdot F^{T}\right) - 3\right) - P(\mathrm{Det}(F) - 1)\right] r\mathrm{d}r\mathrm{d}\theta\mathrm{d}z, \tag{3.2}$$

where P is a Lagrange multiplier pressure field enforcing incompressibility. This model is exact for Gaussian polymer networks, and valid until deformations of several hundred percent in lightly cross-linked gels/elastomers [24] including the polyacrylamide gels used in our experiments [133]. It is also the simplest large-deformation elastic model, and correspondingly offers the clearest exposition of geometrically motivated instabilities.

Minimizing the total energy (3.1) with respect to variations in $\mathbf{u}$ and P gives the expected equations of mechanical equilibrium, and the constraint of incompressibility,

$$\begin{aligned} \nabla\cdot\sigma &= 0 \\ \implies \mu\nabla^2\mathbf{u} - \mathrm{Det}\,(F)\,F^{-T}\cdot\nabla P &= 0 \qquad (3.3)\\ \mathrm{Det}(F) &= 1, \qquad (3.4) \end{aligned}$$

where

$$\sigma = \frac{\partial W}{\partial F} = \left(\mu F - PF^{-T}\right), \tag{3.5}$$

is the PK1 large deformation stress. These bulk equations are accompanied by the natural inner and outer boundary conditions:

$$(\sigma + P_f F^{-T}) \cdot \hat{\mathbf{r}}\big|_{r=a,b} = 0, \tag{3.6}$$

where the boundary fluid pressure $P_f = P_{in}, 0$ at $r = a, b$ respectively.

3.3.1 Base state solution

We restrict attention to axisymmetric displacements $\mathbf{u} = (u_r, 0, u_z)$. We first recall the forms of the gradient operators in the above equations, using commas to denote partial derivatives (see Appendix A for vector and matrix identities):

$$\nabla P = \begin{pmatrix} P_{,r} \\ 0 \\ P_{,z} \end{pmatrix} \tag{3.7}$$

$$\nabla \mathbf{u} = \begin{pmatrix} u_{r,r} & 0 & u_{r,z} \\ 0 & \frac{u_r}{r} & 0 \\ u_{z,r} & 0 & u_{z,z} \end{pmatrix} \tag{3.8}$$

$$\nabla^2 \mathbf{u} = \begin{pmatrix} u_{r,rr} + \frac{u_{r,r}}{r} - \frac{u_r}{r^2} + u_{r,zz} \\ 0 \\ u_{z,rr} + \frac{u_{z,r}}{r} + u_{z,zz} \end{pmatrix}. \tag{3.9}$$

Before considering the peristaltic instability we first consider the system with a uniform dilation:

$$\mathbf{u} = u_0(r)\hat{\mathbf{r}} \qquad P = \mu P_0(r). \tag{3.10}$$

The terms become

$$\nabla P = \mu \begin{pmatrix} P_0'(r) \\ 0 \\ 0 \end{pmatrix} \tag{3.11}$$

$$\nabla^2 \mathbf{u} = \begin{pmatrix} u_0''(r) + \frac{u_0'(r)}{r} - \frac{u_0(r)}{r^2} \\ 0 \\ 0 \end{pmatrix} \tag{3.12}$$

and the deformation gradient F and $\mathrm{Det}\,(F)\,F^{-T}$ are then

$$F = \begin{pmatrix} 1+u_0'(r) & 0 & 0 \\ 0 & 1+\frac{u_0(r)}{r} & 0 \\ 0 & 0 & 1 \end{pmatrix} \tag{3.13}$$

$$\mathrm{Det}\,(F)\,F^{-T} = \begin{pmatrix} 1+\frac{u_0(r)}{r} & 0 & 0 \\ 0 & 1+u_0'(r) & 0 \\ 0 & 0 & 1+u_0'(r)+\frac{u_0(r)}{r}(1+u_0'(r)) \end{pmatrix}. \tag{3.14}$$

Using these expressions, (3.3) and (3.4) become

$$r^2 u_0''(r) + r u_0'(r) - u_0(r) - r\,(r+u_0(r))\,P_0'(r) = 0, \tag{3.15}$$

$$u_0(r) + (r+u_0(r))\,u_0'(r) = 0. \tag{3.16}$$

The incompressibility condition (3.16) is solved by

$$u_0(r) = \sqrt{r^2+c^2} - r \equiv R - r, \tag{3.17}$$

where the constant of integration, c, parameterizes the degree of cavity dilation, with the inner radius rising by a factor of

$$\lambda = \sqrt{1+c^2/a^2}, \tag{3.18}$$

and the mechanical equilibrium condition (3.15) then gives the form of the pressure field

$$P_0(r) = \frac{1}{2}\left[\frac{r^2}{r^2+c^2} - \ln\left(\frac{r^2}{r^2+c^2}\right)\right] + q. \tag{3.19}$$

The constants c and q are determined by the boundary conditions (3.6) at $r=a$ and $r=b$,

$$\left(\frac{P_{in}}{\mu} - P_0(a)\right)(a+u_0(a)) + a(1+u_0'(a)) = 0, \tag{3.20}$$

$$-P_0(b)(b+u_0(b)) + b(1+u_0'(b)) = 0. \tag{3.21}$$

By substituting (3.19) into (3.20) and (3.21), we obtain expression for q and P_{in} as a function of c

$$q = \frac{1}{2}\left[\frac{b^2}{b^2+c^2} + \ln\left(\frac{b^2}{b^2+c^2}\right)\right], \tag{3.22}$$

$$\begin{aligned} P_{in} &= \frac{\mu}{2}\left[\ln\left(\frac{b^2}{b^2+c^2}\right) - \ln\left(\frac{a^2}{a^2+c^2}\right) + \frac{b^2}{b^2+c^2} - \frac{a^2}{a^2+c^2}\right] \\ &= \frac{\mu}{2}\left[-\ln\left(1+(a/b)^2(\lambda^2-1)\right) + \ln\left(\lambda^2\right) + \frac{1}{1+(a/b)^2(\lambda^2-1)} + \frac{1}{\lambda^2}\right] \\ &= \frac{\mu}{2}\left[g(1+(a/b)^2(\lambda^2-1)) - g(\lambda^2)\right], \end{aligned} \tag{3.23}$$

where the function $g(x) \equiv (1/x) - \ln(x)$. This predicted dilation is plotted for a range of values of a/b in Fig. 3.7. Dilation rises monotonically with P_{in}, and diverges at $P_{in} = \mu \log(b/a)$. If $b = a + t \approx a$, (a thin-walled pipe) this critical pressure reduces to $P_{in} \approx \mu t/a$, the signature scaling of elastic instabilities in membrane tubes [22, 99–102, 125–130]. Conversely, in the $b \to \infty$ (bulk solid) limit, (3.23) becomes

$$P_{in} = \frac{\mu}{2}\left[1 + \ln(\lambda^2) - \lambda^{-2}\right], \tag{3.24}$$

showing that the channel dilates, but only diverges at infinite pressure. In contrast, the result for a spherical cavity, $P_{in} = \frac{\mu}{2}\left[5 - 4\lambda^{-1} - \lambda^{-4}\right]$, diverges at $P_{in} = \frac{5}{2}\mu$, a celebrated result known as solid cavitation (see Section 1.3.7).

3.3.2 Linear stability analysis

To understand this peristaltic transition, we examine the stability of uniform dilation to small perturbations, $\mathbf{u} = u_0(r)\hat{\mathbf{r}} + \delta\mathbf{u}$ and $P = \mu P_0(r) + \delta P$. They induce the first order change in the deformation gradient $\delta F = \nabla\delta\mathbf{u}$ and the PK1 stress

$$\begin{aligned} \delta\sigma &= \mu\delta F - \delta\left(P\mathrm{Det}\,(F)\,F^{-T}\right) \\ &= \mu\delta F - \delta P F_0^{-T} - \mu P_0 \delta\left(\mathrm{Det}\,(F)\,F^{-T}\right), \end{aligned} \tag{3.25}$$

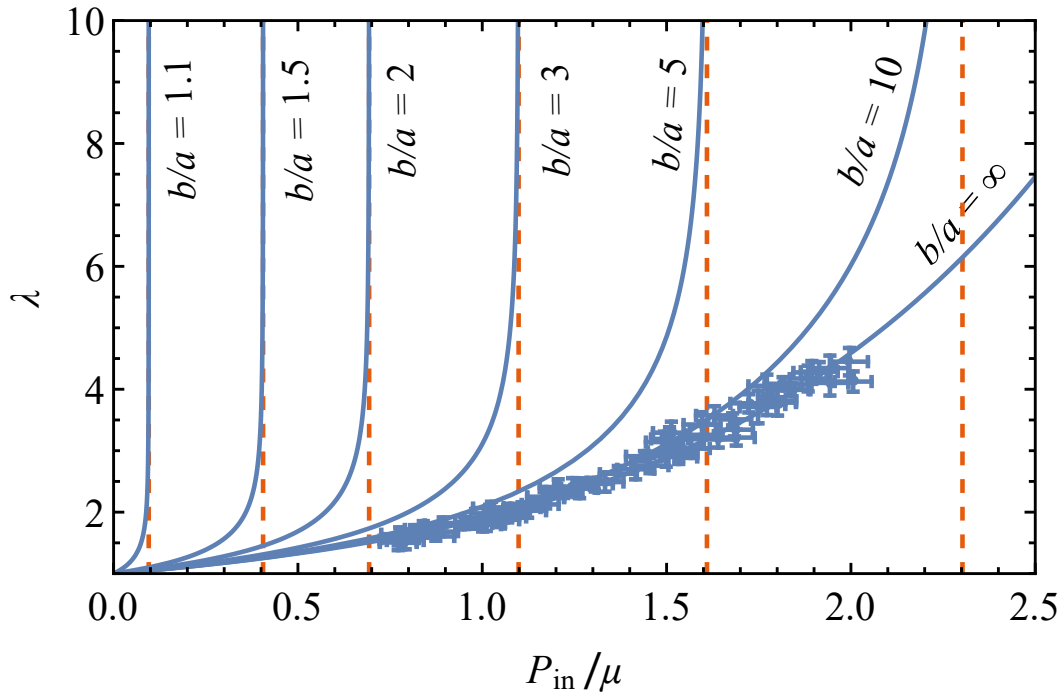

Fig. 3.7 Dilation factor, λ, of a cylindrical channel as a function of its interior driving pressure P_{in}, for a range of aspect ratios b/a. The predicted dilation diverges at $P_{in} = \mu \log(b/a)$, a thick-walled balloon instability, but a channel through a bulk solid ($b \to \infty$) never diverges. Experimental points are individual constant-pressure measurements from three channels through polyacrymide slabs, reproducing the bulk neo-Hookean theoretical dilation. Experimental data from [116].

where F_0 is the unperturbed deformation gradient. We also use the fact that $\mathrm{Det}(F_0) = 1$ to simplify the expression. Equations (3.3) and (3.4) need to be satisfied by the perturbation:

$$\begin{aligned} \nabla \cdot \delta\sigma &= 0 \\ \implies \mu\nabla^2\delta\mathbf{u} - F_0^{-T}\cdot\nabla\delta P - \mu\delta\left(\mathrm{Det}(F)F^{-T}\right)\cdot\nabla P_0 &= 0, \qquad (3.26) \\ \delta\mathrm{Det}(F) &= 0 \\ \implies \mathrm{Tr}\left(F_0^{-1}\delta F\right) &= 0, \qquad (3.27) \end{aligned}$$

with the perturbed boundary conditions

$$\left[\delta\sigma - P_f\delta\left(\mathrm{Det}(F)F^{-T}\right)\right]\cdot\hat{\mathbf{r}}\big|_{r=a,b} = 0. \qquad (3.28)$$

Using a sinusoidal perturbation as an ansatz:

$$\delta\mathbf{u} = f_r(r)\cos(kz)\hat{\mathbf{r}} + f_z(r)\sin(kz)\hat{\mathbf{z}}, \qquad (3.29)$$

$$\delta P = \mu P_1(r)\cos(kz). \qquad (3.30)$$

We then have

$$\nabla\delta P = \mu\begin{pmatrix} P_1'(r)\cos(kz) \\ 0 \\ -kP_1(r)\sin(kz) \end{pmatrix} \qquad (3.31)$$

$$\nabla^2\delta\mathbf{u} = \begin{pmatrix} \left(f_r''(r) - k^2 f_r(r) + \frac{f_r'(r)}{r} - \frac{f_r(r)}{r^2}\right)\cos(kz) \\ 0 \\ \left(f_z''(r) - k^2 f_z(r) + \frac{f_z'(r)}{r}\right)\sin(kz) \end{pmatrix} \qquad (3.32)$$

$$\delta F = \begin{pmatrix} f_r'(r)\cos(kz) & 0 & -kf_r(r)\sin(kz) \\ 0 & \frac{f_r(r)}{r}\cos(kz) & 0 \\ f_z'(r)\sin(kz) & 0 & kf_z(r)\cos(kz) \end{pmatrix} \qquad (3.33)$$

$$\delta\left(\mathrm{Det}(F)F^{-T}\right) = \begin{pmatrix} \frac{f_r(r)+kRf_z(r)}{r}\cos(kz) & 0 & -\frac{Rf_z'(r)}{r}\sin kz \\ 0 & (f_r'(r) + \frac{krf_z(r)}{R})\cos(kz) & 0 \\ \frac{kRf_r(r)}{r}\sin(kz) & 0 & (\frac{f_r(r)}{R} + \frac{Rf_r'(r)}{r})\cos kz \end{pmatrix}. \qquad (3.34)$$

Only the terms at first order in the perturbation are included. The equations of mechanical equilibrium (3.26), after some simplifications, are then

$$rR^4\left(rf_r''(r)+f_r'(r)-RP_1'(r)\right)+r^2f_r(r)\left(r^2-R^2\left(k^2R^2+2\right)\right)+kRf_z(r)\left(r^2-R^2\right)^2=0, \tag{3.35}$$

$$kf_r(r)\left(r^2-R^2\right)^2+rR^3\left(rf_z''(r)+f_z'(r)-k^2rf_z(r)+krP_1(r)\right)=0, \tag{3.36}$$

and the incompressibility condition (3.27) becomes

$$R\left(Rf_r'(r)+krf_z(r)\right)+rf_r(r)=0. \tag{3.37}$$

Solving (3.36) and (3.37) and provide expressions for f_z and P_1:

$$f_z(r)=-\frac{rf_r(r)+R^2f_r'(r)}{krR}, \tag{3.38}$$

$$P_1(r)=\frac{rR^3(k^2rf_z(r)-f_z'(r)-rf_z''(r))-k(R^2-r^2)^2f_r(r)}{kr^2R^3}. \tag{3.39}$$

Substituting these expressions into (3.35), we obtain a fourth order differential equation for f_r:

$$R^2\Bigg[f_r'(r)\left(-2k^2r^4-r^2\left(1-k^2R^2\right)-3R^2\right)+r\Big[f_r''(r)\left(-k^2r^4+r^2\left(1-k^2R^2\right)+3R^2\right)$$
$$+r\left(rR^2f_r^{(4)}(r)+f_r^{(3)}(r)\left(r^2-2R^2\right)\right)\Big]\Bigg]+k^2rf_r(r)\left(r^4\left(k^2R^2-2\right)+r^2R^2+2R^4\right)=0. \tag{3.40}$$

The boundary conditions (3.28) at $r=a$ and $r=b$ are

$$R(a)f_z'(a)-kaf_r(a)=0 \tag{3.41}$$

$$aR(a)^2f_r'(a)-a^2f_r(a)-ka^2R(a)f_z(a)-R(a)^3P_1(a)=0 \tag{3.42}$$

$$R(b)f_z'(b)-kbf_r(b)=0 \tag{3.43}$$

$$bR(b)^2f_r'(b)-b^2f_r(b)-kb^2R(b)f_z(b)-R(b)^3P_1(b)=0, \tag{3.44}$$

where $R(x)=\sqrt{x^2+c^2}$. The forth order differential equation and boundary conditions (3.40–3.44) is a generalized eigensystem for the critical dilation, λ, required for the instability.

Previous authors have solved this system for modestly thick tubes [128] ($b-a \sim a$) which, like their thin-walled counterparts, first become unstable via long-wavelength modes. Such modes vanish beyond a critical wall thickness, leading these authors to conclude that sufficiently thick pipes are stable. However, inspired by our experimental observations, we use MATLAB's [134] `bvp4c` command to solve the eigensystem. The `bvp4c` command solves the boundary value problem for ordinary differential equations by using a finite difference method. We routinely search, numerically, for finite wavelength solutions ($k \sim 1/a$) in a tube which is sufficiently thick ($b = 1000a$) to approximate a bulk solid. We then iterate over k to find the first unstable mode with lowest threshold λ, from which the threshold cavity pressure can be calculated via (3.23). This would be the critical value of P_{in} for the instability and the critical wavenumber.

3.4 Results

In Figs 3.8–3.9, the results for a channel through a bulk ($b = 1000a$) solid are summarized. We plot the form of this solution in Fig. 3.8, showing the displacement fields take maximum values near the cavity, and only penetrate a distance $\sim 10a$ into the bulk, confirming the outer boundary is effectively at infinity. The variation of threshold pressure with wavelength is plotted in Fig. 3.9. Although the resulting threshold curve is very flat, it does have a minimum (indicated with a star) corresponding to the first unstable mode. This first unstable mode occurs at $\lambda = 4.824$ (requiring $P_{in} = 2.052\mu$) and with a wavelength $2\pi/k = 12.278a$.

The theoretical predictions are also compared with the axisymetric finite element calculations (Section 3.2) with ($b/a \geq 60$) and threshold measurements obtained in "unloading" experiments, in which a channel is pressurized well beyond the point of instability then quasi-statically depressurized until peristalsis vanishes. In particular, we show in Fig. 3.10 that both numerical and experimental cavities indeed become unstable at $P_{in} = 2.05\mu$ over a range of gel moduli. In the finite element analysis, long cavities select the expected $2\pi/k = 12.278a$ wavelength (Fig. 3.11), but we can artificially fix the wavelength via periodic boundary conditions. In Fig. 3.9, we confirm that these alternative wavelengths become unstable at the corresponding (higher) predicted pressures. In experiments, we cannot prescribe a wavelength, but we find the instability naturally occurs with a broad range of wavelengths (a signature of the very flat theoretical wavelength-threshold curve) and, in each case, peristalsis vanishes close to the predicted threshold pressure for that wavelength. The experimental instability is often observed at pressures slightly below the theoretical value, which we attribute to the finite slab thickness.

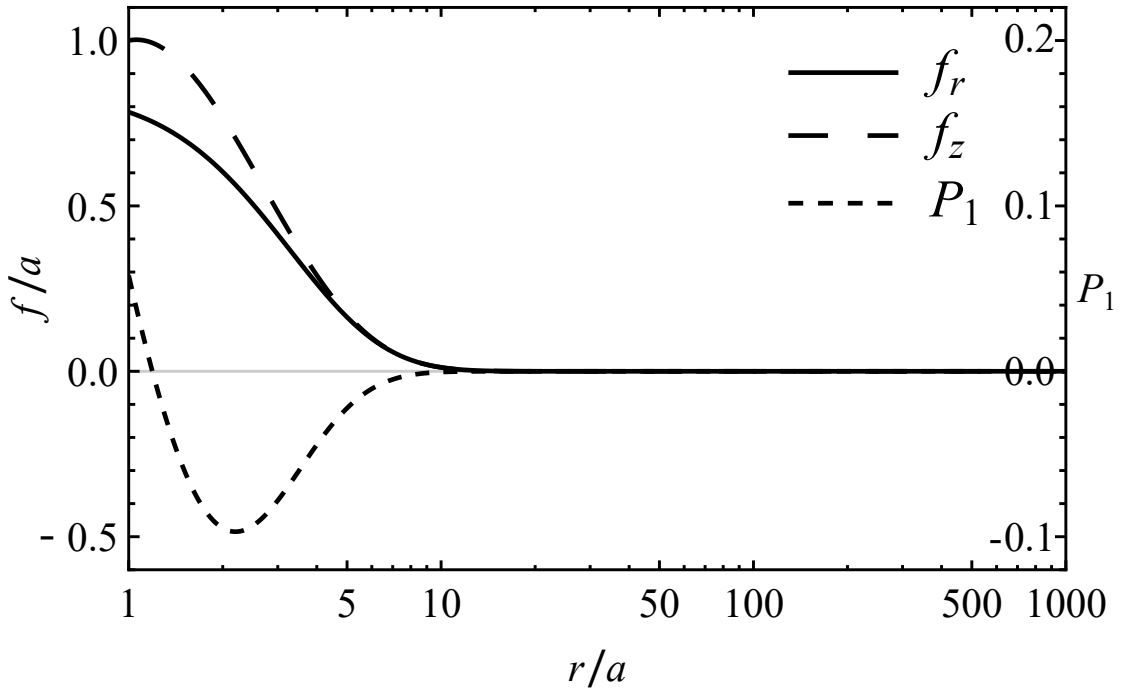

Fig. 3.8 Form of the peristaltic fields f_x, f_z and P_1 for the first unstable wavelength, $2\pi/k = 12.278a$ resulting from the stability analysis.

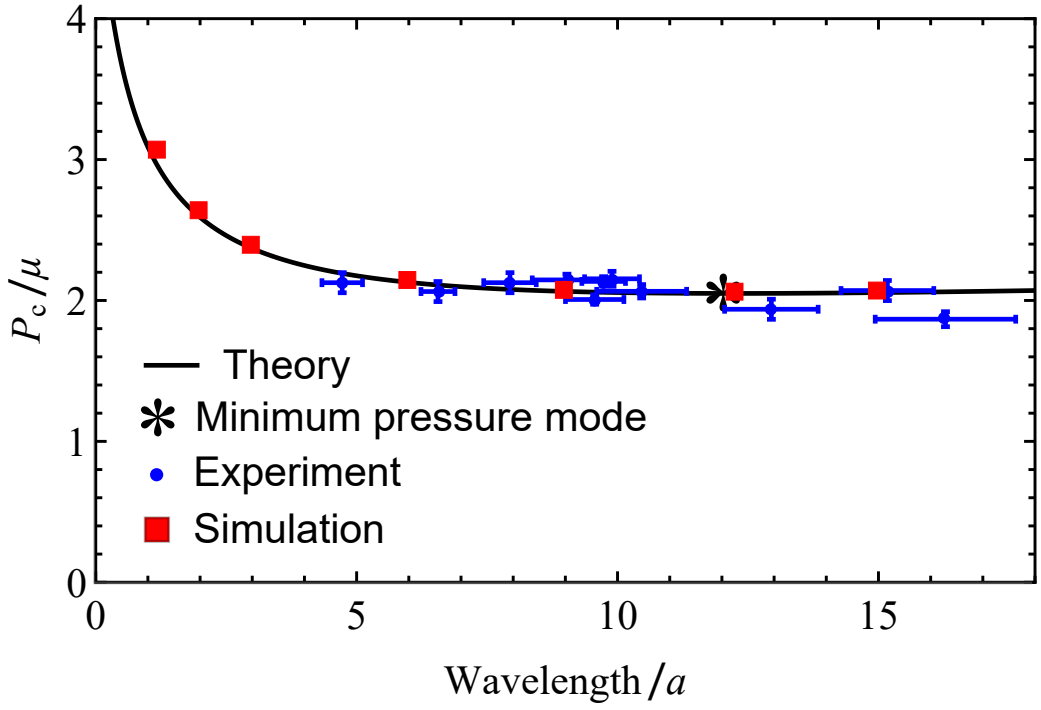

Fig. 3.9 Theoretical, numerical and experimental treatment of the peristaltic instability in a channel though a bulk solid. The plot shows the critical pressure for each wavelength to become unstable. Experimental data from [116].

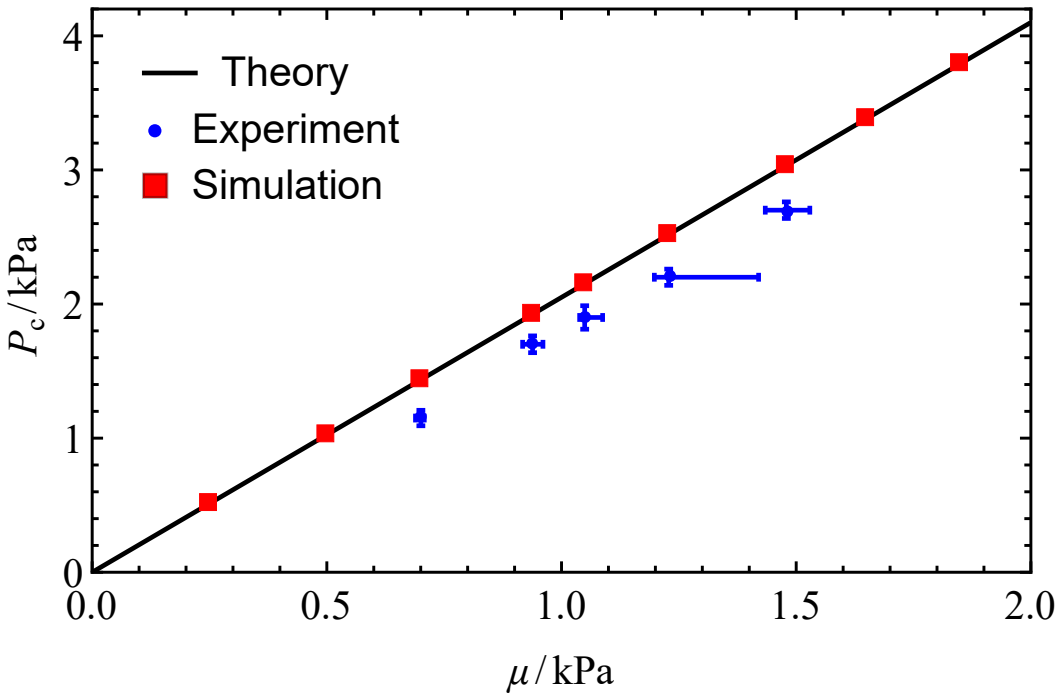

Fig. 3.10 Critical pressure for instability as a function of elastic modulus from theory, numerical simulation and experiments. Experimental data from [116].

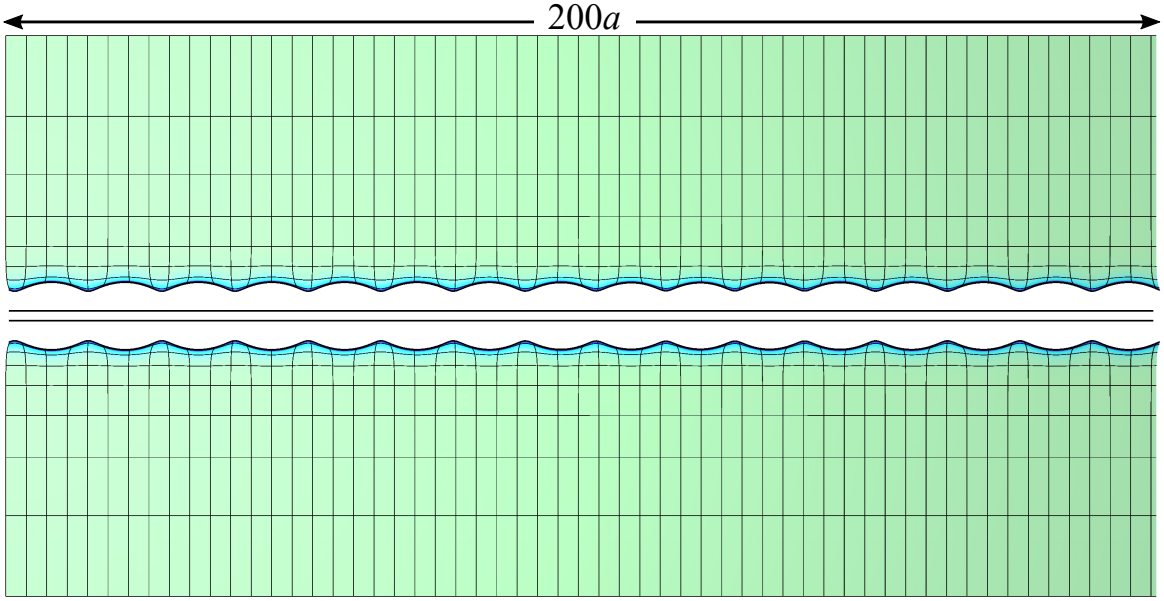

Fig. 3.11 Finite element calculation for a long simulation domain (length of $200a$ as shown) with an internal pressure of $P = 2.1\mu$. The dashed line denotes the undeformed cavity radius. The simulation selects a wavelength of $200a/16 = 12/5a$. Periodicity constrains the simulated wavelength to be of the form $200a/n$, where n is an integer, so this is the possible value closest to $12.278a$, the wavelength predicted linear stability for an infinitely long cavity through a bulk solid.

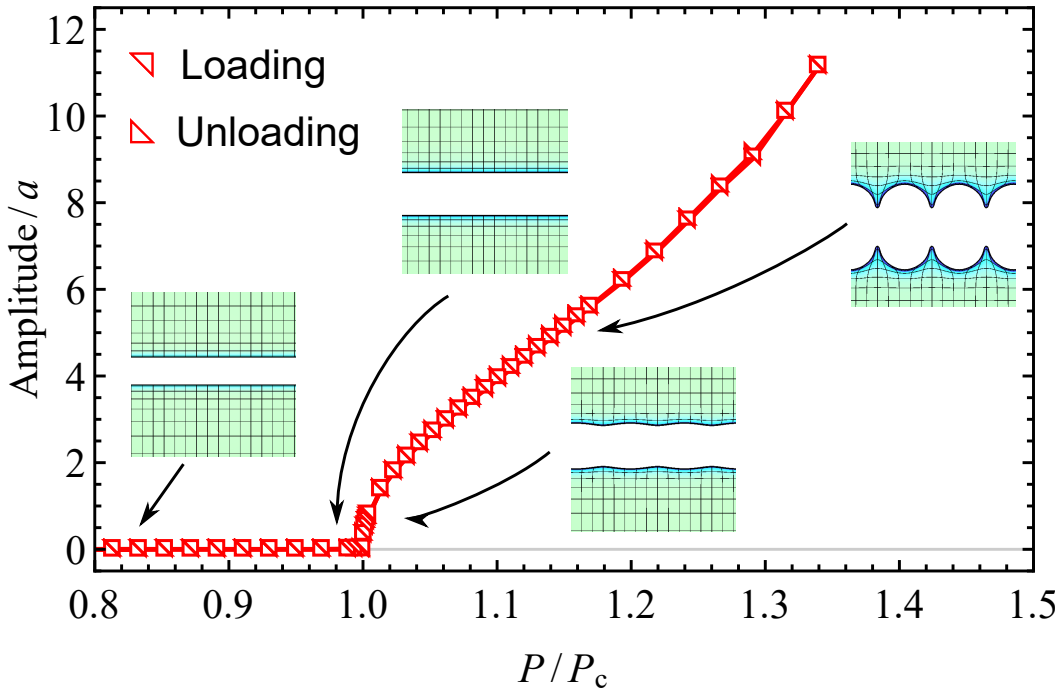

Fig. 3.12 The amplitude of the peristaltic instability as the cavity pressure is increased (loading) and decreased (unloading).

The stability analysis is limited to onset, but our finite element calculations can explore the peristaltic shape far beyond threshold. We conducted a numerical loading and unloading cycle in a bulk solid (Fig. 3.12). The plot demonstrates that the amplitude increases from zero as P exceeds P_c for both loading and unloading curve without hysteresis, indicating the instability to be supercritical (continuous). Repeating this exercise with different wavelengths reveals that the energy-minimizing wavelength lengthens slightly (Fig. 3.13) beyond threshold. The optimal wavelength starts from that predicted by linear stability at threshold, and lengthens modestly and smoothly beyond threshold. The plot calculated by comparing the energy for multiple finite-element hysteresis-loops with different but individually fixed wavelengths.

3.5 Discussion

Overall, our analysis leads to a simple conclusion: the driver for peristalsis is that, for a given inflated channel volume, the peristaltic form requires less overall deformation and lower the elastic energy. An instructive comparison is to the surface tension driven instability (see Section 1.3.9), in which peristalsis occurs because it reduces a cylinder's surface area under surface tension for a given volume, and hence reduces its surface energy [60]. Here, peristalsis relieves the base-state stretch and saving elastic energy. The base-state stretch

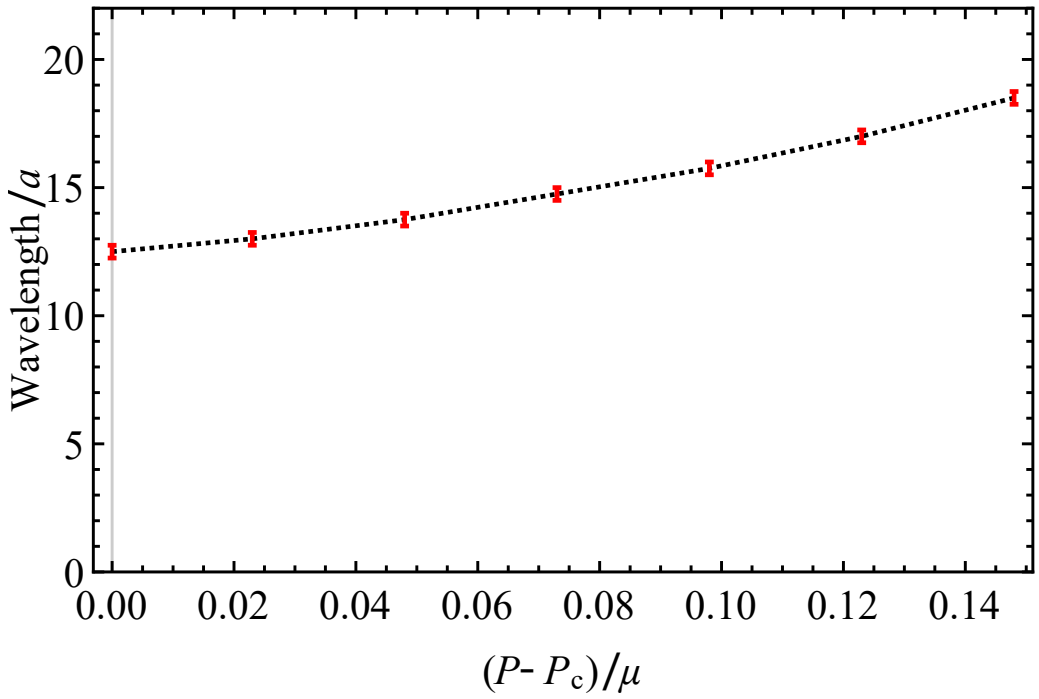

Fig. 3.13 Wavelength corresponding to the minimum effective energy, $E_{el} - PV$, for peristaltic modes past threshold.

(3.17) decays into the bulk over the length scale a, and the energetically optimal peristaltic fields will penetrate this dilated region, where they relieve strain, but not further where they would add strain and cost energy. As is characteristic of oscillating elastic fields, the peristaltic field's penetration distance is set by their wavelength, resulting in an optimal wavelength proportional to a. Since this is a geometric mechanism, we expect peristalsis to be generic in sufficiently deformable elastic channels. In the next paragraphs, we show how robust peristalsis is to changes in geometry and choice of elastic material.

First, the instability at finite b/a is analysed. The stability equations (3.35–3.37) only depend on the cavity pressure via the dilation it produces (λ) and only depend on b in the outer boundary condition (3.44), where the peristaltic solutions are decayed. Therefore, the instability has a universal form in all channels with even modestly large b/a, which all become unstable via the bulk solid solution, although the critical pressure is reduced in accordance with (3.24). The relation between the threshold pressure and wavelength are plotted for several values of b/a in Fig. 3.14, showing how the threshold pressure changes as b/a get larger, along with numerical data to verify the results. In Fig. 3.15, the full form of the threshold dilation, pressure and wavelength as a function of b/a are shown. As anticipated, these only deviate appreciably from the bulk form when $b/a \lesssim 10$, with the wavelength growing and the critical dilation falling in finite systems.

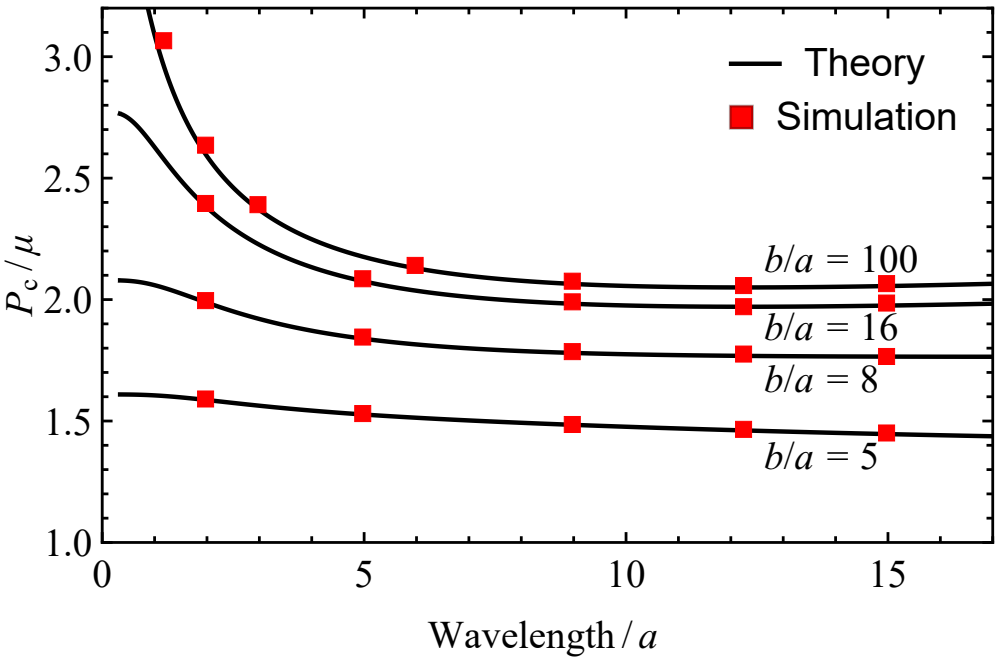

Fig. 3.14 Critical pressure against wavelength for finite aspect ratio b/a.

Secondly, we analyse the peristaltic instability beyond neo-Hookean materials. The Mooney-Rivlin model can capture a more accurate prediction compared to real material as it has more parameters than the neo-Hookean model. This is done by using the Mooney-Rivlin energy density function given by (1.45). Repeating the bulk stability analysis, we find the base state is identical, whilst the stability equations become more complicated, but still admit a numerical solution. Fig. 3.16 shows the critical dilation, pressure and wavelength of the first unstable mode as a function of the Mooney-Rivlin parameter C_2/C_1. The result shows that as the ratio of the parameters C_2/C_1 increases, departing further from the neo-Hookean limit, the threshold dilation, pressure as well as the wavelength increase. For a high C_2/C_1, we expect the instability to become a long-wavelength mode.

In addition, there is the Gent model that is worth considering. Most elastomers and gels are neo-Hookean at modest strains, but have a finite extensibility, owing to their finite length chains. This is represented by the parameter J_m in the energy density (1.40). Using the energy density function (1.40), the linear stability analysis for a bulk solid is repeated. Fig. 3.17 summarizes the linear stability result as a function of J_m. The result shows that finite extensibility (finite J_m) generates only modest changes in the form of peristalsis, but eliminates the instability entirely for $J_m < 35$, corresponding to materials with a limiting uniaxial extension factor of $\lambda \lesssim 6$.

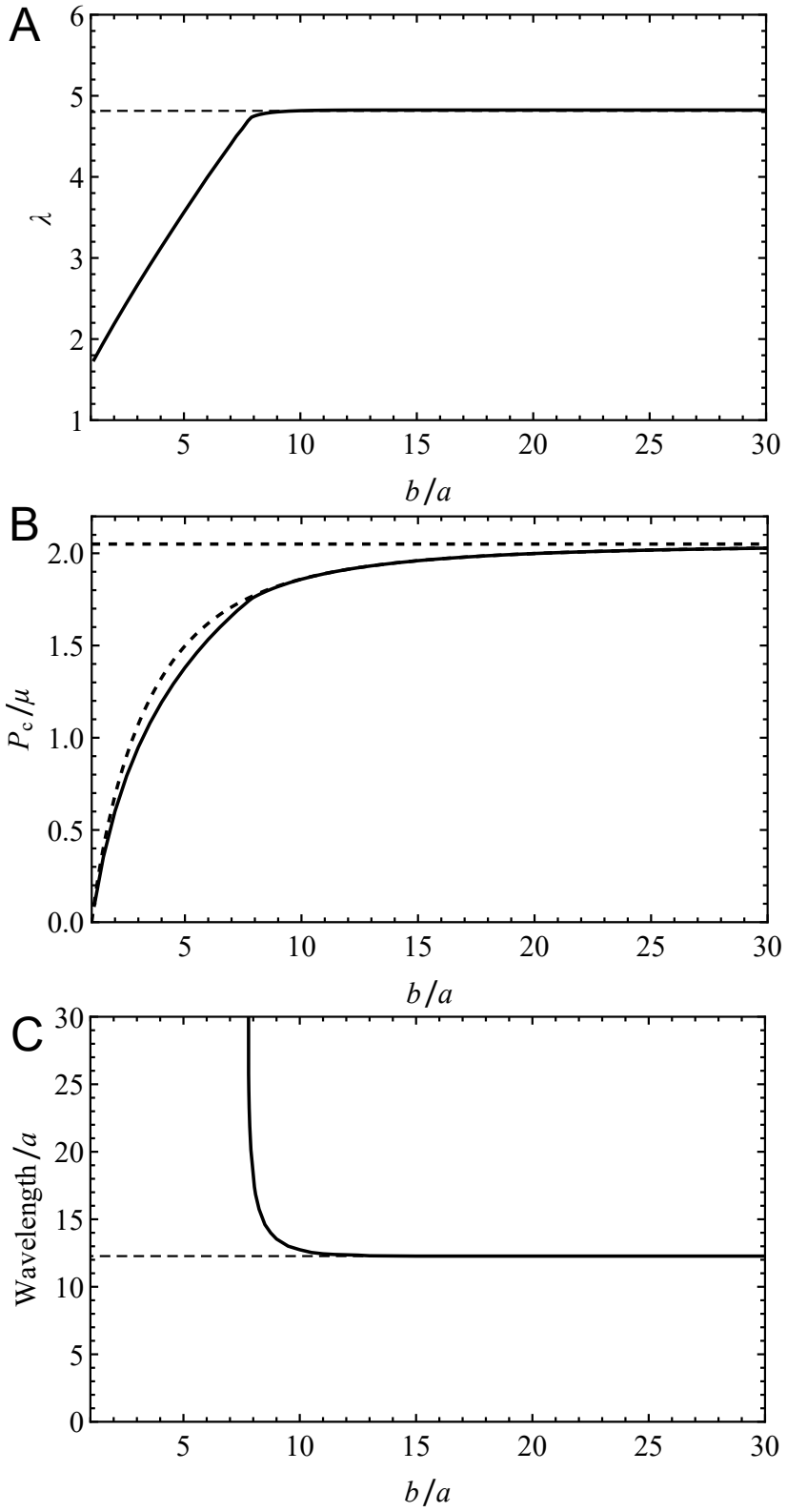

Fig. 3.15 (A) Critical dilation, (B) critical pressure and (C) critical wavelength ($2\pi/k$) against aspect ratio b/a.

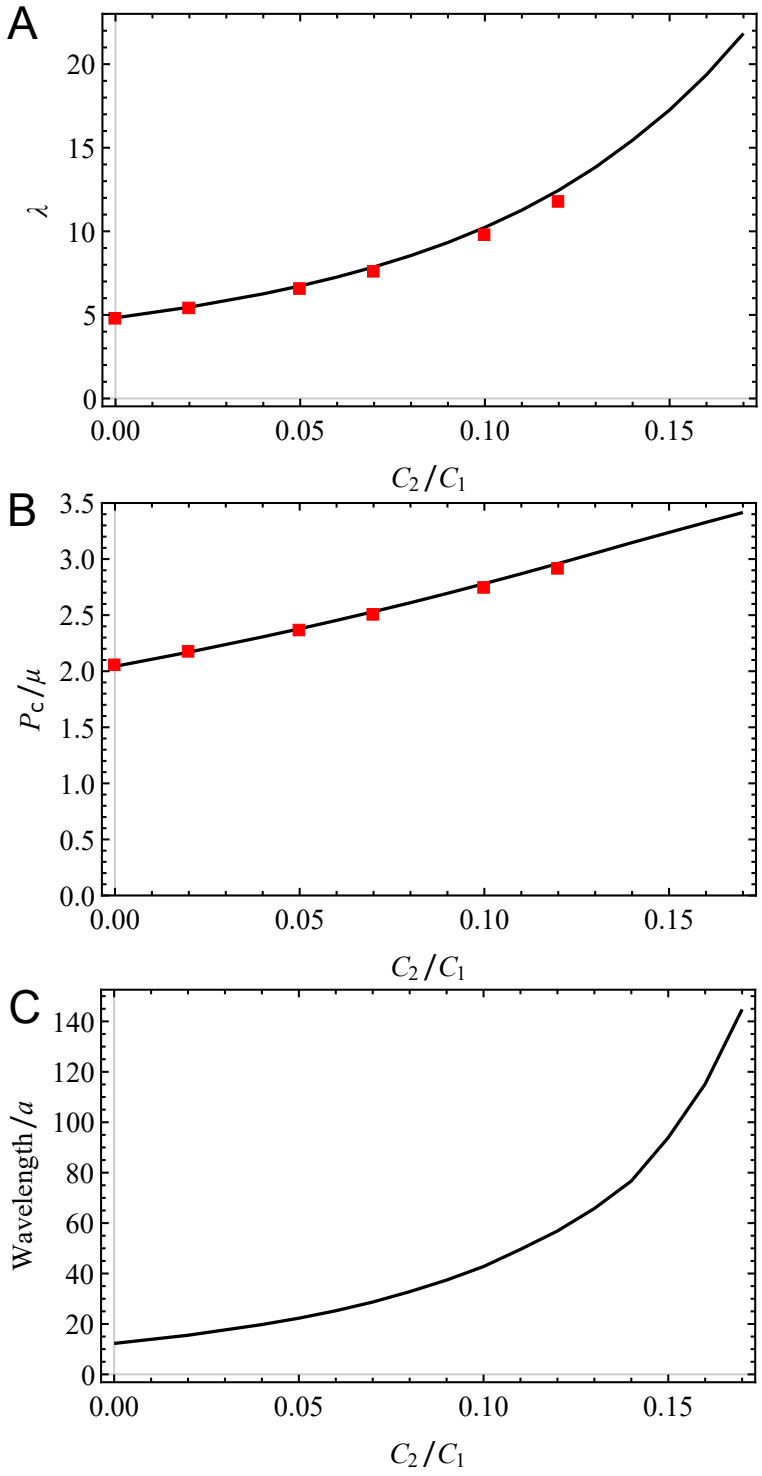

Fig. 3.16 (A) Critical dilation, (B) critical pressure and (C) critical wavelength ($2\pi/k$) against the parameter C_2/C_1 for Mooney-Rivlin solid. Black line is the theoretical prediction. Red squares are from numerical simulation.

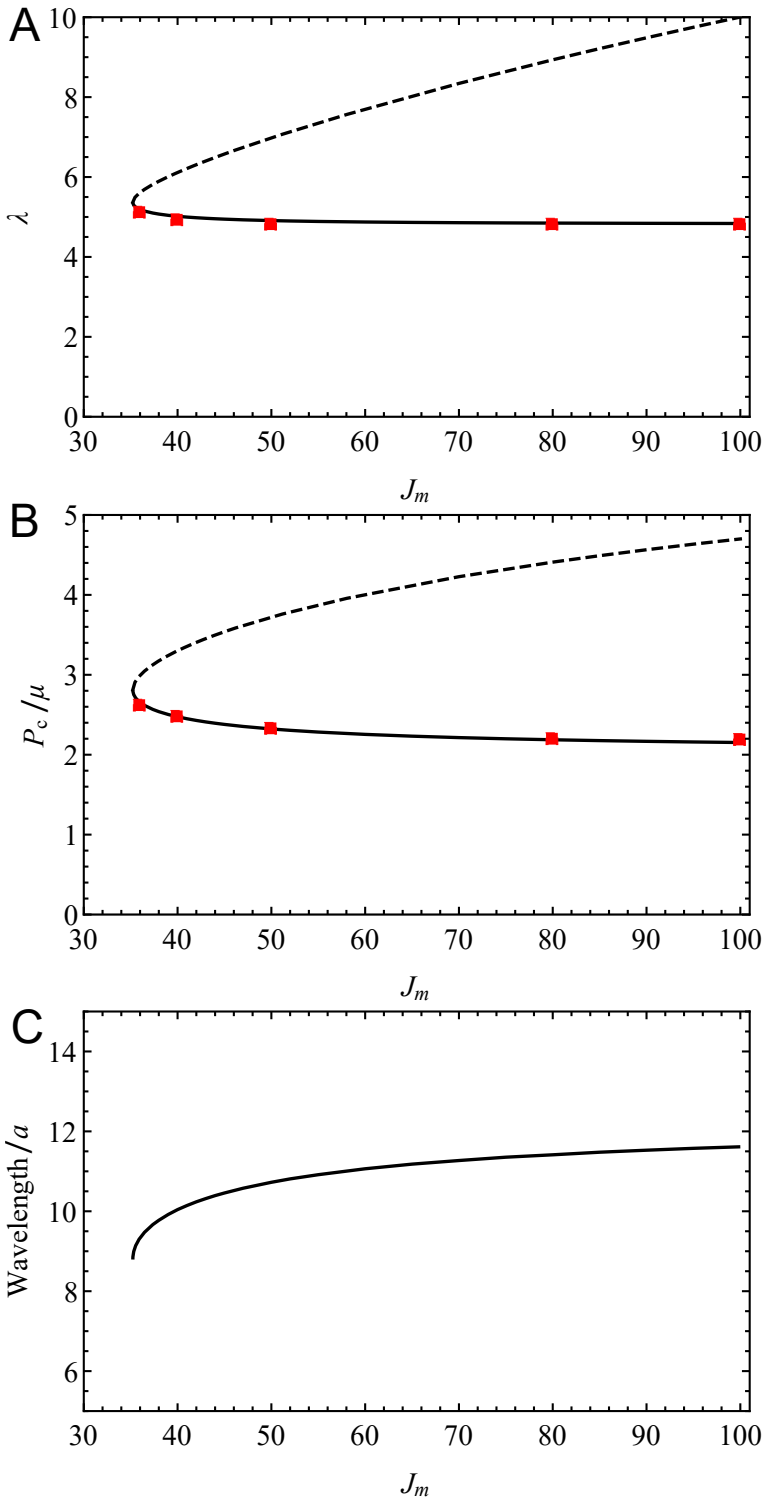

Fig. 3.17 (A) Critical dilation, (B) critical pressure and (C) critical wavelength ($2\pi/k$) against the parameter J_m for Gent solid. Black line is the theoretical prediction. Dashed line denotes the maximum value of dilation and pressure that the solid remains peristalsis. Red squares are from numerical simulation.

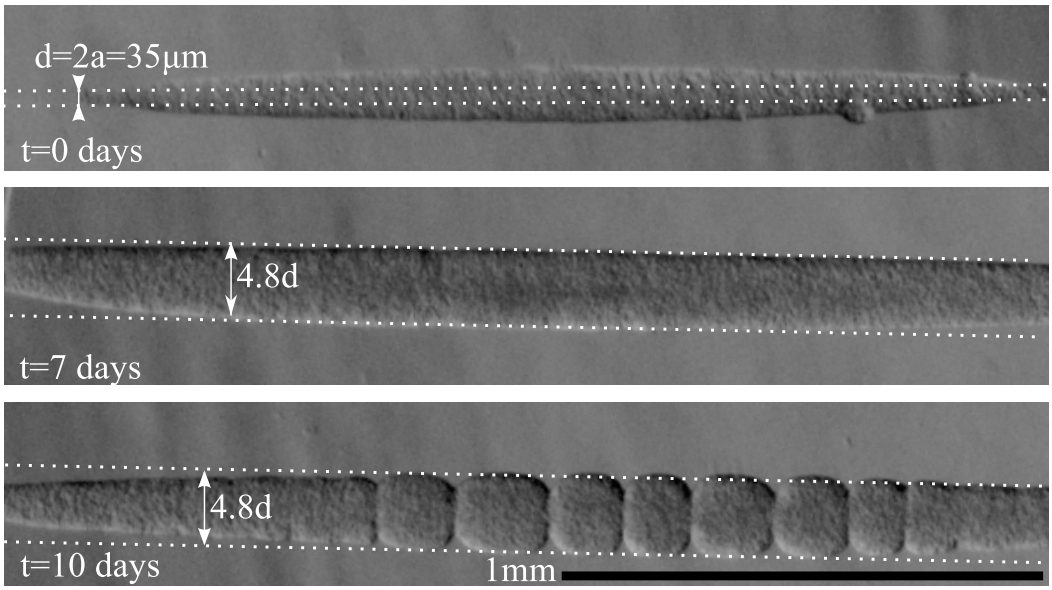

Fig. 3.18 Instability when an embryonic stem cell tissue grows inside a channel. Dashed lines indicate initial channel diameter $d = 2a$ (top), and predicted threshold diameter for instability ($4.8d$, middle, bottom). Taken from [116].

We also speculate that the peristaltic instability will also manifest in biology, sculpting channels during both pathological and developmental processes. Indeed, Leonavicius and Srinivas [116] first observed peristalsis in hydrogel channels containing growing mouse embryonic stem cell tissues (Fig. 3.18). More precisely, they injected a dense suspension of murine embryonic stem cells into a 35 μm diameter ($a = 17.5\mu$m) channel, which rapidly adhered into a monolithic tissue. This tissue grew for ten days within the channel, nourished by cell culture media. Such embryonic stem cell tissue is a soft incompressible solid with a finite yield stress, and dilates the channel as it grows. The tissue solidity arises because the cells are both individually elastic (with moduli $\sim$ 100 Pa [135]) owing to their cytoskeleton, and adhere to each other by expression of e-cadherin [136]. They found that disrupting either aspect (using Cytochalasin D [137] or EDTA [138] respectively) lead to a tissue which could no longer deform the hydrogel. With the undisrupted culture, peristalsis appeared on day seven, when the central channel dilation achieved the expected threshold of $\lambda \approx 4.8$. As in pressure-controlled experiments, peristalsis had uneven wavelengths, varying between $7a$ and $12a$, reflecting the instability's flat critical pressure versus wavelength curve (Fig. 3.9).

3.6 Conclusion and further work

In summary, we have shown that a cylindrical channel through a soft solid will spontaneously adopt a peristaltically undulating shape when bearing a pressure comparable to the solid's shear modulus. The instability takes a simple form in channels through bulk neo-Hookean solids, occurring at a critical pressure (2.052μ) proportional to the channel shear modulus, and with a wavelength that is proportional to the cavity radius. Assuming a finite threshold and wavelength, these scalings are an inevitable consequence of the scale invariance of elasticity, which means channel radius is the only length scale in the problem, and the elastic modulus is the only stress scale. Solid cavitation of bulk spherical cavities follows the same scale-free stress scaling ($P_c = 2.5\mu$), but we note bulk peristalsis of cylindrical cavities requires less pressure.

Peristalsis is also expected in finite solids, provided $b/a \gtrsim 7$, and strain-stiffening materials provided they are sufficiently deformable. In some less-deformable elastic media, the strain concentrations associated with peristalsis will precipitate fracture and failure, suggesting peristalsis places a fundamental limit on the pressure a channel can bear, just as Euler buckling limits loading of columns. Conversely, in sufficiently deformable solids, peristalsis offers a route to reversibly introduce periodicity into a channel, potentially allowing a highly reflective photonic (electromagnetic) or phononic (acoustic) stopband [139, 140] to be switched within a deformable waveguide.

In biology, one commonly encounters thin-walled tubes through soft tissues. Such tubes can be included in the current framework by adding a thin tube of different elastic material, with modulus $\mu_{\text{tube}} = \eta\mu$, at the inner radius of the channel. Under inflation this system must span from conventional long-wavelength tube instabilities at high η, to finite wavelength peristalsis at low η, and mapping this transition is likely to be a rich and biologically relevant subject for future investigations.

Chapter 4

Pattern formation in soft layer buckling instability

In this chapter, I address the question of how we can predict the patterns that arise from elastic instabilities. To do this, I turn to a well-known elastic instability that forms pattern on the surface: the wrinkling of elastic layer on a compliant substrate. First, I will give an overview of this instability. If a thin elastic layer is adhered to a substrate and then caused to enter compression, it will buckle into a pattern of relief [66]. Such layer/substrate buckling is a rich pattern-forming system, with many different topographies emerging depending on the layer/substrate stiffness ratio, the layer/substrate thickness ratio, the degree of compressibility, and the degree and anisotropy of compression. This richness has been exploited by evolution, which uses layer/substrate buckling to sculpt organs during development [39–46], including the folds on the surface of the mammalian brain [3–10], and the loops and villi of the gut [33–35]. Layer/substrate buckling also offers an attractive mechanism for scientists and engineers to generate and switch topography, providing a route to robust shape generation [141, 142] and allowing the creation of surfaces with switchable adhesion [143, 144], wettability [145–147], photonics [148–150] and encapsulation [151, 152].

On a theoretical level, there has been much work on characterizing the thresholds and wavelengths for these buckling instabilities [66, 68, 153–159], but less is understood about the emergent patterns. In this chapter, we use higher order perturbation theory to tackle the problem of pattern selection in an important subset of such buckling instabilities, which occur when the elastic layer enters compression due to isotropic (equibiaxial) growth, swelling or expansion relative to the substrate. Our main conclusion is that, close to threshold, such layers buckle subcritically into patterns of hexagonal dents. Although our calculations are for specific layer/substrate properties (neo-Hookean materials, infinite substrate), we argue

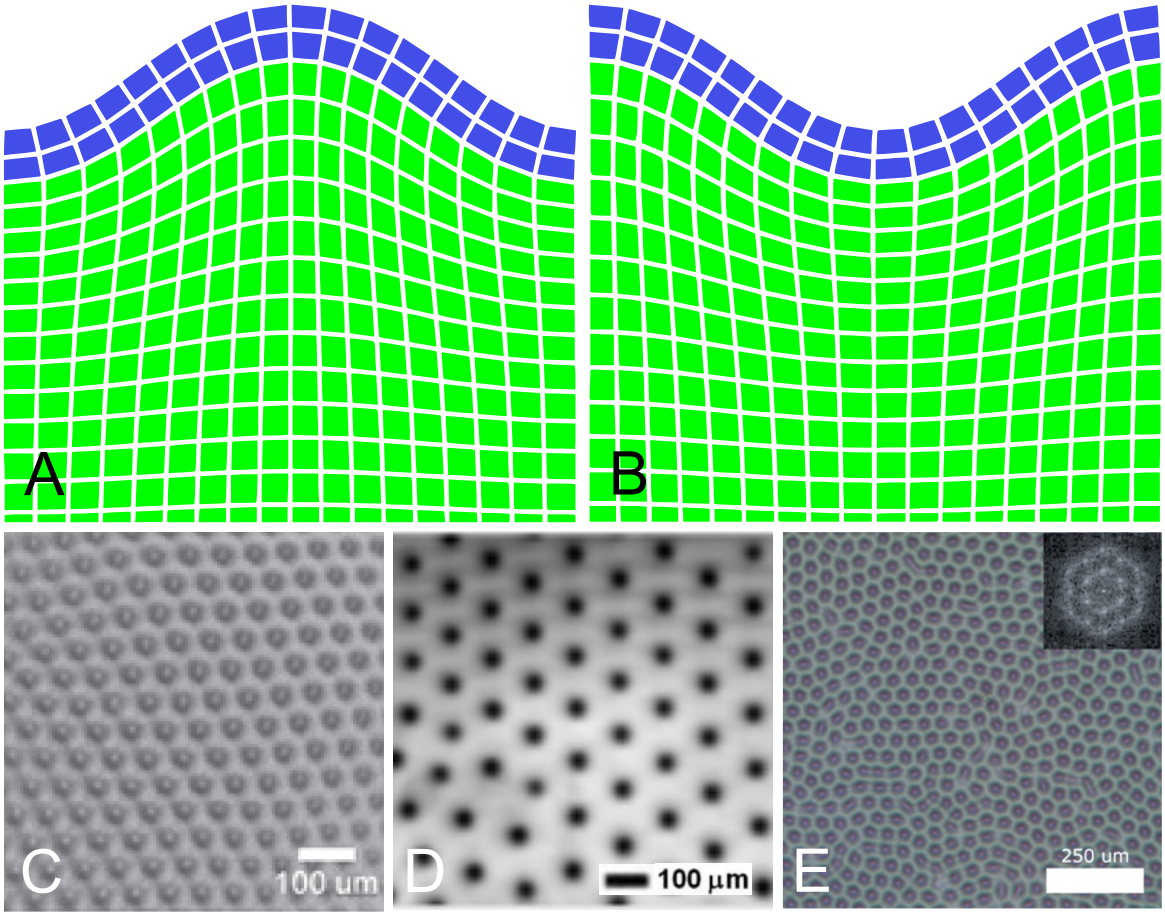

Fig. 4.1 Schematic diagrams showing deformation of (A) a bump and (B) a dent. (C–E) Hexagonal dents formed by wrinkling of a stiff layer on a soft substrate. The thin stiff layer is formed by oxidizing the hydrogel substrate. The solvent vapor is then introduced to swell the oxidized layer. Taken from [53, 54, 160].

that hexagonal patterns are a consequence of the symmetry of the system, and hence will be generic in all transversely isotropic elastic surface instabilities.

Our layer/substrate system spans three distinct regimes. The best studied is a stiff layer on a soft substrate, such as a metal layer on an elastomer substrate. If such a system is heated, the metal will expand relative to the substrate, enter compression, and then buckle into a pattern of relief. This process is a form of Euler buckling, but with a finite wavelength emerging from a trade-off between the bending stiffness of the layer and the substrate elasticity [66, 161]. Experimentally, such systems produce herringbone patterns far beyond threshold [53, 162], which have been modelled theoretically using an elastic (Foppl-von Karman) plate adhered to a linear elastic substrate [160, 162–164]. However, close to threshold, such models predict square/checkerboard buckling patterns [160, 165], whereas patterns of hexagonal dents are

observed experimentally and numerically (Figs 4.1C–E) [53, 54, 78, 160, 166]. Here, we argue that the plate/linear-substrate model fails because it possesses an unphysical inversion symmetry. A normal displacement of the plate $u_z(x,y)$ encoding a bump (Fig. 4.1A) is physically different from $-u_z(x,y)$ encoding a dent (Fig. 4.1B), and this difference must underpin the experimental formation of hexagonal dents rather than bumps. In contrast, the plate/linear-substrate energy is invariant under such topography inversion as the plate itself is up/down symmetric, and the (linear-elastic) substrate energy is a quadratic function of displacement. A theoretical prediction of the hexagonal dent pattern clearly requires a model without this inversion symmetry.

The inspiration for how to proceed comes from the other two regimes. The opposite regime is a soft layer on a rigid substrate, for example a hydrogel layer adhered to a glass slide. If the hydrogel is induced to swell, it enters compression, and undergoes a surface instability known as creasing or sulcification [15, 16, 74, 167], which forms a pattern of cusped self-contacting surface furrows. To understand this instability theoretically, one must use a geometrically nonlinear hyperelastic model for the soft layer (typically a neo-Hookean model) with a clamped bottom boundary modelling the substrate [168]. Such a model dramatically breaks topographical inversion symmetry via the non-linearities of large deformation geometry: simply inverting a cusped surface furrow (a sulcus/crease) would yield an unphysical state with singular energy. Previous authors [69, 169] have studied pattern formation in this system using higher order perturbation theory and found that patterns of hexagonal dents are indeed favoured. However, ironically, experimental [170] and numerical [76] studies show that in this regime, the pattern near threshold is in fact a square of cusped furrows. The mismatch arises because sulcification occurs via an exotic non-linear instability [74] which cannot be treated perturbatively, but these theoretical studies nevertheless establish that geometrically non-linear elasticity can break inversion symmetry and favours hexagonal dents.

Between these extremes is an intermediate regime: a growing soft-layer adhered to a soft substrate. This mechanically intriguing regime spans the transition from conventional stiff-soft wrinkling to soft-stiff sulcification, and characterizes many biological buckling systems [3–10, 33–35, 39–46]. Recently there has been much work on the onset of instability in this regime, using geometrically non-linear neo-Hookean elastic models for both the layer and the substrate [78, 88, 171, 172]. These studies have largely focused on two-dimensional linear stability analysis (i.e. uniaxial growth/compression yielding pure sinusoidal stripe patterns) and have documented how the wavelength and threshold of instability move as a function of layer/substrate modulus ratio, and identified the modulus ratio at which conventional finite wavelength buckling is replaced by sulcification. What emerges clearly from these studies

is that, at least in this intermediate regime, geometric non-linearity plays a role in even the onset of instability, with the wavelengths and thresholds deviating from those predicted by the traditional plate/linear-substrate model. Further evidence of the role of substrate non-linearity is provided in [85, 86, 173] where a substrate pre-stretch/pre-compression is shown to favour the formation of surface ridges/furrows respectively, demonstrating that substrate non-linearity not only matters, but also breaks pattern inversion symmetry.

In this chapter, we pursue the natural next step by taking such a fully geometrically non-linear elastic model of a neo-Hookean growing layer on a neo-Hookean substrate, and using it to address pattern selection. This fully non-linear model correctly lacks topography inversion symmetry. In the first section, we argue that, on symmetry grounds, this means hexagonal buckling patterns will generically appear subcritically and be favoured near threshold. In the following sections, we verify and extend this basic understanding by explicitly conducting higher order perturbation theory on the neo-Hookean layer/substrate, to evaluate the amplitude and energy of stripe, square and hexagonal elastic solutions near threshold. The full neo-Hookean model is significantly more complicated than the previously used plate/linear-substrate and neo-Hookean-layer/clamped-bottom-boundary models, so throughout this chapter, we evaluate the higher order fields using computer algebra from Mathematica [174] via `Solve` and `DSolve` functions, which analytically solve algebraic and differential equations respectively. However, at each stage, we are able to verify our computer-algebra predictions against symmetry-constrained finite element calculations, lending confidence to their accuracy. These analytic and computational calculations reveal that, for incompressible systems, hexagonal dent patterns are favoured, whereas for sponge-like compressible systems, hexagonal bumps are favoured. These conclusions break down when the layer is less than twice as stiff as the substrate, as then all types of pattern become subcritical, an expected signature of the transition to the sulcification regime. Finally, to emphasize the relationship between hexagonal patterns and inversion symmetry, we consider a stiff layer sandwiched between a matching pair of soft substrate and superstrate. This system has a true inversion symmetry, and correspondingly forms supercritical square patterns rather than subcritical hexagons.

4.1 Geometrically non-linear model for layer/substrate

Our system consists of a compressed layer adhered to a relaxed infinite substrate, and we seek to determine the selected buckling pattern by finding the configuration that minimizes the system's total elastic energy. More precisely, in Cartesian coordinates, we consider an elastic half space occupying $z < 0$ coated with an elastic layer occupying $0 < z < a$.

In this flat configuration, the substrate is elastically relaxed, but the layer has undergone equibiaxial growth/swelling/expansion post adhesion to the substrate such that, if it were released, it would extend equibiaxially in the x–y plane by a factor of g. When g exceeds a threshold value g^*, the layer will buckle into a non-flat pattern of topography with lower elastic energy. If, in this buckling, the layer/substrate undergo a displacement field $\mathbf{u} = (u_x(x,y,z), u_y(x,y,z), u_z(x,y,z))$, the full local shape changes are encoded by the deformation gradient (also known as the transformation matrix) $F_{ij} = \delta_{ij} + \partial_j u_i$ (where δ_{ij} it the Kronecker delta symbol), and the local elastic energy density is a function of this shape change $W(F)$. The total elastic energy is then the integral of $W(F)$ over the entire $-\infty < z < a$ volume, but since this energy is extensive, we normalize per-unit-area in the x–y plane,

$$E_{el} = \int_{z=-\infty}^{z=a} \langle W(F) \rangle \, \mathrm{d}z. \tag{4.1}$$

where angle brackets denote and in-plane average, $\langle f \rangle = \lim_{l\to\infty} \frac{1}{l^2} \int_{x=-l}^{x=l} \int_{y=-l}^{y=l} f \mathrm{d}x\mathrm{d}y$. Minimizing this energy with respect to variations in $\mathbf{u}$ leads to the expected bulk equation of mechanical equilibrium

$$\nabla \cdot \boldsymbol{\sigma} = \mathbf{0}, \tag{4.2}$$

where $\boldsymbol{\sigma} = \frac{\partial W}{\partial \nabla \mathbf{u}}$ is the large-strain PK1 stress tensor. This bulk equation is augmented by the natural boundary conditions, which require the top surface to be stress free, and the stress to be continuous at the layer/substrate interface:

$$\boldsymbol{\sigma} \cdot \hat{\mathbf{z}}\big|_{z=a} = \mathbf{0} \quad \text{and} \quad \boldsymbol{\sigma} \cdot \hat{\mathbf{z}}\big|_{z=0^+} = \boldsymbol{\sigma} \cdot \hat{\mathbf{z}}\big|_{z=0^-}, \tag{4.3}$$

where the superscript in $z = 0^{\pm}$ indicate the value is just above/below $z = 0$. In addition, layer/substrate adhesion requires the displacement field to be continuous at the interface

$$\mathbf{u}\big|_{z=0^+} = \mathbf{u}\big|_{z=0^-}. \tag{4.4}$$

For most of our work, we model the substrate and layer as incompressible neo-Hookean solids with shear moduli μ_2 and $\mu_1 \equiv \eta\mu_2$. Renormalizing both moduli by μ_2, the modulus and growth in both the layer and substrate are given by the piecewise functions:

$$(\tilde{\mu}, \tilde{g}) = \begin{cases} (\eta, g) & 0 < z < a, \\ (1,1) & z < 0. \end{cases} \tag{4.5}$$

Incompressibility requires $\mathrm{Det}(F) = 1$, meaning that, if material from either the layer or substrate was allowed to relax to its elastic ground-state, it would undergo the homogeneous deformation $G = \mathrm{diag}(\tilde{g}, \tilde{g}, 1/\tilde{g}^2)$, which is identity in the substrate. The full neo-Hookean form for $W(F)$, covering both the layer and the substrate, is thus

$$W = \frac{1}{2}\tilde{\mu}\left[\mathrm{Tr}\left(F \cdot G^{-1} \cdot G^{-T} \cdot F^T\right) - 3\right] - P(\mathrm{Det}(F) - 1) \tag{4.6}$$

where P is a Lagrange multiplier pressure field enforcing incompressibility. In this case, the PK1 stress tensor evaluates to

$$\sigma = \tilde{\mu} F G^{-1} G^{-T} - P\,\mathrm{cof}(F), \tag{4.7}$$

where $\mathrm{cof}(F) = \mathrm{Det}(F)F^{-T}$ refers to the cofactor of F, and one must also minimize the energy over variations in P yielding a further bulk equation of incompressibility:

$$\mathrm{Det}(F) = 1. \tag{4.8}$$

4.2 Approach: series expansion of the energy in the amplitude

Our task is now to construct solutions to the above bulk/boundary equations for different types of pattern and evaluate their corresponding elastic energies. In general, such patterns will have large amplitudes, and require intractable fully non-linear solutions, so our strategy is to look at patterns that are perturbatively close to the flat state. To do this, we conduct the elastic energy minimization in two stages. We first minimize the energy over configurations with small amplitude ε then, second, minimize the energy over ε to find the true minimum. This two-step approach has two advantages: it circumvents difficulties of self-consistency and solvability that commonly complicate higher order perturbation theory, and clarifies the origin of the hexagonal patterns. To constrain the amplitude during the first stage, we introduce a Lagrange multiplier L which enforces the root-mean-square amplitude of the surface:

$$E = E_{el} + L\left\langle u_z^2\big|_{z=a} - \varepsilon^2 \right\rangle. \tag{4.9}$$

The new term only contributes on the top ($z = a$) surface, so minimizing E with respect to variations in $\mathbf{u}$, L (and P for the incompressible case) yields the same bulk and boundary equations as before, except it introduces an external stress at the top surface $2Lu_z(x, y, z = a)\hat{\mathbf{z}}$,

so the boundary condition on the top surface is modified to:

$$(\boldsymbol{\sigma}\cdot\hat{\mathbf{z}}+2Lu_z\hat{\mathbf{z}})|_{z=a}=\mathbf{0}. \tag{4.10}$$

This is equivalent to the solvability conditions that need to be imposed at the higher order post buckling analysis [175]. Finally, minimizing E over L yields the imposed constraint on the amplitude,

$$\sqrt{\langle u_z^2\rangle|_{z=a}}=|\varepsilon|. \tag{4.11}$$

Since ε is now guaranteed to be a small amplitude, we can expand all the fields in a series expansion in ε:

$$\begin{aligned}\mathbf{u}(x,y,z)&=\sum_{n=1}^{\infty}\varepsilon^n\mathbf{u}_n(x,y,z),\\ P(x,y,z)&=\tilde{\mu}P_0(z)+\sum_{n=1}^{\infty}\varepsilon^n\tilde{\mu}P_n(x,y,z)\\ L&=L_0+\sum_{n=1}^{\infty}\varepsilon^nL_n.\end{aligned} \tag{4.12}$$

Our strategy is then to substitute these expansions into the bulk and boundary equations, expand the equations in ε, and solve order-by-order to build up series solutions for the fields. These solutions can then be substituted into E, to yield a Landau-like series solution of the energy in ε as in Section 1.4:

$$E=E_0+\sum_{n=1}^{\infty}\varepsilon^nE_n. \tag{4.13}$$

Finally, we conduct the second step: we truncate this energy series at sufficient order and minimize over ε to find the amplitude and elastic energy of the solution.

4.3 The inevitability of hexagonal patterns

In the above scheme, the first order equations ($O(\varepsilon)$) will be linear equations in the first order fields, corresponding to the equations of linear stability analysis. Since we expect periodic buckling patterns, it is natural to express the first order fields as a sum of trigonometric components with k-vectors in the x–y plane. However, since the first order equations are linear, these components can be treated separately, so it is sufficient to consider a single trigonometric component such as $u_{1z}=f_1(z)\cos(kx)$, which would give a stripe buckling pattern on the surface.

Having made this initial ansatz, the full set of first order fields can be found from the first order bulk and boundary equations. As discussed in Section 1.4, E_1 always vanishes. The first order solutions are sufficient to evaluate E_2, and the sign of E_2 then determines whether, for very small amplitudes, the buckling solution saves or costs energy, and hence whether the flat state is stable. By definition, the transition from stable to unstable happens at g^*, so we expect the energy series to take the form, $E = E_0 + C_2(g - g^*)\varepsilon^2$. In general, the value of g^* that emerges from this calculation will depend on the details of the model (modulus ratio, compressible versus incompressible etc.) and the value of k. It is then necessary to find the k with the smallest g^*, which will be the first unstable buckling mode. The first order solution (linear stability analysis) thus delivers the threshold g^* and wavelength $l = 2\pi/k$ of the buckling instability.

Nonetheless, linear stability analysis is insufficient to predict the stripe amplitude, as one cannot minimize E over ε without higher order terms. Furthermore, since all in-plane directions are equivalent, the values of g^* and C_2 do not depend on the (in-plane) direction of the k vector, so linear stability analysis cannot predict the direction stripes form in. Indeed, any linear combination of stripes in different directions but with the same magnitude of k must also solve the linear first order equations and become unstable at the same threshold, but will produce very different patterns of topography. In this chapter, we consider three basic topographical patterns, stripes, squares (checkerboards) and hexagons, encoded by the following linear combinations:

$$\begin{aligned} \text{stripe}: &\quad u_{1z} \sim \cos(kx) \\ \text{square}: &\quad u_{1z} \sim \cos(kx) + \cos(ky) \\ \text{hexagon}: &\quad u_{1z} \sim \cos(kx) + \cos(kx_1) + \cos(kx_2), \end{aligned} \tag{4.14}$$

where $x_1 = \frac{x}{2} + \frac{\sqrt{3}y}{2}$ and $x_2 = -\frac{x}{2} + \frac{\sqrt{3}y}{2}$. Since these patterns will all have the same threshold under linear stability analysis, to predict which pattern forms one must go beyond linear stability analysis and calculate higher order elastic fields and higher order terms in E to establish which pattern is the true energetic minimizer. We note that herringbone patterns, which have different wavelengths in the x and y directions, are guaranteed to have a higher threshold, so they are not candidates for the energy minimizer near threshold and must arise in stiff layer buckling via a secondary bifurcation.

Although these different patterns generate first order fields that are trivial linear combinations of the initial stripe solution, these different starting points generate different higher order fields, and different higher order terms in the energy. In general, it is sufficient to solve

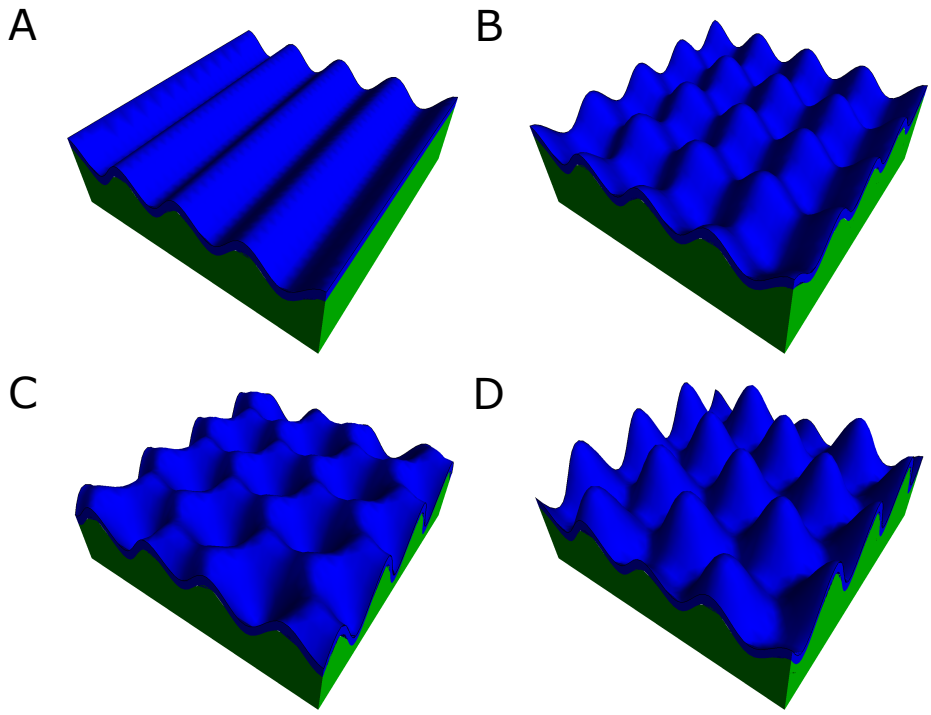

Fig. 4.2 Schematic diagram for different patterns (A) stripe, (B) square (C) positive hexagon and (D) negative hexagon.

the fields to third order, which allows us to evaluate the energy series to fourth order:

$$E = E_0 + C_2(g - g^*)\varepsilon^2 + C_3\varepsilon^3 + C_4\varepsilon^4 + O(\varepsilon^5), \tag{4.15}$$

where the values of C_3 and C_4 will depend on the pattern in question. The key observation is that, as clearly seen in Fig. 4.2, inverting the first order stripe and square patterns (i.e. setting $\varepsilon \to -\varepsilon$) is equivalent to a simple translation of the pattern in the x–y plane, and therefore cannot change the energy of the solution. In contrast, with hexagons the same inversion turns a pattern of bumps into a non-equivalent pattern of dents that should have a different elastic energy. This inversion symmetry of the first order stripe and square patterns requires the coefficient of the odd orders to vanish since $+\varepsilon$ and $-\varepsilon$ are equivalent. The energy expansion becomes

$$E = E_0 + C_2(g - g^*)\varepsilon^2 + C_4\varepsilon^4 + O(\varepsilon^5). \tag{4.16}$$

The instability will be supercritical if $C_4 > 0$. As discussed in Section 1.4, the amplitude beyond threshold that minimizes the energy (4.17) can be calculated as

$$\varepsilon^* = \sqrt{\frac{-C_2(g - g^*)}{2C_4}}. \tag{4.17}$$

The amplitude increases continuously for $g > g^*$, so the amplitude is indeed arbitrarily small close to threshold, and the series truncation is self-consistent. Past threshold, the energy of the buckled state is

$$E = E_0 - \frac{C_2^2(g-g^*)^2}{4C_4}, \tag{4.18}$$

which falls continuously from E_0 beyond threshold. Conversely, for the hexagonal patterns, C_3 will not vanish. This cubic term is always unbounded from below, so one still needs the fourth order term before truncating:

$$E = E_0 + C_2(g-g^*)\varepsilon^2 + C_3\varepsilon^3 + C_4\varepsilon^4 + O(\varepsilon^5). \tag{4.19}$$

The instability is subcritical, with a jump in the amplitude at threshold from zero to

$$\varepsilon = -\frac{3C_3}{4C_4}. \tag{4.20}$$

Thus, the sign of C_3 determines the sign of ε and hence whether hexagonal dents or bumps are formed. Importantly, at threshold, $g = g^*$, in the hexagonal case, the energy also jumps, to a value of:

$$E = E_0 - \frac{27C_3^4}{256C_4^3}, \tag{4.21}$$

(see Section 1.4 for the calculations). This finite energy jump at threshold will always place hexagonal patterns below the continuously falling energies generated by square and stripe patterns, so we conclude that hexagonal patterns will be formed. This conclusion is rather general, since the same symmetry considerations will apply to any transversely isotropic surface elastic instability.

We note that the truncation of the energy series is problematic in the hexagonal case, since the instability jumps to a finite amplitude at threshold, so the amplitude ε is not arbitrarily small, and the removed terms may be important. The resulting finite-amplitude hexagonal states may therefore differ appreciably from the actual hexagonal solutions, though in practice we find the disagreements are small. Moreover, since the theory is accurate for small ε, it is guaranteed to capture the loss of stability of the flat state correctly, including whether the transition is subcritical, and which sign of ε is chosen, even if it fails to capture the full details high-amplitude solution. Hence, the approach will predict the category of the pattern in spite of the missing details.

This symmetry argument has long been understood in fluids, where it explains the hexagonal patterns formed in Rayleigh-Taylor (gravitational) fingering, Rayleigh-Benard convection [176, 177], and the Rosensweig ferrofluid instability [178–181]. However, the

argument has only recently been applied to solid instabilities in the context of the Biot creasing/sulcification instability [69, 169]. As mentioned in the beginning of the chapter, they found that hexagonal dents are the energetically favourable pattern whereas the square of cusped furrows emerges from experiment and numerical simulation instead. We will discuss this discrepancy at the end of the chapter.

4.4 Pattern formation in an incompressible neo-Hookean layer and substrate

Although the above argument offers strong reasons to expect hexagonal buckling patterns, there are still good reasons to explicitly conduct the perturbation theory and compute the energy coefficients. Firstly, it is also possible for the symmetry argument to fail. If C_4 is negative for squares or stripes then these patterns will also form subcritically, so the theory does not reveal which pattern is preferred. In addition, the C_3 coefficient may vanish "accidentally" in a given system, even though it is permitted on symmetry grounds, making hexagonal patterns also supercritical, in which case the value of C_4 for the different patterns will determine the optimum pattern. Secondly, even if the argument holds, it is still necessary to compute the coefficients to determine the sign of C_3, and hence whether patterns of hexagonal bumps or dents will be favoured. In this section, we explicitly compute the fields and energy coefficients for the incompressible neo-Hookean layer/substrate system described in section 4.1. We first note that, following the series expansion in (4.12), we can also expand F, σ and W in ε:

$$\begin{aligned} F &= I + \sum_{n=1}^{\infty} \varepsilon^n F_n \\ \sigma &= \sigma_0 + \sum_{n=1}^{\infty} \varepsilon^n \sigma_n \\ W &= W_0 + \sum_{n=1}^{\infty} \varepsilon^n W_n. \end{aligned} \tag{4.22}$$

From the definition of F, it is immediately clear that $F_n = \nabla \mathbf{u}_n$, but finding the corresponding expressions for σ_n and W_n is more involved, as they involve $\mathrm{Det}\,(F)$ and $\mathrm{cof}\,(F)$. We reserve these explicit calculations for later sections, but it is useful to recall at the outset the following two 3×3 matrix identities:

$$\mathrm{Det}\,(A) = \frac{1}{6}\left(\mathrm{Tr}\,(A)^3 - 3\mathrm{Tr}\left(A^2\right)\mathrm{Tr}\,(A) + 2\mathrm{Tr}\left(A^3\right)\right), \tag{4.23}$$

$$\operatorname{cof}(A) = \frac{1}{2} I \left(\operatorname{Tr}(A)^2 - \operatorname{Tr}\left(A^2\right) \right) - A^T \operatorname{Tr}(A) + A^T \cdot A^T. \tag{4.24}$$

Furthermore, inserting the series expansion for F into the previous matrix identities yields the general fourth order expansions of $\operatorname{Det}(F)$ and $\operatorname{cof}(F)$,

$$\begin{aligned}
\operatorname{Det}(F) &= 1 + \varepsilon \operatorname{Tr}(F_1) + \varepsilon^2 \left(\operatorname{Tr}(F_2) + \frac{\operatorname{Tr}(F_1)^2 - \operatorname{Tr}\left(F_1^2\right)}{2} \right) \\
&+ \varepsilon^3 \left(\operatorname{Tr}(F_3) + \frac{\operatorname{Tr}(F_1)^3 - 3\operatorname{Tr}(F_1)\operatorname{Tr}\left(F_1^2\right) + 2\operatorname{Tr}\left(F_1^3\right)}{6} + \operatorname{Tr}(F_1)\operatorname{Tr}(F_2) - \operatorname{Tr}(F_1 \cdot F_2) \right) \\
&+ \varepsilon^4 \Bigg(\operatorname{Tr}(F_4) + \operatorname{Tr}(F_1)\operatorname{Tr}(F_3) - \operatorname{Tr}(F_1 \cdot F_3) - \operatorname{Tr}(F_1)\operatorname{Tr}(F_1 \cdot F_2) + \operatorname{Tr}\left(F_1^2 \cdot F_2\right) \\
&\qquad + \tfrac{1}{2} \left(\operatorname{Tr}(F_2)^2 - \operatorname{Tr}\left(F_2^2\right) + \operatorname{Tr}(F_1)^2 \operatorname{Tr}(F_2) - \operatorname{Tr}\left(F_1^2\right) \operatorname{Tr}(F_2) \right) \Bigg) + O(\varepsilon^5),
\end{aligned} \tag{4.25}$$

$$\begin{aligned}
\operatorname{cof}(F) &= I + \varepsilon \left(\operatorname{Tr}(F_1) I - F_1^T \right) \\
&+ \varepsilon^2 \left(\operatorname{Tr}(F_2) I - F_2^T + \tfrac{1}{2} \left(\operatorname{Tr}(F_1)^2 - \operatorname{Tr}(F_1 \cdot F_1) \right) I - \operatorname{Tr}(F_1) F_1^T + F_1^T \cdot F_1^T \right) \\
&+ \varepsilon^3 \left(\operatorname{Tr}(F_3) I - F_3^T + I \left(\operatorname{Tr}(F_2)\operatorname{Tr}(F_1) - \operatorname{Tr}(F_2 \cdot F_1) \right) \right. \\
&\qquad \left. - F_2^T \operatorname{Tr}(F_1) - F_1^T \operatorname{Tr}(F_2) + F_2^T \cdot F_1^T + F_1^T \cdot F_2^T \right) \\
&+ \varepsilon^4 \Big(\operatorname{Tr}(F_4) I - F_4^T + \tfrac{1}{2} \left(\operatorname{Tr}(F_2)^2 - \operatorname{Tr}(F_2 \cdot F_2) \right) + \operatorname{Tr}(F_1)\operatorname{Tr}(F_3) - \operatorname{Tr}(F_1 \cdot F_3) \\
&\qquad - F_3^T \operatorname{Tr}(F_1) - F_1^T \operatorname{Tr}(F_3) - F_2^T \operatorname{Tr}(F_2) + F_2^T \cdot F_2^T + F_3^T \cdot F_1^T + F_1^T \cdot F_3^T \Big) + O(\varepsilon^5).
\end{aligned} \tag{4.26}$$

4.4.1 The flat state

Substituting the σ expansions into the equations of equilibrium and expanding to $O(\varepsilon^0)$, we see that the flat state we are perturbing around must satisfy

$$\nabla \cdot \sigma_0 = \mathbf{0}, \qquad \operatorname{Det}(I) = 1 \tag{4.27}$$

in the bulk, and

$$\sigma_0 \cdot \hat{\mathbf{z}}\big|_{z=a} = \mathbf{0}, \qquad \sigma_0 \cdot \hat{\mathbf{z}}\big|_{z=0^+} = \sigma_0 \cdot \hat{\mathbf{z}}\big|_{z=0^-} \tag{4.28}$$

on the boundaries. Inserting the F expansion into the definition of σ, we see that

$$\sigma_0 = \tilde{\mu} \begin{pmatrix} 1/\tilde{g}^2 - P_0 & 0 & 0 \\ 0 & 1/\tilde{g}^2 - P_0 & 0 \\ 0 & 0 & \tilde{g}^4 - P_0 \end{pmatrix}, \tag{4.29}$$

which indeed is divergence free provided P_0 is constant, meaning both bulk equations are satisfied. The boundary conditions at $z = a$ and $z = 0$ then determine the flat-state pressure as

$$P_0 = \tilde{g}^4. \tag{4.30}$$

4.4.2 First order perturbation theory

The $O(\varepsilon)$ terms in the bulk equations are:

$$\nabla \cdot \sigma_1 = \mathbf{0}, \qquad \mathrm{Tr}\,(F_1) = \nabla \cdot \mathbf{u}_1 = 0, \tag{4.31}$$

the first order boundary conditions are,

$$\sigma_1 \cdot \hat{\mathbf{z}}|_{z=a} = -2L_0 u_{1z}\, \hat{\mathbf{z}}|_{z=a} \tag{4.32}$$

$$\sigma_1 \cdot \hat{\mathbf{z}}|_{z=0^+} = \sigma_1 \cdot \hat{\mathbf{z}}|_{z=0^-} \tag{4.33}$$

$$\mathbf{u}_1|_{z=0^+} = \mathbf{u}_1|_{z=0^-}, \tag{4.34}$$

and the first order amplitude equation is

$$\left\langle u_{1z}^2 \right\rangle\big|_{z=a} = 1. \tag{4.35}$$

Inserting the expansion for $\mathrm{cof}\,(F)$ into the general expression for σ, we see that

$$\sigma_1 = \tilde{\mu} \left(F_1 G^{-1} G^{-T} + P_0 F_1^T - P_1 I \right). \tag{4.36}$$

The first order energy coefficient is $E_1 = \int W_1 \mathrm{d}V$, which we expect to be zero, as it is the first order deviation away from the equilibrium flat state. More explicitly, inserting the expansion for $\mathrm{Det}\,(F)$ into W gives $W_1 = \sigma_0 F_1 = \sigma_0 \nabla \mathbf{u}_1$, which is not zero, but which gives zero for E_1 after integration by parts. The energy coefficient we are ultimately seeking to calculate is $E_2 = \int W_2 \, \mathrm{d}V$, so we expand W to second order, giving

$$W_2 = \tfrac{1}{2} \tilde{\mu} \left(\mathrm{Tr}\left(F_1 \cdot G^{-1} \cdot G^{-T} \cdot F_1^T \right) - P_0 \mathrm{Tr}\left(F_1 \cdot F_1 \right) \right),$$

where we have used incompressibility to eliminate the $P_1 \mathrm{Tr}\,(F_1)$ term and omitted a $\sigma_0 F_2$ term as it will also integrate to zero in E_2.

For the stripe pattern, the first order displacement field has a single trigonometric component $u_{1z} \sim f_z(z)\cos(kx)$, which requires sympathetically varying fields of the form

$$\mathbf{u}_1 = \begin{pmatrix} f_x(z)\sin(kx) \\ 0 \\ f_z(z)\cos(kx) \end{pmatrix} \tag{4.37}$$
$$P_1 = f_p(z)\cos(kx),$$

so the first order correction to the deformation gradient is

$$F_1 = \nabla \mathbf{u}_1 = \begin{pmatrix} k f_x(z)\cos(kx) & 0 & f_x'(z)\sin(kx) \\ 0 & 0 & 0 \\ -k f_z(z)\sin(kx) & 0 & f_z'(z)\cos(kx) \end{pmatrix}. \tag{4.38}$$

Substituting these forms for F_1 and σ_1 into the bulk equations, the first order incompressibility equation is:

$$k f_x(z) + f_z'(z) = 0, \tag{4.39}$$

and the first order mechanical equilibrium equations are:

$$\tilde{g}^2 k f_p(z) - k^2 f_x(z) + \tilde{g}^6 f_x''(z) = 0 \tag{4.40}$$
$$k^2 f_z(z) + \tilde{g}^2 f_p'(z) - \tilde{g}^6 f_z''(z) = 0. \tag{4.41}$$

These can be algebraically solved for f_p and f_x,

$$f_p(z) = \frac{\tilde{g}^6 f_z'''(z) - k^2 f_z'(z)}{\tilde{g}^2 k^2} \tag{4.42}$$
$$f_x(z) = -\frac{f_z'(z)}{k}, \tag{4.43}$$

then substituting these results into the second mechanical equilibrium equation yields a fourth order differential equation for f_z:

$$k^4 f_z(z) - (1+\tilde{g}^6) k^2 f_z''(z) + \tilde{g}^6 f_z^{(4)}(z) = 0, \tag{4.44}$$

where $f^{(n)}$ is the notation for the n$^{\text{th}}$ derivative of f. The equation (4.44) is solved by the form,

$$f_z(z) = \begin{cases} e^{-kz/g^3}A_1 + e^{kz/g^3}A_2 + e^{-kz}A_3 + e^{kz}A_4 & z > 0, \\ e^{kz}(B_1 + zB_2) & z < 0, \end{cases} \tag{4.45}$$

where A_i and B_i are constants of integration, and we have excluded solutions that diverge as $z \to -\infty$. The values of A_i, B_i and L_0 must be found from the boundary conditions (4.32-4.35). The normal stress condition on the top surface (the z component of (4.32)) is a linear equation for L_0, solved in terms of the A_i and B_i as:

$$L_0 = -\frac{\sigma_{1zz}}{2u_{1z}}\bigg|_{z=a}. \tag{4.46}$$

The remaining six boundary conditions (amplitude, surface shear stress, $2\times$ interfacial stress continuity, $2\times$ interfacial displacement continuity) are six linear equations in the form

$$\underbrace{\begin{pmatrix} e^{-ka/g^3} & e^{ka/g^3} & e^{-ka} & e^{ka} & 0 & 0 \\ e^{-ka/g^3}b & e^{ka/g^3}b & 2e^{-ka}g^6 & 2e^{ka}g^6 & 0 & 0 \\ -2g^3\eta & 2g^3\eta & -b\eta & b\eta & -2g^2 & 0 \\ b\eta & b\eta & 2g^6\eta & 2g^6\eta & -2g^2 & -2g^2/k \\ 1 & 1 & 1 & 1 & -1 & 0 \\ 1 & -1 & g^3 & -g^3 & g^3 & g^3/k \end{pmatrix}}_{M} \begin{pmatrix} A_1 \\ A_2 \\ A_3 \\ A_4 \\ B_1 \\ B_2 \end{pmatrix} = \begin{pmatrix} \sqrt{2} \\ 0 \\ 0 \\ 0 \\ 0 \\ 0 \end{pmatrix}, \tag{4.47}$$

where $b = 1 + g^6$. The non-zero source on the right of this matrix equation arises from the amplitude equation, and ensures that there is always a solution, of the form $(A_1, A_2, A_3, A_4, B_1, B_2) = M^{-1}(\sqrt{2}, 0, 0, 0, 0, 0)$. This solution corresponds, for each value of g, to a solution with the small but prescribed amplitude ε imposed by the external surface stress L_0. The resulting expressions for A_i and L_0 are rather cumbersome, so we do not display them here. The threshold for spontaneous instability arises at the critical degree of growth g^* for which this solution has $L_0 = 0$. This means the solution arises without external stress at the instability threshold. The a sign change in L indicates its changing role from enhancing to reducing instability amplitude. To find the threshold value g^*, one must simply solve the additional threshold equation $L_0 = 0$ for g. This equation cannot be solved analytically but is straightforward to solve numerically at any numerical values of k and η. Fig. 4.3 characterizes the results of this stability analysis. Fig. 4.3A shows the threshold g^*as a function of wavelength, $l = 2\pi/k$, for different η and Figs 4.3B and C shows the threshold and the wavelength of the first unstable mode, obtained by numerically minimizing Fig. 4.3A

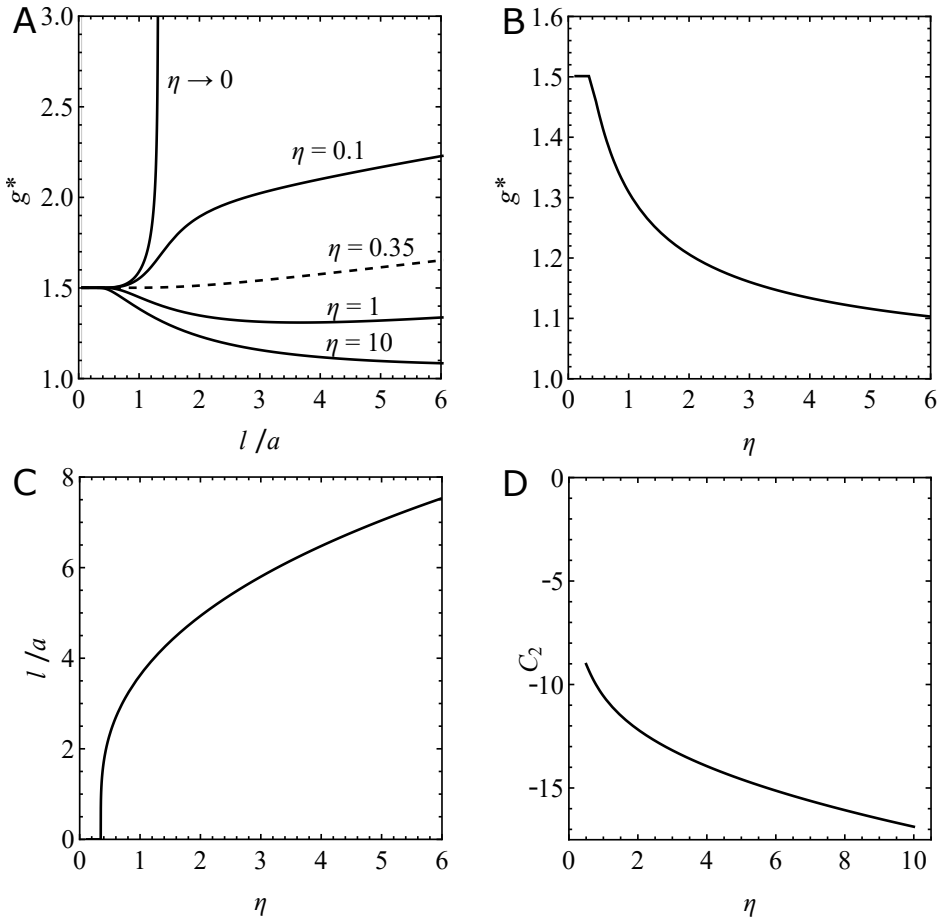

Fig. 4.3 (A) Threshold value of growth g as a function of wavelength at different values of stiffness ratio, η. (B) and (C) threshold growth and the wavelength of the first unstable mode (D) The second order energy coefficient C_2, of the first unstable mode as a function of the stiffness ratio, η.

over wavelengths. As expected, for stiff layers the critical wavelength grows with layer stiffness, and the buckling mode is a form of Euler buckling constrained by the substrate. In the other extreme, for $\eta \lesssim 0.35$ the first unstable mode has zero wavelength at $g = 1.501$, the hallmark of the pathological Biot surface instability. From previous work, we know that this Biot instability is never observed, because it is always preceded by the non-linear sulcus/crease forming instability which, in neo-Hookean solids occurs at $g^* \approx 1.34$. In our system, this nonlinear instability occurs before the linear instability for $\eta \lesssim 0.86$, which is thus the limit of validity of our perturbative approach.

Although the above treatment deals with stripe patterns, first order square patterns and hexagonal patterns are simple linear combinations of this underlying stripe pattern, and hence

described by the same elastic solution. For the square pattern we have

$$\mathbf{u} = \frac{\varepsilon}{\sqrt{2}} \begin{pmatrix} f_x(z)\sin(kx) \\ f_x(z)\sin(ky) \\ f_z(z)(\cos(kx)+\cos(ky)) \end{pmatrix} \tag{4.48}$$
$$P = P_0(z) + \frac{\varepsilon}{\sqrt{2}} f_p(z)(\cos(kx)+\cos(ky)),$$

and for the hexagonal pattern we have

$$\mathbf{u} = \frac{\varepsilon}{\sqrt{3}} \begin{pmatrix} f_x(z)\left(\sin(kx)+\frac{1}{2}(\sin(kx_1)-\sin(kx_2))\right) \\ f_x(z)\frac{\sqrt{3}}{2}(\sin(kx_1)+\sin(kx_2)) \\ f_z(z)(\cos(kx)+\cos(kx_1)+\cos(kx_2)) \end{pmatrix} \tag{4.49}$$
$$P = P_0(z) + \frac{\varepsilon}{\sqrt{3}} f_p(z)(\cos(kx)+\cos(kx_1)+\cos(kx_2)),$$

where the overall pre-factors have been chosen so that all three patterns have the same root-mean-squared amplitude. The value of E_2 is the same for each pattern, as the integrand underlying E_2 is quadratic in the elastic fields, so cross-terms between different trigonometric components in the square/hexagonal patterns integrate to zero. As expected, E_2 vanishes at g^*, indicating a transition from stability to instability. We calculate C_2 as

$$C_2 = \left.\frac{\partial E_2}{\partial g}\right|_{g=g*}, \tag{4.50}$$

so that, to quadratic order, the energy can be written as $E = E_0 + C_2(g-g^*)\varepsilon^2$. Using computer algebra, we are able to calculate this derivative analytically, then substitute in numerical threshold values for g^* and k, leading to a numerical value of C_2 for each value of η, which is plotted in Fig. 4.3D.

4.4.3 Second order perturbation theory

The $O(\varepsilon^2)$ terms in the bulk equations are:

$$\nabla\cdot\sigma_2 = \mathbf{0}, \qquad \mathrm{Tr}\,(F_2) = \tfrac{1}{2}\mathrm{Tr}\left(F_1^2\right), \tag{4.51}$$

the second order boundary conditions are,

$$\sigma_2 \cdot \hat{\mathbf{z}}|_{z=a} = -2\,(L_1 u_{1z} + L_0 u_{2z})\hat{\mathbf{z}}|_{z=a} \tag{4.52}$$

$$\sigma_2 \cdot \hat{\mathbf{z}}|_{z=0^+} = \sigma_2 \cdot \hat{\mathbf{z}}|_{z=0^-} \tag{4.53}$$

$$\mathbf{u}_2|_{z=0^-} = \mathbf{u}_2|_{z=0^+}\,, \tag{4.54}$$

and the second order amplitude equation is

$$\langle u_{1z} u_{2z} \rangle|_{z=a} = 0. \tag{4.55}$$

Again, expanding σ using the general expansion of $\mathrm{cof}\,(F)$, the expression of σ_2 is

$$\sigma_2 = \tilde{\mu}\left(F_2 \cdot G^{-1} \cdot G^{-T} - P_2 I + P_1 F_1^T + P_0\left(F_2^T - F_1^T \cdot F_1^T\right)\right). \tag{4.56}$$

These equations must be solved for $\mathbf{u}_2$, P_2 and L_1. The equations are linear in these variables but, as seen in (4.51) and (4.56), they also contain quadratic source terms in the first order fields. These quadratic terms introduce trigonometric components corresponding to all the sums and differences of the k vectors in the first order solutions, so at second and higher order the different patterns produce solutions that are not simple linear combinations of each other, and indeed each equation becomes the sum of several different in-plane modes. Our approach is to substitute trial solutions for each pattern that are sums of all permissible in-plane modes but with unknown z dependence, then require each mode in each equation to vanish separately. This produces a long set of bulk and boundary equations, which are algebraically tedious but mechanically simple to solve for the unknown z variation in the second order fields.

After finding the fields, we can integrate the third order energy density coefficient,

$$W_3 = \tilde{\mu}\left(\mathrm{Tr}\left(F_1 \cdot G^{-1} \cdot G^{-T} \cdot F_2^T\right) - P_0\left(\tfrac{1}{3}\mathrm{Tr}\left(F_1^3\right) - \mathrm{Tr}\left(F_1 \cdot F_2\right)\right)\right)$$

to find the coefficient C_3 that we are seeking. As earlier, we have omitted a $\sigma_0 F_3$ term in this expansion, as it will integrate to zero in C_3. As with C_2, the integration can be done using computer algebra, but our final result is the evaluation of this algebraic expression at the numerically found threshold for instability.

4.4.4 Third order perturbation theory

The $O(\varepsilon^3)$ terms in the bulk equations are:

$$\nabla \cdot \sigma_3 = \mathbf{0}, \qquad \mathrm{Tr}\,(F_3) = \mathrm{Tr}\,(F_1 F_2) - \tfrac{1}{3}\mathrm{Tr}\left(F_1^3\right), \tag{4.57}$$

the third order boundary conditions are,

$$\sigma_3 \cdot \hat{\mathbf{z}}\big|_{z=a} = -2(L_2 u_{1z} + L_1 u_{2z} + L_0 u_{3z})\,\hat{\mathbf{z}}\big|_{z=a} \tag{4.58}$$

$$\sigma_3 \cdot \hat{\mathbf{z}}\big|_{z=0^+} = \sigma_3 \cdot \hat{\mathbf{z}}\big|_{z=0^-} \tag{4.59}$$

$$\mathbf{u}_3\big|_{z=0^-} = \mathbf{u}_3\big|_{z=0^+}, \tag{4.60}$$

and the third order amplitude equation is

$$\left\langle u_{1z} u_{3z} + \tfrac{1}{2} u_{2z}^2 \right\rangle\big|_{z=a} = 0. \tag{4.61}$$

Again, expanding σ using the general expansion of $\mathrm{cof}\,(F)$, the expression of σ_3 is

$$\begin{aligned}\sigma_3 = \tilde{\mu}\,&\left(F_3 \cdot G^{-1} \cdot G^{-T} - P_3 I + P_2 F_1^T + P_1\left(F_2^T - F_1^T \cdot F_1^T\right)\right.\\ &\left. + P_0\left(\tfrac{1}{3}\mathrm{Tr}\left(F_1^3\right) I + F_3^T + F_1^T \mathrm{Tr}\,(F_2) - F_2^T \cdot F_1^T - F_1^T \cdot F_2^T\right)\right).\end{aligned} \tag{4.62}$$

These equations must be solved for $\mathbf{u}_3$, P_3 and L_2. Again, the equations are linear in the solution variables, but this time the "source" terms are cubic terms of the first and second order fields, so there will be in-plane trigonometric components corresponding to all three-fold sums of initial k vectors, leading to a very large total number of equations to solve. After finding the fields, we can integrate the fourth order energy density coefficient,

$$\begin{aligned}W_4 = \tilde{\mu}\,&\left[\mathrm{Tr}\left(\tfrac{1}{2} F_2 \cdot G^{-1} \cdot G^{-T} F_2^T + F_1 \cdot G^{-1} \cdot G^{-T} \cdot F_3^T\right)\right.\\ &\left. - P_0\left(\mathrm{Tr}\left(F_1^2 \cdot F_2\right) - \mathrm{Tr}\,(F_1 \cdot F_3) - \tfrac{1}{2}\left(\mathrm{Tr}\,(F_2)^2 + \mathrm{Tr}\left(F_2^2\right)\right)\right)\right]\end{aligned} \tag{4.63}$$

to find the coefficient C_4 that we are seeking. As earlier, we have omitted a $\sigma_0 F_4$ term in this expansion, as it will integrate to zero in C_4. As with C_2 and C_3, the integration can be done using computer algebra, but our final result is the evaluation of the resulting algebraic expression at the numerically found threshold for instability.

4.4.5 Stripe pattern results

As noted in the previous two sections, the second and third order fields are expected to require all trigonometric components that are two-fold and three-fold sums of the k vectors of the first order field. In the case of a stripe pattern, this leads us to consider the form:

$$\begin{aligned}
u_x(x,z) =& \varepsilon f_{x,1,1}(z)\sin(kx) + \varepsilon^2(f_{x,2,1}(z)\sin(2kx)) \\
&+ \varepsilon^3(f_{x,3,1}(z)\sin(kx) + f_{x,3,2}(z)\sin(3kx)) + O(\varepsilon^4) \\
u_z(x,z) =& \varepsilon f_{z,1,1}(z)\cos(kx)\varepsilon^2(f_{z,2,1}(z) + f_{z,2,2}(z)\cos(2kx)) \\
&+ \varepsilon^3(f_{z,3,1}(z)\cos(kx) + f_{z,3,2}(z)\cos(3kx)) + O(\varepsilon^4) \\
P(x,z) =& P_0(z) + \varepsilon f_{p,1,1}(z)\cos(kx) + \varepsilon^2(f_{p,2,1}(z) + f_{p,2,2}(z)\cos(2kx)) \\
&+ \varepsilon^3(f_{p,3,1}(z)\cos(kx) + f_{p,3,2}(z)\cos(3kx)) + O(\varepsilon^4)
\end{aligned} \tag{4.64}$$

where the $f_{x,m,n}(z)$, $f_{z,m,n}(z)$ and $f_{p,m,n}(z)$ indicate unknown functions describing the z variation of the n^{th} trigonometric component (in u_x, u_y and P respectively) at m^{th} order in ε, so in the notation from the first order perturbation theory $f_{x,1,1} = f_x$, $f_{z,1,1} = f_z$ and $f_{p,1,1} = f_p$. Although we have found these first order fields by hand, we now use the computer algebra package in Mathematica to solve at higher orders.

More precisely, we first substitute these forms into the bulk equations and boundary/amplitude conditions, expand the equations in ε, separate the first, second and third order equations (as we did by hand in the previous two sections) and then further separate these equations into their different trigonometric components, yielding a long list of bulk and boundary equations at each order in ε. Reminiscent of first order, at each successive order ε^m the equations arising from the bulk equations are a linear algebraic/differential set of equations for the $f_{x,m,n}(z)$, $f_{z,m,n}(z)$ and $f_{p,m,n}(z)$, which Mathematica is able to solve analytically as a set using the function `DSolve`, thereby introducing a number of constants of integration.

We next substitute these solutions into the elastic energy, expand in ε and explicitly integrate over the total volume, to find an exact expression for each energy coefficient $E_0 ... E_4$, though in terms of the as-yet unknown constants of integration. Fortunately, the equations arising from the boundary/amplitude condition form a linear set of equations for the constants of integration, with a single unique solution which Mathematica is again able to find analytically using the function `Solve`. Finally, we substitute these expressions for the constants into $E_0 ... E_4$, and evaluate the resulting expressions at the numerically characterized point of instability to find C_3 and C_4.

As anticipated, the third order coefficient C_3 vanishes identically for the stripe pattern upon conducting the in-plane integration. We show the energy coefficients C_4 for the stripe

pattern as a function of η, (evaluated at each η at the value of g^* and k of the first unstable mode) in Fig. 4.4A. The C_4 coefficient is positive except when $\eta < 0.78$, meaning that that the stripe pattern will be supercritical for a stiff layer but subcritical in a very soft layer. However, since this transition occurs below the sulcification limit at $\eta_s = 0.86$, it cannot be observed in practice. Using the results in (4.17–4.18), we can predict the amplitude and the energy for the stripe pattern close to threshold, and these are plotted for $\eta = 3$ in Figs 4.4C and D.

We performed a numerical finite element analysis to verify these theoretical predictions. To do so, we used large-strain, fully non-linear finite elements, but constrained the pattern to stripes by choosing the domain of the simulation as a rectangular unit cell, with the longer side equal to predicted wavelength and a periodic boundary condition. The simulated pattern is shown in Fig. 4.4B, and the simulated amplitude and energy are compared with the theoretical prediction in Fig. 4.4C, showing a good agreement (with no fitting parameters of any kind) especially close to the threshold, and thereby lending confidence to our analytical calculation. No hysteresis loop is observed from the numerical results as expected from a supercritical instability.

4.4.6 Square pattern results

The expression for the displacement fields including higher order terms for square and hexagonal patterns are much more complicated than that of that stripe pattern. For the square pattern, we can write the displacement field as:

$$\begin{aligned} u_z(x,y,z) =& \varepsilon \sum_{n=1}^{2} f_{z,1,n}(z)\cos(\mathbf{k}_n^{(1)}\cdot\mathbf{x}) + \varepsilon^2 \sum_{n=1}^{5} f_{z,2,n}(z)\cos(\mathbf{k}_n^{(2)}\cdot\mathbf{x}) \\ &+ \varepsilon^3 \sum_{n=1}^{8} f_{z,3,n}(z)\cos(\mathbf{k}_n^{(3)}\cdot\mathbf{x}) \end{aligned} \tag{4.65}$$

here $\mathbf{x} = (x,y)$, $\mathbf{k}_1^{(1)} \equiv \mathbf{k}_1 = k\hat{\mathbf{x}}$ and $\mathbf{k}_2^{(1)} \equiv \mathbf{k}_2 = k\hat{\mathbf{y}}$. The notation $\mathbf{k}_n^{(i)}$ indicates the n^{th} component wavevector at the i^{th} order. Because of the square symmetry, field u_z must be invariant under rotation symmetry $x \to y, y \to -x$. There are also reflection symmetries under $x \to -x$ and under $y \to -y$. This means we require $f_{z,1,1}(z) = f_{z,1,2}(z)$. To construct the ansatz for the next order, we know that the higher order trigonometric terms must come from the product of lower order terms. Hence, the possible wavevectors are $\mathbf{k}_1^{(2)} = \mathbf{0}$, $\mathbf{k}_2^{(2)} = 2\mathbf{k}_1$, $\mathbf{k}_3^{(2)} = 2\mathbf{k}_2$, $\mathbf{k}_4^{(2)} = \mathbf{k}_1 + \mathbf{k}_2$ and $\mathbf{k}_5^{(2)} = \mathbf{k}_1 - \mathbf{k}_2$. Again, symmetry requires $f_{z,2,2}(z) = f_{z,2,3}(z)$ and $f_{z,2,4}(z) = f_{z,2,5}(z)$. At third order, we need all possible sums of the three instances of $\mathbf{k}_1$

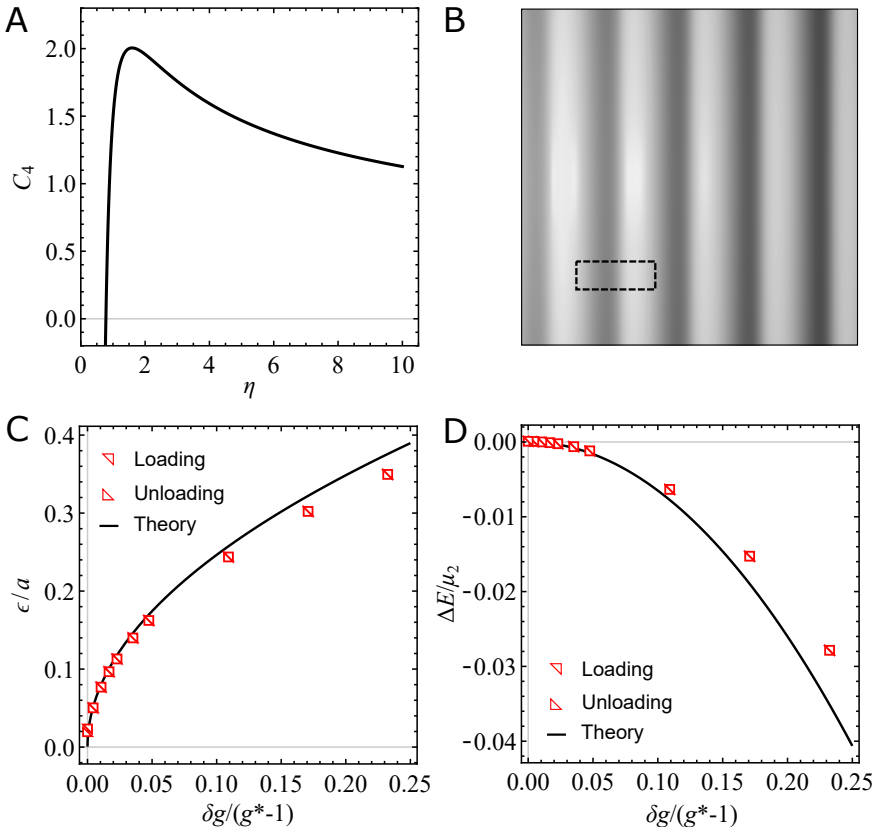

Fig. 4.4 (A) The energy coefficient C_4 (B) Numerical simulated pattern at $g = 1.18$ for $\eta = 3$. Dashed lines show a simulation unit cell. (C) Amplitude and (D) energy per slab volume as a function of growth from the threshold, $\delta g = g - g^*$, for stripe pattern at $\eta = 3$.

or $\mathbf{k}_2$, which are

$$\mathbf{k}_1^{(3)} = \mathbf{k}_1, \quad \mathbf{k}_2^{(3)} = \mathbf{k}_2, \quad \mathbf{k}_3^{(3)} = 3\mathbf{k}_1, \quad \mathbf{k}_4^{(3)} = 3\mathbf{k}_2, \quad \mathbf{k}_5^{(3)} = \mathbf{k}_1 - 2\mathbf{k}_2,$$

$$\mathbf{k}_6^{(3)} = \mathbf{k}_1 + 2\mathbf{k}_2, \quad \mathbf{k}_7^{(3)} = 2\mathbf{k}_1 - \mathbf{k}_2, \quad \mathbf{k}_8^{(3)} = 2\mathbf{k}_1 + \mathbf{k}_2,$$

with $f_{z,3,1}(z) = f_{z,3,2}(z)$, $f_{z,3,3}(z) = f_{z,3,4}(z)$ and $f_{z,3,5}(z) = f_{z,3,6}(z) = f_{z,3,7}(z) = f_{z,3,8}(z)$. The form of the field $f_{p,m,n}(z)$ follows from u_z with different function $f_{z,m,n}(z)$. The form of u_x and u_y can be more complicated as they do not have the rotational symmetry but still possess the reflection symmetry (over x-axis for u_x and y-axis for u_y). However, incompressibility condition (4.31) hints us the form of u_x and u_z:

$$\mathrm{Det}(F) - 1 = \frac{\partial u_z}{\partial z} + \frac{\partial u_x}{\partial x} + \frac{\partial u_y}{\partial y} + O(\varepsilon^2) = 0 \tag{4.66}$$

at the lowest order. Their corresponding derivatives must have the trigonometric components as that of u_z in the same order. We could write down

$$\begin{aligned} u_x(x,y,z) =& \varepsilon \sum_{n=1}^{2} f_{x,1,n}(z) \sin(\mathbf{k}_n^{(1)} \cdot \mathbf{x}) + \varepsilon^2 \sum_{n=1}^{5} f_{x,2,n}(z) \sin(\mathbf{k}_n^{(2)} \cdot \mathbf{x}) \\ &+ \varepsilon^3 \sum_{n=1}^{8} f_{x,3,n}(z) \sin(\mathbf{k}_n^{(3)} \cdot \mathbf{x}). \end{aligned} \tag{4.67}$$

The function $f_{x,2,1}(z) = 0$ as its term is independent of the x and y coordinates. The y-reflection symmetry demands $f_{x,1,2}(z) = f_{x,2,3}(z) = f_{x,3,2}(z) = f_{x,3,4}(z) = 0$, $f_{x,2,4}(z) = f_{x,2,5}(z)$, $f_{x,3,5}(z) = f_{x,3,6}(z)$ and $f_{x,3,7}(z) = f_{x,3,8}(z)$. Under the rotation transformation $x \to y, y \to -x$, the field u_x becomes u_y. Hence, u_y can be written as

$$\begin{aligned} u_y(x,y,z) =& \varepsilon \sum_{n=1}^{2} f_{y,1,n}(z) \sin(\mathbf{k}_n^{(1)} \cdot \mathbf{x}) + \varepsilon^2 \sum_{n=1}^{5} f_{y,2,n}(z) \sin(\mathbf{k}_n^{(2)} \cdot \mathbf{x}) \\ &+ \varepsilon^3 \sum_{n=1}^{8} f_{y,3,n}(z) \sin(\mathbf{k}_n^{(3)} \cdot \mathbf{x}). \end{aligned} \tag{4.68}$$

where

$$f_{y,1,2}(z) = f_{x,1,1}, \quad f_{y,2,3}(z) = f_{x,2,2}(z), \quad f_{y,2,4}(z) = -f_{y,2,5}(z) = f_{x,2,4}(z),$$

$$f_{y,3,2}(z) = f_{x,3,1}(z), \quad f_{y,3,4}(z) = f_{x,3,3}(z), \quad -f_{y,3,5}(z) = f_{y,3,6}(z) = f_{x,3,7}(z),$$

$$-f_{y,3,7}(z) = f_{y,3,8} = f_{x,3,5}(z)$$

while the rest of $f_{y,m,n}(z)$ are zero. With these ansatzes in the displacement fields, we can proceed to solve the bulk and boundary equations to obtain the functions $f_{l,m,n}(z)$.

Having obtained the form of the displacement fields, we are able to substitute these forms into the energy/equations, and find a complete third order solution in the same manner as for stripes. Again, the coefficient C_3 vanishes upon in-plane integration of the energy, and we plot the form of the coefficient C_4 as a function of η in Fig. 4.5. In this case C_4 is also positive for stiff layers, meaning the instability is supercritical, and we can again predict the amplitude and energy of instability close to the threshold. However, in this case, C_4 becomes negative for $\eta < 2.23$ indicating a transition to a subcritical instability at this value of η, which is above the sulcification point, and therefore in the domain of validity of the theory. Below this point, we cannot estimate the amplitude or energy of the instability (as this would require C_6) but we can be confident the instability is subcritical.

To test these predictions, we again perform numerical finite element calculations, this time selecting $\eta = 1.5, 3$ and 10, to span the predicted supercritical to subcritical transition. In this case, we constrained the finite elements to a square pattern by using a square unit cell with the side equal to the predicted wavelength. As seen in Fig. 4.5, the transition is indeed supercritical for $\eta = 10$, and in good agreement with the theoretical prediction. For $\eta = 1.5$, the transition is indeed subcritical, as predicted. For $\eta = 3$, the transition is supercritical as predicted, but the actual amplitude and energy are in poor agreement, which we attribute to the fact that C_4 is almost zero (as it is close to the positive-negative transition) so higher orders are required for an accurate prediction even close to threshold.

4.4.7 Hexagonal pattern results

For hexagonal pattern, we start with $u_z(x,y,z) = \varepsilon \sum_{n=1}^{3} f_{z,1,n}(z)\cos(\mathbf{k}_n^{(1)} \cdot \mathbf{x}) + O(\varepsilon^2)$ where $\mathbf{k}_1^{(1)} \equiv \mathbf{k}_1 = k\hat{\mathbf{x}}$, $\mathbf{k}_2^{(1)} \equiv \mathbf{k}_2 = k(\frac{1}{2}, \frac{\sqrt{3}}{2}) = k\hat{\mathbf{x}}_1$ and $\mathbf{k}_3^{(1)} \equiv \mathbf{k}_3 = k(-\frac{1}{2}, \frac{\sqrt{3}}{2}) = k\hat{\mathbf{x}}_2$. The hexagonal symmetry requires u_z to be invariant under $x \to x_1$, $x_1 \to x_2$, $x_2 \to -x$. This means that $f_{z,1,1}(z) = f_{z,1,2}(z) = f_{z,1,3}(z)$. We follow the same principle as before and write the series as in (4.65). At second order, the possible wavevectors are:

$$\mathbf{k}_1^{(2)} = \mathbf{0}, \quad \mathbf{k}_2^{(2)} = 2\mathbf{k}_1, \quad \mathbf{k}_3^{(2)} = 2\mathbf{k}_2, \quad \mathbf{k}_4^{(2)} = 2\mathbf{k}_3,$$

$$\mathbf{k}_5^{(2)} = \mathbf{k}_2 - \mathbf{k}_3 = \mathbf{k}_1, \quad \mathbf{k}_6^{(2)} = \mathbf{k}_3 + \mathbf{k}_1 = \mathbf{k}_2, \quad \mathbf{k}_7^{(2)} = \mathbf{k}_2 - \mathbf{k}_1 = \mathbf{k}_3,$$

$$\mathbf{k}_8^{(2)} = \mathbf{k}_1 + \mathbf{k}_2, \quad \mathbf{k}_9^{(2)} = \mathbf{k}_2 + \mathbf{k}_3, \quad \mathbf{k}_{10}^{(2)} = \mathbf{k}_1 - \mathbf{k}_3.$$

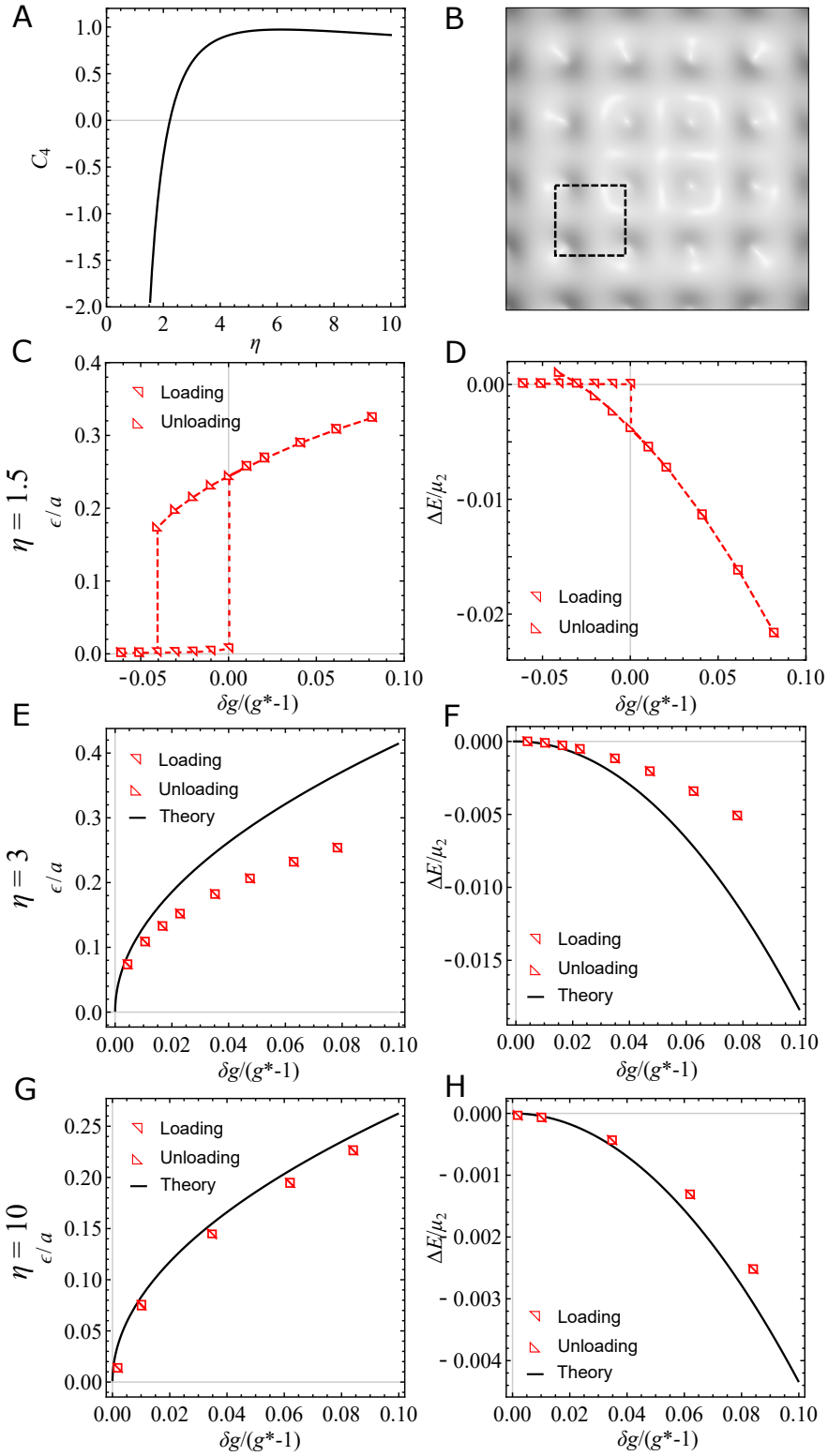

Fig. 4.5 (A) The energy coefficient C_4. (B) Numerical simulated pattern at $g = 1.18$ for $\eta = 3$. Dashed lines show a simulation unit cell. (C–H) Amplitude and energy per slab volume as a function of growth from the threshold, $\delta g = g - g^*$, for square pattern at $\eta = 1.5, 3$ and 10.

From symmetry, the relations between the function $f_{z,2,n}(z)$ are

$$f_{z,2,2}(z) = f_{z,2,3}(z) = f_{z,2,4}(z),$$

$$f_{z,2,5}(z) = f_{z,2,6}(z) = f_{z,2,7}(z),$$

$$f_{z,2,8}(z) = f_{z,2,9}(z) = f_{z,2,10}(z).$$

At third order, we have

$$\mathbf{k}_1^{(3)} = \mathbf{k}_1 - \mathbf{k}_2 + \mathbf{k}_3 = \mathbf{0},$$
$$\mathbf{k}_2^{(3)} = \mathbf{k}_1, \quad \mathbf{k}_3^{(3)} = \mathbf{k}_2, \quad \mathbf{k}_4^{(3)} = \mathbf{k}_3,$$
$$\mathbf{k}_5^{(3)} = 2\mathbf{k}_1, \quad \mathbf{k}_6^{(3)} = 2\mathbf{k}_2, \quad \mathbf{k}_7^{(3)} = 2\mathbf{k}_3,$$
$$\mathbf{k}_8^{(3)} = 3\mathbf{k}_1, \quad \mathbf{k}_9^{(3)} = 3\mathbf{k}_2, \quad \mathbf{k}_{10}^{(3)} = 3\mathbf{k}_3,$$
$$\mathbf{k}_{11}^{(3)} = \mathbf{k}_1 + \mathbf{k}_2, \quad \mathbf{k}_{12}^{(3)} = \mathbf{k}_2 + \mathbf{k}_3, \quad \mathbf{k}_{13}^{(3)} = \mathbf{k}_1 - \mathbf{k}_3.$$
$$\mathbf{k}_{14}^{(3)} = 2\mathbf{k}_1 + \mathbf{k}_2, \quad \mathbf{k}_{15}^{(3)} = 2\mathbf{k}_2 + \mathbf{k}_3, \quad \mathbf{k}_{16}^{(3)} = 2\mathbf{k}_3 - \mathbf{k}_1.$$
$$\mathbf{k}_{17}^{(3)} = 2\mathbf{k}_1 - \mathbf{k}_3, \quad \mathbf{k}_{18}^{(3)} = 2\mathbf{k}_2 + \mathbf{k}_1, \quad \mathbf{k}_{19}^{(3)} = 2\mathbf{k}_3 + \mathbf{k}_2,$$

and the rotation and reflection symmetries require

$$f_{z,3,2}(z) = f_{z,3,3}(z) = f_{z,3,4}(z),$$

$$f_{z,3,5}(z) = f_{z,3,6}(z) = f_{z,3,7}(z),$$

$$f_{z,3,8}(z) = f_{z,3,9}(z) = f_{z,3,10}(z),$$

$$f_{z,3,11}(z) = f_{z,3,12}(z) = f_{z,3,13}(z),$$

$$f_{z,3,14}(z) = f_{z,3,15}(z) = f_{z,3,16}(z) = f_{z,3,17}(z) = f_{z,3,18}(z) = f_{z,3,19}(z).$$

The full form of u_z is hence

$$\begin{aligned} u_z(x,y,z) =& \varepsilon \sum_{n=1}^{3} f_{z,1,n}(z)\cos(\mathbf{k}_n^{(1)}\cdot\mathbf{x}) + \varepsilon^2 \sum_{n=1}^{10} f_{z,2,n}(z)\cos(\mathbf{k}_n^{(2)}\cdot\mathbf{x}) \\ &+ \varepsilon^3 \sum_{n=1}^{19} f_{z,3,n}(z)\cos(\mathbf{k}_n^{(3)}\cdot\mathbf{x}) \end{aligned} \tag{4.69}$$

The displacement field u_x and u_y are more difficult to construct than the square pattern case as there is no x–y symmetry. The rotational symmetry that transforms u_x into u_y is no longer

valid. However, the general form similar to (4.67) and (4.68) can still be used:

$$\begin{aligned} u_x(x,y,z) =& \varepsilon \sum_{n=1}^{3} f_{x,1,n}(z)\sin(\mathbf{k}_n^{(1)}\cdot\mathbf{x}) + \varepsilon^2 \sum_{n=1}^{10} f_{x,2,n}(z)\sin(\mathbf{k}_n^{(2)}\cdot\mathbf{x}) \\ &+ \varepsilon^3 \sum_{n=1}^{19} f_{x,3,n}(z)\sin(\mathbf{k}_n^{(3)}\cdot\mathbf{x}) \end{aligned} \tag{4.70}$$

$$\begin{aligned} u_y(x,y,z) =& \varepsilon \sum_{n=1}^{3} f_{y,1,n}(z)\sin(\mathbf{k}_n^{(1)}\cdot\mathbf{x}) + \varepsilon^2 \sum_{n=1}^{10} f_{y,2,n}(z)\sin(\mathbf{k}_n^{(2)}\cdot\mathbf{x}) \\ &+ \varepsilon^3 \sum_{n=1}^{19} f_{y,3,n}(z)\sin(\mathbf{k}_n^{(3)}\cdot\mathbf{x}) \end{aligned} \tag{4.71}$$

We cannot have x or y independent components for u_x and u_y so $f_{x,2,1}(z) = f_{x,3,1}(z) = f_{y,2,1}(z) = f_{y,3,1}(z) = 0$. The x-axis reflection symmetry grants the following relations for u_x:

$$f_{x,1,2}(z) = -f_{x,1,3}(z), \quad f_{x,2,3}(z) = -f_{x,2,4}(z), \quad f_{x,2,6}(z) = -f_{x,2,7}(z),$$

$$f_{x,2,8}(z) = f_{x,2,10}(z), \quad f_{x,2,9}(z) = 0, \quad f_{x,3,3}(z) = -f_{x,3,4}(z),$$

$$f_{x,3,6}(z) = -f_{x,3,7}(z), \quad f_{x,3,9}(z) = -f_{x,3,10}(z),$$

$$f_{x,3,11}(z) = f_{x,3,13}(z), \quad f_{x,3,12}(z) = 0, \quad f_{x,3,14}(z) = f_{x,3,16}(z),$$

$$f_{x,3,15}(z) = -f_{x,3,19}(z), \quad f_{x,3,16}(z) = -f_{x,3,18}(z),$$

and the y-axis reflection symmetry grants the following relations for u_y:

$$f_{y,1,1}(z) = f_{y,2,2}(z) = f_{y,2,5}(z) = f_{y,3,2}(z) = f_{y,3,5}(z) = f_{y,3,8}(z) = 0,$$

$$f_{y,1,2}(z) = f_{y,1,3}(z), \quad f_{y,2,3}(z) = f_{y,2,4}(z), \quad f_{y,2,6}(z) = f_{y,2,7}(z),$$

$$f_{y,2,8}(z) = -f_{y,2,10}(z), \quad f_{y,3,3}(z) = f_{y,3,4}(z), \quad f_{y,3,6}(z) = f_{y,3,7}(z),$$

$$f_{y,3,9}(z) = f_{y,3,10}(z), f_{y,3,11}(z) = -f_{y,3,13}(z), f_{y,3,14}(z) = -f_{y,3,17}(z)$$

$$f_{y,3,15}(z) = f_{y,3,19}(z), \quad f_{y,3,16}(z) = f_{y,3,18}(z).$$

To find relations between these functions, we can use the rotational symmetry of the displacement field $\mathbf{u} = (u_x, u_y, u_z)$. The field is invariant under a 60-degree rotation around $\hat{\mathbf{z}}$ with $x \to x_1, x_1 \to x_2, x_2 \to -x$ transformation. At first order, working in the x–y basis, we

must have

$$\begin{pmatrix} 1/2 & -\sqrt{3}/2 \\ \\ \sqrt{3}/2 & 1/2 \end{pmatrix} \begin{pmatrix} f_{x,1,1}(z)\sin(kx_1)+ \\ f_{x,1,2}((z)(\sin(kx_2)+\sin(kx)) \\ \\ f_{y,1,2}(z)(\sin(kx_2)-\sin(kx)) \end{pmatrix} = \begin{pmatrix} f_{x,1,1}(z)\sin(kx)+ \\ f_{x,1,2}(\sin(kx_1)-\sin(kx_2)) \\ \\ f_{y,1,2}(z)(\sin(kx_1)+\sin(kx2)) \end{pmatrix}. \tag{4.72}$$

Solving the equations give us

$$f_{x,1,1}(z) = 2f_{x,1,2}(z) = \frac{2f_{y,1,2}(z)}{\sqrt{3}}.$$

Using this principle for the higher order components, we obtain:

$$f_{x,2,2}(z) = 2f_{x,2,3}(z) = \frac{2f_{y,2,3}(z)}{\sqrt{3}},$$

$$f_{x,2,5}(z) = 2f_{x,2,6}(z) = \frac{2f_{y,2,6}(z)}{\sqrt{3}},$$

$$f_{x,2,8}(z) = \sqrt{3}f_{y,2,8}(z) = \frac{\sqrt{3}f_{y,2,9}(z)}{2},$$

$$f_{x,3,2}(z) = 2f_{x,3,3}(z) = \frac{2f_{y,3,3}(z)}{\sqrt{3}},$$

$$f_{x,3,5}(z) = 2f_{x,3,6}(z) = \frac{2f_{y,3,6}(z)}{\sqrt{3}},$$

$$f_{x,3,8}(z) = 2f_{x,3,9}(z) = \frac{2f_{y,3,9}(z)}{\sqrt{3}},$$

$$f_{x,3,11}(z) = \sqrt{3}f_{y,3,11}(z) = \frac{\sqrt{3}f_{y,3,12}(z)}{2}.$$

As for the square pattern, we substitute these forms into the energy/equations, and find a complete third order solution in the same manner as for stripes and squares. We summarize the energy coefficient C_3 and C_4 in Figs 4.6A and B. In this case, the coefficient C_3 does not vanish, but is positive for all η, leading us to conclude that the hexagonal instability is subcritical and will produce patterns of hexagonal dents, as previously observed in experiment. The coefficient C_4 is similar in magnitude to that for the stripe patterns, and changes sign from positive to negative at $\eta = 0.95$, but since the instability is already subcritical this is of little consequence.

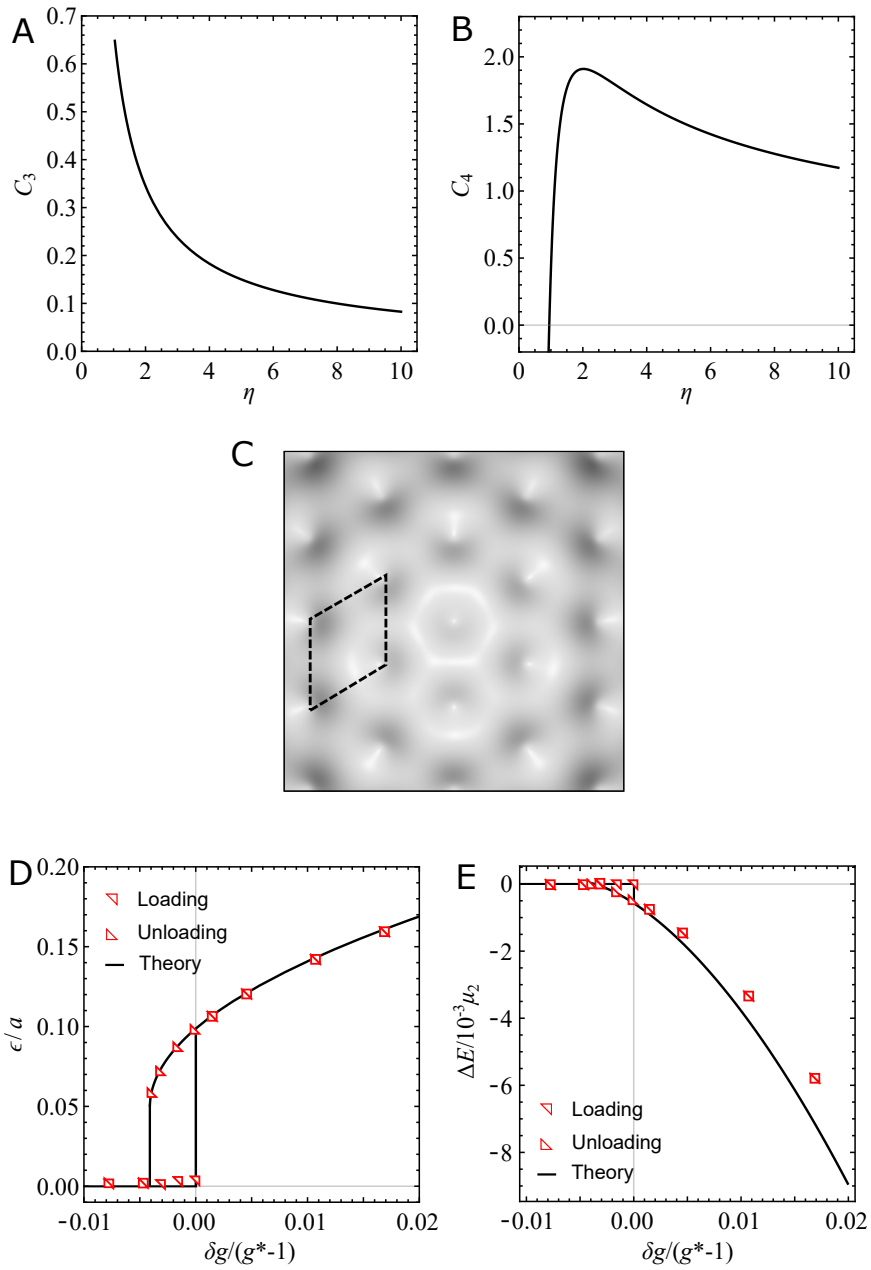

Fig. 4.6 (A) The energy coefficient C_4. (B) Numerical simulated pattern at $g = 1.18$ for $\eta = 3$. Dashed lines show a simulation unit cell. (C) Amplitude and (D) energy per slab volume as a function of growth from the threshold, $\delta g = g - g^*$, for hexagonal pattern at $\eta = 3$.

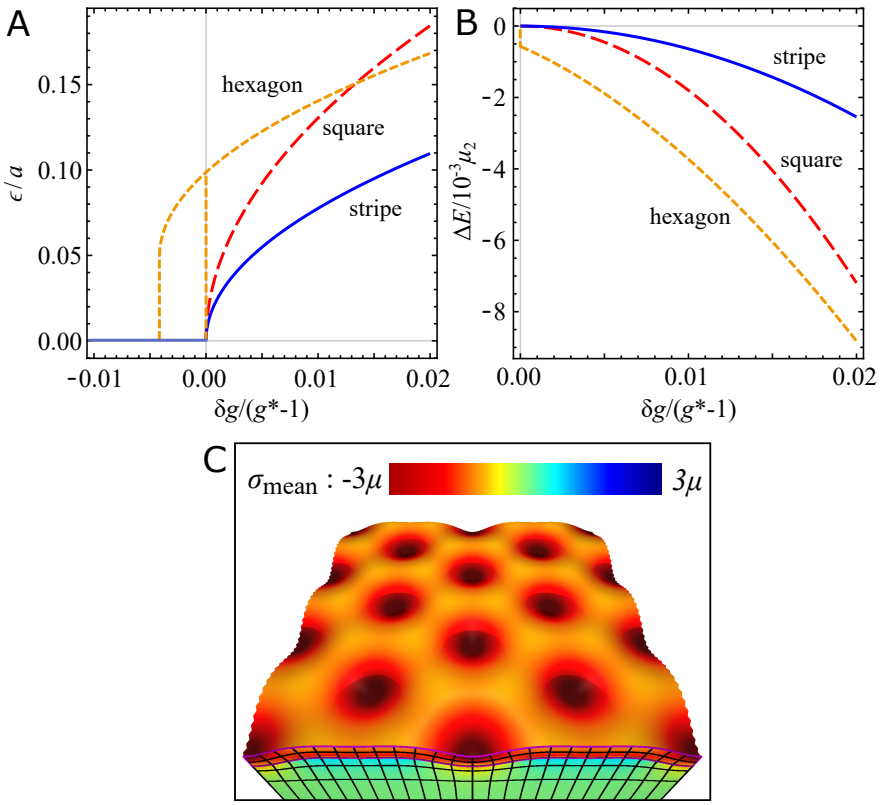

Fig. 4.7 Comparison of the amplitude and energy each pattern: (A) Amplitude and (B) energy per unit volume as a function of growth from the threshold, $g - g^*$, for each pattern at $\eta = 3$. (C) Hexagonal pattern in a large square domain numerical simulation for $\eta = 3$ at $g = 1.24$. The colour scheme denotes the mean hydrostatic stress, $\sigma_{\text{mean}} = (\sigma_{xx} + \sigma_{yy} + \sigma_{zz})/3$.

In the region where $C_3 > 0$ and $C_4 > 0$, we are able to estimate the energy and amplitude after instability, though we emphasize that in this case it is only an estimate, since the subcritical jump produces a non-small amplitude that is beyond the validity of perturbation theory. We again plot these predictions at $\eta = 3$ in Figs 4.6D and E, and compare them to fully non-linear finite element solutions. These finite element calculations confirm that the hexagonal instability is subcritical, and agree with the predicted subcritical amplitude and energy remarkably well.

4.4.8 Summary of instability in a neo-Hookean bilayer

To summarize our results, we compare the predicted amplitude and energy close to the threshold at $\eta = 3$ in Fig. 4.7. As anticipated, the hexagonal pattern is the only subcritical pattern, and thus has the lowest energy close to threshold, in accordance with our earlier symmetry argument. We further verify this conclusion by conducting a final finite element

calculation on a large square domain with periodic boundary conditions, which nevertheless spontaneously produced a hexagonal pattern close to threshold (Fig. 4.7C).

4.5 Compressible neo-Hookean layer/substrate: manipulating C_3

For hexagonal patterns, the sign of C_3 determines whether the pattern forms as bumps or dents, so a key motivation for actually calculating the energy coefficients is to determine this sign. For an incompressible layer on an incompressible substrate, we found in the previous section that C_3 remains positive for all stiffness ratios, leading to patterns of dents. We now look at varying another parameter, the bulk modulus of the system, and show that this allows a sign change for C_3 and hence a change from dents to bumps. More precisely, we consider a system in which both layer and substrate are compressible, with each having same ratio between their bulk and shear modulus, given by $K \equiv \kappa/\mu$. We then perform a series-based energy calculation similar to the previous section but with a compressible version of the neo-Hookean energy density,

$$W = \frac{1}{2}\tilde{\mu}\left[\frac{\mathrm{Tr}B_G}{J^{2/3}} - 3 + K(J-1)^2\right] \tag{4.73}$$

where $J = \mathrm{Det}(F)$ and $B_G = F \cdot G^{-1} \cdot G^{-T} \cdot F^T$. Minimizing this energy with respect to $\mathbf{u}$ gives the same equation of mechanical equilibrium, $\nabla \cdot \sigma = \mathbf{0}$, and the same boundary conditions (4.3–4.4) as before, but with a new compressible PK1 stress tensor:

$$\sigma = \tilde{\mu}\left[\frac{1}{J^{2/3}}\left(B_G - \frac{\mathrm{Tr}B_G}{3}I\right) + KJ(J-1)I\right]F^{-T}. \tag{4.74}$$

However, as we will see in the next section, in the compressible case there is a uniform displacement of the top surface even in the flat state solution, so we must modify the form of the amplitude constraint to:

$$\sqrt{\langle (u_z - \langle u_z \rangle)^2 \rangle|_{z=a}} = |\varepsilon|. \tag{4.75}$$

The total energy, with the Lagrange multiplier term, is thus

$$E = E_{el} + L\left\langle (u_z - \langle u_z \rangle)^2 - \varepsilon^2 \right\rangle\Big|_{z=a}, \tag{4.76}$$

and the modified top-surface stress boundary condition is

$$(\sigma \cdot \hat{\mathbf{z}} + 2L(u_z - \langle u_z \rangle)\hat{\mathbf{z}})|_{z=a} = \mathbf{0}. \tag{4.77}$$

4.5.1 The flat state

As in the incompressible case, we first solve for the flat base state, which must satisfy

$$\nabla \cdot \sigma_0 = \mathbf{0}, \tag{4.78}$$

subjected to the same boundary conditions as the incompressible system. This time $F_0 \neq I$ as the mechanical equilibrium is satisfied by a uniform deformation in the thin layer in response to the growth,

$$\mathbf{u}_0(x,y,z) = (0,0,(\tilde{\gamma}-1)z) \tag{4.79}$$

$$F_0 = \mathrm{diag}(1,1,\tilde{\gamma}), \tag{4.80}$$

where the constant $\tilde{\gamma}$ is just unity in the substrate:

$$\tilde{\gamma} = \begin{cases} \gamma & 0 < z < a, \\ 1 & z < 0. \end{cases} \tag{4.81}$$

The boundary condition at the free surface $\sigma_0 \cdot \hat{\mathbf{z}}|_{z=a} = 0$ grants us

$$(\gamma - 1)K + \frac{2(g^6\gamma^2 - 1)}{3g^2\gamma^{5/3}} = 0, \tag{4.82}$$

which dictates the relationship between γ, g and K. Equation (4.82) cannot be solved analytically for γ, but we can easily evaluate γ numerically for given g and K, as shown in Fig. 4.8, to determine the optimal degree of compression in any given system.

4.5.2 First order perturbation theory

The bulk equation at $O(\varepsilon)$, again, is

$$\nabla \cdot \sigma_1 = \mathbf{0}. \tag{4.83}$$

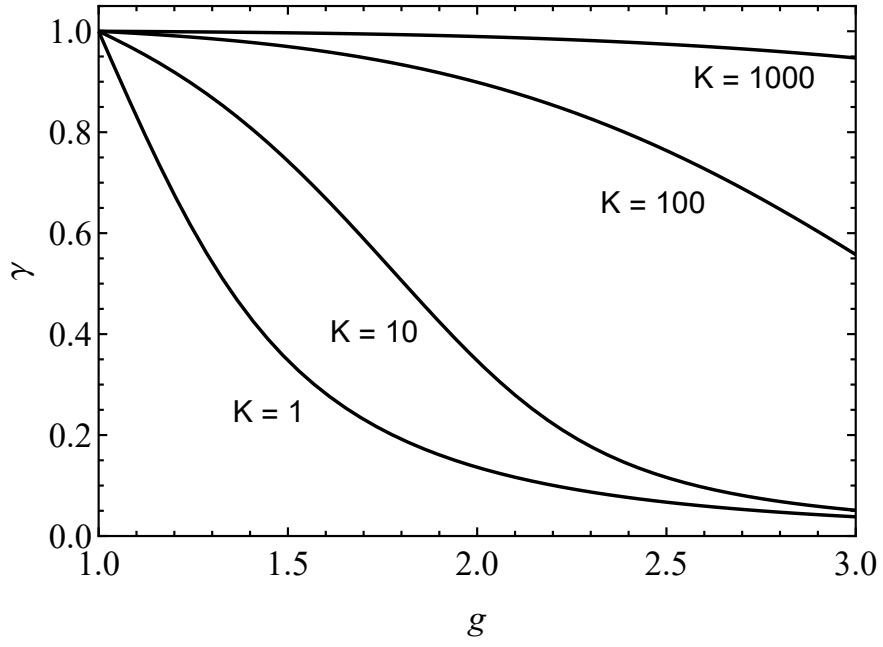

Fig. 4.8 The flat state deformation γ as a function of growth, g, for different bulk modulus to shear modulus ratio, K.

For the stripe pattern (with the same form of $\mathbf{u}_1$ as the incompressible system, (4.37)) the mechanical equilibrium condition gives coupled differential equations for f_x and f_z:

$$k^2 g_1 f_x + k g_2 f_z' - 9\tilde{\gamma}^2 \tilde{g}^6 f_x'' = 0 \tag{4.84}$$

$$9\tilde{\gamma}^2 k^2 f_z - k g_2 f_x' - g_3 f_z'' = 0, \tag{4.85}$$

where the constants $g_1 ... g_4$ are given by:

$$\begin{aligned}
g_1 &= \tilde{\gamma}^2 \left(9K\tilde{\gamma}^{8/3}\tilde{g}^2 + 5\tilde{\gamma}^2\tilde{g}^6 + 7\right), \\
g_2 &= \tilde{\gamma} \left(9K\tilde{\gamma}^{8/3}\tilde{g}^2 - \tilde{g}^6\tilde{\gamma}^2 + 4\right), \\
g_3 &= \left(9K\tilde{\gamma}^{8/3}\tilde{g}^2 + 2\tilde{\gamma}^2\tilde{g}^6 + 10\right), \\
g_4 &= \frac{g_2^2}{9\tilde{\gamma}^2} - \frac{g_1 g_3}{9\tilde{\gamma}^2} - 9\tilde{\gamma}^2\tilde{g}^6 \\
&= 9K\tilde{\gamma}^{14/3} g^8 + 9K\tilde{\gamma}^{8/3}\tilde{g}^2 + \tilde{\gamma}^4\tilde{g}^{12} + 17\tilde{\gamma}^2\tilde{g}^6 + 6.
\end{aligned}$$

As in the incompressible case, uncoupling (4.84) and (4.85) yields a constant-coefficient fourth order differential equation in $f_z(z)$:

$$k^4 g_1 f_z(z) - k^2 g_4 f_z''(z) + g_3 \tilde{g}^6 f_z^{(4)}(z) = 0, \tag{4.86}$$

although the coefficients now have algebraically complex dependence on γ and g, encoded in $g_1 \cdots g_4$.

Solving (4.84) and (4.86) gives the form of the displacement fields:

$$f_z(z) = \begin{cases} A_1 e^{kG_- z} + A_2 e^{-kG_- z} + A_3 e^{kG_+ z} + A_4 e^{-kG_+ z} & 0 < z < a, \\ (B_1 + zB_2) e^{kz} & z < 0. \end{cases} \tag{4.87}$$

$$f_x(z) = \int \frac{9k^2 \tilde{\gamma}^2 f_z(z) - g_3 f_2''(z)}{g_2 k} dz, \tag{4.88}$$

where two more constants $G_\pm = \sqrt{\frac{g_4 \pm \sqrt{g_4^2 - 4 g_1 g_3 g^6}}{2 g_3 g^6}}$ have been introduced. Finally, we look at the boundary conditions at the first order. The normal stress boundary condition is, as before,

$$L_0 = -\frac{\sigma_{1zz}}{2 u_{1z}}. \tag{4.89}$$

The rest of the boundary conditions, which are too large to display here, provide linear equations for the constants of integration in the form $M \cdot (A_1, A_2, A_3, A_4, B_1, B_2) = (\sqrt{2}, 0, 0, 0, 0, 0)$, which can be solved to find the form of the constants. As before, the threshold is found by solving (4.89) with $L_0 = 0$. The result threshold is shown in Fig. 4.9.

4.5.3 Second order perturbation

For the next order in ε, the same analysis is repeated with higher order fields as with the incompressible case. At second order, the mechanical equilibrium must be satisfied

$$\nabla \cdot \sigma_2 = 0. \tag{4.90}$$

At this order, the bulk and the boundary equations become algebraically complicated, making us unable to solve them analytically even with Mathematica. However, the equations are still linear: the complication arises from the increasing complexity of the surds that form the constant coefficients of the different forms, such as the form of $G_\pm$. Thus, if we insert numerical values for the parameters (g, k, η, K), these surds immediately reduce into individual floating-point numbers, and Mathematica is then able to solve the system. We

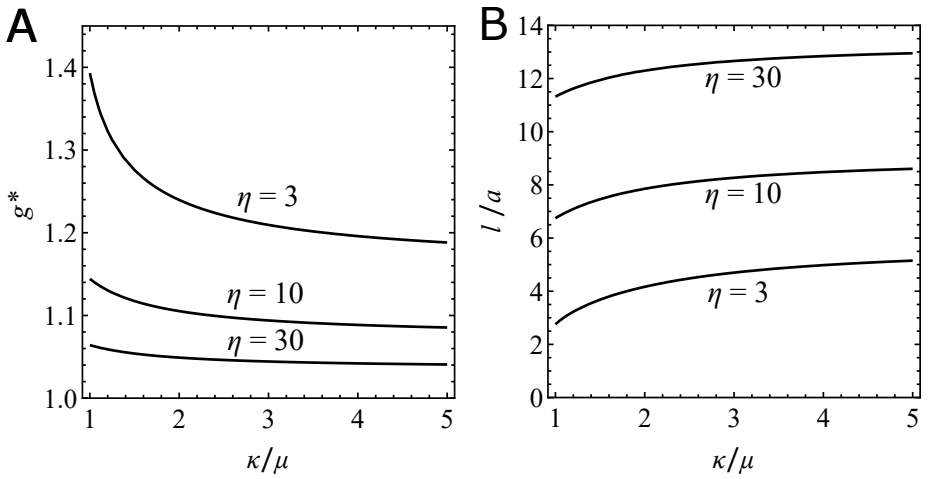

Fig. 4.9 (A) Threshold growth and (B) wavelength for the first unstable mode for compressible solid with modulus ratio $\eta = 3, 10$ and 30 as a function of bulk modulus to shear modulus ratio.

thereby solve the equations at second order for $\eta = 3$ at the threshold growth g^* and use the result to calculate C_3.

Fig. 4.10A shows the analytical calculation of coefficient C_3 as a function of K. The key point is that C_3 changes sign at $K \approx 2.5$ (for $\eta = 3$) and hence the pattern should change from hexagonal bumps at $K > 2.5$ to hexagonal dents at $K < 2.5$. This value of bulk modulus to shear modulus ratio is equivalent to a Poisson ratio of $\sim$0.32, which is a realistic value for many foams, sponges and corks. To confirm this prediction, we conducted many finite element calculations on a large unconstrained domain for systems spanning $K = 2.5$. As shown in Fig. 4.10B the selected pattern changes at $K = 2.5$ as expected. Close to $K = 2.5$, stripe pattern appears instead of hexagon. This is because, as C_3 approaches zero, the hexagonal pattern loses its advantage of being a subcritical instability. For $\eta = 10$ and 30, the sign inversion also appears at slightly different K, suggesting that the sign inversion might be generic. Overall, this calculation reveals the importance and value of actually evaluating C_3 to determine the observed pattern.

4.6 Imposing inversion symmetry

The non-zero value of C_3, and the corresponding subcriticality of the hexagonal patterns, has its origin in the lack of inversion symmetry. To emphasize this, we return to the incompressible model and, finally, consider a growing layer sandwiched between an infinitely deep substrate and a matching superstrate. This system has a full inversion symmetry, so C_3 must vanish, meaning hexagons will no longer be subcritical. In this case, shown in

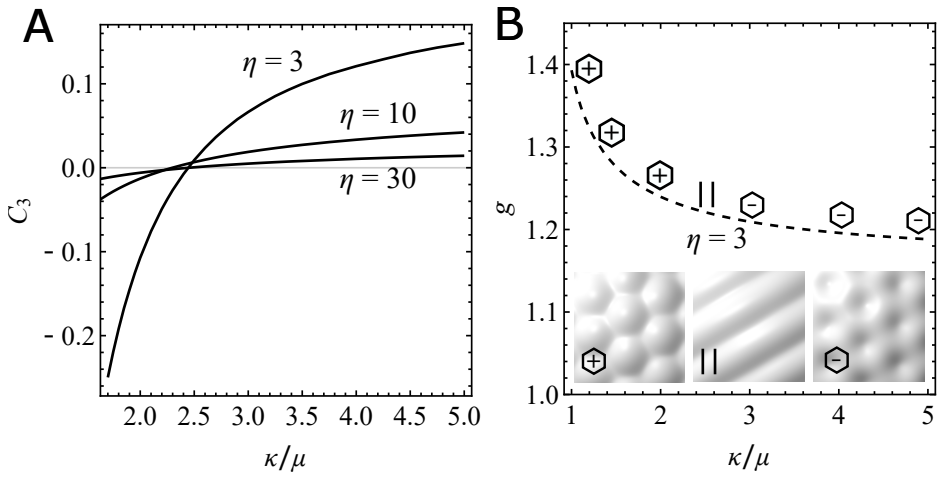

Fig. 4.10 (A) Coefficient C_3 as a function of the bulk modulus to shear modulus ratio, $K = \kappa/\mu$ for $\eta = 3, 10$ and 30. (B) Threshold growth and the patterns closed to the threshold, at $g - g^* = 2.5\% \times (g-1)$, as a function of K. Images taken from $K = 2, 2.5$ and 5 respectively.

Fig. 4.11A, we have:

$$(\tilde{\mu}, \tilde{g}) = \begin{cases} (1,1) & z > a/2, \\ (\eta, g) & -a/2 < z < a/2, \\ (1,1) & z < -a/2. \end{cases}$$

The bulk equations remain the same as in Section 4.4, but the boundary conditions now need to be applied at the top and bottom of the layer, so we now have:

$$\begin{aligned} \boldsymbol{\sigma} \cdot \hat{\mathbf{z}}\big|_{z=\frac{a}{2}^-} &= \boldsymbol{\sigma} \cdot \hat{\mathbf{z}}\big|_{z=\frac{a}{2}^+} \\ \boldsymbol{\sigma} \cdot \hat{\mathbf{z}}\big|_{z=-\frac{a}{2}^-} &= \boldsymbol{\sigma} \cdot \hat{\mathbf{z}}\big|_{z=-\frac{a}{2}^+}, \end{aligned} \tag{4.91}$$

for the stress boundary conditions, while the displacement continuity conditions become

$$\begin{aligned} \mathbf{u}\big|_{z=\frac{a}{2}^-} &= \mathbf{u}\big|_{z=\frac{a}{2}^+}, \\ \mathbf{u}\big|_{z=\frac{a}{2}^-} &= \mathbf{u}\big|_{z=\frac{a}{2}^+}. \end{aligned} \tag{4.92}$$

Finally, we constrain the amplitude on the upper interface between the growing layer and the superstate, in the same way as before:

$$E = E_{el} + L\left\langle u_z^2 - \varepsilon^2 \right\rangle\big|_{z=\frac{a}{2}^-}. \tag{4.93}$$

The constraint is applied at $z = a/2^-$ and thus modifies the stress boundary condition at $z = a/2$:

$$(\boldsymbol{\sigma}\cdot\hat{\mathbf{z}} + 2Lu_z\hat{\mathbf{z}})\big|_{z=\frac{a}{2}^-} = \boldsymbol{\sigma}\cdot\hat{\mathbf{z}}\big|_{z=\frac{a}{2}^+}. \tag{4.94}$$

We can now repeat our analysis up to third order perturbations. At each order, the bulk equations and their solutions have the same form as in the layer/substrate case (as do the energy density expressions $W_2 ... W_4$), except the substrate solution is now repeated in the superstrate. For example, for stripe patterns, the displacement field at $O(\varepsilon)$ becomes:

$$f_z = \begin{cases} e^{-kz}(B_1 + zB_2) & z > -a/2, \\ e^{-kz/g^3}A_1 + e^{kz/g^3}A_2 + e^{-kz}A_3 + e^{kz}A_4 & \\ & -a/2 < z < a/2, \\ e^{kz}(B_3 + zB_4) & z < -a/2. \end{cases} \tag{4.95}$$

However, substituting these fields into the boundary conditions gives different answers for the constants of integration. For example, substituting (4.95) into the boundary conditions give the threshold condition

$$L_0 = \left.\frac{\sigma_{1zz}}{2u_{1z}}\right|_{z=\frac{a}{2}^+} - \left.\frac{\sigma_{1zz}}{2u_{1z}}\right|_{z=\frac{a}{2}^-}, \tag{4.96}$$

as well as linear equations for the constants of integrations of the form $M(A_1, A_2, A_3, A_4, B_1, B_2, B_3, B_4) = (\sqrt{2}, 0, 0, 0, 0, 0, 0, 0)$, where matrix M is given by

$$\begin{pmatrix} e^{-\frac{ka}{2g^3}} & e^{\frac{ka}{2g^3}} & e^{-\frac{ka}{2}} & e^{\frac{ka}{2}} & 0 & 0 & 0 & 0 \\ b\eta e^{-\frac{ka}{2g^3}} & b\eta e^{\frac{ka}{2g^3}} & 2g^6\eta e^{-\frac{ka}{2}} & 2g^6\eta e^{\frac{ka}{2}} & -2g^2e^{-\frac{ka}{2}} & (2/k-a)g^2e^{-\frac{ka}{2}} & 0 & 0 \\ b\eta e^{\frac{ka}{2g^3}} & b\eta e^{-\frac{ka}{2g^3}} & 2g^6\eta e^{\frac{ka}{2}} & 2g^6\eta e^{-\frac{ka}{2}} & 0 & 0 & -2g^2e^{-\frac{ka}{2}} & (a-2/k)g^2e^{-\frac{ka}{2}} \\ -2g^3\eta e^{\frac{ka}{2g^3}} & 2g^3\eta e^{-\frac{ka}{2g^3}} & -b\eta e^{\frac{ka}{2}} & b\eta e^{-\frac{ka}{2}} & 0 & 0 & -2g^2e^{-\frac{ka}{2}} & ag^2e^{-\frac{ka}{2}} \\ e^{-\frac{ka}{2g^3}}/g^3 & -e^{\frac{ka}{2g^3}}/g^3 & e^{-\frac{ka}{2}} & -e^{\frac{ka}{2}} & -e^{-\frac{ka}{2}} & (1/k-a/2)e^{-\frac{ka}{2}} & 0 & 0 \\ e^{-\frac{ka}{2g^3}} & e^{\frac{ka}{2g^3}} & e^{-\frac{ka}{2}} & e^{\frac{ka}{2}} & -e^{-\frac{ka}{2}} & -ae^{-\frac{ka}{2}}/2 & 0 & 0 \\ e^{\frac{ka}{2g^3}}/g^3 & -e^{-\frac{ka}{2g^3}}/g^3 & e^{\frac{ka}{2}} & -e^{-\frac{ka}{2}} & 0 & 0 & e^{-\frac{ka}{2}} & (1/k-a/2)e^{-\frac{ka}{2}} \\ e^{\frac{ka}{2g^3}} & e^{-\frac{ka}{2g^3}} & e^{\frac{ka}{2}} & e^{-\frac{ka}{2}} & 0 & 0 & -e^{-\frac{ka}{2}} & ae^{-\frac{ka}{2}}/2 \end{pmatrix}. \tag{4.97}$$

The threshold is again found by solving $L_0 = 0$, and the resulting threshold and wavelength of the first unstable mode are summarized in Figs 4.11B and C. By solving for the constants of integration, we can then evaluate E_2 by integrating W_2 over the full space. C_2 can then be obtained as shown in Fig. 4.11D.

Repeating the analysis at the higher orders, we can determine the coefficients C_3 and C_4. As anticipated, the coefficient C_3 evaluates to zero even for hexagons. C_4 is plotted as a function of η for all patterns in Fig. 4.11E. In the sandwiched system, squares have

the smallest value of C_4 for $\eta \gtrsim 2$, indicating that squares are the lowest energy pattern close to threshold. However, we note that the differences in C_4 are rather small, so this conclusion may become inaccurate quite shortly beyond threshold. In the opposite range, $\eta \lesssim 2$, the stripe becomes the optimum pattern instead. Finite elements analysis on a single-wavelength square domain verifies the amplitude and energy prediction for square patterns and the supercritical nature of the instability (Figs 4.11F and G). Without prescribing any symmetries, finite elements on a large square domain correctly select squares at $\eta = 10$ (Fig. 4.11H). As indicated in Fig. 4.11B, repeating these simulations at smaller values of η confirms the transition to stripe morphologies, in good agreement with the analytic theory.

4.7 Numerical analysis

Our numerical analysis uses an explicit finite element method to simulate the system (Chapter 2). The simulations were done in a unit cell, with the dimension $L_x \times L_y$ that can produce each pattern; rectangular cells for stripes and squares, and a 60°-rhomboid cell for hexagons. The periodic boundary conditions were applied in the x and y directions. The growing layer and the substrate have thickness of L_z and L_s. The corresponding number of mesh elements are given by n_x, n_y, n_z and n_s. The substrate mesh elements are coarsened in the z-direction as they are further away from the growing layer by 19.2% per element. The system used a large bulk modulus of $\kappa = 10^2\mu$ to simulate incompressibility. For determining the appeared patterns, Figs 4.7C, 4.10B, 4.11B and H were performed on large square domains that can have multiple wavelengths of any patterns. The parameters are summarized in Table 4.1.

Fig.	$L_x \times L_y \times L_z$	L_s	$n_x \times n_y \times n_z$	n_s
4.4	$5.8 \times 1 \times 1$	13.4	$108 \times 16 \times 26$	24
4.5B, E, F	$5.8 \times 5.8 \times 1$			
4.5C, D	$4.4 \times 4.4 \times 1$	13.4	$108 \times 108 \times 26$	24
4.5G, H	$9.1 \times 9.1 \times 1$			
4.6	$6.7 \times 6.7 \times 1$	13.4	$108 \times 108 \times 26$	24
4.7	$20 \times 20 \times 1$	13.4	$96 \times 96 \times 8$	24
4.10	$15 \times 15 \times 1$	13.4	$108 \times 108 \times 26$	24
4.11F, G	$7.1 \times 7.1 \times 1$	13.4	$60 \times 60 \times 8$	24
4.11H	$28 \times 28 \times 1$	13.4	$150 \times 150 \times 8$	24

Table 4.1 The parameters used in the numerical analysis for the soft layer buckling instability.

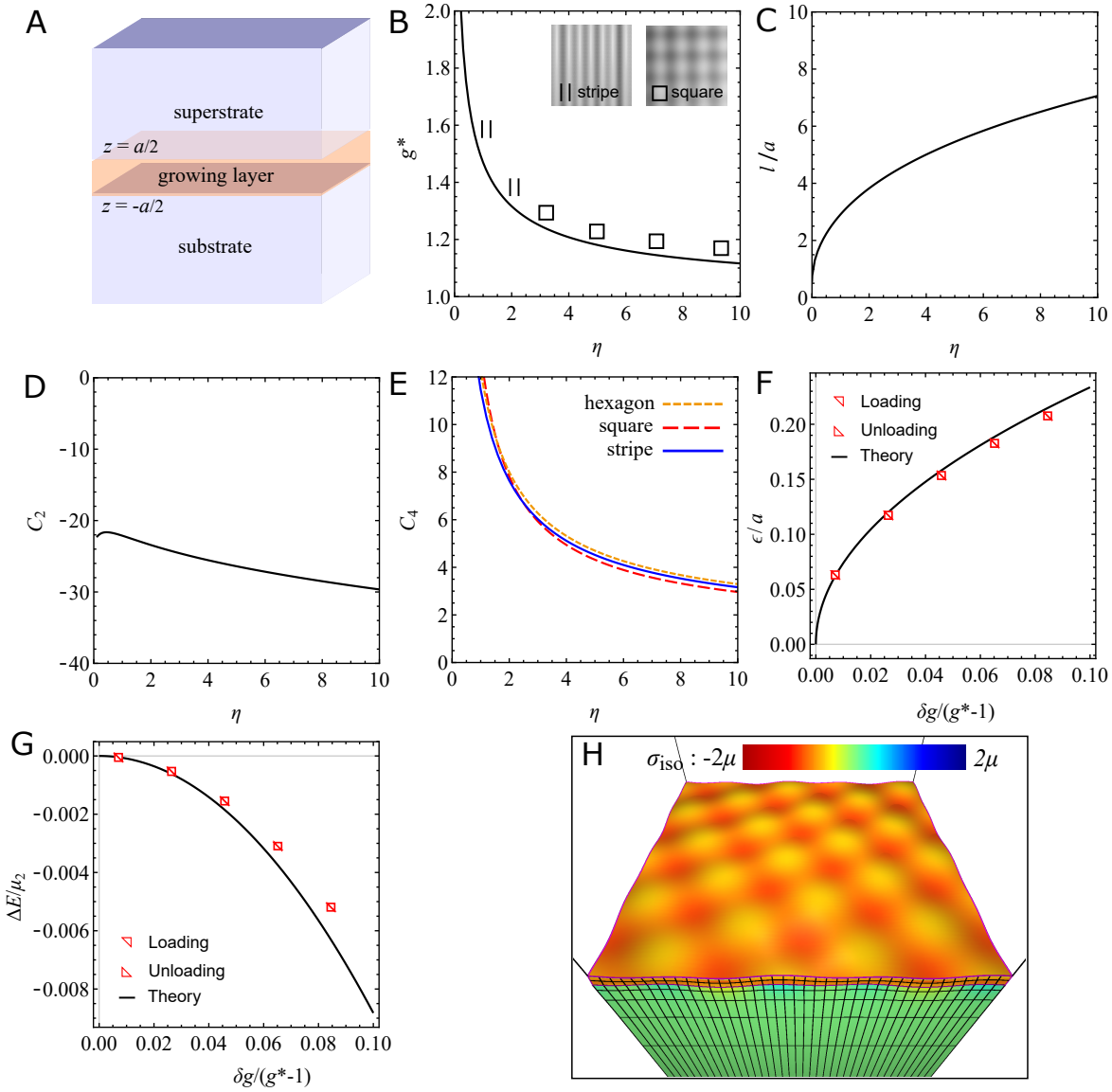

Fig. 4.11 (A) Schematic diagram for the sandwiched layer system. (B) Threshold growth and the patterns closed to the threshold at $g - g^* = 5\% \times (g^* - 1)$. (C) wavelength for the first unstable mode for sandwiched layer. (D) and (E) Energy coefficients C_2 and C_4 as a function of η for a sandwiched layer. (F) and (G) Amplitude and energy as a function of growth from the threshold, $\delta g = g - g^*$ at $\eta = 10$. (H) Square pattern for $\eta = 10$ at $g = 1.123$.

4.8 Discussion and Conclusion

Our ambition in this work has been to understand, theoretically, the hexagonal dent patterns that forms close to threshold in the (equibiaxial) compressive buckling of a stiff layer on a soft substrate. Our method essentially mirrors that introduced by Koiter [113] to study the buckling patterns in shells: in short, we use higher order perturbation theory to construct elastic solutions corresponding to patterns with different symmetry, and predict the pattern with the lowest elastic energy. Our approach differs from previous work on layer/substrate buckling, which incorrectly predicts square patterns close to threshold [160, 165], because we use a geometrically non-linear elastic model for both the layer and the substrate, leading to an energy which is not invariant under pattern inversion. Our key finding is that this lack of inversion symmetry underpins the formation of hexagonal dents.

To clarify this link between inversion symmetry and hexagonal pattern, we first minimize the elastic energy over patterns with fixed (root-mean-square) amplitude ε, and then minimize over ε. This allows us, between the two steps, to construct a Landau-like series expansion of the elastic energy in ε. In the case of stripe and square patterns, pattern inversion ($\varepsilon \to -\varepsilon$) simply translates the pattern in the $x-y$ plane, so the energy does not change. This limits the Landau expansion to the form $E = E_0 + C_2(g-g^*)\varepsilon^2 + C_4\varepsilon^4 + O(\varepsilon^5)$ and hence produces a supercritical instability. However, for hexagons $\varepsilon \to -\varepsilon$ turns a pattern of bumps into a physically different pattern of dents, allowing a $C_3\varepsilon^3$ term in the energy to persist. The hexagonal transition is thus subcritical, strongly suggesting that hexagonal patterns will be favoured close to threshold.

The above argument has actually been used initially by Jia and Ben Amar [69] to study soft slab that swells while adhered to a rigid foundation: the $\eta \to 0$ limit of our system. In their study, the elastic fields are truncated at first order, but then the energy is expanded to higher order to evaluate the energy coefficients (C_2, C_3, C_4) for each pattern. This approach has the correct symmetry, and correspondingly gives a C_3 term for hexagons. However, since the higher order fields are neglected, the values of C_3 and C_4 are only estimates. Indeed, the calculation yields positive C_4 values for all patterns and hence a prediction of hexagonal patterns, whereas our full high order calculations reveal that (in the $\eta \to 0$ limit) C_4 is negative for all patterns, and hence the optimal pattern cannot be determined. This unusual behaviour is a signature of the non-linear onset of the Biot sulcal/crease instability, which puts it beyond the reach of perturbation theory [74], but we note that finite element calculations reveal that square patterns are favoured close to threshold [76].

A year later, Ciarletta conducted a full higher order treatment of the same $\eta \to 0$ system [169], but with the addition of surface tension. In the low surface-tension limit, Ciarletta finds negative C_4 values in agreement with our work, while in the high-surface tension limit

C_4 becomes positive regularizing the instability. However, Ciarletta does not deploy the above symmetry argument at all, because he believes, in our view mistakenly, that the energy has inversion symmetry, and hence that C_3 is always zero. The resulting expansion is thus unable to distinguish hexagonal dents and bumps, and leads to the conclusion that all patterns are supercritical in the high-surface tension limit (where C_4 is positive) whereas inclusion of C_3 would render the hexagonal pattern subcritical.

Finally, very recently, a high order Koiter method was used by Chakrabarti et al. [182] to analyse pattern formation in solid gravity driven fingering, [62]. These authors conducted a full calculation, and found that $C_3 > 0$, showing that patterns of hexagonal dents will appear subcritically. However, they also find that square patterns are subcritical (i.e. $C_4 < 0$), so the optimal pattern again cannot be formally determined. Fortunately, in this case, finite elements confirm that hexagonal dents are indeed favoured.

These previous studies, and our own on layer-substrate buckling, highlight two general messages. The first is the importance of symmetry in the selection of hexagonal patterns: to get the right answer, one must use a theory with the correct symmetry. The second is the importance of conducting a full higher order series expansion to actually calculate the higher order energy coefficients, rather than simply relying on the symmetry argument to predict hexagons. The value of C_3 determines whether one expects up or down hexagons (illustrated by our finite bulk-modulus case) so its value must be explicitly calculated. Furthermore, the value of C_4 determines whether other patterns are also subcritical, thereby allowing the system to sidestep the symmetry argument altogether. In our case, these full high order calculations have only been possible via computer algebra, but the good match between our results and our finite element calculations (without any fitting parameters) lends credibility to our results.

In the future, our method could also easily be extended to other elastic systems, including finite depth layer/substrate systems, multi-layer systems, and systems with surface tension. It will also be important to consider the high η limit of our fully non-linear theory, to make better contact with the extensive work on plates adhered to linear substrates. Hopefully one can derive a simple effective model for this high stiffness limit, which probably mirrors the previous plate/substrate models, but with some degree of substrate non-linearity. Within such a simplified model, one might succeed in calculating the energy coefficients analytically, rather than resorting to computer algebra. However, as any term that breaks inversion symmetry is likely to lead to hexagonal patterns, there is a real risk of getting the right answer for the wrong reasons, and great care will be needed to identify, self consistently, what non-linear effects should be retained. Within such a model, one might also tackle the

secondary bifurcation to the ubiquitous herringbone patterns found in stiff/soft systems, and address the width of the post-threshold compression window that gives rise to hexagons.

Chapter 5

Pattern formation in gravity driven instability

In the previous section, I have demonstrated how the high order perturbative method can be used to predict the pattern forms by the soft layer wrinkling instability. As the approach is general, it can also be used to find the pattern in other surface elastic instabilities. In this chapter, I will apply the theory to predict the pattern arises in the gravity driven instability, which is the solid analogue to the Rayleigh-Taylor instability in fluids (see Subsection 1.3.5). The instability has been discovered by Mora et al. [62] with experimental observation and linear stability analysis, which predicts the threshold and wavelength of the instability. However, the pattern formation in this instability is still not well understood theoretically. This would be a good chance to verify my method and see whether it can make a correct prediction.

5.1 Non-linear model

First, let us consider an incompressible neo-Hookean soft solid slab with thickness a, density ρ and shear modulus μ are attached below a rigid substrate. The slab is affected by a gravitational field $-g\hat{\mathbf{z}}$ (Fig. 5.1). The energy density of the slab, consisting of the elastic and the gravitational potential energy along with the incompressibility constraint term, can be written as

$$W(F) = \frac{1}{2}\mu\left[\mathrm{Tr}\left(F\cdot F^{T}\right)-3\right]+\rho g(z+u_z)-P\left(\mathrm{Det}(F)-1\right) \quad 0<z<a, \tag{5.1}$$

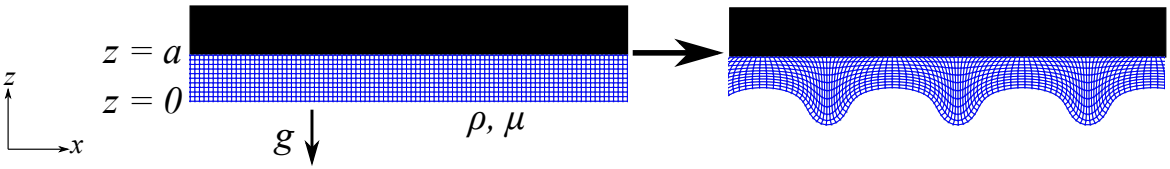

Fig. 5.1 Schematic diagram for the gravity driven instability. The flat state (left) becomes unstable (right) in the presence of gravity.

where u_z is the z-component of the displacement field $\mathbf{u}$ and F is the deformation gradient defined by $F = I + \nabla\mathbf{u}$. As before, the total energy functional is to be minimized with respect to the deformation gradient,

$$E_{el} = \int_0^a \langle W(F) \rangle \, \mathrm{d}z, \tag{5.2}$$

where angle brackets denote an in-plane average. Minimizing the energy gives us

$$\nabla \cdot \sigma - \mu\tilde{\rho}\hat{\mathbf{z}} = 0, \tag{5.3}$$

$$\mathrm{Det}(F) = 1, \tag{5.4}$$

where $\tilde{\rho} = \rho g/\mu$ and σ is the PK1 stress tensor given by,

$$\sigma = \mu F - P\,\mathrm{cof}(F). \tag{5.5}$$

The boundary conditions also need to be satisfied. We require the lower surface to be stress-free and the displacement at $z = a$ needs to be zero:

$$\sigma \cdot \hat{\mathbf{z}}|_{z=0} = \mathbf{0} \quad \text{and} \quad \mathbf{u}|_{z=a} = \mathbf{0}. \tag{5.6}$$

5.2 Series expansion of the energy in the amplitude

As before, we will expand the energy as a function of amplitude ε. The following constraint term is applied:

$$E = E_{el} + L\left\langle u_z^2|_{z=0} - \varepsilon^2 \right\rangle, \tag{5.7}$$

which constrains the root-mean-square amplitude at the bottom ($z = 0$) surface,

$$\sqrt{\langle u_z^2 \rangle|_{z=a}} = |\varepsilon|. \tag{5.8}$$

The boundary condition on the bottom surface is then modified to:

$$(\sigma \cdot \hat{\mathbf{z}} + 2Lu_z\hat{\mathbf{z}})|_{z=0} = \mathbf{0}. \tag{5.9}$$

Expand all the fields in a series expansion in ε:

$$\begin{aligned} \mathbf{u}(x,y,z) &= \sum_{n=1}^{\infty} \varepsilon^n \mathbf{u}_n(x,y,z), \\ P(x,y,z) &= \mu P_0(z) + \sum_{n=1}^{\infty} \varepsilon^n \mu P_n(x,y,z) \\ L &= L_0 + \sum_{n=1}^{\infty} \varepsilon^n L_n. \end{aligned} \tag{5.10}$$

E, F, σ and W can then be expressed in series expansion as in (4.22).

5.3 Pattern formation in an incompressible neo-Hookean layer under gravity

5.3.1 The flat state

At zero order, the bulk equations (5.3, 5.4) are

$$\nabla \cdot \sigma_0 - \mu\tilde{\rho}\hat{\mathbf{z}} = \mathbf{0}, \quad \mathrm{Det}\,(I) = 1, \tag{5.11}$$

with the boundary conditions

$$\sigma_0 \cdot \hat{\mathbf{z}}|_{z=0} = \mathbf{0}, \quad \mathbf{u}_0|_{z=a} = \mathbf{0}. \tag{5.12}$$

Inserting the F expansion into the definition of σ, we see that

$$\sigma_0 = \mu(1 - P_0(z))I. \tag{5.13}$$

The bulk equation then becomes

$$P_0'(z) + \tilde{\rho} = 0, \tag{5.14}$$

which is solved by taking account of the boundary conditions,

$$P_0(z) = 1 - \tilde{\rho}z. \tag{5.15}$$

5.3.2 First order perturbation theory

The calculation here and at higher orders essentially mirror those in Chapter 4. The $O(\varepsilon)$ terms in the bulk equations are:

$$\nabla \cdot \sigma_1 = \mathbf{0}, \qquad \mathrm{Tr}\,(F_1) = \nabla \cdot \mathbf{u}_1 = 0, \tag{5.16}$$

the first order boundary conditions are,

$$\sigma_1 \cdot \hat{\mathbf{z}}|_{z=0} = -2L_0 u_{1z}\,\hat{\mathbf{z}}|_{z=0}\,, \qquad \mathbf{u}_1|_{z=0} = 0, \tag{5.17}$$

and the first order amplitude equation is

$$\left\langle u_{1z}^2 \right\rangle\big|_{z=0} = 1. \tag{5.18}$$

Inserting the expansion for $\mathrm{cof}(F)$ into the general expression for σ, we see that

$$\sigma_1 = \mu\left(F_1 + P_0 F_1^T - P_1 I\right). \tag{5.19}$$

The first order energy coefficient, E_1, is zero as before. To find E_2, we expand W to second order,

$$W_2 = \tfrac{1}{2}\mu\left(\mathrm{Tr}\left(F_1 \cdot F_1^T\right) - P_0 \mathrm{Tr}\left(F_1 \cdot F_1\right)\right).$$

The displacement fields take the same forms as in Chapter 4. For the stripe pattern, the first-order displacement field looks like, as before,

$$\mathbf{u}_1 = \begin{pmatrix} f_x(z)\sin(kx) \\ 0 \\ f_z(z)\cos(kx) \end{pmatrix} \tag{5.20}$$
$$P_1 = f_p(z)\cos(kx).$$

Substituting the field into the bulk equations, the first order incompressibility equation is:

$$k f_x(z) + f_z'(z) = 0, \tag{5.21}$$

and the first order mechanical equilibrium equations are:

$$\begin{aligned} k f_p(z) + f_x''(z) - k^2 f_x(z) + k\tilde{\rho} f_z(z) &= 0, \\ -k\tilde{\rho} f_x(z) + k^2 f_z(z) + f_p'(z) - f_z''(z) &= 0, \end{aligned} \tag{5.22}$$

which can be algebraically solved for f_p and f_x,

$$f_x(z) = -\frac{f_z'(z)}{k}, \tag{5.23}$$

$$f_p(z) = -\tilde{\rho} f_z(z) - f_z'(z) + \frac{f_z'''(z)}{k^2}. \tag{5.24}$$

Substituting these results into the second mechanical equilibrium equation yields a fourth order differential equation for f_z:

$$k^4 f_z(z) - 2k^2 f_z''(z) + \tilde{g}^6 f_z^{(4)}(z) = 0, \tag{5.25}$$

which is solved by the form,

$$f_z(z) = (A_1 + kzA_2)e^{-kz} + (A_3 + kzA_4)e^{kz}, \tag{5.26}$$

where A_i are constants of integration. The values of A_i and L_0 can then be obtained from the boundary conditions (5.17) and (5.18). The normal stress condition on the bottom surface (the z component of (5.17)) is a linear equation for L_0, solved in terms of A_i:

$$L_0 = -\left.\frac{\sigma_{1zz}}{2u_{1z}}\right|_{z=0} = -\frac{\tilde{\rho}}{2} + k\frac{A_1 - A_3}{A_1 + A_3}. \tag{5.27}$$

The remaining four boundary conditions (amplitude, surface shear stress, $2\times$ displacement) are four linear equations, which can be expressed as a matrix equation:

$$M\begin{pmatrix} A_1 \\ A_2 \\ A_3 \\ A_4 \end{pmatrix} = \begin{pmatrix} 1 & 0 & 1 & 0 \\ 1 & -1 & 1 & 1 \\ e^{-ka} & kae^{-ka} & e^{ka} & kae^{ka} \\ -e^{-ka} & e^{-ka}(1-ka) & e^{-ka} & e^{ka}(1+ka) \end{pmatrix}\begin{pmatrix} A_1 \\ A_2 \\ A_3 \\ A_4 \end{pmatrix} = \begin{pmatrix} \sqrt{2} \\ 0 \\ 0 \\ 0 \end{pmatrix}, \tag{5.28}$$

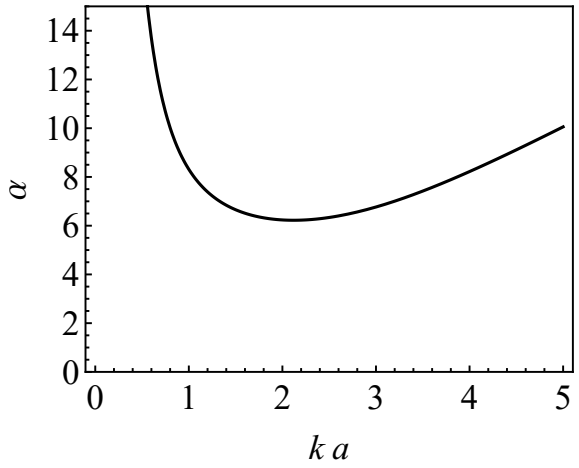

Fig. 5.2 Plot of $\alpha = \rho g a/\mu$ as a function of wavenumber at the threshold of the instability. The minimum of the plot denotes the critical value of α and the critical wavelength.

where the matrix M is the coefficient matrix of (A_1, A_2, A_3, A_4). The constants of integration can be obtained from $(A_1, A_2, A_3, A_4) = M^{-1}(\sqrt{2}, 0, 0, 0)$:

$$
\begin{aligned}
A_1 &= \frac{\sqrt{2}e^{2\tilde{k}}(e^{2\tilde{k}} + 1 - 2\tilde{k} + 2\tilde{k}^2)}{e^{4\tilde{k}} - 4\tilde{k}e^{2\tilde{k}} - 1} \\
A_2 &= \frac{\sqrt{2}e^{2\tilde{k}}(e^{2\tilde{k}} + 1 - 2\tilde{k})}{e^{4\tilde{k}} - 4\tilde{k}e^{2\tilde{k}} - 1} \\
A_3 &= -\frac{\sqrt{2}(1 + e^{2\tilde{k}}(1 + 2\tilde{k} + 2\tilde{k}^2))}{e^{4\tilde{k}} - 4\tilde{k}e^{2\tilde{k}} - 1} \\
A_4 &= \frac{\sqrt{2}(1 + e^{2\tilde{k}}(1 + 2\tilde{k}))}{e^{4\tilde{k}} - 4\tilde{k}e^{2\tilde{k}} - 1},
\end{aligned}
\tag{5.29}
$$

where $\tilde{k} = ka$. The threshold for the instability can be found by setting $L_0 = 0$, which simplifies to the threshold condition:

$$
\alpha = 2ka\left(\frac{\cosh(2ka) + 2(ka)^2 + 1}{\sinh(2ka) - 2ka}\right), \tag{5.30}
$$

where $\alpha = \tilde{\rho} a = \rho g a/\mu$ is the dimensionless parameter that triggers the instability. In Fig. 5.2, the threshold α is plotted as a function of wavenumber. Minimizing α with respect to the wavelength, we obtain the critical value of α at $\alpha^* = 6.223$, which is the minimum value of α that require for the instability, and the corresponding wavenumber $k^* a = 2.12$, corresponding to a wavelength of $2.96a$, which agree with results from [62].

For square and hexagonal patterns, the same analysis can be repeated using the same fields as in the soft layer buckling instability (4.48) and (4.49). The energy E_2 would be the same as they are linear combinations of multiple stripe modes. By substituting the form of A_i into the W_2 and integrate to obtain E_2, using the first unstable mode wavenumber $k = k^*$. As before, the energy is written as a series expansion of amplitude:

$$E = C_2(\alpha - \alpha^*)\varepsilon^2 + C_3\varepsilon^3 + C_4\varepsilon^4 + O(\varepsilon^5). \tag{5.31}$$

We can then calculate the coefficient C_2 as before:

$$C_2 = \left.\frac{\partial E_2}{\partial \alpha}\right|_{\alpha=\alpha*} = -\frac{1}{2}\mu, \tag{5.32}$$

which is a negative value as we expected. We can then proceed to the second and third order as in the soft layer buckling instability. The bulk and boundary equations at these orders are the same as in Section 4.4.

5.3.3 Second order perturbation theory

At second order, the bulk equations are

$$\nabla \cdot \sigma_2 = \mathbf{0}, \qquad \mathrm{Tr}\,(F_2) = \tfrac{1}{2}\mathrm{Tr}\left(F_1^2\right), \tag{5.33}$$

and the boundary conditions are

$$\begin{aligned} \sigma_2 \cdot \hat{\mathbf{z}}|_{z=0} &= -2\,(L_1 u_{1z} + L_0 u_{2z})\hat{\mathbf{z}}|_{z=0}\,, \\ \mathbf{u}_2|_{z=a} &= 0, \\ \langle u_{1z} u_{2z}\rangle|_{z=0} &= 0, \end{aligned} \tag{5.34}$$

where the second correction in the PK1 stress, σ_2, is

$$\sigma_2 = \mu\left(F_2 - P_2 I + P_1 F_1^T + P_0\left(F_2^T - F_1^T \cdot F_1^T\right)\right). \tag{5.35}$$

By solving these equations for $\mathbf{u}_2$, P_2 and L_1, the third order energy density coefficient can then be evaluated,

$$W_3 = \mu\left(\mathrm{Tr}\left(F_1 \cdot F_2^T\right) - P_0\left(\tfrac{1}{3}\mathrm{Tr}\left(F_1^3\right) - \mathrm{Tr}\,(F_1 \cdot F_2)\right)\right)$$

to find the coefficient C_3.

5.3.4 Third order perturbation theory

Similarly, at third order, the bulk equations are

$$\nabla \cdot \sigma_3 = \mathbf{0}, \qquad \mathrm{Tr}\,(F_3) = \mathrm{Tr}\,(F_1 F_2) - \tfrac{1}{3}\mathrm{Tr}\left(F_1^3\right), \tag{5.36}$$

and the boundary equations are

$$\sigma_3 \cdot \hat{\mathbf{z}}\big|_{z=0} = -2\left(L_2 u_{1z} + L_1 u_{2z} + L_0 u_{3z}\right)\hat{\mathbf{z}}\big|_{z=0}, \tag{5.37}$$

$$\mathbf{u}_3\big|_{z=a} = 0, \tag{5.38}$$

$$\left\langle u_{1z} u_{3z} + \tfrac{1}{2} u_{2z}^2 \right\rangle\big|_{z=0} = 0$$

where the expression of σ_3 is

$$\begin{aligned}\sigma_3 = \mu\Big(&F_3 - P_3 I + P_2 F_1^T + P_1\left(F_2^T - F_1^T F_1^T\right)\\ &+P_0\left(\tfrac{1}{3}\mathrm{Tr}\left(F_1^3\right) I + F_3^T + F_1^T \mathrm{Tr}\,(F_2) - F_2^T F_1^T - F_1^T F_2^T\right)\Big).\end{aligned} \tag{5.39}$$

We can integrate the fourth order energy density coefficient,

$$W_4 = \mu\left[\mathrm{Tr}\left(\tfrac{1}{2}F_2 F_2^T + F_1 F_3^T\right) - P_0\left(\mathrm{Tr}\left(F_1^2 F_2\right) - \mathrm{Tr}\,(F_1 F_3) - \tfrac{1}{2}\left(\mathrm{Tr}\,(F_2)^2 + \mathrm{Tr}\left(F_2^2\right)\right)\right)\right]$$

to find the coefficient C_4. The coefficients will depend on the pattern. In the next subsection, I will summarize these coefficients and the instability behaviour for each pattern.

5.3.5 Stripe pattern results

The form of displacement fields at higher order is identical to those in the buckling soft instability. The bulk and boundary equations are then again solved using these fields via Mathematica's [174] `DSolve` and `Solve` commands. The energy coefficients C_3 and C_4 near the threshold can then be obtained:

$$C_3 = 0, \qquad C_4 = 0.225\mu. \tag{5.40}$$

This means the system is supercritical under the stripe pattern. Nonetheless, in order to calculate a more accurate post-buckling amplitude, we can expand the coefficient further from the threshold as function of $\delta\alpha$, with $\delta\alpha = \alpha - \alpha^*$. This is not entirely accurate beyond threshold as we still have to use the critical wavenumber at threshold for the calculation, k^*, which might not be the optimal wavelength away from threshold. In addition, we expand

the energy series further to $O(\varepsilon^6)$. The calculation is straight forward for stripe pattern but requires more algebraic power, so the details will be omitted. The coefficients for stripe patterns are summarized here:

$$\begin{aligned} C_2/\mu &= -0.5 \\ C_4/\mu &= 0.225 - 0.457\delta\alpha + O(\delta\alpha^2) \\ C_6/\mu &= 8.421 + 0.645\delta\alpha + O(\delta\alpha^2). \end{aligned} \tag{5.41}$$

The amplitude and energy are then found by minimizing the energy series. To verify the prediction, a finite element analysis is performed to compare the amplitude and the energy of the instability with our calculation. The stripe pattern can be captured by simulating the system in two dimensions. Here, we use a periodic boundary condition with a domain size equal to the threshold critical wavelength, which should fit well with the coefficient expansion in $\delta\alpha$. The numerical results are shown in Fig. 5.3. The amplitude plot (Fig. 5.3B) shows that the instability is supercritical as we predicted.

5.3.6 Square and hexagonal pattern results

Again, the same form of displacement fields from soft buckling instability can be reused here. The coefficients C_3 and C_4 (at $\delta\alpha = 0$) can then be evaluated:

$$C_3/\mu = \begin{cases} 0 & \text{for square} \\ -0.649 & \text{for hexagonal,} \end{cases} \tag{5.42}$$

$$C_4/\mu = \begin{cases} -4.323 & \text{for square} \\ -0.141 & \text{for hexagonal.} \end{cases} \tag{5.43}$$

This suggests subcriticality for both the square and hexagonal patterns. Furthermore, this implies that the stripe, which is supercritical, is less favourable than the other two with subcritical instabilities. Our calculation is insufficient to determine whether the square or the hexagonal pattern is more energetically favourable since the C_4 coefficients are negative and prevent us to even estimate the post-threshold amplitudes. Calculating the next order energy coefficient is difficult for the square and hexagonal patterns as it involves solving a numerous number of differential equations. Nonetheless, the negative sign of C_3 suggest to us that hexagonal pattern might favour positive amplitude (hexagonal dents) as observed by [62].

To investigate whether the square or the hexagonal pattern is more favourable and to verify our prediction on the subcriticality of the instability, we perform a finite element analysis.

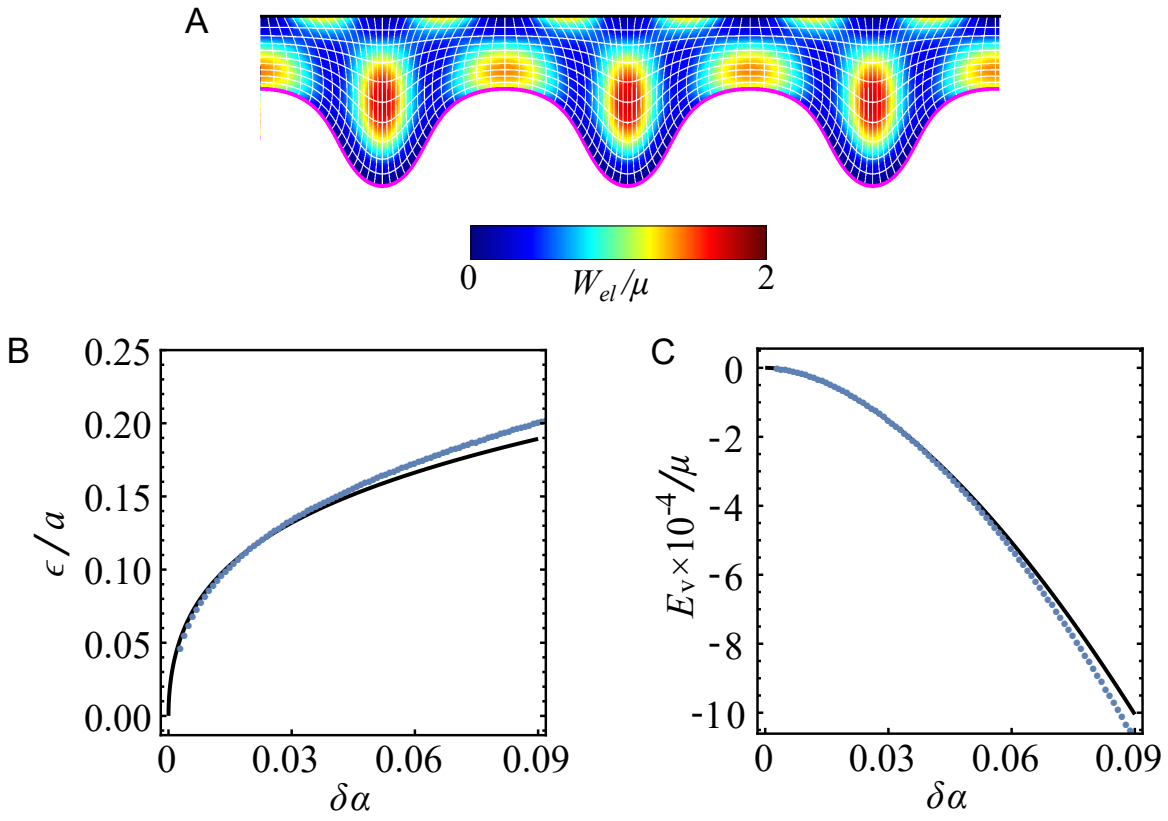

Fig. 5.3 Numerical results for the gravity driven in two dimensions. (A) The deformed lattice. Colour indicates elastic potential energy density. (B) root-mean-square amplitude of the instability as a function of $\delta\alpha = \alpha - \alpha^*$. (C) Energy associated with the instability per unit volume as a function of α. Dots are numerical results. Solid line is the theoretical prediction.

The subcriticality can be identified from the hysteresis loops in the loading-unloading curves, which are a signature of subcritical instabilities. Furthermore, the energy of the instabilities could also be obtained from the simulation, which can be used to observe the jump in the energy for subcritical instabilities.

As the parameter α exceeds the threshold, a pattern with hexagonal dents is formed (Fig. 5.4A) in a large-domain numerical simulation, as we expected. We can also investigate the stripe and square patterns by using appropriate unit cells for the simulation domain. Figs 5.4B and C shows the stripe and square patterns obtained from the simulation. Fig. 5.5 shows plots of amplitude and average energy per unit volume for each pattern against the parameter α from the numerical analysis. Fig. 5.5A consists of loading and unloading curves. For the stripe pattern, the amplitude increases continuously from the threshold and the loading and unloading curves are on top of each other, indicating that the instability is supercritical. On the other hand, square and hexagon patterns exhibit hysteresis loops. The

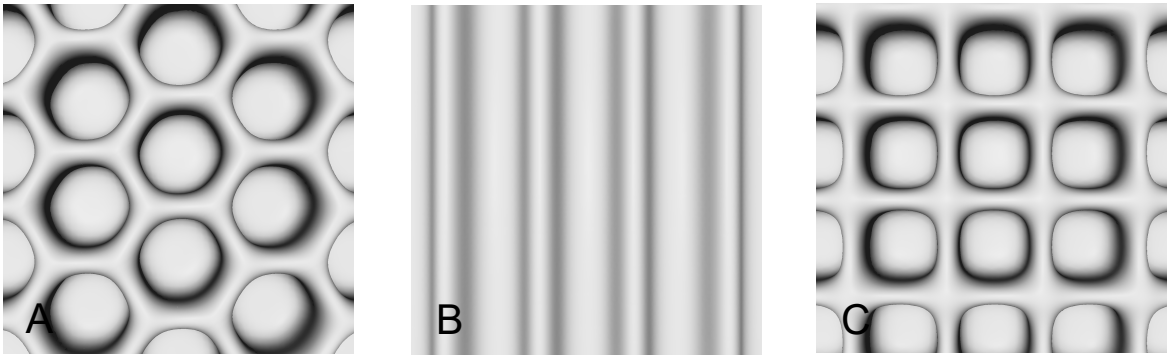

Fig. 5.4 Numerical results for the gravity driven instability with different patterns. The unit cells were repeated to show many wavelengths of the patterns: (A) hexagon, (B) stripe and (C) square. (B) and (C) are simulated using unit cells that constraint the symmetry of the pattern.

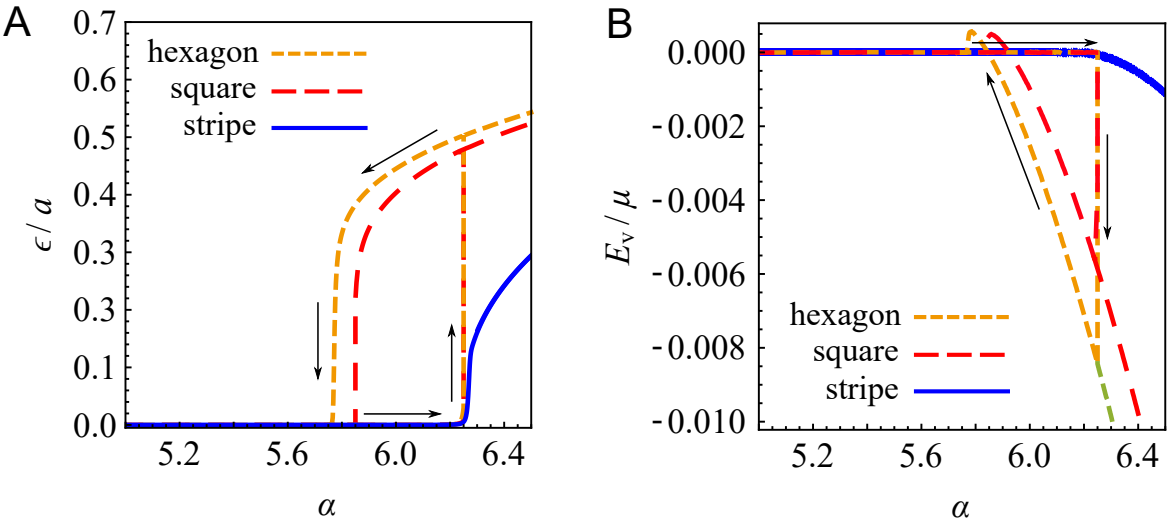

Fig. 5.5 Hysteresis loops of the loading-unloading curve for gravity driven instability with stripe, square and hexagonal patterns. (A) Amplitude and (B) energy change from the non-perturbed state.

unloading curves go to zero amplitude (flat state) at α lower than α^*. There are big jumps in the amplitude for both cases, suggesting that the instability is strongly subcritical for both cases. Fig. 5.5B also shows jumps in the energy for square and hexagon but not for stripe. The energy drop for hexagon pattern is the greatest and hence is indeed favourable.

5.4 Numerical analysis

The simulations were done in a unit cell, with the dimension $L_x \times L_y \times L_z$ with the number of mesh elements $n_x \times n_y \times n_z$. The parameters used in finite element analysis are summarized in Table 5.1. The system used a large bulk modulus of κ to simulate incompressibility. I have used a large bulk modulus in a two-dimensional simulation to improve the accuracy for plotting the amplitude and energy in Fig. 5.3. The other figures are generated with three-dimensional simulations which are slower to run. Hence, a smaller but sufficient value bulk modulus is used for these figures.

5.5 Discussion and Conclusion

Here, we have shown that our method can also be used for gravity driven instability, agreeing with our claim that the method is general to any elastic instabilities in soft solids. We predict the supercriticality in the two-dimensional system, where the stripe is the only possible pattern, which is verified by our numerical results. However, due to non-linearity of the problem, we were not able to make a decisive prediction on the pattern formed with our theory in three-dimensional system. Nevertheless, our numerical result made a good agreement with the theory that subcriticality of hexagonal pattern is the strongest and makes it the emergent pattern as well as correctly predict the sign of the hexagons.

Only recently (December 2018) Chakrabarti et al. [182] use a similar perturbative method to study the pattern selection in this system. They show that the stripe is supercritical, whereas square and hexagon are subcritical, with hexagonal dents being the energetically favourable pattern, which agrees perfectly with our calculation. This clearly suggests that

Fig.	$L_x \times L_y \times L_z$	$n_x \times n_y \times n_z$	κ/μ
5.3	$3 \times 0 \times 1$	$240 \times 0 \times 80$	10^4
5.4A	$10 \times 10 \times 1$	$60 \times 60 \times 10$	10^2
5.4B, C	$2.96 \times 2.96 \times 1$	$25 \times 25 \times 10$	10^2
5.5	$2.96 \times 2.96 \times 1$	$50 \times 50 \times 20$	10^2

Table 5.1 The parameters used in the numerical analysis for the gravity driven instability.

our and their methods are equivalent. Like us, they were not able to calculate the instability amplitude for the subcritical square and hexagonal patterns. For the hexagon, they only calculate C_3, which tells them the sign of the hexagonal pattern but not C_4, although C_4 does not provide information on the amplitude as it is negative.

An obvious further step in this case would be to calculate the next order coefficient C_5 and C_6 for square and hexagonal patterns to predict the post-buckling amplitude and see whether the calculation can tell which one has lower energy. It would also be interesting to see whether we could change the pattern in the gravity driven instability. We could try inverting the sign of C_3, as in the case of soft layer buckling instability, by changing the bulk modulus. However, as gravity already breaks the inversion symmetry in the energy, simply sandwiching the layer does not impose the symmetry. Nonetheless, it will alter the coefficients which could change the pattern of the instability.

Chapter 6

Manipulating wrinkling patterns with Bravais lattice of holes

As seen in Chapter 4, an elastic solid bilayer system with a stiff skin layer forms surface wrinkles to release in-plane compression of the stiff layer. Most studies on this wrinkling instability consider a homogeneous surface system, where wrinkling and its further bifurcation occurs as global events over the entire surface, with a single pattern. The pattern can be the hexagonal pattern for equibiaxial stress, stripe pattern for non-equibiaxial stress or herringbone pattern for stress beyond threshold. However, there remains much to be explored about the control of instability morphology, and in particular how to configure instabilities, such as wrinkling and creasing, to desired patterns with selective distribution covering the surface and bespoke thresholds for the formation and evolution of instabilities. In this chapter, I investigate a method of inducing wrinkling patterns by explicitly patterning the surface, paving a way to manipulate the instability morphologies to create various different patterns which can be easily controlled. This is a collaborative work with D. Wang et al. [142], for which I contribute the theoretical analysis (Section 6.2).

We see that the ability to control the formation and development of wrinkling patterns is highly desirable for engineering applications such as strain sensing structures, actuating units in wearable devices, healthcare devices and bio-fluidic devices. A simple strategy is to employ structural confinement, by introducing a Bravais lattice of holes, to regulate the in-plane stress map on the surface. The term Bravais lattice refers to an infinite array of discrete points generated by a set of discrete translation operations [183], commonly used to describe crystal structures in crystallography. In our context, these discrete points are the holes. The localization of stress due to confinement nucleates the wrinkling network from the edges of Bravais lattice holes, forming unique patterns that can be controlled by the geometry of the lattice. At higher compression, the stress localisation also generates a

localized wrinkle-crease transition before developing into global creasing. Experiments and numerical analysis are combined to analyse the induced in-plane stress and the morphology of the wrinkling pattern under the confinement.

6.1 Experiment

The Bravais lattice template was prepared by lithographically fabricating SU-8 pillars on a silicon wafer (Fig. 6.1a). The Bravais pattern was then transferred to a soft substrate by coating the template with a thin (125 μm) layer of softer polydimethylsiloxane (PDMS), with a shear modulus ≈ 0.1 MPa, which was then cured on a substantially pre-stretched elastic "mounting" base layer (thickness ≈ 3 mm, shear modulus ≈ 0.35 MPa). After curing, the PDMS structure was released from the template, aided by a salinization treatment applied to the template to reduce surface adhesion. Under compression, patterned surfaces composed of polygonal shapes, i.e., triangles, squares, etc., can yield strain energy concentrations and localized bulk deformations around their corners, making it difficult to reach the energy threshold to trigger the surface instability over the bulk surface. Therefore, patterned surfaces with circular (hole) shapes were used to avoid strain energy localization and also expected that the holes can be used to regulate the formation of instabilities. Two different Bravais lattices (Figs 6.1b–e), square and centred square, were employed with varied geometrical aspect ratios, hole diameter (Φ), hole distance (D), hole depth (h), to establish a range of patterned soft surfaces. Finally, oxygen plasma treatment was used to create a thin stiff layer on the patterned soft substrate (Fig. 6.1f) prior to the compression.

Upon subsequent release of the mounting layer from a pre-stretched length L_0 to a length L, the patterned PDMS layer is under compression, which is characterized by the nominal (far-field) uniaxial compressive strain $\varepsilon = L_0/L - 1$. The oxygen plasma effect was examined on a surface with pattern features of $D = 160$ μm, $\Phi = 80$ μm, $h = 20$ μm. For surfaces without plasma treatment, the holes slowly closed as the compressive strain increased, but no surface wrinkling was observed. In contrast, on the plasma treated surface, a series of patterned surface instabilities was observed as compression increased, starting with wrinkles formed at $\varepsilon \approx 0.04$, then in-plane wrinkling bifurcation (period doubling) at $\varepsilon \approx 0.08$, followed by the nucleation of creasing (wrinkling-creasing transition) at $\varepsilon \approx 0.1$, and global creasing at $\varepsilon \approx 0.3$, and finally the closure of lattice holes at $\varepsilon \approx 0.55$. The morphological development of the surfaces was characterized under reflected light optical microscopy to study the dynamic surface evolution with different lattice arrays. A series of observations were made at the same strain sequence to reveal surface states at the same deformation level.

For the pattern with a square lattice (Fig. 6.1g), the in-plane wrinkle pattern appears to be lateral straight stripes and does not change much with different aspect ratios (Fig. 6.2). In contrast, the pattern with centred square lattice is more interesting and we see three types of in-plane wrinkling patterns formed at small compressive stress with a high sensitivity to the aspect ratios of lattice applied. For $D/\Phi = 1$, an in-plane curved stripes pattern is developed with a strong dependency on the local strain concentration determined by the lattice hole and aspect ratio of lattice array (Fig. 6.1h). Straight wrinkle stripes pattern is evident when $D/\Phi = 2$ (Fig. 6.1i), which is similar to the surface patterned with square lattice. However, an in-plane "star" wrinkle pattern is generated for $D/\Phi = 4$ (Fig. 6.1j), the wrinkle morphology shows a 2D periodic distribution around each hole with a "star" shape, implying a diagonal strain energy localization.

At higher compression, all patterned surfaces develop morphological evolutions showing a wrinkle-crease transition, the surface creases nucleate at the edge of lattice hole perpendicular to the compression direction at $\varepsilon \approx 0.06$ – 0.013. The creases progress as the compression increases, and fully cover the surface at $\varepsilon \approx 0.3$. Among these morphological transitions, an interesting phenomenon is discovered that a single crease can be generated on the surface with centred square lattice holes ($D = 80$ μm, $\Phi = 20$ μm, $h = 20$ μm). This has great potential to enable new types of surface actuator with targeted compression effects within the scale of a few micrometres. It should also be noted that the critical strains for initializing the transition ($\varepsilon \approx 0.06$ – 0.013) are much lower than the typical critical strain value of $\varepsilon_{\text{crease}} \approx 0.35$ – 0.55 [184, 185]. The reason is that the global strain level does not well reflect the strain localization on the structural confined surface. The strain energy localization at a curved boundary near a hole edge for a patterned surface could be several folds of that on a non-patterned surface.

After plasma treatment for 10 seconds, the surface modulus measurement (Fig. 6.3) obtained by atomic force microscopy (AFM) indentation suggests the plane-strain elastic modulus mismatch between the film and the substrate is about $\bar{E}_f/\bar{E}_s \approx 25$, where $\bar{E}_f$ and $\bar{E}_s$ refer to the plane-strain elastic modulus for the oxidized stiff layer and PDMS substrate, respectively, which are related to their Young's moduli, E, by $\bar{E} = E/(1-\nu^2)$, where ν is the Poisson ratio. Accordingly, the critical strain for wrinkling from linear stability analysis [66] is $\varepsilon_w = 0.25(3\bar{E}_s/\bar{E}_f)^{2/3} = 0.061$, which agrees well with our result of $\varepsilon \approx 0.068 \pm 0.008$ for a non-patterned surface. However, it does not agree with the case of a lattice patterned surface, in which wrinkle patterns are already present at $\varepsilon \approx 0.06$, indicating that wrinkling occurs at a lower threshold strain as a result of strain localization near the lattice holes.

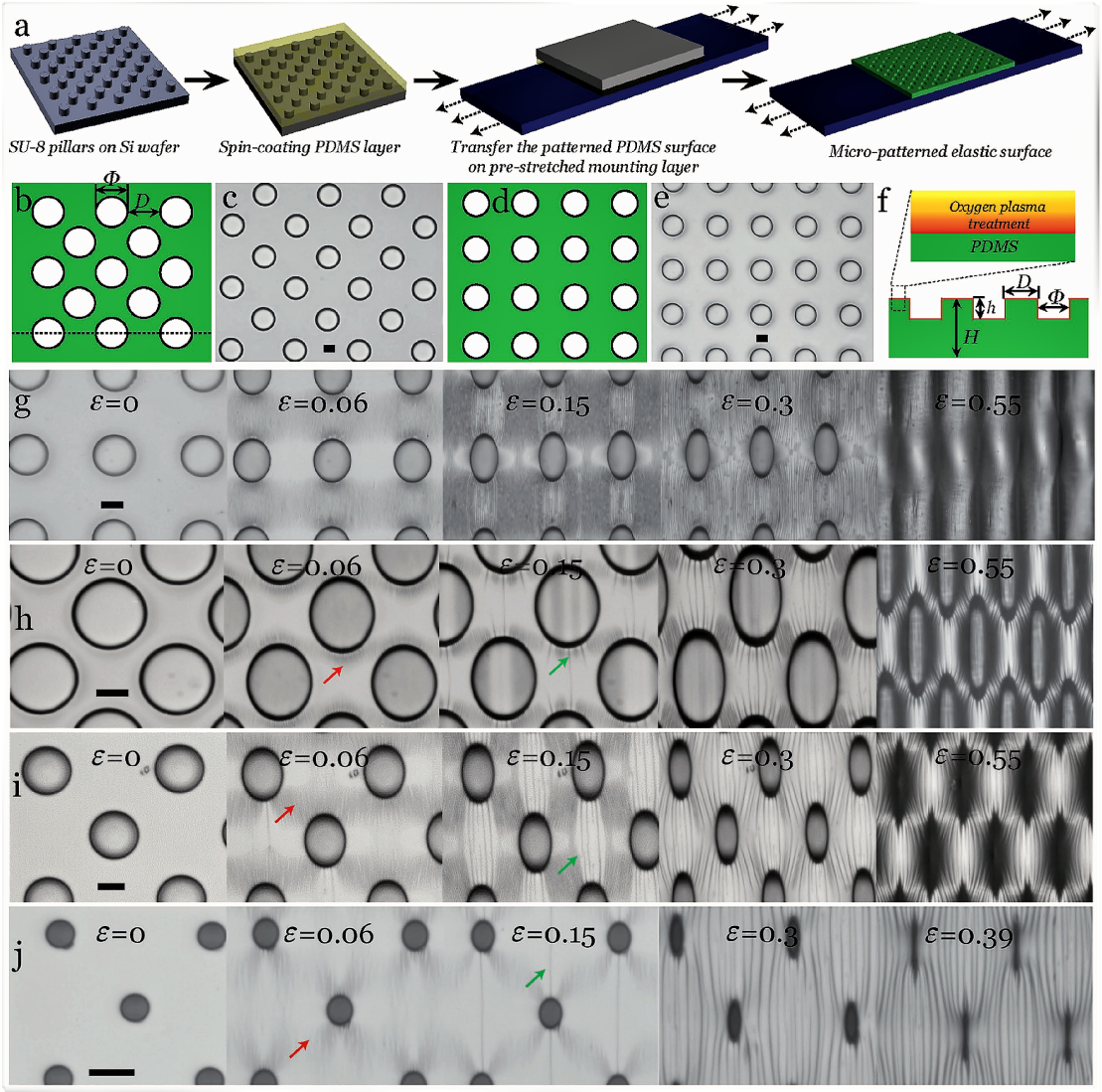

Fig. 6.1 Illustration of design and fabrication process of structural confinements and guided formation of surface morphologies under compression. (a) The structural surface was fabricated by spin-coating a thin PDMS precursor layer on a lithographically made template (SU-8 pillars array on a silicon wafer), then transferring and curing the thin PDMS layer (≈125 μm) onto the top of a pre-stretched mounting elastomer layer with thickness ≈3 mm. Two in-plane arrays with varied aspect ratios are designed, (b) illustration and (c) optical microscopy for centred square lattice array, (d) illustration, and (e) optical microscopy for square lattice array. (f) The microfabricated surface was treated with oxygen plasma to achieve a stiff skin layer (≈50 nm). (g) The observation of surface morphology changes on square lattice array patterned surface at different compression levels. (h-j) The observation of surface morphology changes on a centred lattice array patterned surface at the same compression sequences in (g) with different aspect ratios. The wrinkle patterns are marked with red arrows and creases are marked with green arrows. All images in this Fig. have been formatted with the same scale bar of 20 μm. Taken from [142].

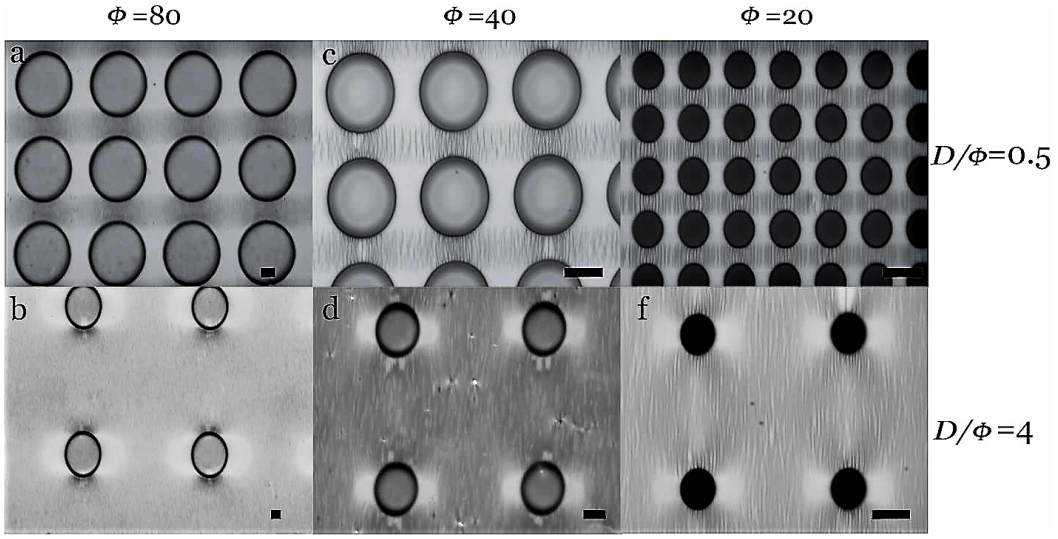

Fig. 6.2 The formation of the lateral wrinkle pattern for the square lattice patterned surface with different geometrical aspect ratio, showing the straight belt wrinkle formation for all aspect ratios. Taken from [142].

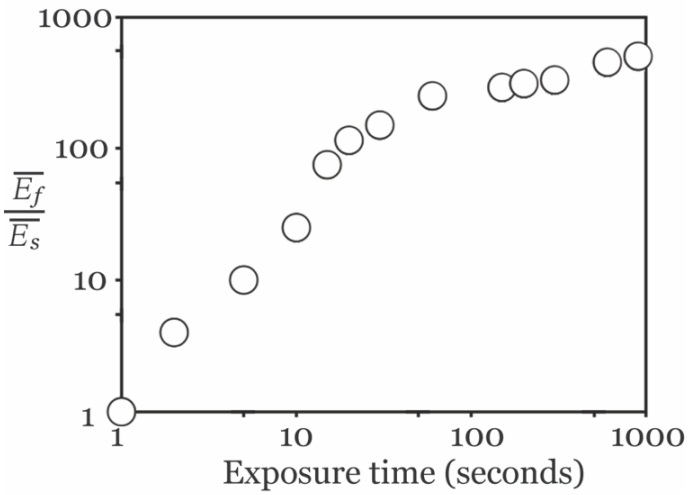

Fig. 6.3 The modulus ratio as a function of plasma treating duration. Taken from [142].

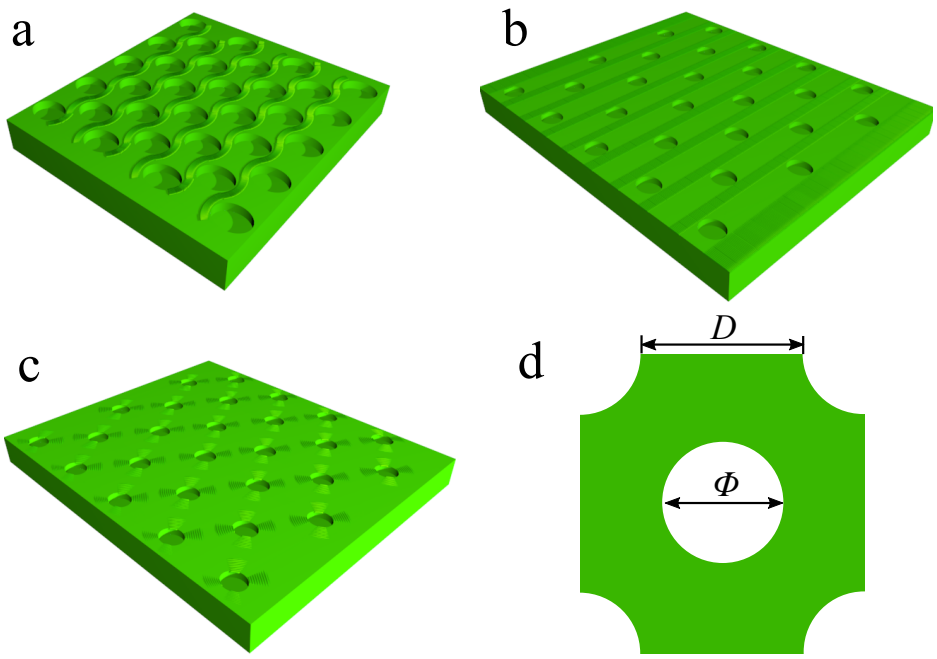

Fig. 6.4 Schematic diagrams for the three wrinkling patterns that are generated from the centred square lattice as (a) curved ribbon as observed in Fig. 6.1h, (b) straight belt as observed in Fig. 6.1i and (c) star shape as observed in Fig. 6.1j. (d) A representative unit area is chosen for numerical analysis. Taken from [142].

6.2 Theoretical analysis

To understand the instability patterns (Figs 6.4a–c) and thresholds observed from experiment, a numerical analysis is performed by calculating the pattern of deformation under the imposed global compressive strain for lattice patterned surfaces (Fig. 6.4d). Deformation around a single hole, square and centred square arrays of holes has been previously studied within linear elasticity [186, 187], and generally produce stress concentrations near the holes. To generalize these results to our bilayer lattices, we modelled the patterned substrate as a linear-elastic 2D plane-strain system consisting of an infinite incompressible elastic material containing the appropriate infinite lattice of holes. We consider a square unit cell of the resulting system (centred square patterned surface), and use numerical analysis to solve the plane-strain field in response to an imposed compressive strain, $\varepsilon_{\text{plain}}$, in the x-direction and, as measured in experiments, a sympathetic extension of $0.3\varepsilon_{\text{plain}}$ in the y-direction, and with stress-free boundary conditions at the edges of the holes. The subscript "plain" refers to the global strain/stress that the non-patterned, i.e. plain, system would undergo.

The numerical analysis used a finite element package in Mathematica [174] to solve the 2D plane-strain linear elasticity problem for the deformation in the patterned soft substrate. A

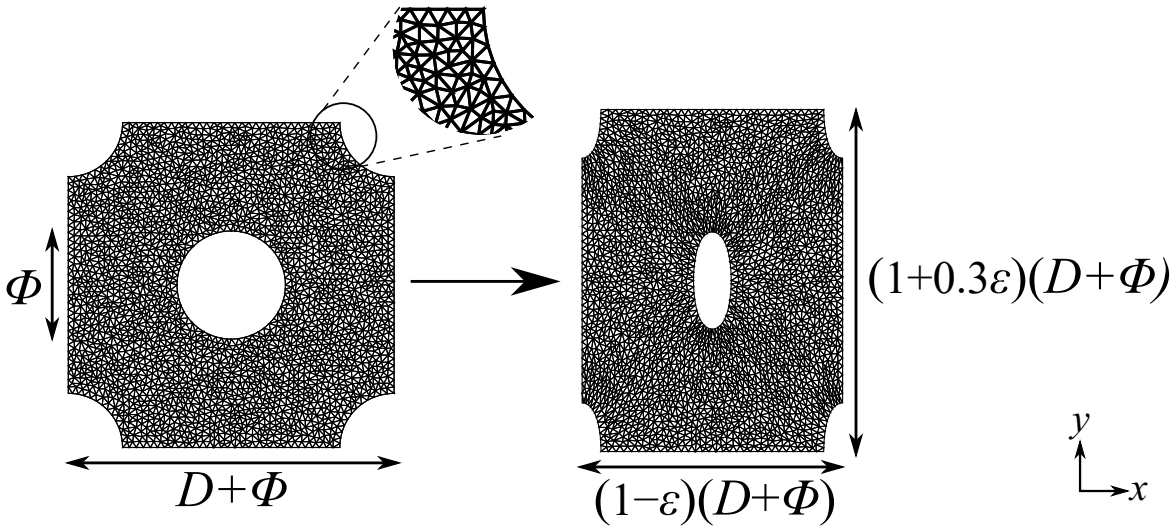

Fig. 6.5 Discretized mesh elements for the numerical analysis of a unit cell: (left) non-deformed unit cell, (right) deformed unit cell with a macroscopic strain $\varepsilon = 0.3$.

repeatable 2D unit cell was first defined with the geometry corresponding to the experiment and, as seen in Fig. 6.5, the finite element package discretized the domain with a fine mesh consisting of around 4000 triangles was described. A plane-strain deformation was then assumed, described by the 2D displacement field $(u(x,y)\hat{\mathbf{x}} + v(x,y)\hat{\mathbf{y}})$ so the plane-strain stress tensor, using linear elasticity,

$$\sigma = \frac{E}{1+\nu}\begin{pmatrix} \frac{(1-\nu)u_{,x}+\nu v_{,y}}{1-2\nu} & \frac{u_{,y}+v_{,x}}{2} \\ \frac{u_{,y}+v_{,x}}{2} & \frac{\nu u_{,x}+(1-\nu)v_{,y}}{1-2\nu} \end{pmatrix}, \tag{6.1}$$

where E is the Young's modulus, ν is the Poisson's ratio, and the comma-notation denotes partial derivatives. The Mathematica [174] finite element package then solved the mechanical equilibrium condition

$$\nabla \cdot \sigma = 0 \tag{6.2}$$

in the meshed domain via the command `NDSolve` with "`FiniteElement`" option, subject to the boundary conditions that $\sigma \cdot \hat{\mathbf{n}} = 0$ on the hole edges, and that the straight edges of the cell move with the macroscopic strain of the underlying substrate ($-\varepsilon$ in the x-direction and 0.3ε in the y-direction) as seen in Fig. 6.5.

Having solved for the displacement fields, we plot the local maximum compressive strain in our solutions, $\varepsilon_{\text{pattern}}$, as a fraction of $\varepsilon_{\text{plain}}$, in Fig. 6.6a, for several different aspect ratios of lattice. We see that the compressive strain is strongly localized around the holes. In centred square lattices with smaller holes, there are also clearly star-shaped patterns of increased compression running between the holes.

We next calculate the wrinkling pattern on the stiff plasma-treated skin, assuming that the stiff film directly follows the deformation in the soft substrate. To determine whether the region is unstable toward wrinkling, the stress tensor was diagonalized to find its maximum compressive stress, σ_c. By applying the standard result for wrinkling on a substrate, which is that wrinkling will occur at when the compressive stress exceeds the critical stress given by [66]

$$\sigma_c > \frac{1}{4}\left(3\frac{\bar{E}_s}{\bar{E}_f}\right)^{2/3}\bar{E}_f, \tag{6.3}$$

which is another form of (1.88). Taking the physically reasonable modulus ratio $\bar{E}_f/\bar{E}_s = 100$, we plot, in Fig. 6.6b, how the predicted wrinkle regions grow as the global compression is increased.

The wrinkle direction (the short lines in Fig. 6.6b) was taken to be perpendicular to the principal direction of the maximum compressive stress. The value of this compressive stress, as a fraction of the compressive stress that would be observed in a non-patterned system, is plotted for each lattice in Fig. 6.6c, as a function of distance from the centre of the central hole, along the line shown in the bottom of Fig. 6.6a.

For a centred square lattice patterned surface, we see that the compressive stress is strongly enhanced at the edge of hole, particularly in lattices with small holes, explaining why wrinkling occurs earlier in patterned systems. We see, in accordance with experiment, that moving from large holes to small holes does indeed change the wrinkling pattern from wavy lines, to straight lines, to stars, and that the patterns with smaller holes wrinkle at smaller global compressions, because the compressive stress is more concentrated around the hole.

We show the same plots for a simple square lattice in Fig. 6.7, showing compression concentration in lateral straight stripes through the holes at all aspect ratios of pattern. The wrinkling patterns shows a good agreement with the experiment Fig. 6.2.

6.3 Post wrinkling bifurcation analysis

We see that strain localization from patterning the surface allows the wrinkle to emerge at lower strain level. We also expect patterning to also reduce the thresholds for further bifurcations such as period doubling and creasing, but they cannot be effectively identified under reflective optical microscopy.

To unveil more details on the surface morphology development, atomic force microscopy was used to track the surface as the compressive strain was gradually increased, focusing on the region of stress concentration “above” a hole as indicated by the dashed box in Fig. 6.8a.

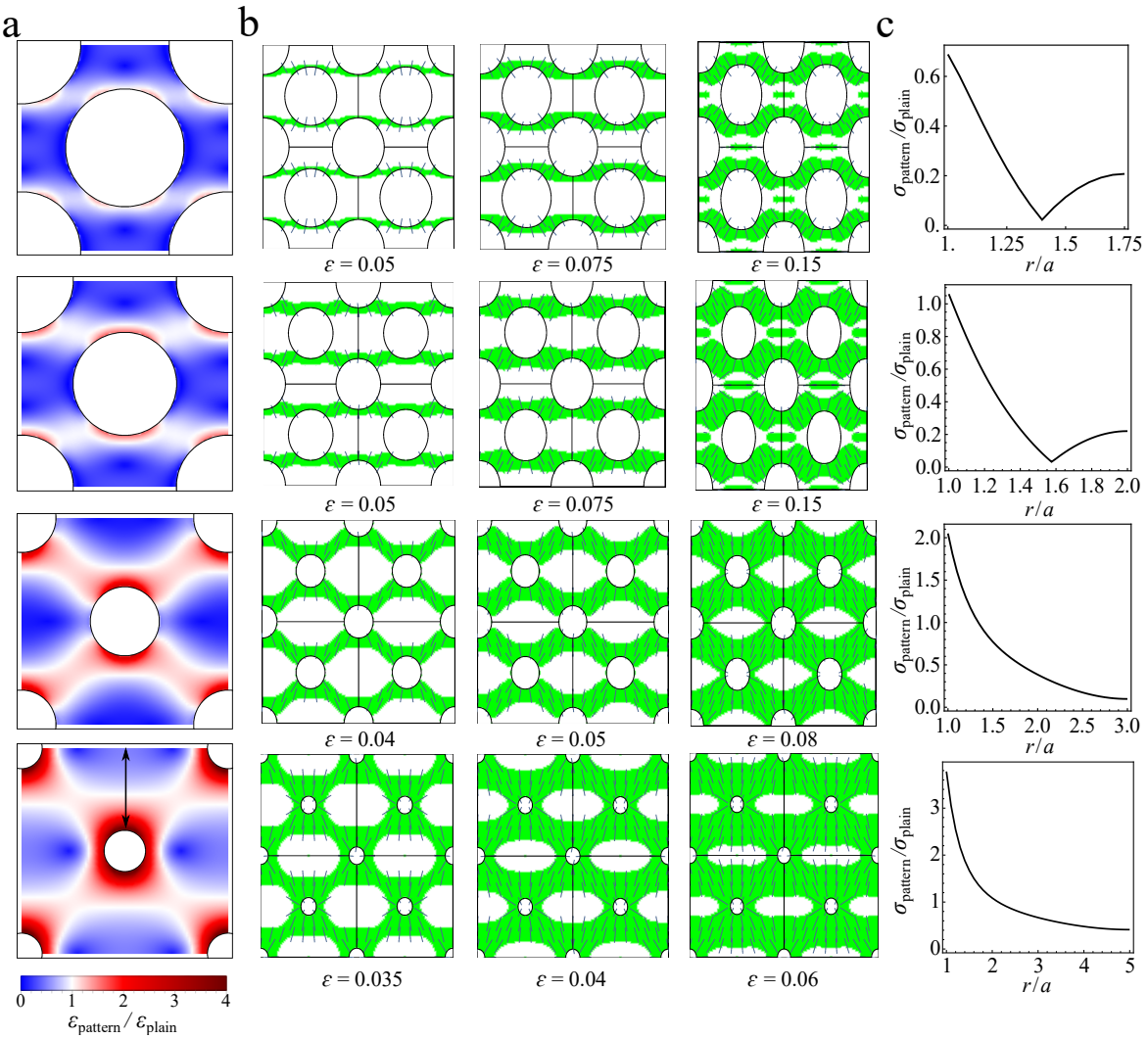

Fig. 6.6 Numerical analysis for centred square patterned samples. (a) Compression of the patterned substrate relative to the compression of the non-patterned substrate. Blue and red indicate the less and more compressive areas. (b) Evolution of wrinkling region as a function of applied strain in the deformed bilayer system with patterned holes. Green areas are the wrinkling regions. Lines indicate the direction along which the wrinkles will grow. (c) Compressive stress in the stiff layer in the patterned bilayer system relative to the non-patterned system values at different position from the rim of the hole of radius a (maximum stress) to the edge of the unit cell (see arrow in (a) bottom). All plotted with D/Φ = 0.75, 1, 2, and 4.

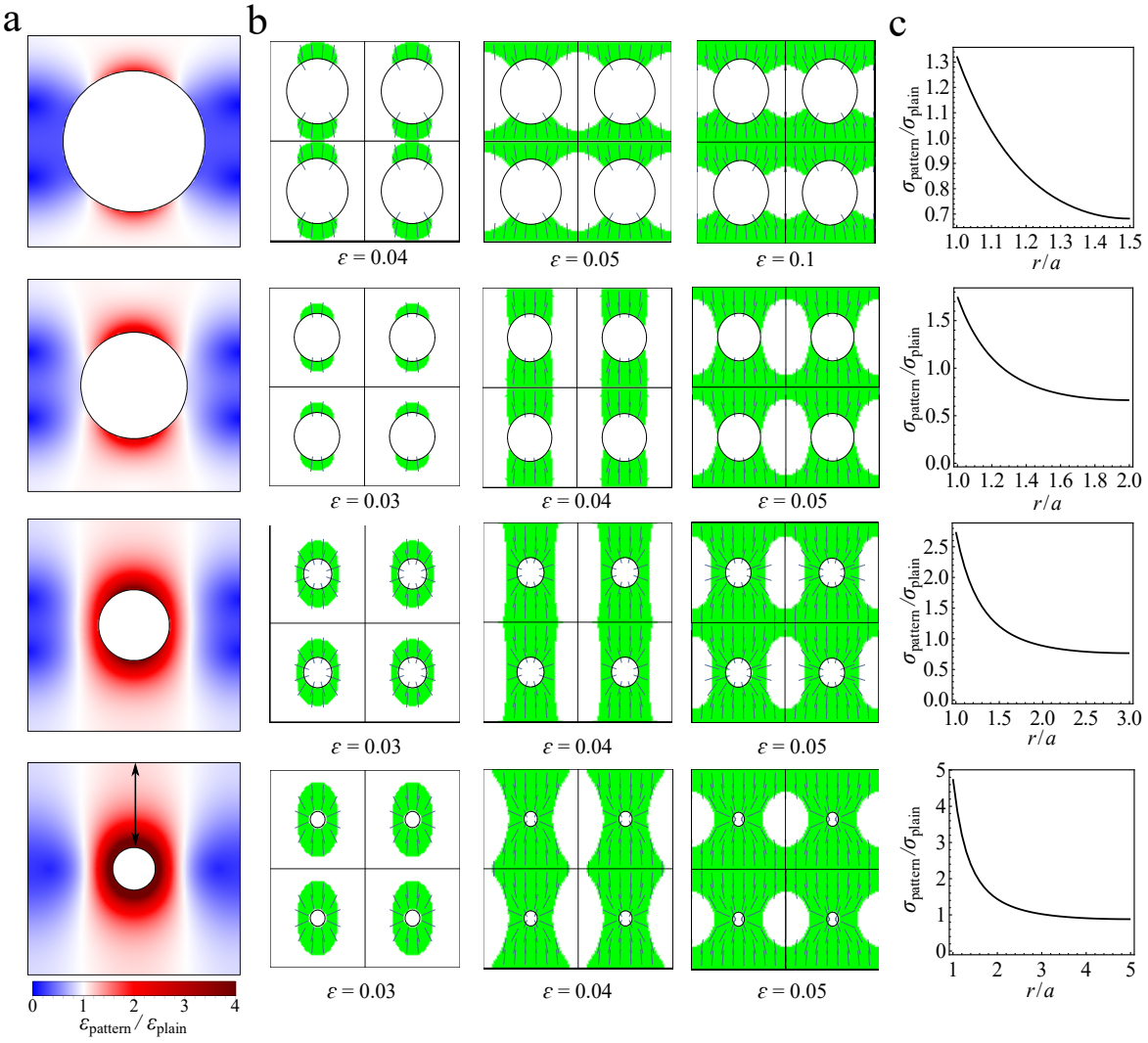

Fig. 6.7 Numerical analysis for square patterned samples. (a) Compression of the patterned substrate relative to the compression of the non-patterned substrate. Blue and red indicate the less and more compressive areas. (b) Evolution of wrinkling region as a function of applied strain in the deformed bilayer system with patterned holes. Green areas are the wrinkling regions. Lines indicate the direction along which the wrinkles will grow. (c) Compressive stress in the stiff layer in the patterned bilayer system relative to the non-patterned system values at different position from the rim of the hole of radius a (maximum stress) to the edge of the unit cell (see arrow in (a) bottom). All plotted with $D/\Phi = 0.5$, 1, 2 and 4.

For the centred square patterned surface with aspect ratio of $D = 80\ \mu$m, $\Phi = 40\ \mu$m, $h = 43\ \mu$m, we found the onset of wrinkling starts at a small compressive strain of $\varepsilon = 0.02$ (Figs 6.8b–c) and progress to cover the region by $\varepsilon = 0.11$. The initial wavelength (λ_0) is predicted to be $\lambda_0 = (2\pi h_f)(\bar{E}_f/3\bar{E}_s)^{1/3}$ [66, 68], or 700 nm for an oxidized layer thickness of $h_f = 55$ nm, which is in reasonable agreement with the measured value of $\sim$850 nm. The progressive wrinkling over this range of strain presumably reflects the influence of the energy boundaries resulting from the local strain concentration. We also find the creases start to nucleate at $\varepsilon = 0.11$, and start to grow at $\varepsilon = 0.15$, then fully cover the region at $\varepsilon = 0.25$. A hierarchical surface is formed at $\varepsilon = 0.55$, where we can see the periodic surface under the reflective optical microscopy in Fig. 6.8d.

There is clearly a lattice guided formation of wrinkle at $\varepsilon = 0.02$ with non-uniform amplitude distribution which reveals the state of energy concentration, where the hole edge perpendicular to the compression axis scores the highest (Fig. 6.8c). The period doubling pattern can be observed at $\varepsilon = 0.15$ with every second wrinkle growing in amplitude while its neighbours shrink. The strain value for this bifurcation is also smaller than the reported strain value $\sim$0.17 [84]. From $\varepsilon = 0.15$, further compression does not noticeably influence the in-plane morphology, since the AFM result cannot reflect the out of plane deformation toward the substrate, i.e., self-contact area of the crease. Therefore, we add the cross-sectional scanning data of the film from laser-scanning confocal fluorescence microscopy (LSCM, Fig. 6.8e) to reveal the out of plane morphological development for the selected area (Fig. 6.8f). At a strain of $\varepsilon = 0.15$ (Fig. 6.8c), the LSCM data shows a shallow crease depth (self-contact area) within 100 nm, where it is considered as the onset of the crease. Similar with the wrinkling, this second bifurcation is found to be highly sensitive to the presence of the holes (Fig. 6.9). At higher compressive strains, the crease depth develops under higher compressive strains and extends to all scanned areas.

We next consider the lattice pattern effects on post wrinkling bifurcations occurring at a higher strain level. It should be noted that the crease nucleates but it does not grow across the regime adjoining the lattice holes (Fig. 6.10) for $D/\Phi \leq 1$. We expect this may arise due to the viscoelastic nature of the substrate, and/or the influence of strong stress concentration near the holes. A brief classification of the transitions based on the crease number initiated is summarized in Figs 6.11a–c for the lattice patterned surface with aspect ratio $D/\Phi > 1$. There are two transition types (single crease and multiple creases) for the stripe pattern, and the formation of creasing is revealed in Fig. 6.11d. The "star" type wrinkle pattern seems more likely to generate a single crease when being further compressed.

We next plot the normalized wrinkle amplitude (A/λ_0) as a function of the nominal applied strain on a non-patterned surface (Fig. 6.11e) and a Bravais lattice patterned surface

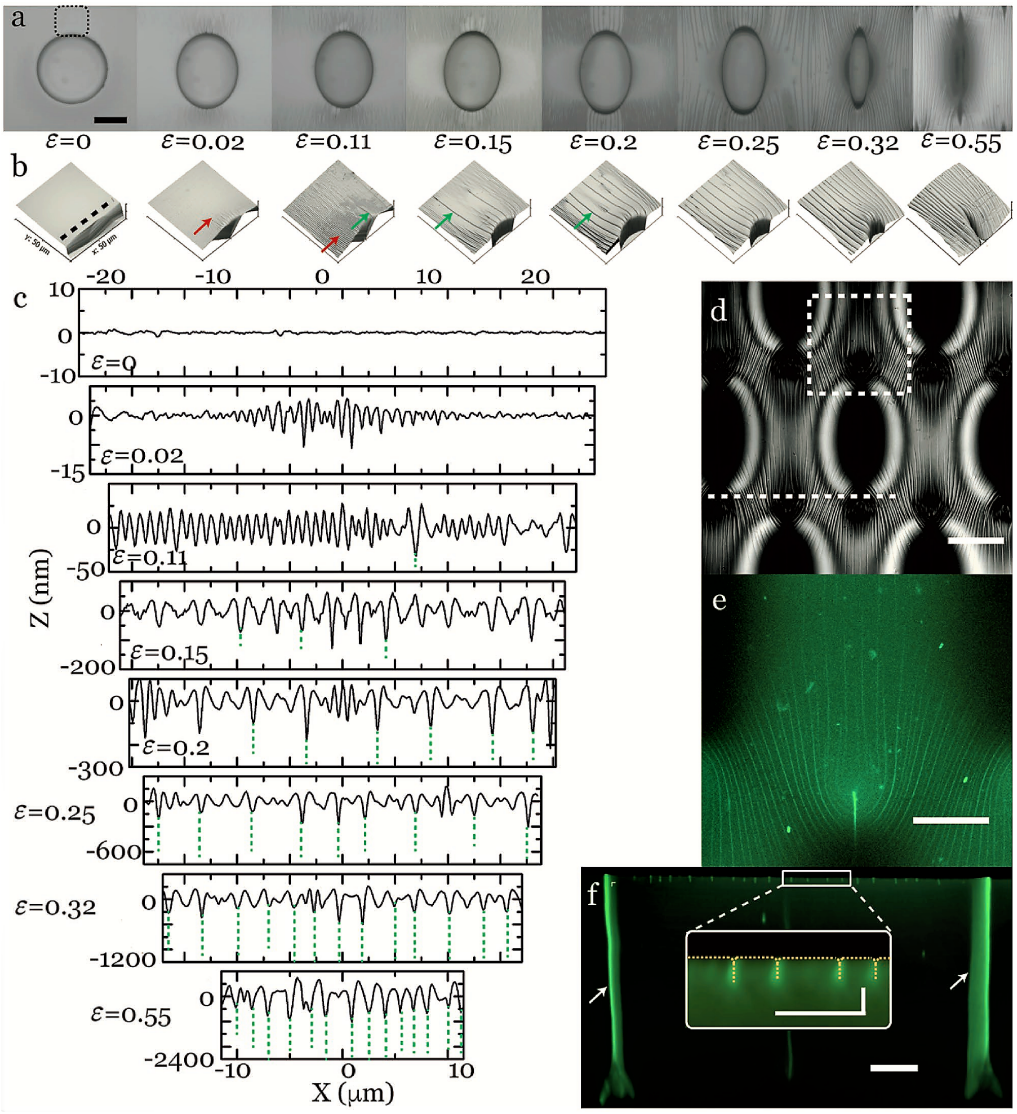

Fig. 6.8 Characterization of the instabilities on the single hole and their evolutions under the uniaxial compression. (a) Top view observations and (b) AFM profiling of the selected area in (a) for surface morphology changes under the uniaxial compression for a unit area (centred square lattice array) with in-plane aspect ratio of $D = 80\ \mu$m, $\Phi = 40\ \mu$m, $h = 43\ \mu$m. The arrows point to where the wrinkles (red) and creases (green) begin to from (c) The surface morphology development is plotted with the dependency on compression strain, the surface starts to initialize localized wrinkles on $\varepsilon = 0.02$, then develops into periodic doubling at $\varepsilon = 0.15$, the surface starts to form creases locally at $\varepsilon = 0.2$, where the sharp self-contacts within the PDMS (green dashed lines) are detected by LSCM, and finally the creasing develops globally. (d) The reflective image shows a surface hierarchy formed when the hole reached the "off" state at a compression deformation of 0.55. Laser confocal scanning reveals (e) the in-plane distribution of creases and (f) the out of plane morphology developed into the PDMS substrate for the selected area in (d), the arrows show the high intensity fluorescence signal due to the closure of neighbouring holes. The scale bars for the inset figures in (d–f) are 40, 18, 3 μm respectively. Taken from [142].

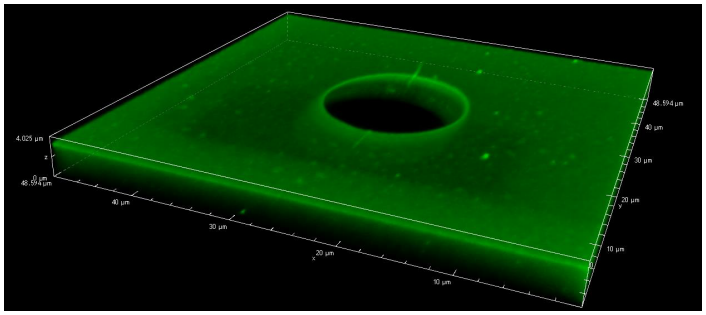

Fig. 6.9 LCSM scanning to view the initialising of the creasing on the targeted area for the centred square lattice patterned surface with aspect ratio of Φ= 20 μm, h =43 μm, D/Φ =4. Taken from [142].

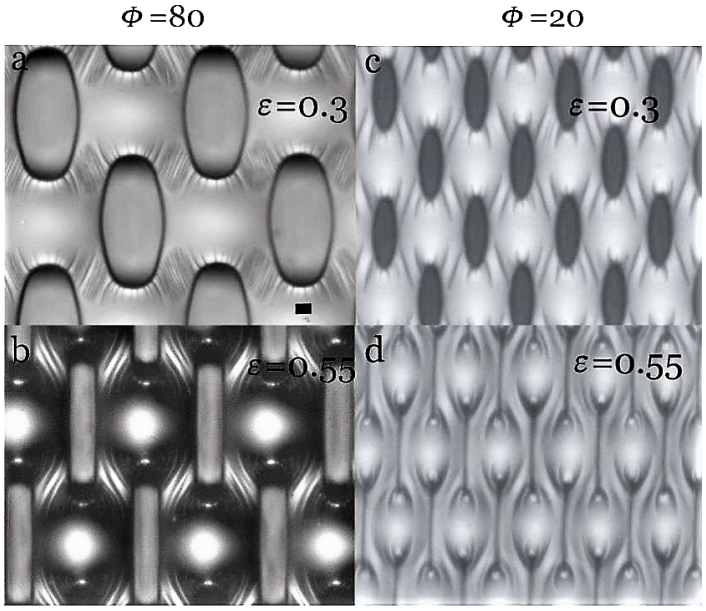

Fig. 6.10 The deformation of patterned surface under higher compression for aspect ratio $D/\Phi = 1$. Taken from [142].

(Fig. 6.11f, $D = 80$ μm, $\Phi = 40$ μm, $h = 43$ μm). In each case, beyond wrinkling onset, two additional instabilities/bifurcations are seen, corresponding to period doubling and then crease formation. However, both the onset of wrinkling and the further bifurcations occur at considerably lower global strains in the patterned system: the critical wrinkle strain for the patterned surface of $\sim$0.02 is less than one third of that in the flat surface ($\varepsilon \approx 0.068$), the critical strain for periodic doubling in the patterned surface is $\sim$0.06, whereas it is $\sim$0.18 in flat surface, and for the final bifurcation, the wrinkle-crease transition, the critical strain needed is $\sim$0.08 in the patterned surface, which is less than half of that for the flat surface ($\varepsilon \approx 0.22$). We can understand this threshold reduction effect by considering the stress concentration in our analytic calculations for systems with $D/\Phi = 2$ (seen in Fig. 6.6g), which exhibit a two-fold stress concentration at the edge of the hole relative to the non-patterned system, and hence predicts two-fold reduction in the various thresholds. The discrepancy between this calculation and the observed three-fold reduction is probably due to our analytic plane-strain approximation not capturing the full 3D structure of the actual deformation field.

It is important to understand quantitatively how these instabilities develop in the presence of the curved boundary from the edge of lattice holes. Thus, we plot the normalized strains for the onset of each instability as a function of the radius of lattice hole for $D/\Phi = 2$. As seen in Fig. 6.11g, the critical strains are clearly separated in different ranges, while the size of the holes influence the strains significantly. The overall strains are reduced as a result of the strain localization guided by the curved boundary, and it seems the strains for each instability are likely to collapse, which agrees well with the reported value by Kim that the doubling bifurcations are likely to be mixed with creasing with the $\bar{E}_f/\bar{E}_s$ value in the range of 14–47 [82, 83]. A key advantage of the elastic instability enabled technology is that, as an elastic process, it should yield a low degree of hysteresis. We then investigate the hysteresis of the lattice patterned surface with labelling the lateral dimension change in the hole (Fig. 6.11h). The results suggest a robust transformation, which indicates that the viscoelastic relaxation of the soft PDMS layer used here is less important.

6.4 Conclusion

We present an approach to generate periodic planar wrinkle 2D patterns and controllable instability evolution toward a hierarchical surface by preplacing Bravais lattice patterns on the surface as in-plane structural confinements. The bilayer system shows bistabilities at certain well-defined strain values initializing the wrinkles and further elastic bifurcations at the designated areas/locations which are closely related to the geometries of the confinements.

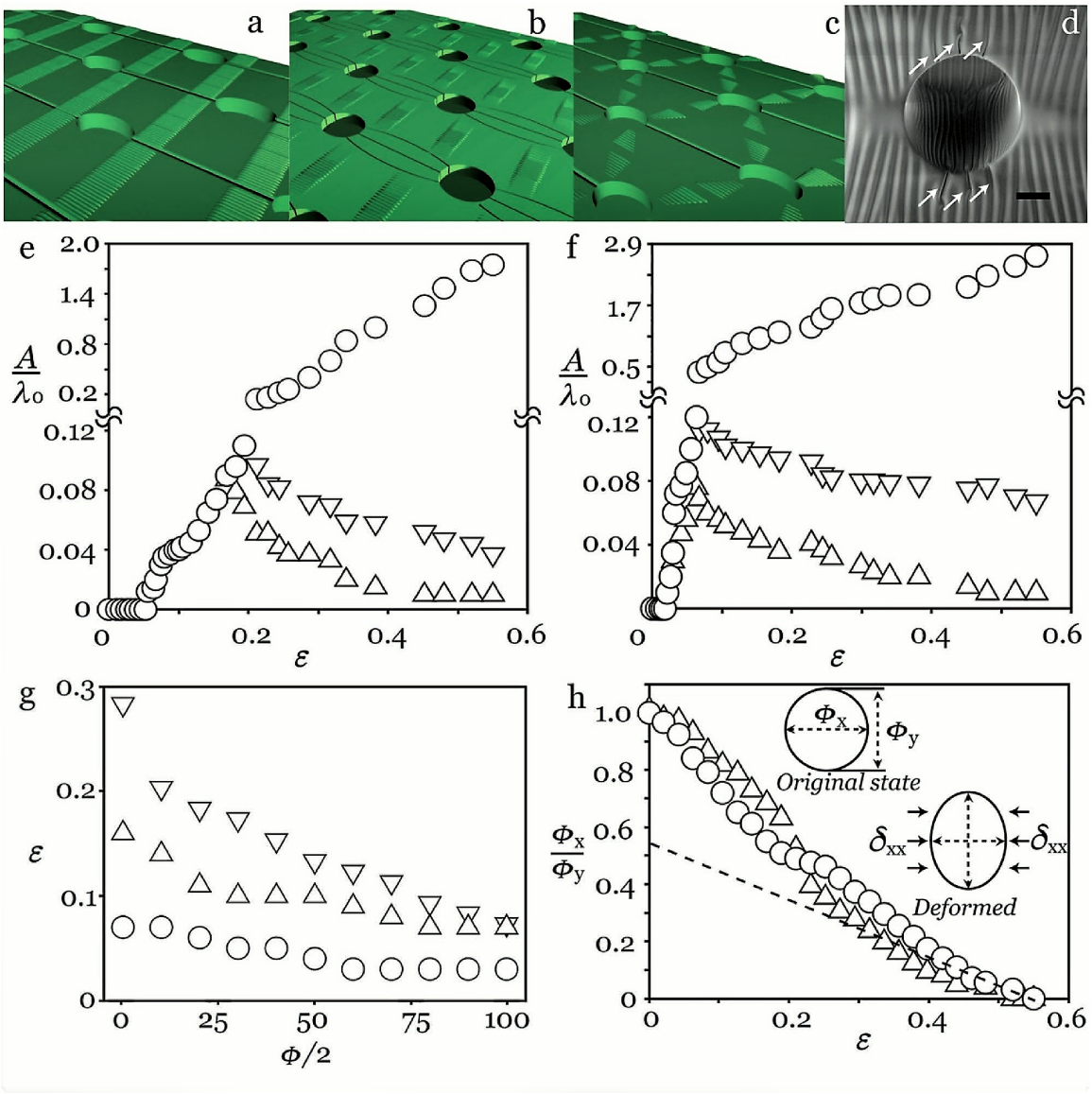

Fig. 6.11 The evolution of surface morphology at higher compression, from wrinkling to creasing. Schematic illustrations of the transition from wrinkling to creasing for different harmonic patterns, (a) straight belt, (b) curved ribbon, and (c) star shape. (d) scanning electron microscope (SEM) image reveals the transition moment from wrinkling to creasing with the captured initialization of creases. The normalized amplitudes of surface features A/λ_0 reveal two post-wrinkling bifurcations with increasing strain for (e) homogeneous PDMS surface and (f) patterned PDMS surface (centred lattice) with in-plane aspect ratio of $D = 80\ \mu$m, $\Phi = 40\ \mu$m, $h = 43\ \mu$m. Normalized amplitudes change along with two bifurcations and represented with first order (◯), second order (△), and third order (▽). (g) The critical strains for initiating wrinkle (◯), periodic doubling (△), creasing (▽) for the centred square array with different diameter. (h) The compression (△) and recovery (◯) curves show the hysteresis and nonlinearity on the deformation of a single hole under uniaxial compression. Taken from [142].

The formation of lateral wrinkle patterns has been studied with the dependencies on the geometrical variables of in-plane confinements and the results are in good agreement with the predictions from numerical analysis. At higher compression, we also reveal a targeted formation of wrinkle-to-crease transition as result of the reorganization of surface strain field. We anticipate this localized formation of surface instabilities, and the demonstration of bistability over a substantial range of strains will open new opportunities for applications of elastic instabilities on responsive surfaces for future lab-on-chip devices, by enabling delicate responses to mechanical inputs as selectively sensing or actuating structures.

Chapter 7

Conclusion and Further work

7.1 Conclusion

It is well established that soft materials undergo elastic instabilities in response to compression or stretching, leading to the formation of geometric patterns such as wrinkles and creases. Such instabilities are also known to play a crucial morphological role in biological systems, as evident in brain and villous folds. Yet the understanding of how and why these shapes arise remains far from complete. In this thesis, I have explored different ways of shape formation by utilizing elastic instabilities. I have carried out extensive analyses of 1) peristaltic instability in soft solids, 2) formation of hexagonal dents pattern in the soft layer buckling and gravity driven instabilities and 3) an approach to creating wrinkling patterns through strain topology manipulation.

In Chapter 3, I aimed to investigate instability in soft channels under inflation. Via linear stability analysis, I have uncovered a new elastic instability, namely the peristaltic instability. When subject to a pressure increase, a cylindrical cavity through a soft solid reversibly undergoes elastic instability and exhibits a peristaltically undulating shape. The instability adopts a simple form and is observed at a critical pressure that is a simple multiple of the channel shear modulus, with a wavelength a multiple of the cavity radius. These scalings are inevitably caused by the scale invariance of elasticity, similar to the solid cavitation. It can be concluded that such peristalsis arises because it relieves strain and saves elastic energy. Importantly, we found that mouse embryonic stem cell tissues grown inside a hydrogel channel similarly show peristalsis, indicating that peristaltic instability is a ubiquitous biological phenomenon. Together, this peristaltic instability provides us a way to introduce a tuneable undulating morphology by pressuring a soft cavity.

In Chapter 4 and 5, the main goal was to understand the mechanism of pattern selection in two elastic instabilities: soft layer wrinkling on a compliant substrate and gravity driven

instability. Employing high order perturbation theory, I constructed elastic solutions that correspond to patterns with different types of symmetry. To predict which pattern would be selected based on the lowest elastic energy, the competition between each basic pattern in the known pattern-inducing elastic instabilities was investigated and analysed both analytically and numerically. I have found that hexagonal dents are favoured over other patterns and their formation is a consequence of the lack of inversion symmetry. By evaluating the energy expansions, we can determine whether the instability is supercritical or subcritical, as well as predicting the instability amplitude and energy. The lack of inversion symmetry in the hexagon pattern allows odd terms in our energy expansion to persist, making the instability generally subcritical. Overall, I have shown that, in most cases, we only need to calculate the energy coefficients to predict which pattern will emerge, and by manipulating them, the pattern can be chosen.

Last but not least, in Chapter 6, I pursued the investigation of an approach to inducing wrinkling patterns by manipulating the strain topology with lattice of holes. We employed a simple strategy of patterning the surface with a Bravais lattice of holes to create in-plane structural confinements. This gives rise to localized stress in the system, which in turn initializes unique wrinkling patterns and further elastic bifurcations in an area-dependent manner. The formation of these wrinkles also depends on the geometries of the lattice, meaning we can manipulate where the wrinkles appear in the system. In addition, the stress localization at high compression reveals a localized wrinkle-crease transition due to the reorganized surface strain field.

All these different ideas of shape formation and manipulation entail many far-reaching applications such as understanding morphogenesis as well as manufacturing patterned surface on devices.

7.2 Further work

There are still many questions that have not been explored in this thesis. Here, I provide a non-exhaustive list of a related possible projects on shape formation via elastic instabilities.

7.2.1 Different elastic instabilities

Discovering more instabilities would be beneficial toward understanding shape formation in both biological and engineering system. There are many well-studied instabilities in fluids. Some of them also have analogues in elastic solids such as Taylor-Couette, Rayleigh-Plateau

and Rayleigh-Taylor instabilities. One might be able to find a new elastic instability that share similar characteristics with existing fluid instabilities.

An interesting area to look at is the instability that involve both fluids and elastic solids. Examples are wrinkling of an elastic sheet when placed on a liquid drop [188] or wrinkling of a thin elastic sheet supported by fluid under compression [189]. Peristaltic instability is also one of them as the internal pressure of the cavity is usually caused by the fluid inside. One could also ask whether a layer of fluid could cause an underneath layer of elastic solid to become unstable similar to the solid gravity driven instability.

In addition, solids like nematic liquid crystalline elastomers (LCEs) order can be manipulated using heat, light or electric field. This can cause the solid to change in length thereby creating stretch or compression, which might generate wrinkling pattern. Hence, LCEs might be a rich area to explore different kinds of elastic instabilities. There are already a number of studies on elastic instabilities in this system such as wrinkling of film on a nematic substrate [190, 191], fingering in nematic films [192], and swelling of a nematic filament [193].

7.2.2 Surface tension

In real systems, surface tension is presented. Previous works show that surface tension influences the instability by introducing a length scale, i.e. the elastocapillary length, which would alter the wavelength of the instability as well as the threshold. This might affect the conclusion in the peristaltic, soft layer buckling and gravity driven instabilities. We know that surface tension can also make a cavity through a soft solid becomes unstable towards a long wavelength instability [60]. There is a question about what would happen when the cavity is subjected to both internal pressure and surface tension. This could happen, for instance, when a cavity through hydrogels is pumped with air. For the buckling of a soft layer on a rigid substrate, a surface tension can change the instability from subcritical to supercritical [169]. Would this also happen for the gravity driven instability? Understanding how surface tension influence the instability energy coefficients and the pattern selection in these two instabilities would be interesting.

7.2.3 Non-equibiaxial growth

For the soft layer buckling instability, equibiaxial growth/compression induces a hexagonal pattern. However, non-equibiaxial growth/compression would favour stripe corresponded to the direction of the largest growth as the threshold growth of the wrinkling in that direction is the smallest. It would be interesting to understand the transition between the two cases. What happen to the system if the growth/compression is gradually changed from equibiaxial

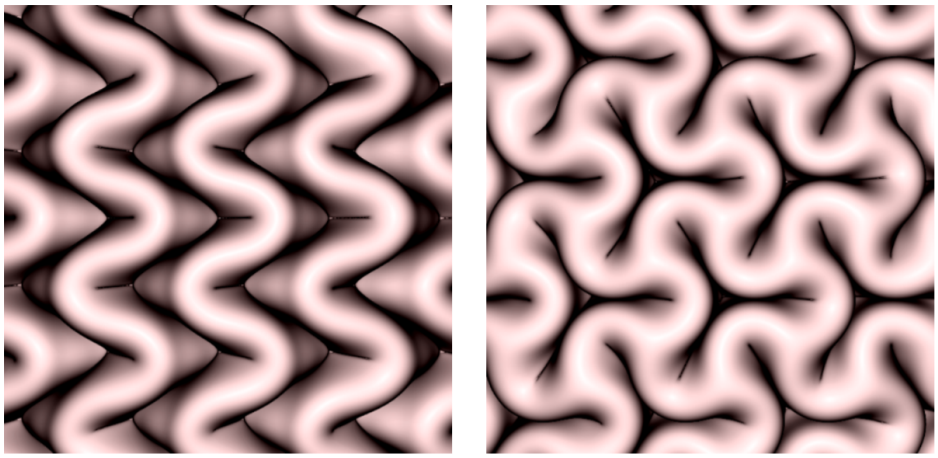

Fig. 7.1 Simulated (left) herringbone pattern and (right) labyrinth pattern for a layer/substrate system under a equibiaxial growth with stiffness ratio $\eta = 3$ far from threshold, taken form [78].

to non-equibiaxial? There were some attempts to analyse this problem with a simplify model such as linear substrate model [165], which, as discussed, predict an incorrect pattern for an equibiaxial growth. A similar analysis with a full neo-Hookean model might provide us a more convincing answer.

7.2.4 Herringbone and labyrinth patterns

Different patterns that are not studied in Section 4.1 such as the herringbone and labyrinth patterns (see Fig. 7.1) arise further away from the threshold for soft layer buckling instability. These patterns are interested by the community as they are observed in nature such as in epithelium of a developing gut [33] and folding in brains [77]. Many existing theories have captured the formation of pattern including the threshold and the wavelength of these pattern but most of them using plate model on a linear substrate [163, 164, 162]. An energy comparison of these two patterns with the basic patterns using the full neo-Hookean model would enlighten us about the transition from hexagonal dents to these patterns. A challenge would be to calculate the energy hexagonal mode far from its threshold as one might question the accuracy of the perturbative energy prediction.

References

[1] R. W. Ogden. *Non-Linear Elastic Deformations*. Dover, 1984.

[2] S. Timoshenko and J. Gere. *Theory of Elastic Stability*. McGraw-Hill, 1963.

[3] D. P. Richman, R. M. Steward, J. W. Hutchinson, and V. S. Jr. Caviness. Mechanical model of brain convolutional development. *Science*, 189:18–21, 1975.

[4] R. Toro and Y. Burnod. A morphogenetic model for the development of cortical convolutions. *Cereb. Cortex*, 15:1900–13, 2005.

[5] P. V. Bayly, R. J. Okamoto, G. Xu, Y. Shi, and L. A. Taber. A cortical folding model incorporating stress-dependent growth explains gyral wavelengths and stress patterns in the developing brain. *Phys. Biol.*, 10:016005, 2013.

[6] S. Budday, P. Steinmann, and E. Kuhl. The role of mechanics during brain development. *J. Mech. Phys. Solids*, 72:75–92, 2014.

[7] T. Tallinen, J. Y. Chung, J. S. Biggins, and L. Mahadevan. Gyrification from constrained cortical expansion. *PNAS*, 111:12667–12672, 2014.

[8] T. Tallinen, J. Y. Chung, F. Rosseau, N. Girard, J. Lefevre, and L. Mahadevan. On the growth and form of cortical convolutions. *Nat. Phys.*, 12:588–593, 2016.

[9] J. Bradbury. Molecular insights into human brain evolution. *PLoS Biol.*, 3:e50, 2005.

[10] G. Xu, A. K. Knudsen, K. Dikranian, C. D. Kroenke, P. V. Bayly, and L. A. Taber. Axons pull on the brain, but tension does not drive cortical folding. *J. Biomech. Eng.*, 132:071013, 2010.

[11] M. E. Gurtin. *An Introduction to Continuum Mechanics*. Academic Press, 1982.

[12] A. J. M. Spencer. *Continuum Mechanics*. Longman, 1980.

[13] S. G. Mikhlin. *Variational methods in mathematical physics*. Pergamon Press, 1964.

[14] R. S. Rivlin. Large elastic deformations of isotropic materials I. fundamental concept. *Phil. Trans. R. Soc. Lond. A*, 241(822):459–490, 1948.

[15] M. A. Biot. *Mechanics of Incremental Deformations*. Wiley, New York, 1965.

[16] M. A. Biot. Surface instability of rubber in compression. *Appl. sci. Res.*, 12:168–182, 1963.

[17] E. W. Wilkes. On the stability of a circular tube under end thrust. *Quart. Joarn. Mecb. and Applied Math*, VIII:89–100, 1955.

[18] F. Pan and M. F. Beatty. Remarks on the instability of an incompressible and isotropic hyperelastic, thick-walled cylindrical tube. *J. Elasticity*, 48:219–239, 1997.

[19] A. N. Gent and I. S. Cho. Surface instabilities in compressed or bent rubber blocks. *Rubber Chemistry and Technology*, 72(2):253–262, 1999.

[20] M. Ben Amar and A. Goriely. Growth and instability in elastic tissues. *J. Mech. Phys. Solids*, 53:2284–2319, 2005.

[21] A. Goriely, M. Destrade, and M. Ben Amar. Instabilities in elastomers and in soft tissues. *The Quarterly Journal of Mechanics and Applied Mathematics*, 59:615–630, 2006.

[22] R. W. Ogden. Large deformation isotropic elasticity–on the correlation of theory and experiment for incompressible rubberlike solids. *Proc. R. Soc. Lond. A*, 326(1567):565–584, 1972.

[23] L. R. G. Treloar. The elasticity of a network of long-chain molecules—ii. *Trans. Faraday Soc.*, 39:241–246, 1943.

[24] H. M. James and E. Guth. Theory of the elastic properties of rubber. *J. Chem. Phys.*, 11(10):455–481, 1943.

[25] A. N. Gent. A new constitutive relation for rubber. *Rubber Chemistry Tech.*, 69:59–61, 1996.

[26] C. O. Horgan and G. Saccomandi. A molecular-statistical basis for the Gent constitutive model of rubber elasticity. *J. Elasticity*, 68:167–176, 2002.

[27] C. O. Horgan and G. Saccomandi. Constitutive models for compressible nonlinearly elastic materials with limiting chain extensibility. *J. Elasticity*, 77:123–138, 2004.

[28] C. O. Horgan. The remarkable Gent constitutive model for hyperelastic materials. *Int. J. Non Linear Mech. Tech.*, 68:9–16, 2015.

[29] L. Horny, T. Adamek, and R. Zitny. Age-related changes in longitudinal prestress in human abdominal aorta. *Arch. Appl. Mech.*, 83:875–888, 2013.

[30] C. O. Horgan and G. Saccomandi. A description of arterial wall mechanics using limiting chain extensibility constitutive models. *Biomechan. Model Mechanobiol.*, 1:251–266, 2003.

[31] M. Mooney. A theory of large elastic deformation. *J. Appl. Phys*, 11:582, 1940.

[32] R. S. Rivlin. Large elastic deformations of isotropic materials IV. Further developments of the general theory. *Phil. Trans. R. Soc. Lond. A*, 241(835):379–397, 1948.

[33] A. E. Shyer, T. Tallinen, Nandan L. Nerurkar, Z. Wei, E. S. Gil, D. L. Kaplan., C. J. Tabin, and L. Mahadevan. Villification: How the gut gets its villi. *Science*, 342:212–218, 2013.

[34] T. Savin, N. A. Kurpios, A. E. Shyer, P. Florescu, H. Liang, L. Mahadevan, and C. J. Tabin. On the growth and form of the gut. *Nature*, 476:57–63, 2011.

[35] E. Hannezo, J. Prost, and J. F. Joanny. Instabilities of monolayered epithelia: shape and structure of villi and crypts. *Phys. Rev. Lett.*, 107:078104, 2011.

[36] A. E. Shyer, T. R. Huycke, L. Mahadevan, and C. J. Tabin. Bending gradients: How the intestinal stem cell gets its home. *Cell*, 161:569–580, 2015.

[37] M. J. Razavi, R. Pidaparti, and X. Wang. Surface and interfacial creases in a bilayer tubular soft tissue. *Phys. Rev. E*, 94:022405, 2016.

[38] Wim M. van Rees, E. Vouga, and L. Mahadevan. Growth patterns for shape-shifting elastic bilayers. *PNAS*, 10:1073, 2017.

[39] D. E. Moulton and A. Goriely. Circumferential buckling instability of a growing cylindrical tube. *J. Mech. Phys. Solids*, 59:527–537, 2011.

[40] M. Diab, T. Zhang, R. Zhao, H. Gao, and K.-S. Kim. Ruga mechanics of creasing: from instantaneous to setback creases. *Proc. R. Soc. A*, 469(2157):20120753, 2013.

[41] B. Li, Y.-P. Cao, X.-Q. Feng, and H. Gao. Surface wrinkling of mucosa induced by volumetric growth: Theory, simulation and experiment. *J. Mech. Phys. Solids*, 59:758–774, 2011.

[42] M. J. Razavi, R. Pidaparti, and X. Wang. Surface and interfacial creases in a bilayer tubular soft tissue. *Phys. Rev. E*, 94(2):022405, 2016.

[43] P. Ciarletta and M. Ben Amar. Growth instabilities and folding in tubular organs: a variational method in non-linear elasticity. *Int. Journal. Non Linear Mech.*, 47(2):248–257, 2012.

[44] K. Efimenko, M. Rackaitis, E. Manias, A. Vazili, L. Mahadevan, and J. Genzer. Nested self-similar wrinkling patterns in skins. *Nature Mat.*, 4:293–297, 2005.

[45] M. Kücken and A. C. Newell. A model for fingerprint formation. *EPL (Europhysics Letters)*, 68(1):141, 2004.

[46] J. Dervaux, Y. Couder, M.-A. Guedeau-Boudeville, and M. Ben Amar. Shape transition in artificial tumors: From smooth buckles to singular creases. *Phys. Rev. Lett.*, 107:018103, 2011.

[47] N. Arun, A. Sharma, V. B. Shenoy, and K. S. Narayan. Electric-field-controlled surface instabilities in soft elastic films. *Adv. Mater.*, 18(5):660–663, 2006.

[48] Q. Wang, L. Zhang, and X. Zhao. Creasing to cratering instability in polymers under ultrahigh electric fields. *Phys. Rev. Lett.*, 106(11):118301, 2011.

[49] J. Huang, T. Li, C. C. Foo, J. Zhu, D. R. Clarke, and Z. Suo. Giant, voltage-actuated deformation of a dielectric elastomer under dead load. *Appl. Phys. Lett.*, 100(4):041911, 2012.

[50] H. Bense, M. Trejo, E. Reyssat, J. Bico, and B. Roman. Buckling of elastomer sheets under non-uniform electro-actuation. *Phys. Rev. Lett.*, 13:2876–2885, 2017.

[51] K. Danas and N. Triantafyllidis. Instability of a magnetoelastic layer resting on a non-magnetic substrate. *J. Mech. Phys. Solids*, 69:67–83, 2014.

[52] E. Sultan and A. Boudaoud. The buckling of a swollen thin gel layer bound to a compliant substrate. *J. Appl. Mech.*, 75:051002, 2008.

[53] D. Breid and A. J. Crosby. Surface wrinkling behavior of finite circular plates. *Soft Matter*, 5:425–431, 2009.

[54] M. G., J. A. Burdick, and S. Yang. Solvent induced transition from wrinkles to creases in thin film gels with depth-wise crosslinking gradients. *Soft Matter*, 6:5795–5801, 2010.

[55] Z. Wu, N. Bouklas, and R. Huang. Swell-induced surface instability of hydrogel layers with material properties varying in thickness direction. *Int J Solids Struct.*, 50:578–587, 2013.

[56] S. Mora, C. Maurini, T. Phou, J.-M. Fromental, B. Audoly, and Y. Pomeau. Solid drops: Large capillary deformations of immersed elastic rods. *Phys. Rev. Lett.*, 111:114301, 2013.

[57] S. Mora, T. Phou, J.-M. Fromental, L. M. Pismen, and Y. Pomeau. Capillarity driven instability of a soft solid. *Phys. Rev. Lett.*, 105:214301, 2010.

[58] E. S. Matsuo and T. Tanaka. Patterns in shrinking gels. *Nature*, 358:482–485, 1992.

[59] M. Taffetani and P. Ciarletta. Elastocapillarity can control the formation and the morphology of beads-on-string structures in solid fibers. *Phys. Rev. E*, 91:032413, 2015.

[60] C. Xuan and J. S. Biggins. Finite-wavelength surface-tension-driven instabilities in soft solids, including instability in a cylindrical channel through an elastic solid. *Phys. Rev. E*, 94(2):023107, 2016.

[61] C. Xuan and J. S. Biggins. Plateau-Rayleigh instability in solids is a simple phase separation. *Phys. Rev. E*, 95(5):053106, 2017.

[62] S. Mora, T. Phou, J.-M. Fromental, and Y. Pomeau. Gravity driven instability in elastic solid layers. *Phys. Rev. Lett.*, 113:178301, 2014.

[63] X. Liang and S. Cai. Gravity induced crease-to-wrinkle transition in soft materials. *Appl. Phys. Lett.*, 106:041907, 2015.

[64] D. Riccobelli and P. Ciarletta. Rayleigh–Taylor instability in soft elastic layers. *Phil. Trans. R. Soc. A*, 375:20160421, 2017.

[65] S. P. Timoshenko and J. M. Gere. *Theory of Elastic Instability*. McGraw Hill, 2 edition, 1961.

[66] H. G. Allen. *Analysis and Design of Sandwich Panels*. Pergamon, New York, 1969.

[67] W. S. Slaughter. *The Linearized Theory of Elasticity*. Springer Science & Business Media, 2002.

[68] Y. Cao and J. W. Hutchinson. Wrinkling phenomena in neo-Hookean film/substrate bilayer. *J. Appl. Mech.*, 79:031019, 2012.

[69] F. Jia and M. Ben Amar. Theoretical analysis of growth or swelling wrinkles on constrained soft slabs. *Soft Matter*, 9:8216–8226, 2013.

[70] T. Hwa and M. Kardar. Evolution of surface patterns on swelling gels. *Phys. Rev. Lett.*, 51:106–109, 1988.

[71] A. Onuki. Theory of pattern formation in gels: Surface folding in highly compressible elastic bodies. *Phys. Rev. A*, 39:5932–5948, 1989.

[72] S. A. Silling. Creasing singularities in compressible elastic materials. *J. Appl. Mech*, 58:70–74, 1991.

[73] A. Ghatak and A. Lal Das. Kink instability of a highly deformable elastic cylinder. *Phys. Rev. Lett.*, 99:076101, 2007.

[74] E. Hohlfeld and L. Mahadevan. Unfolding the sulcus. *Phys. Rev. Lett.*, 106:105702, 2011.

[75] E. Hohlfeld and L. Mahadevan. Scale and nature of sulcification patterns. *Phys. Rev. Lett.*, 109:025701, 2012.

[76] T. Tallinen, J. S. Biggins, and L. Mahadevan. Surface sulci in squeezed soft solids. *Phys. Rev. Lett.*, 110:024302, 2013.

[77] J. Bradbury. Molecular insights into human brain evolution. *PLoS Biol*, 3:e50, 2005.

[78] T. Tallinen and J. S. Biggins. Mechanics of invagination and folding: Hybridized instabilities when one soft tissue grows on another. *Phys. Rev. E*, 92:022720, 2015.

[79] L. Jin, A. Auguste, R. C. Hayward, and Z. Suo. Bifurcation diagrams for the formation of wrinkles or creases in soft bilayers. *J. Appl. Mech.*, 82:061008, 2015.

[80] Q. Wang and X. Zhao. Phase diagrams of instabilities in compressed film-substrate systems. *J. Appl. Mech.*, 81:051004, 2014.

[81] Q. Wang and X. Zhao. A three-dimensional phase diagram of growth-induced surface instabilities. *Scientific Reports*, 5:8887, 2015.

[82] M. Diab, T. Zheng, R. Zhao, H. Gao, and K.-S. Kim. Ruga mechanisc of creasing: from instantaneous to setback creases. *EPL (Europhysics Letters)*, 68:141–146, 2004.

[83] R. Zhao, T. Zhang, M. Diab, H. Gao, K.-S., and Kim. The primary bilayer ruga-phase diagram i: Localizations in ruga evolution. *Extreme Mechanics Letter*, 4:76–82, 2015.

[84] F. Brau, H. Vandeparre, A. Sabbah, C. Poulard, A. Boudaoud, and P. Damman. Multiple-length-scale elastic instability mimics parametric resonance of nonlinear oscillators. *Nat. Phys.*, 7:56–60, 2011.

[85] Y. Cao and J. W. Hutchinson. From wrinkles to creases in elastomers: the instability and imperfection-sensitivity of wrinkling. *Proc. R. Soc. A*, 468:94–115, 2012.

[86] J. W. Hutchinson. The role of nonlinear substrate elasticity in the wrinkling of thin films. *Proc. R. Soc. A*, 371:20120422, 2013.

[87] S. Budday, E. Kuhl, and J. W. Hutchinson. Period-doubling and period-tripling in growing bilayered systems. *Philos Mag (Abingdon)*, 98:3208–3224, 2015.

[88] A. Auguste, L. Jin, Z. Suo, and R. C. Hayward. Post-wrinkle bifurcations in elastic bilayers with modest contrast in modulus. *Extreme Mechanics Letters*, 11:30–36, 2017.

[89] G. I. Taylor. The instability of liquid surfaces when accelerated in a direction perpendicular to their planes. I. *Proc. R. Soc. London Ser. A*, 201:192, 1950.

[90] D. H. Sharp. An overview of Rayleigh-Taylor instability. *Physica D: Nonlinear Phenomena*, 12:3–10, 1984.

[91] H. Lamb. *Hydrodynamics*. Cambridge University Press, 6th edition, 1994.

[92] P. G. Saffman and G. I. Taylor. The penetration of a fluid into a porous medium or hele-shaw cell containing a more viscous liquid. *Proc. R. Soc. A*, 245:312, 1958.

[93] D. Bensimon, L. P. Kadanoff, S. Liang, B. I. Shraiman, and C. Tang. Viscous flows in two dimensions. *Rev. Mod. Phys.*, 58:977, 1986.

[94] K. R. Shull, C. M. Flanigan, and A. J. Crosby. Fingering instabilities of confined elestic layers in tension. *Phys. Rev. Lett.*, 84:3057–3060, 1999.

[95] J. S. Biggins, B. Saintyves, Z. Wei, E. Bouchaud, and L. Mahadevan. Digital instability of a confined elastic meniscus. *PNAS*, 110:12545–12548, 2013.

[96] B. Saintyves, O. Dauchot, and E. Bouchaud. Bulk elastic fingering instability in hele-shaw cells. *Phys. Rev. Lett.*, 111:047801, 2013.

[97] J. S. Biggins, Z. Wei, and L. Mahadevan. Fluid-driven fingering instability of a confined elastic meniscus. *EPL (Europhysics Letters)*, 110:34001, 2015.

[98] A. N. Gent and P. B. Lindley. Internal rupture of bonded rubber cylinders in tension. *Proc. R. Soc. Lond. A*, 249:195–205, 1959.

[99] A. N. Gent. Elastic instabilities of inflated rubber shells. *Rubber Chemistry and Technology*, 72(2):263–268, 1999.

[100] A. N. Gent. Elastic instabilities in rubber. *Int. J. Non Linear Mech.*, 40:165–175, 2005.

[101] H. Alexander. The tensile instability of an inflated cylindrical membrane as affected by an axial load. *Int. J. Mech. Sci.*, 13(2):87–95, 1971.

[102] A. Mallock. II. Note on the instability of india-rubber tubes and balloons when distended by fluid pressure. *Proc. Royal Soc. Lond.*, 49(296-301):458–463, 1891.

[103] F. Meng, J. Z. Y. Chen, M. Doi, and Z. Ouyang. The phase diagram and radial collapse of an inflated soft tube under twist. *Soft Matter*, 11:7046, 2015.

[104] P. G. de Gennes, F. Brochard-Wyart, and D. Quere. *Capillarity and Wetting Phenonemena*. Springer, New York, 2004.

[105] J. W. Strutt and L. Rayleigh. On the instability of jets. *Proceedings of the London Mathematical Society*, s1-10(1):4–13, 1878.

[106] B. Roman and J. Bico. Elasto-capillarity: deforming an elastic structure with a liquid droplet. *J. Phys.: Condens. Matter*, 22:493101, 2010.

[107] R. W. Style, C. Hyland, R. Boltyamskiy, J. S. Wettlaufer, and E. R. Dufrense. Surface tension and contact with soft elastic solids. *Nat. Com.*, 4:2728, 2013.

[108] J. Bico, E. Reyssat, and B. Roman. Elastocapillarity: When surface tension deforms elastic solids. *Annul. Rev. Fluid Mech.*, 50:629–659, 2018.

[109] E. Orowan. Surface energy and surface tension in solids and liquids. *Proc. Roy. Soc. Lond. A*, 316:473–491, 1970.

[110] M. E. Avery and J. Mead. Surface properties in relation to atelectasis and hyaline membrane disease. *AMA Am. J. Dis. Child*, 97:517–523, 1959.

[111] A. L. Hazel and M. Heil. Surface-tension-induced buckling of liquid-lined elastic tubes: a model for pulmonary. *Proceedings of the Royal Society A: Mathematical, Physical and Engineering Science*, 106:041907, 2005.

[112] L. D. Landao. On the theory of phase transitions. *Zh. Eksp. Teor. Fiz.*, 7:19–32, 1937.

[113] W. T. Koiter. *Over de stabiliteit van het elastisch evenwicht (On the Stability of Elastic Equilibrium)*. PhD thesis, Polytechnic Institute of Delft, 1945.

[114] J. E. Akin. *Finite Element Analysis for Undergraduates*. Academic Press, London, 1986.

[115] I. Babuška and M. Suri. Locking effects in the finite element approximation of elasticity problems. *Proc. Roy. Soc. Lond. A*, 62(1):439–463, 1992.

[116] N. Cheewaruangroj, K. Leonavicius, S. Srinivas, and J. S. Biggins. Peristaltic elastic instability in an inflated cylindrical channel. *Phys. Rev. Lett.*, 122:068003, 2019.

[117] T. J. Pedley, G. K. Batchelor, H. K. Moffat, and M. G. Worster. Blood flow in arteries and veins. *Perspectives in fluid dynamics: a collective introduction to current research*, pages 105–158, 2000.

[118] M. A. Unger, H. Chou, T. Thorsen, A. Scherer, and S. R. Quake. Monolithic microfabricated valves and pumps by multilayer soft lithography. *Science*, 288(5463):113–116, 2000.

[119] Y. Xia and G. M. Whitesides. Soft lithography. *Annual review of materials science*, 28(1):153–184, 1998.

[120] J. C. McDonald, D. C. Duffy, and J. R. Anderson. Fabrication of microfluidic systems in poly (dimethylsiloxane). *Electrophoresis*, pages 27–40.

[121] T. Thorsen, S. J. Maerkl, and S. R. Quake. Microfluidic large-scale integration. *Science*, 298(5593):580–584, 2002.

[122] H. Chou, M. A. Unger, and S. R. Quake. A microfabricated rotary pump. *Biomedical Microdevices*, 3(4):323–330, 2001.

[123] I. E. Araci, B. Su, S. R. Quake, and Y. Mandel. An implantable microfluidic device for self-monitoring of intraocular pressure. *Nat. med.*, 20(9):1074, 2014.

[124] A. Koh, D. Kang, Y. Xue, S. Lee, R. M. Pielak, J. Kim, T. Hwang, S. Min, A. Banks, P. Bastien, M. C. Manco, L. Wang, K. R. Ammann, K. Jang, P. Won, S. Han, R. Ghaffari, U. Paik, M. J. Slepian, G. Balooch, Y. Huang, and J. A. Rogers. A soft, wearable microfluidic device for the capture, storage, and colorimetric sensing of sweat. *Science Translational Medicine*, 8(366):366ra165–366ra165, 2016.

[125] A. H. Corneliussen and R. T. Shield. Finite deformation of elastic membranes with application to the stability of an inflated and extended tube. *Archive for Rational Mechanics and Analysis*, 7(1):273–304, 1961.

[126] R. T. Shield. On the stability of finitely deformed elastic membranes. *Zeitschrift für angewandte Mathematik und Physik ZAMP*, 23(1):16–34, Jan 1972.

[127] D. M. Haughton and R. W. Ogden. Bifurcation of inflated circular cylinders of elastic material under axial loading—I. Membrane theory for thin-walled tubes. *J. Mech. Phys. Solids*, 27(3):179–212, 1979.

[128] D. M. Haughton and R. W. Ogden. Bifurcation of inflated circular cylinders of elastic material under axial loading—II. Exact theory for thick-walled tubes. *J. Mech. Phys. Solids*, 27(5-6):489–512, 1979.

[129] Y. B. Fu, S. P. Pearce, and Kuo-Kang Liu. Post-bifurcation analysis of a thin-walled hyperelastic tube under inflation. *Int. J. Non Linear Mech.*, 43(8):697–706, 2008.

[130] F. Meng, J. Z. Y. Chen, Z. Ouyang, et al. Phase diagrams and interface in inflating balloon. *AIChE Journal*, 60(4):1393–1399, 2014.

[131] C. A. Schneider, W. S. Rasband, and Eliceiri K, W. NIH Image to ImageJ: 25 years of image analysis. *Nat. Methods.*, 9(7):671–675, 2012.

[132] J. R. Tse and A. J. Engler. Preparation of hydrogel substrates with tunable mechanical properties. *Current protocols in cell biology*, pages 10–16, 2010.

[133] J. Tang, J. Li, J. J. Vlassak, and Z. Suo. Fatigue fracture of hydrogels. *Extreme Mechanics Letters*, 10:24–31, 2017.

[134] The MathWorks Inc. Matlab, version 9.1.0 (r2016a), 2016.

[135] S. Pagliara, K. Franze, C. R. McClain, G. W. Wylde, C. L. Fisher, R. J. M. Franklin, A. J. Kabla, U. F. Keyser, and K. J. Chalut. Auxetic nuclei in embryonic stem cells exiting pluripotency. *Nat. mat.*, 13(6):638, 2014.

[136] T. Pieters and F. van Roy. Role of cell-cell adhesion complexes in embryonic stem cell biology. *J. Cell Sci.*, 127(Pt 12):2603–13, 2014.

[137] J. F. Casella, M. D. Flanagan, and S. Lin. Cytochalasin D inhibits actin polymerization and induces depolymerization of actin filaments formed during platelet shape change. *Nature*, 293(5830):302, 1981.

[138] T. L. Le, J. L. Stow, et al. Recycling of E-cadherin: a potential mechanism for regulating cadherin dynamics. *The Journal of cell biology*, 146(1):219–232, 1999.

[139] L. Rayleigh. XXVI. On the remarkable phenomenon of crystalline reflexion described by Prof. Stokes. *The London, Edinburgh, and Dublin Philosophical Magazine and Journal of Science*, 26:256, 1888.

[140] K. Bertoldi and M. C. Boyce. Mechanically triggered transformations of phononic band gaps in periodic elastomeric structures. *Phys. Rev. B*, 77:052105, 2008.

[141] J. Marthelot, P.-T. Brun, F. López Jiménez, , and P. M. Reis. Reversible patterning of spherical shells through constrained buckling. *Phys. Rev. Materials*, 1:025601, 2017.

[142] D. Wang, N. Cheewaruangroj, Y. Li, G. Michale, Y. Jiang, D. Wood, J. S. Biggins, and B. B. Xu. Spatially configuring wrinkle pattern and multiscale surface evolution with structural confinement. *Advanced Functional Materials*, page 1704228, 2017.

[143] P.-C. Lin, S. Vajpayee, A. Jagota, C.-Y. Huid, and S. Yang. Mechanically tunable dry adhesive from wrinkled elastomers. *Soft Matter*, 4:1830–1835, 2008.

[144] E. P. Chan, E. J. Smith, R. C. Hayward, and A. J. Crosby. Surface wrinkles for smart adhesion. *Adv. Mater.*, 20:711–716, 2008.

[145] K. Khare, J. Zhou, and S. Yang. Tunable open-channel microfluidics on soft Poly(dimethylsiloxane) (PDMS) substrates with sinusoidal grooves. *Langmuir*, 25(21):12794–12799, 2009.

[146] S. G. Lee, D. Y. Lee, H. S. Lim, D. H. Lee, S. Lee, and K. Cho. Switchable transparency and wetting of elastomeric smart windows. *Adv. Mater.*, 22(44):5013–7, 2010.

[147] X. Huang., Y. Sun, and S. Soh. Stimuli-responsive surfaces for tunable and reversible control of wettability. *Adv. Mater.*, 27(27):4062–8, 2015.

[148] P. Görrn, M. Lehnhardt, W. Kowalsky, T. Riedl, and S. Wagner. Elastically tunable self-organized organic lasers. *Adv. Mater.*, 23(7):869–72, 2011.

[149] E. Lee, M. Zhang, Y. Cho, Y. Cui, J. Van der Spiegel, N. Engheta, and S. Yang. Tilted pillars on wrinkled elastomers as a reversibly tunable optical window. *Adv. Mater.*, 26(24):4127–33, 2014.

[150] S. Zeng, D. Zhang, W. Huang, Z. Wang, S. G. Freire, X. Yu, A. T. Smith, E. Y. Huang, H. Nguon, and L. Sun. Bio-inspired sensitive and reversible mechanochromisms via strain-dependent cracks and folds. *Nature Communications*, 7:11802, 2016.

[151] J. Shim, C. Perdigou, E. R. Chen, K. Bertoldi, and P. M. Reis. Buckling-induced encapsulation of structured elastic shells under pressure. *PNAS*, 109(16):5978–5983, 2012.

[152] P. Christian, H. M. A. Ehmann, O. Werzerbc, and A. M. Coclite. Wrinkle formation in a polymeric drug coating deposited via initiated chemical vapor deposition. *Soft Matter*, 12:9501, 2016.

[153] Z. Y. Huang, W. Hong, and Z. Suo. Nonlinear analyses of wrinkles in a film bonded to compliant substrate. *J. Mech. Phys. Solids*, 53:2101–2118, 2005.

[154] R. Huang and Z. Suo. Instability of a compressed elastic film on a viscous layer. *Int. J. Solids Struct.*, 39:1791–1802, 2002.

[155] H. Jiang, D.-Y. Khang, J. Song, Y. Sun, Y. Huang, and J. A. Rogers. Finite deformation mechanics in buckled thin films on compliant supports. *PNAS*, 104(40):15607–15612, 2007.

[156] H. Jiang, D.-Y. Khang, H. Fei, H. Kim, Y. Huang, J. Xiao, and J. A. Rogers. Finite width effect of thin-films buckling on compliant substrate: Experimental and theoretical studies. *J. Mech. Phys. Solids*, 56:2595–2598, 2008.

[157] S. Wang, J. Song, D.-H. Kim, Y. Huang, and J. A. Rogers. Local versus global buckling of thin films on elastomeric substrates. *Appl. Phys. Lett.*, 93:023126, 2008.

[158] J. Song, H. Jiang, Z.J. Liu, D.Y. Khang, Y. Huang, J. A. Rogers, C. Luc, and C.G. Koh. Buckling of a stiff thin film on a compliant substrate in large deformation. *Int. J. Solids Struct.*, 45:3107–3121, 2008.

[159] S. H. Im and R. Huang. Instability of a compressed elastic film on a viscous layer. *J. Mech. Phys. Solids*, 56:3315–3330, 2008.

[160] S. Cai, D. Breid, A. J. Crosby, Z. Suo, and J. W. Hutchinson. Periodic patterns and energy states of buckled films on compliant substrates. *J. Mech. Phys. Solids*, 59:1094–1114, 2011.

[161] E. Cerda and L. Mahadevan. Geometry and physics of wrinkling. *Phys. Rev. Lett.*, 90:074302, 2003.

[162] X. Chen and J. W. Hutchinson. Herringbone buckling patterns of compressed thin films on compliant substrates. *J. Appl. Mech.*, 71:597–603, 2004.

[163] B. Audoly and A. Boudaoud. Buckling of a thin film bound to a compliant substrate—Part II:: A global scenario for the formation of herringbone pattern. *Phys. Solids*, 56:2422–2443, 2008.

[164] B. Audoly and A. Boudaoud. Buckling of a thin film bound to a compliant substrate—Part III:: Herringbone solutions at large buckling parameter. *Phys. Solids*, 56:2444–2458, 2008.

[165] B. Audoly and A. Boudaoud. Buckling of a thin film bound to a compliant substrate—Part I:: Formulation, linear stability of cylindrical patterns, secondary bifurcations. *Phys. Solids*, 56:2401–2421, 2008.

[166] D. Breid and A. J. Crosby. Effect of stress state on wrinkle morphology. *Soft Matter*, 7:4490–4496, 2011.

[167] S. Cai, D. Chen, Z. Suo, and R. C. Hayward. Creasing instability of elastomer films. *Soft Matter*, 8:1301, 2012.

[168] M. Ben Amar and P. Ciarletta. Swelling instability of surface-attached gels as a model of soft tissue growth under geometric constraints. *J. Mech. Phys. Solid*, 58:935–954, 2010.

[169] P. Ciarletta. Wrinkle-to-fold transition in soft layers under equi-biaxial strain: A weakly nonlinear analysis. *J. Mech. Phys. Solids*, 73:118–133, 2014.

[170] R. C. Hayward V. Trujillo, J. Kim. Creasing instability of surface-attached hydrogels. *Soft Matter*, 4:564–569, 2008.

[171] M. A. Holland, B. Li, X. Q. Feng., and E. Kuhl. Instabilities of soft films on compliant substrates. *J. Mech. Phys. Solids*, 98:350–365, 2017.

[172] S. Budday, S. Andres, B. Walter, P. Steinmann, and E. Kuhl. Wrinkling instabilities in soft bilayered systems. *Phil. Trans. R. Soc. A*, 375:20160163, 2016.

[173] L. Jin, A. Takei, and J. W. Hutchinson. Mechanics of wrinkle/ridge transitions in thin film/substrate systems. *J. Mech. Phys. Solids*, 81:22–40, 2015.

[174] Wolfram Research, Inc. Mathematica, Version 11.0, 2018. Champaign, IL.

[175] Y. Fu and G. A. Rogerson. A nonlinear analysis of in stability of a pre-stressed incompressible elastic plate. *Proc. R. Soc. Lond. A*, 446:233–254, 1994.

[176] H. Bénard. Les tourbillons cellulaires dans une nappe liquide propageant de la chaleur par convection: en régime permanent. *Annales de chimie et de physique*, 1901.

[177] Lord Rayleigh O.M. F.R.S. Lix. on convection currents in a horizontal layer of fluid, when the higher temperature is on the under side. *The London, Edinburgh, and Dublin Philosophical Magazine and Journal of Science*, 32(192):529–546, 1916.

[178] M. D. Cowley and R. E. Rosenweig. The interfacial stability of a ferromagnetic. *J. Fluid Mech.*, 30:671–688, 1967.

[179] A. Gailitis. Formation of the hexagonal pattern on the surface of a ferromagnetic fluid in an applied magnetic field. *J. Fluid Mech.*, 82:401–413, 1977.

[180] Y. Cao and Z. J. Ding. Formation of hexagonal pattern of ferro fluid in magnetic field. *J. Magn. Magn. Mater*, 355:93–99, 2014.

[181] C. Gollwitzer, I. Rehberg, and R. Richter. Via hexagons to squares in ferrofluids: experiments on hysteretic surface transformations under variation of the normal magnetic field. *J. Phys.: Condens. Matter*, 18:S2643–S2656, 2006.

[182] A. Chakrabarti, S. Mora, F. Richard, T. Phou, J.-M. Fromental, Y. Pomeau, and B. Audoly. Selection of hexagonal buckling patterns by the elastic Rayleigh-Taylor instability. *J. Mech. Phys. Solids*, 121:234–257, 2018.

[183] M. A. Bravais. *On the systems formed by points regularly distributed on a plane or in space*. Crystallographic Society of America, 1949.

[184] D. Chen, S. Cai, Z. Suo, and R. C. Hayward. Surface energy as a barrier to creasing of elastomer films: An elastic analogy to classical nucleation. *Phys. Rev. Lett.*, 109:038001, 2012.

[185] D. Chen, J. Yoon, D. Chandra, A. J. Crosby, and R. C. Hayward. Stimuli-responsive buckling mechanics of polymer films. *J. Polym. Sci., Part B: Polym. Phys.*, 52:1441–1461, 2014.

[186] R. W. Bailey and R. Fidler. Stress analysis of plates and shells containing patterns of reinforced holes. *Nuclear Engineering and Design*, 3:41–53, 1966.

[187] M. Kachanov, B. Shafiro, and I. Tsukrov. *Handbook of Elasticity Solutions*. Springer, Dordrecht, 2003.

[188] H. King, R. D. Schroll, B. Davidovitch, and N. Menon. Elastic sheet on a liquid drop reveals wrinkling and crumpling as distinct symmetry-breaking instabilities. *PNAS*, 109(25):9716–9720, 2012.

[189] O. Oshri, F. Brau, and H. Diamant. Wrinkles and folds in a fluid-supported sheet of finite size. *Phys. Rev. E*, 91:052408, 2015.

[190] A. Agrawal, P. Luchette, P. Palffy-Muhoray, S. L. Biswal, W. G. Chapmana, and R. Verduzco. Surface wrinkling in liquid crystal elastomers. *Soft Matter*, 8:7138, 2012.

[191] H. Soni, R. A. Pelcovits, and T. R. Powers. Wrinkling of a thin film on a nematic liquid crystal elastomer. *Phys. Rev. E*, 94:012701, 2016.

[192] M. Ben Amar and L. J. Cummings. Fingering instabilities in driven thin nematic films. *Physics of Fluids*, 13:1160, 2001.

[193] N. Cheewaruangroj and E. M. Terentjev. Shape instability on swelling of a stretched nematic elastomer filament. *Phys. Rev. E*, 92:042502, 2015.

Appendix A

Vector and matrix identities

In this appendix, I present the vector and matrix identities that have been used throughout this thesis.

Vector calculus

Cartesian coordinate (x, y, z)

The comma denotes partial derivative, $u_{z,x} = \frac{\partial u_z}{\partial x}$ and $u_{z,xy} = \frac{\partial^2 u_z}{\partial x \partial y}$.

$$\mathbf{u} = \begin{pmatrix} u_x \\ u_y \\ u_z \end{pmatrix} \qquad \nabla \cdot \mathbf{u} = u_{x,x} + u_{y,y} + u_{z,z}$$

$$\nabla \mathbf{u} = \begin{pmatrix} u_{x,x} & u_{x,y} & u_{x,z} \\ u_{y,x} & u_{y,y} & u_{y,z} \\ u_{z,x} & u_{z,y} & u_{z,z} \end{pmatrix} \qquad \nabla^2 \mathbf{u} = \begin{pmatrix} u_{x,xx} + u_{x,yy} + u_{x,zz} \\ u_{y,xx} + u_{y,yy} + u_{y,zz} \\ u_{z,xx} + u_{z,yy} + u_{z,zz} \end{pmatrix}$$

Cylindrical polar coordinate (r, θ, z)

$$\mathbf{u} = \begin{pmatrix} u_r \\ u_\theta \\ u_z \end{pmatrix} \qquad \nabla \cdot \mathbf{u} = u_{r,r} + \frac{u_r + u_{\theta,\theta}}{r} + u_{z,z}$$

$$\nabla \mathbf{u} = \begin{pmatrix} u_{r,r} & \frac{u_{r,\theta} - u_\theta}{r} & u_{r,z} \\ u_{\theta,r} & \frac{u_r + u_{\theta,\theta}}{r} & u_{\theta,z} \\ u_{z,r} & \frac{u_{z,\theta}}{r} & u_{z,z} \end{pmatrix} \qquad \nabla^2 \mathbf{u} = \begin{pmatrix} u_{r,rr} + \frac{u_{r,r}}{r} + \frac{u_{r,\theta\theta} - u_r - 2u_{\theta,\theta}}{r^2} + u_{r,zz} \\ u_{\theta,rr} + \frac{u_{\theta,r}}{r} + \frac{u_{\theta,\theta\theta} - u_\theta + 2u_{r,\theta}}{r^2} + u_{\theta,zz} \\ u_{z,rr} + \frac{u_{z,\theta\theta}}{r^2} + \frac{u_{z,r}}{r} + u_{z,zz} \end{pmatrix}$$

For an axisymmetric system, $\mathbf{u}(r,\theta,z) = (u_r(r,z), 0, u_z(r,z))$:

$$\mathbf{u} = \begin{pmatrix} u_r \\ 0 \\ u_z \end{pmatrix} \qquad \nabla\cdot\mathbf{u} = u_{r,r} + \frac{u_r}{r} + u_{z,z}$$

$$\nabla\mathbf{u} = \begin{pmatrix} u_{r,r} & 0 & u_{r,z} \\ 0 & \frac{u_r}{r} & 0 \\ u_{z,r} & 0 & u_{z,z} \end{pmatrix} \qquad \nabla^2\mathbf{u} = \begin{pmatrix} u_{r,rr} + \frac{u_{r,r}}{r} - \frac{u_r}{r^2} + u_{r,zz} \\ 0 \\ u_{z,rr} + \frac{u_{z,r}}{r} + u_{z,zz} \end{pmatrix}.$$

Spherical polar coordinate (r,θ,z)

For a spherically symmetric system, $\mathbf{u}(r,\theta,z) = (u_r(r), 0, 0)$:

$$\mathbf{u} = \begin{pmatrix} u_r \\ 0 \\ 0 \end{pmatrix} \qquad \nabla\cdot\mathbf{u} = u_{r,r} + \frac{2u_r}{r}$$

$$\nabla\mathbf{u} = \begin{pmatrix} u_{r,r} & 0 & 0 \\ 0 & \frac{u_r}{r} & 0 \\ 0 & 0 & \frac{u_r}{r} \end{pmatrix} \qquad \nabla^2\mathbf{u} = \begin{pmatrix} u_{r,rr} + \frac{2u_{r,r}}{r} - \frac{2u_r}{r^2} \\ 0 \\ 0 \end{pmatrix}.$$

Matrix calculus

$$\frac{\partial \mathrm{Tr}(A)}{\partial A} = I$$
$$\frac{\partial \mathrm{Tr}(A\cdot B)}{\partial A} = B^T$$
$$\frac{\partial \mathrm{Tr}\left(A\cdot B^T\right)}{\partial A} = B$$
$$\frac{\partial \mathrm{Tr}\left(A\cdot A^T\right)}{\partial A} = 2A$$
$$\frac{\partial \mathrm{Det}(A)}{\partial A} = \mathrm{Det}(A)A^{-T} = \mathrm{cof}(A)$$

Matrix identities

For a 2×2 matrix:

$$\begin{aligned} \mathrm{Det}(A) &= \frac{1}{2}\left(\mathrm{Tr}\,(A)^2 - \mathrm{Tr}\left(A^2\right)\right) \\ \mathrm{adj}(A) &= I\,\mathrm{Tr}\,(A) - A, \end{aligned}$$

where $\mathrm{adj}(A)$ is the adjugate matrix, which is the transpose of the cofactor matrix, $\mathrm{cof}(A)$. For a 3×3 matrix:

$$\begin{aligned} \mathrm{Det}(A) &= \frac{1}{6}\left(\mathrm{Tr}\,(A)^3 - 3\mathrm{Tr}\left(A^2\right)\mathrm{Tr}\,(A) + 2\mathrm{Tr}\left(A^3\right)\right) \\ \mathrm{adj}(A) &= \frac{1}{2}I\left(\mathrm{Tr}\,(A)^2 - \mathrm{Tr}\left(A^2\right)\right) - A\mathrm{Tr}\,(A) + A^2. \end{aligned}$$

Appendix B

Finite element analysis code

The codes that I use for the finite element analysis is adapted from the original code written by Tuomas Tallinen, used in [78]. In this appendix chapter, I present his code, `Gyrus.cpp`, which is written in C++. It uses vector and matrix functions from `vema.h`, but is stand-alone otherwise. The code simulates a growing soft layer with free surface in a simple 2D set up, modelling surface instabilities and formation of folds, gyri and sulci. Minimal implementation using triangular finite elements and an explicit solver to minimize deformation energy (see Section 2.1).

Header file for vector and matrix operations, `vema.h`:

```
#include <cmath>

class Vector{ // class for vector
public:
   double x, y, z;
   Vector(): x(0.0), y(0.0), z(0.0) {};
   Vector(double ax, double ay, double az): x(ax), y(ay), z(az) {};

   double length(){ // length of the vector
      return sqrt(x*x + y*y + z*z);
   }
   double dot(const Vector& b){ // vector dot product
      return x*b.x + y*b.y + z*b.z;
   }
   Vector cross(const Vector& b){ // vector cross product
      return Vector(y*b.z - z*b.y, z*b.x - x*b.z, x*b.y - y*b.x);
   }
```

```
void normalize(){ // normalize the vector
   double temp = 1.0/length();
   x *= temp;
   y *= temp;
   z *= temp;
}
void clear(){
   x = y = z = 0.0;
}
Vector& operator+= (const Vector& b){
   x += b.x;
   y += b.y;
   z += b.z;
   return *this;
}
Vector& operator-= (const Vector& b){
   x -= b.x;
   y -= b.y;
   z -= b.z;
   return *this;
}
Vector& operator*= (const double& c){
   x *= c;
   y *= c;
   z *= c;
   return *this;
}
Vector& operator/= (const double& c){
   x /= c;
   y /= c;
   z /= c;
   return *this;
}
Vector operator+ (const Vector& b){
   Vector r = *this;
   return r += b;
}
Vector operator- (const Vector& b){
   Vector r = *this;
```

```
      return r -= b;
   }
   Vector operator* (const double& c){
      Vector r = *this;
      return r *= c;
   }
   Vector operator/ (const double& c){
      Vector r = *this;
      return r /= c;
   }
};

class Matrix{ // class for matrix
public:
  double a, b, c,
    d, e, f,
    g, h, i;

  Matrix(): a(1.0), b(0.0), c(0.0),
       d(0.0), e(1.0), f(0.0),
       g(0.0), h(0.0), i(1.0) {};

  Matrix(double aa, double ab, double ac,
    double ad, double ae, double af,
    double ag, double ah, double ai):
    a(aa), b(ab), c(ac),
    d(ad), e(ae), f(af),
    g(ag), h(ah), i(ai) {};

  Matrix(Vector c1, Vector c2, Vector c3):
   a(c1.x), b(c2.x), c(c3.x),
   d(c1.y), e(c2.y), f(c3.y),
   g(c1.z), h(c2.z), i(c3.z) {};

  double det(){
    return a*e*i - a*f*h - b*d*i + b*f*g + c*d*h - c*e*g;
  }
  double trace(){
    return a + e + i;
```

```
}
Matrix prod(const Matrix& n) { // matrix multiplication
  return Matrix( a*n.a+b*n.d+c*n.g, a*n.b+b*n.e+c*n.h, a*n.c+b*n.f+c*n.i,
       d*n.a+e*n.d+f*n.g, d*n.b+e*n.e+f*n.h, d*n.c+e*n.f+f*n.i,
       g*n.a+h*n.d+i*n.g, g*n.b+h*n.e+i*n.h, g*n.c+h*n.f+i*n.i );
}
Vector prod(const Vector& v) {
  return Vector( a*v.x+b*v.y+c*v.z, d*v.x+e*v.y+f*v.z, g*v.x+h*v.y+i*v.z );
}
Matrix trans() { // matrix transpose
  return Matrix(a, d, g, b, e, h, c, f, i);
}
Matrix inv() { // matrix inverse
  return Matrix( e*i-f*h, c*h-b*i, b*f-c*e,
       f*g-d*i, a*i-c*g, c*d-a*f,
       d*h-e*g, b*g-a*h, a*e-b*d )/det();
}
Vector EV() {// eigenvectors
 double l1, l2, l3;
 double c1, c0, p, q, phi, t, s;

 c1 = a*e + a*i + e*i - b*b - f*f - c*c;
 c0 = i*b*b + a*f*f + e*c*c - a*e*i - 2.0*c*b*f;
 p = trace()*trace() - 3.0*c1;
 q = trace()*(p - 3.0/2.0*c1) - 27.0/2.0*c0;

 phi = 27.0 * (0.25*c1*c1*(p-c1) + c0*(q + 27.0/4.0*c0));
 phi = 1.0/3.0 * atan2(sqrt(fabs(phi)), q);
 t = sqrt(fabs(p))*cos(phi);
 s = 1.0/sqrt(3.0)*sqrt(fabs(p))*sin(phi);

 l3 = 1.0/3.0*(trace() - t) - s;
 l2 = l3 + 2.0*s;
 l1 = l3 + t + s;
 return Vector(l1, l2, l3);
}
Matrix& operator+= (const Matrix& n){
  a += n.a; b += n.b; c += n.c;
  d += n.d; e += n.e; f += n.f;
```

```
    g += n.g; h += n.h; i += n.i;
    return *this;
  }
  Matrix& operator-= (const Matrix& n){
    a -= n.a; b -= n.b; c -= n.c;
    d -= n.d; e -= n.e; f -= n.f;
    g -= n.g; h -= n.h; i -= n.i;
    return *this;
  }
  Matrix& operator*= (const double& z){
    a *= z; b *= z; c *= z;
    d *= z; e *= z; f *= z;
    g *= z; h *= z; i *= z;
    return *this;
  }
  Matrix& operator/= (const double& z){
    a /= z; b /= z; c /= z;
    d /= z; e /= z; f /= z;
    g /= z; h /= z; i /= z;
    return *this;
  }
  Matrix operator+ (const Matrix& n){
    Matrix r = *this;
    return r += n;
  }
  Matrix operator- (const Matrix& n){
    Matrix r = *this;
    return r -= n;
  }
  Matrix operator* (const double& z){
    Matrix r = *this;
    return r *= z;
  }
  Matrix operator/ (const double& z){
    Matrix r = *this;
    return r /= z;
  }
};
```

Main code for 2D slab growing on a substrate, `Gyrus.cpp`:

```
#include "vema.h"
#include <stdlib.h>
#include <iostream>
#include <fstream>
#include <iomanip>
#include <vector>
using namespace std;

void writePov(Vector*, double*, int, int, int, int, int);

int main(int argc, char* argv[]) {

  const double Pi = acos(-1.0);
  const double W = 0.25; // width of the soft layer
  const double H = 0.1; // depth of the soft layer
  const int Lh = 241; // number of elements in the width direction
  const int Lw = 61; // number of elements in the depth direction
  const int ns = 24; // of which are in the soft layer
  const double totalTime = 40.0;
  const double mui = 1.0; // layer shear modulus
  const double Ki = 1000.0*mui; // layer bulk modulus
  const double muo = 1.0; // substrate shear modulus
  const double Ko = 1000.0*muo; // substrate bulk modulus
  const double alfaxs = 0.6; // loading parameters
  const double alfaxm = 0.8;
  const double alfazs = 0.0;
  const double alfazm = 0.0;
  int di = 10000; // output interval

  const double aw = W/(Lw-1); // horizontal element size
  const double ah = H/ns; // vertical element size
  const double rho = 1.0; // density
  const double dt = 0.2*sqrt(rho*aw*ah/Ki); // time step size
  double gamma = 4.0*aw*aw; // damping parameter
  double time = 0.0; // time
  int timeStep = 0; // time step
```

```
Vector* Ut0 = new Vector[Lw*Lh]; // initial position
Vector* Ut = new Vector[Lw*Lh]; // current position
Vector* Vt = new Vector[Lw*Lh]; // velocities
Vector* Ft = new Vector[Lw*Lh]; // forces
double* We = new double[(Lw-1)*(Lh-1)]; // elastic energy
double* Tmises = new double[(Lw-1)*(Lh-1)]; // Mises stress
double* Tmean = new double[(Lw-1)*(Lh-1)]; // mean isotropic stress

double* vn0t = new double[Lw*Lh]; // volume of the initial nodal element
    in the layer
double* vnt = new double[Lw*Lh]; // volume of the nodal element in the
    layer
double* vn0s = new double[Lw*Lh]; // volume of the initial nodal element
    in the substrate
double* vns = new double[Lw*Lh]; // volume of the nodal element in the
    substrate
double* mn = new double[Lw*Lh]; // mass of the nodal element

int i, j, q;
Matrix I;
double U;
double alfax, alfaz, hgyrrel, dsulc, wsulc;
double Ge = 1.0;
double lambdasmin;

cout.precision(3);
ofstream dat;
dat.precision(6);

// initializing nodes
for (j = 0; j < ns; j++) {
   for (i = 0; i < Lw; i++) {
      Ut[j*Lw + i] = Vector(aw*i, H-ah*j, 0.0);
      Ut0[j*Lw + i] = Ut[j*Lw + i];
      Ut[j*Lw + i].y += (ns-j)*ah*(alfaxs + alfazs + alfaxs*alfazs);
   }
}
double ahs = ah;
for (j = ns; j < Lh; j++) {
```

```
    for (i = 0; i < Lw; i++) {
       Ut[j*Lw + i] = Vector(aw*i, -ahs*(j-ns), 0.0);
       Ut0[j*Lw + i] = Ut[j*Lw + i];
    }
    ahs *= 1.0;
 }

 while (time < totalTime) {

    // Parameters alfax and alfaz are the growth in x and z directions.
    // Here, these parameters are loaded from min to max values.
       alfax = alfaxs + (alfaxm-alfaxs)*time/totalTime;
       alfaz = alfazs + (alfazm-alfazs)*time/totalTime;


    // Assigning mass and volume of each node
    for (i = 0; i < Lw*Lh; i++) { vn0t[i] = 0.0; vnt[i] = 0.0; vn0s[i] =
        0.0; vns[i] = 0.0; mn[i] = 0.0; }
    for (j = 0; j < Lh-1; j++) {

       Matrix G; // Growth matrix
       if (j < ns) {
          G.a = 1.0 + alfax;
          G.e = Ge;
          G.i = 1.0 + alfaz;
       }
       else {
          G.a = 1.0;
          G.e = Ge;
          G.i = 1.0;
       }
       for (i = 0; i < Lw-1; i++) {

          int p1 = j*Lw + i;
          int p2 = j*Lw + i + 1;
          int p3 = (j+1)*Lw + i + 1;
          int p4 = (j+1)*Lw + i;
          int n1, n2, n3;
```

```
for (q = 0; q < 2; q++) {
   if (i%2 + j%2 != 1) {
      if (q == 0) { n1 = p4; n2 = p3; n3 = p1; }
      else { n1 = p2; n2 = p1; n3 = p3; }
   } else {
      if (q == 0) { n1 = p3; n2 = p2; n3 = p4; }
      else { n1 = p1; n2 = p4; n3 = p2; }
   }
   Vector xr1 = Ut0[n2] - Ut0[n1];
   Vector xr2 = Ut0[n3] - Ut0[n1];
   Vector xr3 = Vector(0.0, 0.0, 1.0);
   Matrix Ar = Matrix(xr1, xr2, xr3);
   Ar = G.prod(Ar);
   double vol = Ar.det()/2.0;
   if (j < ns) {
      vn0t[n1] += vol/3.0;
      vn0t[n2] += vol/3.0;
      vn0t[n3] += vol/3.0;
   } else {
      vn0s[n1] += vol/3.0;
      vn0s[n2] += vol/3.0;
      vn0s[n3] += vol/3.0;
   }
   mn[n1] += rho*vol/3.0;
   mn[n2] += rho*vol/3.0;
   mn[n3] += rho*vol/3.0;

   Vector x1 = Ut[n2] - Ut[n1];
   Vector x2 = Ut[n3] - Ut[n1];
   Vector x3 = Vector(0.0, 0.0, 1.0);
   Matrix A = Matrix(x1, x2, x3);
   vol = A.det()/2.0;
   if (j < ns) {
      vnt[n1] += vol/3.0;
      vnt[n2] += vol/3.0;
      vnt[n3] += vol/3.0;
   } else {
      vns[n1] += vol/3.0;
      vns[n2] += vol/3.0;
```

```
            vns[n3] += vol/3.0;
         }
      }
   }
}

// Calculate deformation and nodal force
U = 0.0;
for (j = 0; j < Lh-1; j++) {

   Matrix G; // Growth matrix
   double mu, K;
   if (j < ns) {
      G.a = 1.0 + alfax;
      G.e = Ge;
      G.i = 1.0 + alfaz;
      mu = mui;
      K = Ki;
   }
   else {
      G.a = 1.0;
      G.e = Ge;
      G.i = 1.0;
      mu = muo;
      K = Ko;
   }
   for (i = 0; i < Lw-1; i++) {

      We[j*(Lw-1) + i] = 0.0; Tmises[j*(Lw-1) + i] = 0.0;
          Tmean[j*(Lw-1) + i] = 0.0;
      int p1 = j*Lw + i;
      int p2 = j*Lw + i + 1;
      int p3 = (j+1)*Lw + i + 1;
      int p4 = (j+1)*Lw + i;
      int n1, n2, n3;

      for (q = 0; q < 2; q++) {
         if (i%2 + j%2 != 1) {
            if (q == 0) { n1 = p4; n2 = p3; n3 = p1; }
```

```
   else { n1 = p2; n2 = p1; n3 = p3; }
} else {
   if (q == 0) { n1 = p3; n2 = p2; n3 = p4; }
   else { n1 = p1; n2 = p4; n3 = p2; }
}
Vector xr1 = Ut0[n2] - Ut0[n1];
Vector xr2 = Ut0[n3] - Ut0[n1];
Vector xr3 = Vector(0.0, 0.0, 1.0);
Matrix Ar = Matrix(xr1, xr2, xr3);
Ar = G.prod(Ar);

Vector x1 = Ut[n2] - Ut[n1];
Vector x2 = Ut[n3] - Ut[n1];
Vector x3 = Vector(0.0, 0.0, 1.0);

Vector N1 = Vector(-x1.y, x1.x, 0.0);
Vector N2 = Vector(x2.y, -x2.x, 0.0);
Vector N3 = Vector(-(x2-x1).y, (x2-x1).x, 0.0);

Matrix A = Matrix(x1, x2, x3);
double vol = A.det()/2.0;
Matrix F = A.prod(Ar.inv());
Matrix B = F.prod(F.trans());
double J = F.det();

double J1, J2, J3;
if (j < ns) {
   J1 = vnt[n1]/vn0t[n1];
   J2 = vnt[n2]/vn0t[n2];
   J3 = vnt[n3]/vn0t[n3];
} else {
   J1 = vns[n1]/vn0s[n1];
   J2 = vns[n2]/vn0s[n2];
   J3 = vns[n3]/vn0s[n3];
}
double Ja = (J1 + J2 + J3)/3.0;

Matrix T = (B - I*B.trace()/3.0)*mu/pow(J, 5.0/3.0) +
    I*K*(Ja-1.0); // Cauchy stress is calculated.
```

```
            // Force for each node
            Ft[n1] += T.prod(N1 + N2)*0.5;
            Ft[n2] += T.prod(N1 + N3)*0.5;
            Ft[n3] += T.prod(N2 + N3)*0.5;

            if (timeStep%di == 0) {
            // Calculate elastic energy
               double Ws = 0.5*mu*(B.trace()/pow(J, 2.0/3.0) - 3.0);
               double Wv = 0.5*K*( (J1-1.0)*(J1-1.0) + (J2-1.0)*(J2-1.0) +
                   (J3-1.0)*(J3-1.0) )/3.0;
               U += (Ws + Wv)*vol/J;
               We[j*(Lw-1) + i] += 0.5*(Ws + Wv)/mu;
               Tmises[j*(Lw-1) + i] += sqrt(((T.a-T.e)*(T.a-T.e) +
                   (T.e-T.i)*(T.e-T.i) + (T.a-T.i)*(T.a-T.i) + 6.0*(T.b*T.b
                   + T.c*T.c + T.f*T.f))*0.5)*0.5/mu;
               Tmean[j*(Lw-1) + i] += T.trace()/3.0*0.5/mu;
            }
         }
      }
   }

   // Periodic boundary conditions
   for (j = 0; j < Lh; j++) {
      Ft[j*Lw].x = 0.0;
      Ft[j*Lw + Lw-1].x = 0.0;
   }

   // Base boundary condition
   for (i = 0; i < Lw; i++) {
      Ft[(Lh-1)*Lw + i].clear();
   }

   // Initial force
   if (time < 0.5*totalTime) {
      Ft[0].y -= mui*aw*0.001;
   }

   // Contact force
```

```
      for (i = 1; i < Lw-1; i++) {
         if (Ut[i].x < 0.0) Ft[i].x += -Ut[i].x*Ki*2.0;
      }

      // Output
      if (timeStep%di == 0) {

         hgyrrel = (Ut[Lw-1].y - Ut[ns*Lw + Lw-1].y)/(Ut[0].y - Ut[ns*Lw].y);
         dsulc = (Ut[Lw-1].y - Ut[0].y)/(ns*ah*Ge);
         wsulc = 2.0*W/(ns*ah*Ge);
         cout  << setw(11) << timeStep << setw(11) << time << setw(11) <<
             alfax << setw(11) << U/(W*H*Ge) << setw(11) << wsulc << setw(11)
             << dsulc << setw(11) << hgyrrel << endl;
         timeStep == 0 ? dat.open("Slab.dat") : dat.open("Slab.dat",
             ios::app);
         dat << setw(13) << timeStep << setw(13) << time << setw(13) << alfax
             << setw(13) << U/(W*H*Ge) << setw(13) << wsulc << setw(13) <<
             dsulc << setw(13) << hgyrrel << endl;
         dat.close();
         if (timeStep%(10*di) == 0) {
            writePov(Ut, We, Lw, Lh, ns, timeStep, 0);
            writePov(Ut, Tmises, Lw, Lh, ns, timeStep, 2);
            writePov(Ut, Tmean, Lw, Lh, ns, timeStep, 3);
         }
      }

      // Newtonian dynamics
      for (i = 0; i < Lw*Lh; i++) {
         Ft[i] -= Vt[i]*gamma;
         Vt[i] += Ft[i]/mn[i]*dt;
         Ut[i] += Vt[i]*dt;
         Ft[i].clear();
      }
      timeStep++;
      time += dt;
   }
   return 0;
}
```

```
// Outputting the mesh in pov file
void writePov(Vector* Ut, double* cdata, int Lw, int Lh, int ns, int
    timeStep, int mod) {

   char povname[50];
   double dvsr, addt;
   if (mod == 0) { sprintf(povname, "We%d.pov", timeStep); dvsr = 1.0; addt
       = 0.0; } // Colour coded with energy
   else if (mod == 1) { sprintf(povname, "Wp%d.pov", timeStep); dvsr = 2.0;
       addt = 0.0; } // Unused
   else if (mod == 2) { sprintf(povname, "M%d.pov", timeStep); dvsr = 5.0;
       addt = 0.0; } // Colour coded with Mises stress
   else if (mod == 3) { sprintf(povname, "S%d.pov", timeStep); dvsr = -10.0;
       addt = 0.5*dvsr; } // Colour coded with mean isotropic stress
   ofstream pov(povname);
   pov.setf(ios::fixed);
   pov.precision(5);
   double r, g, b, ee, ctmp;
   int n1, n2, n3;
   int* cnodef = new int[Lw*Lh];

   // Vertex colours
   for (int j = 0; j < Lh; j++)
      for (int i = 0; i < Lw; i++) {
         ctmp = (cdata[min(j, Lh-2)*(Lw-1) + min(i, Lw-2)]
            + cdata[max(j-1, 0)*(Lw-1) + min(i, Lw-2)]
            + cdata[min(j, Lh-2)*(Lw-1) + max(i-1, 0)]
            + cdata[max(j-1, 0)*(Lw-1) + max(i-1, 0)])*0.25;
         ctmp = min(1.0, max(0.0, (ctmp + addt)/dvsr));
         if (ctmp >= 0.0) cnodef[j*Lw + i] = (int)(498.0*ctmp) + 2;
   }

   pov << "background { color rgb <1.0, 1.0, 1.0> }\n";
   pov << "camera { location <0, 0, -1.5> look_at <0, 0, 0> sky <0, 1, 0>
       }\n";
   pov << "light_source { <0, 0, -1.5> color rgb <1, 1, 1> }\n";

   // Triangles
   pov << "#declare half = union {\n";
```

```
pov << "mesh2 { \n";
pov << "vertex_vectors { " << Lw*Lh << ",\n";
for (int j = 0; j < Lh; j++)
   for (int i = 0; i < Lw; i++) {
      pov << "<" << Ut[j*Lw + i].x << "," << Ut[j*Lw + i].y << ",0.0>,\n";
   }
pov << "} texture_list { " << 501 << ",\n";
pov << "texture{pigment{rgb<0.4,0.4,0.4>} finish { ambient 0.5 }}\n";
pov << "texture{pigment{rgb<0.7,0.7,0.6>} finish { ambient 0.5 }}\n";
for (int i = 0; i < 499; i++) {
   ee = (double)i/498.0;
   if ( ee < 0.2 ) { r = 0.0; g = 0.0; b = 0.5 + ee/0.4; }
   if ( ee >= 0.2 && ee < 0.4 ) { r = 0.0; g = (ee-0.2)/0.2; b = 1.0; }
   if ( ee >= 0.4 && ee < 0.6 ) { r = (ee-0.4)/0.2; g = 1.0; b = 1.0 - r;
       }
   if ( ee >= 0.6 && ee < 0.8 ) { r = 1.0; g = 1.0 - (ee-0.6)/0.2; b =
       0.0; }
   if ( ee >= 0.8 ) { r = 1.0 - (ee-0.8)/0.3; g = 0.0; b = 0.0; }
   pov << "texture{pigment{rgb<" << r << "," << g << "," << b << ">}
       finish { ambient 0.5 }}\n";
}
pov << "} face_indices { " << 2*(Lw-1)*(Lh-1) << ",\n";
for (int j = 0; j < Lh-1; j++)
   for (int i = 0; i < 2*(Lw-1); i++) {
      if ((i/2)%2 + j%2 == 1) {
         n1 = (j+1-i%2)*Lw + i/2+i%2;
         n2 = (j+i%2)*Lw + i/2+i%2;
         n3 = (j+1-i%2)*Lw + i/2+1-i%2;
      } else {
         n1 = (j+i%2)*Lw + i/2+i%2;
         n2 = (j+i%2)*Lw + i/2+1-i%2;
         n3 = (j+1-i%2)*Lw + i/2+i%2;
      }
      pov << "<" << n1 << "," << n2 << "," << n3 << ">," << cnodef[n1] <<
          "," << cnodef[n2] << "," << cnodef[n3] << ",\n";
   }
pov << "}}\n";

// Grid
```

```
   for (int j = 0; j < Lh-1; j++)
      for (int i = 0; i < Lw-1; i++) {
         if (i%8 == 0) pov << "cylinder{<" << Ut[j*Lw + i].x << "," <<
            Ut[j*Lw + i].y << ",0.0>,<" << Ut[(j+1)*Lw + i].x << "," <<
            Ut[(j+1)*Lw + i].y << ",0.0>, 0.0006 pigment{rgb<1,1,1>}
            finish{ambient 1}}\n";
         if (j == 0 || j == ns) pov << "cylinder{<" << Ut[j*Lw + i].x << ","
            << Ut[j*Lw + i].y << ",0.0>,<" << Ut[j*Lw + i+1].x << "," <<
            Ut[j*Lw + i+1].y << ",0.0>, 0.0018 pigment{rgb<1,0,1>}
            finish{ambient 1}}\n";
         else if (j%8 == 0) pov << "cylinder{<" << Ut[j*Lw + i].x << "," <<
            Ut[j*Lw + i].y << ",0.0>,<" << Ut[j*Lw + i+1].x << "," <<
            Ut[j*Lw + i+1].y << ",0.0>, 0.0006 pigment{rgb<1,1,1>}
            finish{ambient 1}}\n";
      }
   pov << "}\n";
   pov << "object { half }\n";
   pov << "object { half rotate <0, 180, 0> }\n";
   pov.close();
   delete [] cnodef;
}
```